The Structure of Elliptical Galaxies and Galaxy Clusters

by

David Augustin Buote

Submitted to the Department of Physics
in partial fulfillment of the requirements for the degree of

Doctor of Philosophy

at the

MASSACHUSETTS INSTITUTE OF TECHNOLOGY

June 1995

Author .....
Department of Physics
May 5, 1995

Certified by .....
Claude R. Canizares
Professor
Thesis Supervisor

Accepted by .....
George F. Koster
Chairman, Departmental Graduate Committee

The Structure of Elliptical Galaxies and Galaxy Clusters

by

David Augustin Buote

Submitted to the Department of Physics
on May 5, 1995, in partial fulfillment of the
requirements for the degree of
Doctor of Philosophy

Abstract

I have analyzed the X-ray–emitting gas in elliptical galaxies and galaxy clusters to probe their structure and dynamics. In addition to extending previous studies of detailed hydrostatic modeling of these systems, I have developed a new method to test for the existence of dark matter that is free from uncertainties in the temperature gradients and (in principle) does not require any model fitting. Applying these techniques to ROSAT PSPC data of the E4 galaxy NGC 720 I concluded that the dark matter distribution is highly elongated with ellipticity, $\epsilon \approx 0.5 - 0.7$; similar, but weaker, constraints are obtained for the E7/S0 galaxy NGC 1332. These results provide the first strong evidence for flattened halos in normal (i.e. no polar rings) ellipticals. I have also demonstrated that X-ray analysis of the aggregate shape of a galaxy cluster on scales of $r \sim 1-2$ Mpc is insensitive to subclustering on small scales ($\lesssim$ few hundred kpc). From analysis of ROSAT PSPC data of the aggregate shapes of five Abell clusters I concluded that they are quite elongated ($\epsilon \sim 0.40 - 0.55$) and are consistent with the shapes traced by the galaxy isopleths. Finally, I have devised a method to quantitatively relate the morphologies of clusters to their dynamical states. Applying this method to ROSAT PSPC images of 55 clusters I find that the statistics of this method, *power ratios*, suggest an evolutionary track for the clusters; i.e. the location of a cluster along the track indicates the dynamical state of the cluster and the distribution of clusters along this track measures the formation and evolution of clusters in our sample. In principle power ratios can be used to address any problem where cluster evolution is an issue.

Thesis Supervisor: Claude R. Canizares
Title: Professor

On Dark Matter

by Augustin LaTorre

What wasn't thought was there
Is now assuming status
Whirling globes acting strange
As on an unknown lattice.

By scratching head & with computer
And using higher math
We found out the reason why
The globes had such a path.

And the reason for it all
After computing all the data
Was something unknown hitherto
It is called Dark Matter.

And matter it must be
Though unseen in inky dark
Like the me-ow without the cat
The trill without the lark.

It all seems to reason well
Else Newton's Laws in traction
If a force that was applied
Did not produce reaction.

Acknowledgments

My transformation from a callow acolyte to an adept, at least within a very specialized sphere (or, shall I say, ellipsoid?), has been a journey at times rewarding, often arduous, but never dull. The journey never could have been completed without the advice, encouragement, and support of many professors, fellow graduate students, and especially my family and friends. Since it is impossible to acknowledge everyone, I extend a universal "thanks!" to those special people who, for lack of space (or my memory!), I fail to explicitly recognize.

I must first express warm thanks to my thesis supervisor, Claude Canizares, for suggesting such an interesting research topic and also allowing me the freedom to explore other avenues of my choice. I have greatly appreciated Claude's easy-going style and willingness to send me to relevant conferences and provide the necessary computing resources. Thanks are also due to the other astrophysics professors on my thesis committee: Ed Bertschinger and John Tonry. Ed's cosmology class was probably the most influential course I took at MIT, and I especially value the discussions we had during his office hours. I also thank Ed for welcoming me to his cosmology group meetings which have allowed me to keep abreast of the current trends in theoretical cosmology. I thank John for asking me to investigate his clever geometrical exposition of elementary gravitational-lens theory. The hours I spent with John fleshing out these ideas were certainly some of the most intellectually stimulating of my graduate career.

What can I say about John Tsai? If it were not for John it is unlikely I would have tackled the issue of substructure in clusters and a very important part of my thesis would never have come about. John, many thanks for convincing me that I should think seriously about finding a way to quantify substructure. Working with John has been my first collaboration outside MIT, and I think my independence and confidence have grown as a result. I look forward to continuing our collaboration on the power ratios!

Many graduate students, some graduated, some still here, have either taken the

time to listen to my ramblings about my research, have engaged me in general stimulating scientific discussions, have commiserated with me about all the various indignities that graduate students must inevitably suffer, and have even played some very good games of volleyball of which I had the pleasure of participating. I first thank Eric Gaidos, comrade-in-Canizares, for being an effective "sounding board" by being diligent to always remind me that other viewpoints exist, especially from those who live outside 0.1 - 10 keV. I also want to thank Chris Becker, John Blakeslee, Jim Frederick, Lam Hui, Una Hwang, C.-P. Ma, gene Magnier, Bob Rutledge, Uros Seljak, and Jon Woo for scientific chats over these years. All the current denizens of room 616 – Eric, Bob, Derek, Jeff, and Patrick – I thank you for making this small room always a pleasant environment for work or just shooting-the-breeze. I hope I have not been too insufferable these last few months as my thesis has neared completion and the job situation has become increasingly more depressing. I know you guys won't say anything but I will: Thanks for putting up with me.

My work was made easier by a few scientists who were considerate enough to share their computing resources with me. In particular, I thank Mark Bautz, Dan Dewey, George Ricker, and Mike Wise for kindly allowing me use of their computers.

In this limited space I cannot possibly express all the gratitude I owe to my family and friends, but that does not mean I will not try! Mom and Dad, thanks for your constant encouragement and support, both emotionally and financially, whenever I have needed it – the "care packages" have also been much appreciated! Paul, my bro, same goes to you! I would like to specially thank Nana and Papa for just being so wonderful over these many years. To my buddies Fran and Paul (i.e. Riches): thanks for being there all these years – has it really been *that* long?

Through it all these past five years, the good times, the bad times, the ups and downs, there has been a constant in my life, my best friend, Hweilee. Without her kindness and reassuring warmth I could not have accomplished this thesis while maintaining my sanity. Thanks, Hwei, for everything: it would not have been the same without you!

Finally, I thank my grandfather for his unique interpretation of dark matter.

Contents

List of Tables

Chapter 1

Introduction

1.1 Theoretical Motivation

1.1.1 Dark Matter

Understanding the structure of elliptical galaxies and galaxy clusters is crucial to deciphering the nature and distribution of dark matter in the universe; for a review of dark matter in ellipticals see Ashman (1992) and for clusters see Canizares (1995). Just knowing how much matter is present in these systems is important for cosmology. If ellipticals, like spiral galaxies, generally have halos of dark matter ten times more massive than the visible matter then totalling up the masses of individual galaxies in the universe leads to $\Omega_{gals} \sim 0.01$ which is consistent with all of the dark matter being composed of baryons produced in the early universe (e.g., Rees 1995); microlensing techniques are now being employed to detect baryonic dark matter in our own galaxy (e.g., Paczyński 1995). On comparison of the total M/L for clusters of galaxies to the critical M/L for the universe ($\sim 1,350hL_{\odot}\mathrm{Mpc}^{-3}$), Ω_{clus} is found to be $\sim 0.1 - 0.3$, about ten times larger than the mass predicted by standard Big Bang Nucleosynthesis (e.g., Peebles 1986). Recently, White et al. (1993) have emphasized that the large ratios of gas mass to total gravitating mass in galaxy clusters may have serious repercussions for many cherished notions of the standard cosmology such as the prediction of the abundances of light elements produced in the Big Bang and the

prediction by the inflationary model for the universe that $\Omega = 1$.

Although interesting from purely a dynamics perspective (e.g., de Zeeuw & Franx 1991), the *shapes* of the dark matter halos also provide important insights into cosmological theories not addressed by simply knowing the total amount and radial distribution of the dark matter. The influence of early tidal distortions in the formation of ellipticals and clusters (Binney & Silk 1979; Dubinski 1993), the degree of dissipation of the dark matter (e.g., Strimple & Binney 1979; Aarseth & Binney 1978; Ashman 1992), and the density of the universe (Eisenstein & Loeb 1995) all affect the intrinsic shapes of these systems. N-body simulations of the formation of halos in a universe filled with Cold Dark Matter make definite predictions for the shapes of dark matter halos in ellipticals and clusters. Dissipationless simulations produce galaxy-size halos that are generally prolate-triaxial and have quite flattened halos ($\epsilon \sim 0.5 - 0.6$) with a sharp decline in the number of halos with $\epsilon > 0.6$ (Dubinski & Carlberg 1991). Including the effects of a small dissipational component only slightly reduces the ellipticity of the long axis ($\epsilon \sim 0.5$), but changes the overall shape of the halo to oblate-triaxial (Katz & Gunn 1991; Dubinski 1994). For cluster-size halos the N-body simulations yield similar predictions. Dissipationless simulations produce halos that are prolate-triaxial and generally have $\epsilon \leq 0.5$ but several have ϵ approaching 0.67 (Frenk et al. 1988; Efstathiou et al. 1988); the effects of dissipation make the halos more oblate (Katz & White 1993).

As I embarked on this thesis in 1991 there was no reliable measurement of the intrinsic shape of an elliptical galaxy or galaxy cluster. The best constraints for an early-type galaxy were from analysis of the polar-ring galaxy NGC 4650 by Sackett & Sparke (1991). They concluded that the most likely flattening for the halo is $\epsilon \approx 0.6$, but halos with $\epsilon \approx 0.2 - 0.8$ could not be ruled out. In any event, polar-ring galaxies need not have halos typical of most galaxies. The only study of the intrinsic shape of the dark matter in a galaxy cluster was by Fabricant, Rybicki, & Gorenstein (1984) who used X-ray data to obtain a relatively precise constraint on the ellipticity of $0.36 - 0.41$ for A2256. However, Fabricant later retracted the result in Fabricant, Kent, & Kurtz (1989) because of the suspicion of "substructure" (later confirmed

by Briel et al. 1991) and the belief that such "substructure" rendered invalid the assumption of hydrostatic equilibrium central to their analysis.

1.1.2 Substructure in Galaxy Clusters

Before 1980 galaxy clusters were thought to be relaxed systems similar in dynamics to isothermal spheres (e.g., Sarazin 1986). However, this notion was challenged when multiple peaks, or "substructure", in the galaxy number density of many rich clusters were discovered (see Geller & Beers 1982 and references therein). Geller & Beers undertook the first systematic study of substructure in a sample of 65 rich clusters wherein they defined substructure to be a statistically significant measurement of more than one density peak in the galaxy distribution of a cluster. They concluded that 40% of the clusters in their sample showed evidence for substructure and interpreted this as a signal of their dynamical youth.

The debate over the statistical significance of substructure in clusters raged during the 1980s ending with no general consensus (see West 1990 for a review). Moreover, no effort was made to quantitatively assess the relevance of detected substructure to the dynamical mass estimates of clusters. This lead some investigators (see Fabricant above) to disbelieve any conclusions on cluster mass distributions based on the assumption of hydrostatic equilibrium. Others, like Fitchett (1990), acknowledged that without very high signal-to-noise X-ray maps the detailed (i.e. small scale) cluster mass distribution might not be obtained, but the large scale mass obtained from the assumption of hydrostatic equilibrium would likely be insensitive to small-scale subclustering. Clearly this issue of the dynamical relevance of substructure needs to explored more extensively.

A recent paper by Richstone, Loeb, & Turner (1992) has suggested the exciting possibility that the frequency of substructure in clusters is intimately connected to Ω. They argue that in a low-Ω universe structure forms early and thus clusters should have evolved substantially by our epoch. However, if $\Omega = 1$ clusters are still forming and thus should display various signatures of substructure. The difficulty lies in translating the theory into a precise observational prediction. The definition of

substructure as multiple peaks in the cluster surface density is highly ambiguous; i.e. as an extreme example, each individual galaxy in a cluster represents substructure in the mass distribution but clearly that does not mean a cluster is dynamically young.

Jones & Forman (1992) attempted to devise a more consistent description of substructure by visually separating clusters into six morphological classes. Using a sample of $\sim$ 200 clusters observed with *Einstein*, Jones & Forman computed the frequency of these morphological classes and concluded that about 40% of clusters displayed some type of substructure; recent studies suggest a substantial increase in this percentage (e.g., West 1995). Using the Jones & Forman results, Richstone et al. concluded that $\Omega \gtrsim 0.5$, the only indication for a large Ω consistent with inflation besides analysis of large-scale velocity fields (Dekel 1994).

However, these conclusions are uncertain because it is not clear how the morphological classes of Jones & Forman really relate to the dynamical states of the clusters; e.g., a distant cluster that is not well resolved might appear relaxed while a nearby cluster might show small-scale irregularities but be essentially relaxed on large scales. Even well defined and quantitative measures of cluster morphologies which employ centroid-shifts and axial ratios (Evrard et al. 1993, Mohr et al. 1995) fail to provide any physical connection of these parameters to the dynamical states of clusters. Thus, although these techniques are useful as a first step, they have not fully realized the potential of cluster morphologies to describe the evolutionary states of clusters and thus place reliable constraints on Ω.

1.2 Status of the X-ray Observations

Soon after it was established that the X-ray emission from normal elliptical galaxies (Forman et al. 1979) and galaxy clusters (Mitchell et al. 1976) are the result of thermal emission from hot gas, X-rays became the preferred means to analyze the mass distributions in these systems; for reviews see Sarazin (1986), Fabbiano (1989), and Fitchett (1990). Since the mean free path of the gas in ellipticals ($\sim$ 20 pc) and clusters ($\sim$ 20 kpc) is small over the typical scales that are probed (see Sarazin 1986),

the X-ray–emitting gas may be treated as an isotropic fluid to very good approximation. Hence, the uncertainties in the shape of the velocity dispersion tensor which render inconclusive optical studies of ellipticals (Binney & Mamon 1982; Tonry 1983) and clusters (Merritt 1987) do not apply to X-ray studies. Moreover, X-ray studies of clusters are less susceptible to contamination from foreground / background objects than optical studies. This is because the X-ray luminosity is a strong function of the temperature, or mass, which means that foreground groups contribute proportionally less to the X-ray emission than they do to the galaxy surface density. X-ray studies of clusters also have the advantage that the signal is limited only by the sensitivity of the detector and exposure time of an observation whereas optical studies are limited by the finite number of galaxies

The vast majority of X-ray studies of the mass distributions in ellipticals and clusters, with only a few notable exceptions, analyzed the radial mass distribution assuming spherical symmetry as first described by Fabricant, Lecar, & Gorenstein (1980). Unfortunately, the radial mass distribution is strongly dependent on the temperature gradient of the gas which was not well constrained by previous X-ray detectors. Thus, before the launch of ROSAT in 1990 (Trümper 1983), X-ray techniques failed to accurately determine the dark matter distributions in clusters (Hughes 1989) or establish whether any dark matter is required in ellipticals (Trinchieri, Fabbiano, & Canizares 1986).

Binney & Strimple (1978; Strimple & Binney 1979) pioneered the use of X-ray images to analyze the intrinsic shapes of galaxy clusters. Of particular importance, Strimple & Binney (1979) showed that a cluster of a given shape produced very similar X-ray isophotes when the gas is assumed to be either isothermal or adiabatic; i.e. possible radial temperature gradients in the gas do not seriously affect determination of the intrinsic shapes. Before 1992, only Fabricant, Rybicki, & Gorenstein (1984) and White & Canizares (1987; White 1987) attempted to exploit the work of Binney & Strimple. As I mentioned in §1.1.1, because of possible substructure Fabricant questioned the validity of the assumption of hydrostatic equilibrium and thus his constraints on the intrinsic shape of A2256. White & Canizares (1987), who at-

tempted to study the intrinsic shapes of ellipticals, were foiled by the poor resolution of *Einstein*.

Recently gravitational-lens analysis of the weak distortions of background galaxies in clusters has lead to a powerful, non-parametric, non-dynamical method to measure the projected mass distribution in clusters (Kaiser & Squiers 1993). Because of the required source-lens-observer separations, however, this method is generally restricted to high-redshift clusters ($0.15 \lesssim z \lesssim 0.6$) whereas X-ray methods in principle can be applied at any redshift. This method is also impractical for studying the mass distribution in individual galaxies because the angle subtended by galactic halos at the redshifts required for significant lensing effect contain too few background galaxies for an adequate signal; however, it may be possible to usefully probe the outer portions of galactic halos with this method (i.e. $r \gtrsim 100$ kpc).

1.3 Goals of this Thesis

With the launch of the Position Sensitive Proportional Counter (PSPC) on board ROSAT, and its substantial improvement in spatial resolution, sensitivity, and field of view (Pfeffermann et al. 1987; Aschenbach 1988), X-ray analysis of the mass distributions, and especially the intrinsic shapes, of ellipticals and clusters entered a new era of feasibility. Moreover, the improved spatial resolution allows much more precise investigations of "substructure" in clusters. I took the opportunity provided by the high-quality PSPC data to address the following issues:

- Do elliptical galaxies really have large amounts of dark matter. If so, what is the shape of the dark halo?
- Does the presence of "substructure" in clusters of galaxies invalidate X-ray analysis of its intrinsic shape? If not, what are the intrinsic shapes of some bright, nearby clusters?
- Is there a clear, quantitative way to relate cluster morphologies to their dynamical states?

I analyzed the intrinsic shapes of the E4 galaxy NGC 720 and E7/S0 galaxy NGC 1332 in Chapters 2 and 3 respectively. Using the N-body / hydrodynamic simulation of Katz & White (1993) I examined the reliability of X-ray constraints of intrinsic cluster shapes in Chapter 4. The intrinsic shapes of five Abell clusters are treated in Chapter 5. Finally, I devised a method to quantify the morphologies of galaxy clusters in direct relation to their dynamical state in Chapter 6 and apply the technique to 55 ROSAT PSPC images of Abell clusters in Chapter 7.

REFERENCES

Aarseth, S. J., & Binney, J. J. 1978, MNRAS, 185, 227

Aschenbach, B. 1988, Appl.Optics, 27, No. 8, 1404

Ashman, K. M. 1992, PASP, 104, 1119

Binney, J. J., & Mamon, G. A. 1982, MNRAS, 200, 361

Binney, J. J., & Silk, J. 1979, MNRAS, 188, 273

Binney, J., & Strimple O. 1978, MNRAS, 187, 473

Briel, U. G., et al. 1991, A&A, 246, 10

Canizares, C. R. 1995, in Stellar Populations (IAU Symp. 164), (Dordrecht: Reidel), in press

Dekel, A. 1994, ARA&A, 32, 371

de Zeeuw, T., & Franx, M. 1991, ARA&A, 29, 239

Dubinski, J., & Carlberg, R. 1991, ApJ, 378, 496

Dubinski, J. 1994, ApJ, 431, 617

Efstathiou, G., Frenk, C. S., White, S. D. M., & Davis, M. 1988, MNRAS, 235, 715

Eisenstein, D. J., & Loeb, A. 1994, ApJ, in press

Evrard, A. E., Mohr, J. J., Fabricant, D. G., & Geller, M. J. 1993, ApJ, 419, 9

Fabbiano, G. 1989, ARA&A, 27, 87

Fabricant, D., Lecar, M., & Gorenstein, P. 1980, ApJ, 241, 552

Fabricant, D., Rybicki, F., & Gorenstein, P. 1984, ApJ, 286, 186

Fabricant, D. G., Kent., S. M., & Kurtz, M. J. 1989, ApJ, 336, 77

Fitchett, M. J. 1989, in Clusters of Galaxies (STScI Symp. 4), ed. W. R. Oegerle, M. J. Fitchett, & L. Danly (Cambridge: Cambridge University Press), 111

Forman, W., Schwarz, J., Jones, C., Liller, W., & Fabian, A. 1979, ApJ, 234, 27

Frenk, C. S., White, S. D. M., Efstathiou, G., & Davis, M. 1988, ApJ, 327, 507

Geller, M. J., & Beers, T. C. 1982, PASP, 94, 421

Hughes, J. P. 1989, ApJ, 337, 21

Jones, C., & Forman W. 1991, in Clusters and Superclusters of Galaxies (NATO ASI Vol. 366), ed. A. C. Fabian, (Dordrecht/Boston/London: Kluwer), 49

Kaiser, N., & Squiers, G. 1993, ApJ, 404, 441

Katz, N., & Gunn, J. E. 1991, ApJ, 377, 365

Katz, N., & White, S. D. M. 1993, ApJ, 412, 455

Merritt, D. 1987, ApJ, 313, 121

Mitchell, R. J., Culhane, J. L., Davison, P. J. W., & Ives, J. C. 1976, MNRAS, 176, 29

Mohr, J. J., Evrard, A. E., Fabricant, D. G., & Geller, M. J. 1995, ApJ, in press

Paczyński, B. 1995, in Dark Matter (AIP Conference Proceedings), ed. C. Bennett, (New York: AIP Press), in press

Peebles, P. J. E. 1986, Nature, 321, 27

Pfeffermann, E. et al., 1987, Proc. SPIE, 733, 519

Rees, M. 1995, in Dark Matter (AIP Conference Proceedings), ed. C. Bennett, (New York: AIP Press), in press

Richstone, D. O., Loeb, A., & Turner, E. L. 1992, ApJ, 393, 477

Sackett, P., & Sparke, L. S. 1993, ApJ, 361, 408

Sackett, P., Rix, H-W, Jarvis, B. J., & Freeman, K. C. 1994, ApJ, 436, 629

Sarazin, C. L. 1986, Rev. Mod. Phys., 58, 1

Strimple, O., & Binney, J. 1978, MNRAS, 188, 883

Tonry, J. L. 1983, ApJ, 266, 58

Trinchieri, G., Fabbiano, G., & Canizares, C., 1986, ApJ, 310, 637

Trümper, J. 1983, Adv. Space Res., 2, 241

West, M. J. 1990, in Clusters of Galaxies (STScI Symp. 4), ed. W. R. Oegerle, M. J. Fitchett, & L. Danly (Cambridge: Cambridge University Press), 65

West, M. J. 1995, in Clusters of Galaxies (Proceedings of the 29th Rencontres de Moriond), ed. F. Durret, A. Mazure, J. Trân Thanh Vân, & S. D. M. White (Gif sur Yvette: Frontier Editions), 23

White, J. 1987, B.S. Thesis, Massachusetts Institute of Technology

White, J., & Canizares, C. 1987, BAAS, 19, 682

White, S. D. M., Navarro, J. F., Evrard, A. E., & Frenk, C. S. 1993, Nature , 366, 429

Chapter 2

Geometrical Evidence for Dark Matter: X-ray Constraints on the Mass of the Elliptical Galaxy NGC 720[1]

We first focus our attention on the intrinsic shapes of elliptical galaxies; first the E4 galaxy NGC 720 and then the E7/S0 galaxy NGC 1332 in the following chapter. In this initial study we discovered that the assumption of hydrostatic equilibrium of the X-ray–emitting gas implies that the elongation of the X-ray isophotes allow a direct test of whether mass traces the optical light in a galaxy without requiring knowledge of the temperature gradient of the gas; i.e. a "geometrical" test for dark matter. We find that this new test requires dark matter in NGC 720 that cannot be explained by alternate gravity theories like MOND. We also improved our hydrostatic modeling technique (Buote & Canizares 1992; Buote 1992) to allow determination of the shape of the dark matter itself using the observed distributions of stars and gas. It turns out that our modeling procedure allows the ratio of dark mass to stellar mass to be determined from the X-ray surface brightness without requiring knowledge of the

[1]The majority of this Chapter has been published as Buote & Canizares 1994, ApJ, 427, 86.

distance to the galaxy. Applying these techniques to ROSAT PSPC data for NGC 720 we find strong evidence for a flattened distribution of dark matter with ellipticity $\sim 0.50 - 0.70$ (90% confidence). This is the first strong evidence for a flattened dark halo in a "normal" elliptical (i.e. no polar ring or emission-line disk) and appears to be consistent with halos produced by simulations of a universe filled with cold dark matter (Dubinski & Carlberg 1992; Dubinski 1994).

2.1 Introduction

The nature and distribution of dark matter in the universe persists as one of the most important unresolved problems in astrophysics. Although preciously little is known about the nature of the dark matter, strong constraints on its radial distribution exist on galactic scales from the flat H I rotation curves in spiral galaxies (for reviews see Kormendy & Knapp 1987; Trimble 1987; Ashman 1992) and, recently, gravitational lens models of luminous arcs in clusters of galaxies (for reviews see Blandford & Narayan 1992; Soucail 1992; Refsdal & Surdej 1993) However, there is comparatively little convincing evidence for dark matter in normal elliptical galaxies (for reviews see Kent 1990; de Zeeuw & Franx 1991; Ashman 1992); this lack of evidence is generally attributed to the fact that most optical studies are confined to within an effective radius of the galaxy center where the effects of dark matter may be unimportant.

X-ray emission from hot gas provides perhaps the greatest potential for accurately mapping the mass of ellipticals to large distances (for a review see Fabbiano 1989). The standard method employed to infer the mass from the X-ray gas derives from the equation of hydrostatic equilibrium and the ideal gas equation of state (Fabricant, Lecar, & Gorenstein 1980),

$$M(< r) = -\frac{r k_B T_{gas}(r)}{G\mu m_p}\left(\frac{d\ln \rho_{gas}}{d\ln r} + \frac{d\ln T_{gas}}{d\ln r}\right), \tag{2.1}$$

where T_{gas} is the gas temperature, ρ_{gas} is the gas density, G is Newton's constant, k_B is Boltzmann's constant, μ is the mean atomic weight of the gas, and m_p is the

proton mass; note that this method assumes spherical symmetry of the mass distribution. At a given r, equation (2.1) has three quantities to be determined from observations; i.e. the gas temperature, temperature gradient, and density gradient. Unfortunately, attempts to apply this technique to *Einstein* data of normal elliptical galaxies yielded very uncertain results because the normal ellipticals had poorly determined temperature profiles. For example, Trinchieri, Fabbiano, & Canizares (1986) analyzed *Einstein* images of six early-type galaxies and concluded that the X-ray data were consistent with massive dark halos but halos were not absolutely required by the data. Similarly, employing the improved spectral resolution of the BBXRT to the Virgo elliptical NGC 4472, Serlemitsos et al. (1993), determine that the data does not demand dark matter. However, they conclude that the BBXRT data for the Fornax elliptical NGC 1399 indeed requires significant amounts of dark matter.

Whereas the previous technique embodied by equation (2.1) probes the radial mass distribution, White (1987; White & Canizares 1987), who built upon the pioneering study of Binney & Strimple (1978; Strimple & Binney 1979), introduced a modification of this method to measure the shape of the total gravitating matter in their study of the elliptical galaxy NGC 720 as well as two other early-type galaxies, NGC 1332 and NGC 4697. They relax the assumption of spherical symmetry and assume the gas is isothermal. By using the ratio of potential depth to gas temperature as a fitting parameter, their method is very insensitive to the precise value of the gas temperature. However, they were still unable to obtain meaningful constraints on the shape of the underlying matter because of the large point spread function of the *Einstein* Imaging Proportional Counter (IPC). Buote & Canizares (1992; Buote 1992) utilized the technique of White (1987; White & Canizares 1987) for analysis of five Abell clusters of galaxies. Because of the larger IPC fluxes and spatial extent of the clusters, Buote & Canizares succeeded in measuring the shape of the gravitating matter; they determined the total matter to be significantly rounder than the galaxy isopleths for all of the clusters.

We improve upon the technique of Buote & Canizares (1992; Buote 1992) to mea-

sure the shape and amount of dark matter in the flattened elliptical NGC 720 using the superior X-ray data provided by the *Röntgen Satellite* (ROSAT). By assuming functional forms for the mass of the visible stars, X-ray gas, and dark matter, our method enables direct measurement of the shape of not only the total gravitating matter, but also the dark matter itself; we show that this method yields a mass estimate that is independent of the distance to the galaxy and the temperature of the gas. In addition, by exploiting the relative geometries of the X-ray and optical isophotes (and an assumed model for the potential of the optical light) we introduce a test for dark matter and alternate gravity theories that is highly insensitive to uncertainties in the gas temperature. In §2.2 we discuss the observations and determination of the relevant parameters required for the analysis; in §2.3 we describe our geometrical test for dark matter; in §2.4 we measure the shape and amount of total gravitating matter; in §2.5 we do the same for the dark matter, in §2.6 we discuss the implications of our results; and in §2.7 we present our conclusions.

2.2 Observations and Data Analysis

We selected NGC 720 for analysis as one of two early-type galaxies with flattened optical morphology and high X-ray flux as measured by *Einstein* (e.g., Fabbiano, Kim, & Trinchieri 1992). The optical isophotes have ellipticity $\epsilon \sim 0.40$, which makes NGC 720 one of the flattest ellipticals, and suggests that its intrinsic shape is close to its projection on the sky (Fasano & Vio 1991; Ryden 1991, 1992; Lambas, Maddox, & Loveday 1992). Here ϵ is defined as $1 - b/a$ where a (b) is the major (minor) axis. Assuming the elongation of the stellar distribution indicates elongation of any putative dark matter, then one would expect the X-ray isophotes tracing the gravitational potential (which, however, is always rounder than the parent mass) would be most elongated for galaxies with the flattest optical isophotes. NGC 720 possesses the largest X-ray flux (e.g., Fabbiano et al. 1992) for a flattened normal galaxy and its emission extends over $13'$ on the sky, thus providing many pixels of angular resolution. In addition, NGC 720 is a relatively isolated elliptical (Dressler, Schechter, & Rose

1986) suggesting that its X-ray emission is mostly free of contamination from external effects such as ram-pressure stripping (Schechter 1987). The galaxy was observed with the Position Sensitive Proportional Counter (PSPC) on board ROSAT; for a description of the ROSAT X-ray Telescope see Aschenbach (1988), and Pfeffermann et al. (1987) for a description of the PSPC. Table 1 summarizes the details of the observation.

The distance to NGC 720 has been determined by several different methods, including Hubble flow analysis (e.g., in Canizares, Fabbiano, & Trinchieri 1987), $D_n - \sigma$ (Donnely, Faber, & O'Connell 1990), and surface brightness fluctuations (Tonry & Blakeslee 1993, private communication). The values derived from these methods systematically differ by as much as 9 Mpc with the $D_n - \sigma$ estimate representing the high end ($24.8 h_{80}$ Mpc) and the surface brightness fluctuations the lower end ($15.6 h_{80}$ Mpc). We adopt $D = 20 h_{80}$ Mpc as essentially a mean value for the distance to NGC 720 where $h_{80} \equiv 1$ for $H_0 = 80$ km s^{-1} Mpc^{-1}; at this distance $1'' \sim 0.1$ kpc.

2.2.1 Spatial Analysis

We rebinned the PSPC image of NGC 720 into 15″ pixels, corresponding to a 512×512 field, which effectively optimizes the signal-to-noise ratio. In order to minimize the X-ray background contribution to the galaxy emission and to optimize the PSF of the PSPC (see below), only data from the hard band (0.4 - 2.4 keV) were used.

Employing the standard IRAF-PROS software, we constructed a surface brightness map from the observation by (1) correcting for exposure variations and telescopic vignetting, (2) removing embedded point sources, and (3) subtracting the background. The vignetting correction for NGC 720 is small since only a few percent of the total emission from the galaxy lies $> 6'$ off-axis where this effect becomes important. The standard processing routines identify point sources in the field using a maximum-likelihood method (cf. *detect* task in PROS). We used this source list as a guide to flag sources not associated with the continuum emission of the galaxy. Three additional point sources not included in this list were identified "by eye". All of these sources were flagged and excluded from succeeding analysis.

The final step in the image reduction is the estimation and subtraction of the background. The in-flight software identifies and eliminates effects of the particle background (Snowden et al. 1992). For the remainder of the X-ray background, the standard processing of the observation generates a template to serve as a convenient background estimate. These templates are constructed by subtracting all of the point sources out of the image and then smoothing. For sources with extended emission, these templates may overestimate the background due to incomplete subtraction of the extended source. We investigated this effect by binning the image (corrected as above) into 15″ radial bins centered on the galaxy emission (cf. §2.2.1). In Figure 1 we plot the azimuthally-averaged radial profile of the image between 100″ and 1000″ and compare to the corresponding region of the background template; we do not assign error bars to the background because the systematic errors dominate any statistical errors as a result of the heavy processing of the template. The statistical errors assigned to the image are 68% Poisson confidence limits obtained using the approximate expressions of Gehrels (1986). The template matches the image to better than a few percent for radii greater than 400″ where the background should dominate the galaxy emission; although the figure displays a slight rise in the backgound towards the center, for $r \lesssim 100''$ small errors in the background are unimportant since there the galaxy emission dominates. Hence, the template represents the background adequately for our purposes. We subtract the background template from the image and use only the statistical uncertainties associated with the image in our analysis.

Figure 2 displays isophotes for the reduced image in a $400'' \times 400''$ region centered on the galaxy. We confine our analysis to the region interior to 375″ as that is where the signal-to-noise (S/N) in each bin is $\gtrsim 1$. We have smoothed the image in Figure2 with a circular Gaussian ($\sigma = 11.25''$) for visual clarity although we emphasize that the image used for analysis is not smoothed in this manner.

Radial Profile

We constructed the azimuthally-averaged radial profile of the X-ray surface brightness as follows. We located the origin of the radial profile at the centroid of the galaxy

emission $(\bar{x}, \bar{y})$ determined by computing the first moments of the count distribution,

$$\bar{x} = \frac{1}{N}\sum_{i=1}^{P} n_i x_i \quad \text{and} \quad \bar{y} = \frac{1}{N}\sum_{i=1}^{P} n_i y_i, \tag{2.2}$$

where i denotes the label of the pixel, P represents the total number of pixels included in the summation, n_i is the number of counts in pixel i, (x_i, y_i) are the Cartesian coordinates of pixel i, and $N = \sum_{i=1}^{P} n_i$ is the total number of counts in pixels P. After choosing a center of the galaxy counts "by eye", the moments were computed within a 150″ circular aperture containing $\sim$ 75% of the total counts ($<$ 375″) and then iterated until the centroid varied by $< 0.1\%$. The centroid position obtained, listed in Table 1, agrees with the optical position to a fraction of a pixel. Next we binned the counts into circular annuli of one pixel width (i.e. 15″) centered at $(\bar{x}, \bar{y})$; we explored the effect of using elliptical annuli having the shapes and orientations of the isophotes (cf. 2.2.1) but found no appreciable gain in S/N. The radial profile of the reduced image is displayed in Figure 3. The shape of the radial profile is not particularly sensitive to the initial guess of the centroid or to the size of the centroid aperture.

Previous studies of the X-ray surface brightness distribution (Σ_X) of galaxies (e.g., Forman, Jones, & Tucker 1985; Trinchieri, Fabbiano, & Canizares 1986; hereafter TFC) used the hydrostatic-isothermal King-type model to parameterize Σ_X,

$$\Sigma_X(r) \propto \left[1 + \left(\frac{r}{a_X}\right)^2\right]^{-3\beta+1/2}, \tag{2.3}$$

where a_X and β are free parameters. The assumption of spherical symmetry in the King model, although not strictly valid for the galaxy isophotes (cf. § 2.2.1), has a small effect on fits to the surface brightness profile of NGC 720. The King model serves as a convenient analytic fit to Σ_X, which facilitates computation of the mass of the X-ray gas (§2.5.2). In order to obtain physical constraints on a_X and β, we convolve Σ_X with the PSPC PSF and perform a χ^2 fit to the radial profile. The on-axis PSF described by Hasinger et al. (1992) depends on the energy of the incident photon

and is composed of a circular Gaussian component due to intrinsic broadening, an exponential component due to focus and photon penetration effects, and a Lorentzian component due to mirror scattering. Performing a counts-weighted average of the galaxy spectrum between 0.4 and 2.4 keV, we adopt $E = 0.88$ keV for evaluation of the PSF. We list the results of the fit in Table 2 along with those published by TFC; the best fit model is plotted in Figure 3. The values for a_X obtained by TFC for NGC 720 with the *Einstein* Imaging Proportional Counter (IPC) agree very well with our values, essentially bracketing our results. However, TFC's 90% confidence limits for the slope parameter β are slightly smaller. We can attribute this difference to the fact that TFC include emission from point sources that we have identified and eliminated; the number of such sources increases with distance from the galaxy center. This effect will tend to flatten their radial profile sufficiently to account for the slight systematic shift in β.

Note that the 90% lower limit for $a_x = 12''$ is significantly larger than the optical core radius of $4''$ (§2.5.1). If the temperature gradients are small (which we show in §2.2.2), then the hydrostatic equation (eq. [2.1]) implies that the total matter must have a core parameter similar in magnitude to a_X. Hence, the discrepancy between X-ray and optical core parameters suggests that the total mass can not be described simply by matter distributed like the visible stars. We address this issue in more detail in later sections.

Ellipticities of the X-ray Isophotes

In comparison to optical images of ellipticals, the PSPC X-ray image of NGC 720 has significantly fewer counts ($\sim$ 1500 for $r < 200''$). As a result, our analysis of the morphology of the X-ray surface brightness more closely parallels the analysis of the galaxy isopleths in a rich cluster than the optical isophotes of an elliptical. We measure the flattening and orientation of the X-ray surface brightness using an iterative moment technique derived from the treatment of the dispersion ellipse of the bivariate normal frequency function of position vectors used by Carter & Metcalf (1980; Trumpler & Weaver 1953) to measure the ellipticities of clusters of galaxies.

The parameters obtained from this method, ϵ_M and θ_M, computed within an elliptical region, provide good estimates of the ellipticity (ϵ) and the position angle (θ) of an intrinsic elliptical distribution of constant shape and orientation. For a more complex distribution, ϵ_M and θ_M are average values weighted heavily by the outer parts of the region; in Buote & Canizares (1992) we apply a slight variation of this method to the study of five Abell clusters.

In order to determine these parameters from an image of P pixels having n_i counts in pixel i, one computes the moments,

$$\mu_{mn} = \frac{1}{N}\sum_{i=1}^{P} n_i (x_i - \bar{x})^m (y_i - \bar{y})^n \qquad (m,n \leq 2), \tag{2.4}$$

where as before $N = \sum_{i=1}^{P} n_i$, and $(\bar{x},\bar{y})$ is the centroid given by equation (2.2). Then the ellipticity is,

$$\epsilon_M = 1 - \frac{\Lambda_-}{\Lambda_+}, \tag{2.5}$$

and the position angle of the major axis measured North through East in Celestial coordinates is,

$$\theta_M = \tan^{-1}\left(\frac{\mu_{11}}{\Lambda_+^2 - \mu_{02}}\right) + \frac{\pi}{2}, \tag{2.6}$$

where $\Lambda_\pm (\Lambda_+ \geq \Lambda_-)$ are the positive roots of the quadratic,

$$(\mu_{20} - \Lambda^2)(\mu_{02} - \Lambda^2) = \mu_{11}^2; \tag{2.7}$$

for an elliptical Gaussian distribution, Λ_+ and Λ_- are the respective lengths of the semi-major and semi-minor axes of the contour representing 0.61 times the maximum surface density. The assumption of a Gaussian distribution is not necessary since μ_{mn} is equivalent to the two-dimensional moment of inertia tensor with Λ_+^2 and Λ_-^2 its principal moments. For any elliptical distribution the square root of the ratio of the principle moments of inertia is the axial ratio and thus ϵ_M is the ellipticity.

We begin by defining a circular aperture ($\epsilon_M = 0$) about the centroid determined in §2.2.1 with the initial value of θ_M set arbitrarily to 0. Then we compute the

appropriate μ_{mn} for all of the pixels in this aperture to obtain new values of ϵ_M, θ_M, $\bar{x}$, and $\bar{y}$. Defining a new elliptical aperture with these parameters, we iterate until the parameters change by less than appropriate tolerances. Using the same iterative procedure, we also compute ϵ_M and θ_M within an elliptical annular aperture. The annulus should correspond more closely to a true isophote since only counts in the immediate vicinity of the isophote are used. However, as we discuss below, the values of ϵ_M and θ_M do not significantly differ for the elliptical and annular apertures.

Characterization of the uncertainties in this procedure involves both statistical and systematic effects. Random uncertainties due to Poisson statistics are straightforward and we derive expressions for the 90% confidence estimates $\Delta\epsilon_M$ and $\Delta\theta_M$ in Appendix A.. Quantification of the systematic uncertainties associated with the computation of ϵ_M is more subtle and requires numerical simulations. Using simulated images, Carter & Metcalfe (1980) concluded that ϵ_M deviates from ϵ (true ellipticity) due to the following systematic effects:

1. For distributions where ϵ is small or zero, any random deviations will increase the measured value of ϵ_M.

2. For distributions where ϵ is large, the initial ellipticity of the circular aperture is far from the desired value. The iteration can get caught in a local stable point at a small value of ϵ_M.

The effect of #1 will be most significant for the very central region where the PSF considerably smears the X-ray isophotes (cf. Figure 2) and perhaps the outermost regions where the ellipticity of the gas is poorly constrained (see below). Given the noticeable flattening of the isophotes outside the core, effect #2 will be important for $r \gtrsim 60''$. Although our analyses of the total mass and dark matter distributions in §2.4 and §2.5 do not demand $\epsilon_M = \epsilon$, we do require the value of ϵ_M computed from the data represent the same quantity when computed from the models. Unlike the models, the image contains Poisson noise. In addition to causing effect #1, the noise may also create local stable points in the image not present in the model which could yield erroneous results. In order to understand how to best treat this effect, we

followed Carter & Metcalfe and generated a series of simulated images with surface density,

$$\Sigma(x,y) \propto \left(r_c^2 + x^2 + \frac{y^2}{q^2}\right)^{-1}, \tag{2.8}$$

where $q = 1 - \epsilon$ is the ratio of the semi-minor to the semi-major axis. Poisson noise was added to these distributions with total counts comparable to the PSPC image. We held fixed the length of the semi-major axis and varied the size of the pixels in the simulated images. The results from the simulations demonstrate that the importance of effects 1 & 2, as well as the stability of the iterative procedure, depend on the size of the pixels. For images with a small number of pixels (coarse grid) the iteration becomes unstable and, if indeed it converges, converges to a value of ϵ_M usually unrelated to ϵ. In contrast, when the image has too large a number of pixels (fine grid) the surface density of the image becomes very flat and the value of ϵ_M does not significantly vary from the initial guess; i.e. for the initial circular aperture, ϵ_M does not stray far from zero, regardless of the intrinsic ellipticity of the distribution. Hence one must find the pixel scale which balances the need for sufficient number of pixels to promote convergence stability while also maintaining reasonable signal-to-noise levels in each pixel.

We adopted a simple test for determination of this optimum pixel scale. For a given semi-major axis, we began by computing ϵ_M in the manner described above; i.e. start with a circular aperture and iterate until ϵ_M converges to within a desired tolerance. Then we repeated the iteration with the initial aperture shape set to a finite value of ϵ_M. This yields another, possibly different, measurement of ϵ_M. The spread in these values computed for many different initial ϵ_M's is a measure of the importance of the systematic errors discussed above. On performing these calculations for several semi-major axes using different pixel scales, we selected 5″ for the pixel scale which simultaneously minimized this systematic uncertainty and the statistical error $\Delta\epsilon_M$; at this scale this systematic uncertainty is typically < 0.02 while for the 15″ pixel image it is < 0.04. Hence we reduce systematic uncertainties associated with ϵ_M by using the image prepared as in §2.2.1 except that the pixels are 5″.

In addition to the iterative moments, we also parameterize the shape of the X-ray surface brightness by fitting perfect ellipses to the isophotes following Jedrzejewski (1987; implemented with the *ellipse* task in the IRAF-STSDAS software). This method has the advantage that the computed parameters for ellipticity (ϵ_{iso}) and position angle (θ_{iso}) correspond to an elliptical isophote at a specific radius and thus may provide a more accurate representation of the radial variation in shape and orientation of the surface brightness. Unfortunately this technique, which was developed to study slight departures of optical isophotes from true ellipses, has the disadvantage of having larger statistical uncertainties than the iterative moments; i.e. as applied in STSDAS, the counts associated with fitting an isophote are only a small fraction of those present in the elliptical apertures used to compute the iterative moments. Because of the premium placed on counts, the image with 15″ pixels was used for the ellipse fitting.

We list the ellipticity results in Table 3 and the corresponding position angles in Table 4 for both the iterative moments (computed for an elliptical aperture and an elliptical annular aperture) and the fitted elliptical isophotes; note that these ellipticities include the blurring due to the PSPC PSF which we will account for in our models in the later sections. The statistical uncertainties associated with the iterative moments ($\Delta\epsilon_M$) represent 90% confidence estimates while those of the fitted isophotes ($\Delta\epsilon_{iso}$) reflect 68% values; we note that the listed values of $\Delta\epsilon_M$ agree well with uncertainties estimated from the above Monte Carlo simulations. For each method the ellipticity parameters agree at all r within their statistical uncertainties, where $r = (ab)^{1/2}$ is the average radius of an ellipse having semi-major axis a and semi-minor axis b. Interior to $\sim 30''$, the X-ray isophotes are nearly circular. This could simply result from the circularly-symmetric blurring of the PSF, an effect that is reproduced in the Monte Carlo simulations when a constant ellipticity surface density is convolved with the PSF of the PSPC; this circularity implies that asymmetries due to errors of aspect correction must be quite small. The isophotes become flatter at large radii, reaching a maximum $\epsilon_M \sim 0.25$ at $r \sim 75''$. Constraints on the flattening for r greater than $\sim 100''$ become weaker as the average pixel S/N approaches unity.

The isophote fitting, which is most sensitive to the surface brightness S/N, does not provide meaningful ellipticity limits for r greater than $\sim 90''$. Using the full elliptical aperture, $\epsilon_M \sim 0.15$ for $r \sim 110'' - 140''$ but the lower limit is only 0.06 (90% confidence). At the same large distance from the galaxy center the elliptical annulus computed on the $15''$ pixel image yields $\epsilon_M = 0.13 \pm 0.07$, which has the same statistical uncertainty associated with the full ellipse even though the annulus has $\sim 1/4$ the number of counts. Although the systematic uncertainties become larger at these distances, the Monte Carlo simulations show that systematic effects tend to (but do not always!) underestimate the true ellipticity; i.e. lower limits on ϵ_M derived using the statistical uncertainty are very likely to be conservative estimates. As a result, we measure ϵ_M for as large a distance as possible using the elliptical aperture on the $15''$ image. As a conservative estimate for the outer radius of detectable flattening, we only extend the aperture out to the distance where the systematic uncertainty becomes the same magnitude as $\Delta\epsilon_M$ and the position angle agrees with the inner isophotes within uncertainties (cf. Table 4). At this distance, $r \sim 200''$ and $\epsilon_M = 0.15 - 0.25$ (90% confidence). Of course, ϵ_M computed for the whole elliptical aperture does not exactly correspond to the isophote at that distance, but comparison to the other measurements of the ellipse and annulus in Table 3 suggests that an ellipticity of at least 0.12 for $r \sim 200''$ is not unreasonable; although at these large distances the effects from the exclusion of the embedded point sources may become significant. Thus the X-ray isophotes appear to be significantly flattened out to average radius $150''$ and probably as far as $200''$.

There is no evidence for any position angle twists, although the statistical uncertainties are large for both small and large radii. The values for $\Delta\theta_M$ agree with the Monte Carlo simulations provided $\epsilon_M \gtrsim 0.15$; when the measured ellipticity is smaller, the position angle uncertainties obtained from the simulations are typically two to three times larger than the statistical estimates. We adopt the average isophote position angle $\theta_{xray} \sim 114°$ for $r \sim 70'' - 90''$ where $\Delta\theta_M$ is smallest, ϵ_M is greatest, and there is optimal agreement between all methods.

We examine the possibility that the measured ellipticities and position angles

are actually caused by contamination from unresolved point sources. The centroid position of the fitted isophotes as a function of radius is a sensitive diagnostic of the presence of any substructure. We find that the centroids change by less than 1 pixel (15″) for $a \leq 105''$ and are consistent within their 1σ errors. In order to probe local asymmetries that affect ϵ_M but not the centroid, we examine four different cuts of the image: $x \geq 0$, $x \leq 0$, $y \geq 0$, and $y \leq 0$, where we fix the origin and define the x axis to align with the major axis and the y axis to be the minor axis. For each region, we create a whole image by reflecting it across the major and minor axes into the other regions. We then compute ϵ_M in an elliptical aperture following the same procedure as above. The ellipticities obtained are in excellent agreement with the values listed in Table 3 within their 1σ errors. For the ellipticities having the most well determined flattening in the original image (i.e. $75'' \leq a \leq 105''$), the values for ϵ_M differ by < 0.02 except for the $x \leq 0$ test at $a = 105''$; in this case $\epsilon_M = 0.30$ which exceeds by 0.05 the mean of the other regions, but is still within the 1σ error. Thus, the consistency of all the regions requires that any contamination from unresolved point sources will have to reproduce the symmetry of all four quadrants.

Another means to examine the "lumpiness" of the X-ray image is analogous to the procedure of identifying surface brightness fluctuations of optical images (e.g, Tonry, Ajhar, & Luppino 1990). We construct a model ("bmodel" task in IRAF-STSDAS) of the X-ray surface brightness in a 240″ square region using the results of the fitted X-ray isophotes discussed above. The model is a relatively poor fit to the central 30″ (being too flat) but adequately represents the rest of the region. The residual image obtained from subtracting this model is featureless aside from a $\sim 2\sigma$ spike in central 30″ due to the poor fit there. Note that usually a high order polynomial is fit the the residual image and then subtracted out. Since our image already shows no significant lumpiness after subtraction of the ellipse model, this was not necessary.

To further assess possible asymmetries, we computed one dimensional projections of the image in a 240″ box onto the major and minor axes. We plot the result in Figure 4. The projections qualitatively exhibit the behavior of a flattened ellipsoid; i.e. the minor axis projection has the highest peak and falls off more rapidly than the

major axis projection, although the two distributions are not easily distinguishable in the outer regions when poisson uncertainties are taken into account. In fact, the tails of the projections may be consistent with a slight asymmetry, but the magnitude of such an effect must be small enough to be consistent with the symmetry of ϵ_M implied in the previous analysis. The symmetry displayed by these projections allows a quantitative estimate of the strength of unresolved point sources. We make the conservative estimate of 100 being the maximum counts a source might possess without being detected anywhere on this plot. Now restricting our attention to the $75'' \leq a \leq 105''$ region that contains the isophotes critical to our analyses in the following sections, we estimate that a point source with less than 50 counts will be too weak to affect the ellipticities. We identify 28 sources within the 20 arcminute radius circle of the PSPC ribs that meet these both of these criteria. This number yields a probability of 24% that one point source lies within $60'' - 105''$. However, there is only a 2% chance that two such sources, which are required by the preceding analysis, lie within $75'' \leq a \leq 105''$. Therefore, we conclude that it is very unlikely that contamination from unresolved point sources accounts for our derived ellipticities; we will be able to determine this for certain with our planned observation of NGC 720 with the ROSAT High Resolution Imager (HRI).

The optical isophotes of NGC 720 have been studied by many authors, most recently by Nieto et al. (1992); Sparks et al. (1991); Peletier et al. (1990); Capaccioli, Piotto, & Rampazzo (1988) Jedrzejewski, Davies, & Illingworth (1987); Lauer (1985a,b); and Djorgovski (1985). All of the authors employ some variation of ellipse fitting involving Fourier analyses techniques similar to Jedrzejewski (1987), and all obtain very similar results. Within the $4''$ core radius of the galaxy (e.g., Jedrzejewski et al. 1987), the isophote ellipticity has a value ~ 0.20 , quickly rising to $\epsilon \sim 0.40$ for semi-major axes $a \sim 15''$, then slowly increasing to a maximum ellipticity ~ 0.45 at $a \sim 60''$ that is maintained out to the faintest isophotes $a \sim 100''$. The position angle, in contrast to the shape, maintains a constant magnitude of $\sim 142°$. In Figure 5 we plot the X-ray isophotes depicted as perfect ellipses with ellipticity ϵ_M and position angle θ_M computed with an elliptical aperture; we also include the optical isophotes

using the R-band data from Peletier et al. (1989).

The X-ray isophotes are everywhere rounder than the optical isophotes, but interior to 60″ the comparison is greatly affected by the PSPC PSF. The position angles of the X-ray and optical isophotes appear discrepant by approximately 30° with statistical uncertainty only about $\sim$ 15°. However, the uncertainties are large at small radii where the X-ray isophotes are approximately circular. We have scheduled a high resolution observation with the ROSAT High Resolution Imager to determine whether the inner X-ray isophotes actually twist and align with the optical isophotes. With the PSPC data, though, we conclude that *the major axis of the X-ray isophotes is not aligned with the major axis of the optical isophotes.*

2.2.2 Spectral Analysis

The ROSAT PSPC has moderate spectral resolution with 34 bins spanning the energy range 0.1 - 2.4 keV. With the full-scale PSPC image corrected only for embedded point sources (cf. §2.2.1), we extracted the source counts from a 400″ radius circle using the IRAF-PROS software. An annulus from 600″ - 800″ was used for estimation of the background level which we then multiplied by a normalization factor of 1.1 to account for exposure and vignetting effects. With XSPEC, we fit the background-subtracted spectrum to a single-temperature ($1T$) optically thin plasma incorporating thermal bremsstrahlung and line emission (Raymond & Smith 1977; updated to 1992 version) with interstellar absorption. The temperature, metalicity, hydrogen column density, and emission normalization were free parameters in the fits.

Table 5 summarizes the spectral data and fit results. The Raymond-Smith $1T$ model fits the data quite well. The 90%, 95%, and 99% confidence levels for the three interesting parameters (temperature, abundances, and N_H), are determined by the contours of constant χ^2_{min}+ 6.25, 8.02, and 11.3 respectively; these contours are plotted in Figure 6. The constraints on $N_H = (0.1 - 3.2) \times 10^{20}$ cm^{-2} (95% confidence) are consistent with the galactic column density $N_H = 1.4 \times 10^{20}$ cm^{-2} (Stark et al. 1992). For the abundances, He was fixed at its cosmic value while the heavy element abundances (relative abundances fixed at solar) have 99% confidence

limits 8% - 60% solar. The fits place stringent constraints (95% confidence) on the temperature $T_{gas} = 0.48 - 0.69$ keV ($5 - 8 \times 10^6$ K). This contrasts with the relatively poor constraints of TFC who could only set a 90% lower limit on $T_{gas} = 0.5$ keV.

Although the single-temperature model fits the data well, it is not a unique representation of the spectrum. By fitting a two-temperature model with the heavy element abundances fixed at their solar values we obtain an equally good fit (see Table 5). The model has roughly equal contributions from the low-temperature component ($T \sim 0.45$ keV) and the high-temperature component ($T \sim 1.2$ keV), but the parameters are not precisely constrained. Hence, the PSPC spectrum cannot distinguish between a $2T$ Raymond-Smith model having solar abundances and a $1T$ model with sub-solar abundances. In fact, by simulating (with XSPEC) $2T$ spectra having 100% solar abundances and the same counts and average properties as the NGC 720 spectrum, we find that a $1T$ Raymond-Smith model fit to this simulated $2T$ spectrum will yield a good fit but with the lower temperatures (~ 0.5 keV) and sub-solar abundances ($\sim 20\%$) very similar to our above $1T$ results. Determination of the precise state of the gas requires superior spectral resolution which should be achieved with ASCA and AXAF.

We investigated the presence of temperature gradients by employing the same fitting procedure as above. For examination of radial gradients, we separated the 400″ region into an inner circle (60″) and an outer annulus (120″ - 400″). The results of the fit are listed in Table 5 with only 68% confidence estimates because of the greater uncertainty due to the smaller number of counts in each region; we do not include results for the 60″ - 120″ region because the fewer counts associated with the region yields large uncertainties in the temperature that bracket the results of the other regions. From consideration of the 68% confidence extremes, we constrain the gradient to be $-0.26 < \left(\frac{d \ln T_{gas}}{d \ln r}\right) < 0.22$ (95% confidence), where we have taken mean values of r for each of the regions. If we fix N_H to its Galactic value, we obtain $-0.11 < \left(\frac{d \ln T_{gas}}{d \ln r}\right) < 0.16$ at 95% confidence and $-0.18 < \left(\frac{d \ln T_{gas}}{d \ln r}\right) < 0.21$ at 99% confidence.

In order to set more stringent limits on radial temperature gradients, we apply

a Kolmogorov-Smirnov (K-S) test to the spectra of the two regions (we omitted the 0.1-0.2 keV bins because those are most subject to background uncertainties). The K-S test yields a probability of 30% that the two regions are derived from the same population. This relatively large probability serves as a discriminator for models with steep temperature gradients. To see how sensitive such a test would be in detecting a real temperature gradient we simulate Raymond-Smith spectra (with XSPEC) with statistics appropriate for the PSPC observation of NGC 720; in each region the simulated spectra have Galactic N_H and 50% metallicities but different temperatures. We find that for a temperature in the inner region of $T_{in} = 0.60$ keV and an outer region temperature of $T_{out} = 0.55$ keV, the K-S probability is 15%. However, for a slightly larger gradient (i.e. $T_{in} = 0.60$ keV, $T_{out} = 0.50$ keV), the probability is reduced to 1%. We define spectral models to be inconsistent with the data if in the two regions their K-S probability is $< 1\%$; i.e. greater than a 99% discrepancy. With this criterion, we determine that for reasonable temperature ranges (i.e. $0.3 \sim 1$ keV), the temperature gradient is very precisely constrained to be $\left|\frac{d \ln T_{gas}}{d \ln r}\right| < 0.05$. Hence we find no evidence for significant radial temperature variations

Since azimuthal variations in the temperature might confuse the interpretation of isophote shapes (cf. §2.3.1), we also test for azimuthal gradients. We sliced the 400″ circle into 4 equal wedges of 90°. We defined the edges of the wedges with respect to the major axis to be (1) −45° to +45°, (2) +45° to +135°, (3) +135° to +225°, and (4) +225° to −45°; the major axis is taken along P.A. 114°. We grouped wedges (2) and (4) into a region denoted (A) and regions (1) and (3) were grouped into region (B) in order to improve the statistics. The results of the fits for these regions are listed in Table 5. We find no evidence for a temperature gradient between (A) and (B) and set a 68% confidence upper limit $\Delta T_{gas} = T_A - T_B < 0.2$ keV. A K-S test of (A) and (B) (0.1 - 0.3 keV bins omitted) yields a probability of 70% that the two regions are derived from the same population.

2.3 Geometrical Evidence for the Existence of Dark Matter

2.3.1 Physical Interpretation of the X-ray Isophote Shapes

For the sake of clarity we summarize the physical arguments demonstrating why the X-ray emission traces the three dimensional shape of the gravitational potential. From this property we argue that the X-ray isophotes must, to a good approximation, trace the shape of the projected potential. We then show that this correspondence provides a test for dark matter independent of the gas pressure, and thus independent of the temperature profile of the gas. Finally, we discuss the validity of our assumption of quasi-hydrostatic equilibrium in NGC 720.

Since the sound crossing time for normal galaxies is much less than a Hubble time, and any bulk flows are generally less than the sound speed, the hot gas in elliptical galaxies is, to a good approximation, in a state of quasi-hydrostatic equilibrium with the underlying gravitational potential (e.g., Sarazin 1986; Binney & Tremaine 1987); i.e. $\nabla p_{gas} = -\rho_{gas} \nabla \Phi$, where p_{gas} is the gas pressure, ρ_{gas} is the gas mass density, and Φ is the gravitational potential. Taking the curl of this equation, one obtains $(\nabla \rho_{gas}) \times (\nabla \Phi) = 0$; surfaces of constant ρ_{gas} are surfaces of constant Φ, and thus the X-ray gas density "traces" the shape of the gravitational potential. One does not directly observe the gas density but instead the thermal emission from bremsstrahlung and line emission with volume emissivity (erg cm^{-3} s^{-2}),

$$j_{gas} = n_e n_H \Lambda_{PSPC}(T_{gas}) = 0.22 \left(\frac{\rho_{gas}}{\mu m_p} \right)^2 \Lambda_{PSPC}(T_{gas}); \qquad (2.9)$$

where Λ_{PSPC} is the plasma emissivity convolved with the PSPC spectral response in the hard band (0.4 - 2.4 keV), n_e is the electron number density, n_H is the number density of hydrogen atoms, and μ is the mean atomic weight; the coefficient 0.22 is determined assuming a completely ionized plasma with cosmic abundances. Λ_{PSPC}

is a relatively weak function of temperature. Assuming the X-rays in NGC 720 come from hot gas (see below) the range of N_H, abundances, and T_{gas} obtained from the spectrum (§2.2.2) imply that $\Lambda_{PSPC}(T_{gas})$ may only vary by $< 15\%$ (cf. NRA 91-OSSA-3, appendix F, ROSAT mission description, Figure 10.9, 1991); i.e. Λ_{PSPC} may be considered constant throughout the galaxy.

We may exploit quasi-hydrostatic equilibrium to relate the three dimensional shape of j_{gas} to Φ. Since ρ_{gas} and Φ are constant on isopotential surfaces, the hydrostatic equation implies that p_{gas} must also be constant on the isopotential surfaces. For an ideal gas $p_{gas} \propto \rho_{gas} T_{gas}$ then implies that surfaces of constant T_{gas} are also surfaces of constant Φ. Since $(\nabla \rho_{gas}) \times (\nabla \Phi) = 0$ implies that $\left(\nabla \rho_{gas}^2\right) \times (\nabla \Phi) = 0$, the quantity $\rho_{gas}^2 \Lambda_{PSPC}(T_{gas})$, and hence j_{gas}, must also trace the three dimensional shape of the gravitational potential.

One obtains the X-ray surface brightness (Σ_X) by projecting j_{gas} onto the plane of the sky. Although j_{gas} and Φ have the same three dimensional shapes, it is not true in general that Σ_X has the same shape as the projected potential. For the case where Φ is stratified on concentric similar ellipsoids, Σ_X and the projection of Φ have exactly the same shapes, independent of their three dimensional radial distributions (Stark 1977; Binney 1985; Franx 1988). This is not exactly true for potentials whose shape change with radius. However, one would expect that for small gradients in ellipticity, the projected shapes should closely approximate the similar ellipsoid case.

We have investigated the typical magnitude of such departures by studying simple spheroidal models whose ellipticity varies with radius. In Appendix B. we examine the projected shapes of functions having the same three dimensional shapes and radial slopes appropriate for physical potentials and gas emissivities; we include the specific example of j_{gas} and the potential of the visible stars for NGC 720. We find that for reasonable ellipticity gradients, the ellipticities of the projected distributions differ by no more than ~ 0.04. For the above mentioned special case for NGC 720 we find that ellipticities differ by no more than ~ 0.02. We conclude that *to a good approximation the X-ray isophotes trace the shape of the projected gravitational potential.*

This propinquity of the shapes of the X-ray isophotes and projected potential

contours enables one to assess the validity of any model for the three dimensional potential, independent of the gas pressure and temperature. In particular, we may test whether the potential due to the visible stars can produce the observed shapes of the X-ray isophotes. The only assumptions involved are the choice of the form of the deprojected potential of the visible stars and that quasi-hydrostatic equilibrium is a suitable description of the gas. We perform this test in the following section.

In order to determine whether quasi-hydrostatic equilibrium is a suitable description of the gas in NGC 720, we first mention that the X-ray emission is clearly not the result of discrete sources in the galaxy because the X-ray isophotes do not follow the shape of the optical isophotes (§2.2.1). This property, when coupled with the good fits of the Raymond-Smith model to the spectrum (§2.2.2) and the temperatures derived from them, suggests that the dominant component of the X-ray emission (0.2 - 2.4 keV) from NGC 720 is in the form of hot gas (e.g., Canizares, Fabbiano, & Trinchieri 1987). A possible complication arises since the PSPC spectrum does not rule out a multi-phase medium having cool, dense gas clouds embedded in the hot gas that are not hydrostatically supported. Thomas, Fabian, & Nulsen (1987; Thomas 1988) demonstrated that the mean density and temperature are good descriptions of a multi-phase medium, indicating that a single phase representation of the data should not significantly affect interpretation of the isophote shapes; this may not be true within the inner regions of a strong cooling flow (Tsai 1994), but the isophotes crucial to our analysis are located at relatively large distances ($\sim 10 h_{80}$ kpc) which should lie safely outside the possible cooling-flow-dominated region. One must also consider possible environmental effects. In particular, the shapes of the X-ray isophotes could be distorted by either the gravitational field of a large neighboring galaxy or by ram-pressure stripping if the galaxy is traveling through a dense intergalactic medium (IGM). As indicated by Dressler, Schechter, & Rose (1986), NGC 720 has six faint companions within a 1.5 degree square field, but is quite isolated from other normal galaxies; the closest galaxy with a measured redshift lies 73 arcminutes NW. Since the presence of a dense IGM is generally associated with rich clusters of galaxies, it is unlikely that there exist significant ram-pressure distortions

of NGC 720. In support of this assessment, the isophote centroids and position angles do not exhibit discernible variations with radius. We conclude that the X-ray gas in NGC 720 traces the shape of the underlying gravitational potential.

In principle this halcyon description of quasi-hydrostatic equilibrium may be corrupted by significant bulk motions of the gas; we emphasize that perfect hydrostatic equilibrium is not required, simply that additional gas motions are dynamically small. N-body simulations of hot gas in clusters of galaxies do not show evidence of large streaming motions (e.g., Tsai, Katz, & Bertschinger 1993). One would expect that any streaming motions in ellipticals would be be even less significant than in galaxy clusters since ellipticals are more relaxed systems than galaxy clusters. We are currently investigating the viability of recovering the shape of the gravitational potential by assuming quasi-hydrostatic equilibrium using N-body simulations (Buote & Tsai 1995).

Although streaming may be unimportant in the gas, significant rotation of the gas also could affect its shape. That is, the gas could be flattened because it is spinning, not because the gravitational potential is flattened; i.e. another term must be included in the hydrostatic equation and thus the gas density no longer exactly traces the gravitational potential. NGC 720, like most giant ellipticals, is slowly rotating; the visible stars have a mass-weighted (optical) rotational velocity of 35 km s^{-1} (Busarello, Longo, & Feoli 1992). Using the tensor virial theorem, we conclude that mass-weighted rotational velocities in excess of 150 km s^{-1} are required to flatten the gas to an ellipticity of 0.25, that being the shape of the best-determined X-ray isophotes; note that in the application of the tensor virial theorum we take $W_{ii} = \int \rho_{gas} x_i \frac{\partial \Phi_{stars}}{\partial x_i} d^3x$ (no sum), where ρ_{gas} is the gas density from §2.5.2, Φ_{stars} is the potential inferred from a constant mass-to-light ratio model in §2.5.1, and the integral is evaluated over the volume of the gas spheroid. Unfortunately, the PSPC, as well as all current X-ray instruments, lack the spectral resolution to detect rotation. As a result, we must resort to indirect arguments involving the properties of the visible stars and the likely history of the gas in order to assess the importance of rotation. Since the gas mass of NGC 720 (cf. §2.5.2) is a small fraction of the stellar mass loss

over a Hubble time as is true for most ellipticals (Mathews 1990), the gas should have net angular momentum comparable to that of the stars. Hence, if the gas rotates as fast as the stars, then the rotation is dynamically insignificant. Kley & Mathews (1995), who use hydrodynamic models of gas in elliptical galaxies to demonstrate that cooling gas eventually forms a spinning disk, emphasize that the key to forming disks lies in the fact that although the stellar rotation at any given radius may be dynamically small, conservation of angular momentum can drive up the speed of gas as it falls in to the center of the galaxy. For this scenario to be important for our analysis of NGC 720, then there must have been a significant amount of gas that has fallen in from very large radii and have been deposited at a radius $\sim 90''$. However, about 70% of the mass in visible stars is within $90''$ of NGC 720 indicating that there is insufficient stellar mass at the large radii ($r > 100''$) required to account for such rapidly rotating gas, certainly in quantities to significantly affect the observed isophotes. Therefore, the effects of rotation should not be important for the gas in NGC 720, although we can not rule it out categorically.

2.3.2 Geometric Implications

We now utilize the results of the previous section to determine whether the shapes of the X-ray isophotes are consistent with the assumption that the gas is in quasi-hydrostatic equilibrium with the visible stellar potential; note that the results of this section are intended to be primarily qualitative, we present the detailed modeling of the system in §2.4 and §2.5. In particular, by exploiting the geometrical properties of ellipsoidal potentials, we investigate whether the stellar mass, which is much more centrally condensed than the X-ray emission, can generate the observed flattening of the X-ray isophotes (for discussions of ellipsoidal potentials see Chandrasekhar 1969; Binney & Tremaine 1987). Because the equipotential surfaces exterior to a thin homoeoid (i.e. ellipsoidal shell) are ellipsoids confocal to the homoeoid (independent of its mass), the potential becomes rounder with increasing distance from the homoeoid; interior to the homoeoid, the potential is constant. It follows that an ellipsoidal mass constructed from the sum of similar thin homoeoids will also produce a potential that

becomes rounder with distance (assuming the mass density decreases with distance). When the mass is expressed as a multipole expansion, this result simply reflects the increasing importance of the monopole term with increasing distance from the center of mass.

Assuming the stellar mass is proportional to the stellar light, the results of the previous section show that we may directly compare the shapes of the projected potential surfaces produced by the stars to the observed X-ray isophotes; the effects of self-gravitation of the gas is negligible (cf. §2.5.2) and we neglect it in the following discussion. We show in §2.5.1 that the stellar luminosity density, and hence the stellar mass density, has a radial dependence $\sim r^{-2.6}$ and core radius $r_c \sim 4''$; we take the isodensity surfaces of the stellar ellipsoid to be similar oblate spheroids having $\epsilon_{stars} = 0.40$. The stellar mass is thus considerably more centrally condensed than the X-ray gas for which $r_c \sim 16''$ and $\rho_{gas} \sim r^{-3/2}$ (cf. §2.5.2); yet the X-ray isophotes display significant elongation out to $\sim$ 25 optical core radii. Listed in Table 6 are the ellipticities of the stellar isopotential surfaces (ϵ_{pot}) for (1) three dimensions, (2) projected onto the plane of the sky assuming the symmetry axis lies in the sky plane (cf. §2.4.1), and (3) projected and convolved with the PSPC PSF; in Figure 7 we plot the projected, convolved equipotentials superimposed on the X-ray isophotes. For semi-major axis $105''$, that being the most distant isophote whose shape is very accurately determined, $\epsilon_{pot} \sim 0.10$ is much rounder than the 90% confidence lower limit of the X-ray surface brightness ($\epsilon_M \geq 0.20$); note that for $\epsilon_{stars} = 0.50$, an ellipticity greater than any of the optical isophotes, we obtain $\epsilon_{pot} \sim 0.13$ at $a = 105''$, which is still significantly less than ϵ_M. If the stellar density is instead assumed to be prolate with the same radial dependence, core radius, and ellipticity as the oblate case, then the 3-D prolate potential is flatter than the oblate case at all radii by $\epsilon \sim 0.015$. The projected ellipticities of the prolate spheroid agree very well with the results for the oblate case as is expected since the distinction between prolate and oblate spheroids having ellipticities ~ 0.10 is not large. We also list in Table 6 the ellipticity of the X-ray isophotes ($\epsilon_{isophote}$) predicted from our detailed models of gas in the stellar potential (§2.5) assuming the gas is isothermal and ideal;

note the excellent correspondence between the projected potential ellipticity and the isothermal isophotes. The discrepancy between the expected shape of the stellar potential and the observed X-ray isophotes is actually amplified because a roughly uniform background will tend to decrease the measured values of ϵ_M for the X-ray isophotes (Carter & Metcalfe 1980).

We quantify the reality of this inconsistency with Monte Carlo simulations using the pseudo spheroids discussed in Appendix B.. In the notation of Appendix B., we assume the gas emissivity $j_{gas} \propto (a_0^2 + \xi^2)^{-3/2}$ with the same $\epsilon(r)$ as Φ_{stars}. We project j_{gas} onto the plane of the sky and convolve with the PSPC PSF. Then Poisson counts appropriate to the NGC 720 PSPC observation and a uniform background are added to simulate an observation. After subtracting out a uniform background, the ellipticities are then computed using the iterative moment technique with a circular aperture as described in §2.2.1. In Table 7 we list the results of 1000 simulations for both the oblate and prolate constant mass-to-light ratio models. As expected, the lower bounds on ϵ_M are near 0 as a result of the systematic effects discussed in §2.2.1. However, the upper bounds also show large departures from the mean. For semi-major axis 105″, the value of ϵ_M in the simulations is as large as that measured from the real X-ray data isophotes ($\epsilon_M = 0.25$) in only 1% of the simulations. These simple models demonstrate that the constant mass-to-light ratio models are inconsistent with the observed flattening of the X-ray isophotes at the 99% confidence level; even upon considering the maximum uncertainty due to comparing the projections of non-similar spheroids (cf. Appendix B.), the discrepancy is still robust at the 90% level. This discrepancy is also unlikely due to possible rotation of the gas since upon adding a uniform rotation term to the constant M/L potential we find that mass-weighted velocities $v_0 > 120$ km s^{-1} are required to produce the X-ray ellipticities; such velocities are significantly larger than expected from the stellar rotation and are consistent with the velocities required from the tensor virial theorum obtained in the previous section. Hence, by employing simple arguments involving the properties of spheroids and their potentials, we conclude that an spheroidal mass distribution confined to the shape of the stellar matter cannot produce a gravitational potential

flat enough to yield the observed ellipticities of the X-ray isophotes; a conclusion that is independent of the pressure and temperature of the gas, and the amount of stellar mass. Assuming the gas is in quasi-hydrostatic equilibrium (cf. previous section), then *there must exist in NGC 720 an extended halo of dark matter sufficiently elongated to account for the isophotal flattening.*

In the previous discussion we have ignored the position angle offset of the optical and X-ray major axes. If the stars are solely responsible for the gravitational potential, the gas and stars must be co-axial. In addition, if the stellar ellipsoid is axisymmetric, so must be the gas with the same type of axisymmetry; i.e. if the stars are oblate, the potential, and hence the gas, must also be oblate. For this case there can be no apparent position angle misalignments due to projection on the sky, regardless of any intrinsic variations of ellipticity with radius (e.g., Mihalas & Binney 1981). If the stars are indeed triaxial, then a projected misalignment of the X-ray and optical major axes is theoretically possible. Detailed triaxial models would be required to see if triaxiality can actually explain the observed offset without dark matter. This is moot, given our conclusion that the shape itself requires dark matter, but we will examine such models in a future paper that will include a ROSAT High Resolution Imager (HRI) observation of NGC 720 (see Bertola et. al. 1991 for an example of this problem).

It is difficult to quantify exactly the expected uncertainty associated with the position angle from the above Monte Carlo simulations because when $\epsilon_M \sim 0$, the position angle is not well defined. However, when selecting only those runs where, say, $\epsilon_M \geq 0.10$ ($\sim 400 - 500$ simulations), the position angle uncertainty is $\sim 9°$ at 68% confidence, $\sim 15°$ at 90% confidence, $\sim 20°$ at 95% confidence, and $\sim 27°$ at 99% confidence. For more elongated ϵ_M, the uncertainty is even smaller. The position angle discrepancy between the stellar and X-ray isophotes adopted in §2.2.1 is 28°. For the elongated X-ray isophotes, the position angle implied by the simple models for the visible stellar mass is inconsistent with the observed values at the $\sim 99\%$ level. Hence the offset of the major axes may provide further geometrical evidence for the existence of unseen matter in NGC 720.

2.3.3 Implications for Alternative Theories of Gravitation

The geometrical test for dark matter introduced in the previous section places new constraints on theories of generalized forces. Instead of invoking the existence of unseen mass to explain the flat rotation curves in spiral galaxies, these theories modify the Newtonian force law in such a manner to account for the observed gravitational effects; see Liboff (1992) for a concise summary of this subject and Sanders (1990) for a more extensive review. Perhaps the most successful of these theories is the "Modification of Newtonian Dynamics" (MOND) proposed by Milgrom (1984a,b,c,1986). Milgrom proffers that the gravitational acceleration ($\vec{g}_M$) due to a point mass, M, is characterized by,

$$\vec{g}_M = -\frac{GM}{r^2}\hat{r}, \quad \text{for} \quad |\vec{g}_M| \gg a_0, \tag{2.10}$$

and

$$\vec{g}_M = -\frac{\sqrt{GMa_0}}{r}\hat{r}, \quad \text{for} \quad |\vec{g}_M| \ll a_0, \tag{2.11}$$

where a_0 is the appropriate acceleration scale that yields circular velocities ($v_c \propto M^{1/4}$) consistent with observations of the infrared Tully-Fisher relation for spiral galaxies if $M \propto L$. Bekenstein & Milgrom (1984) formulate MOND as a nonrelativistic potential theory for gravity for which they obtain a field equation,

$$\nabla \cdot [\mu(x)\nabla\Phi_M] = 4\pi G\rho, \tag{2.12}$$

where Φ_M is given by $g_M = -\nabla\Phi_M$, $x = |\nabla\Phi_M|/a_0$, and $\mu(x)$ is some unspecified smooth function (assumed monotonic) appropriately connecting the Newtonian and Milgrom domains; note that this equation is non-linear and thus the principle of linear superposition is not obeyed by MOND.

By exploiting the region in the galaxy where Newtonian gravity applies to high precision (i.e. $g/a_0 \gg 1$), we may obtain robust constraints on the shape of the MOND potential produced by the stars without solving the non-linear field equation

(eq. [2.12]). Consider the MOND potential expressed in terms of spherical harmonics,

$$\Phi(r,\theta,\phi) = \sum_{l,m,i} A^i_{lm}(r) Y^i_{lm}(\theta,\phi), \tag{2.13}$$

where Y^i_{lm} is the spherical harmonic of order l,m with i indicating whether it is even or odd in ϕ. For an arbitrary mass distribution, Milgrom (1986) demonstrates that for $l \neq 0$, $A^i_{lm}(r) \rightarrow a^i_{lm} r^{-\xi_l}$ in the limit $r \rightarrow \infty$, where $\xi_l = [l(l+1)/2]^{1/2}$ and the a^i_{lm} are constants; the $l = 0$ "monopole" term is the spherically-symmetric $\Phi_0(r) = \sqrt{GMa_0}\ln(r)$. It follows then that the lth multipole of MOND decays slower than in the Newtonian theory ($r^{-(l+1)}$), but the spherically-symmetric monopole term does indeed eventually dominate at large distances; i.e. the MOND potential becomes more spherical with distance just as in Newtonian theory (provided, of course, the density is monotonically decreasing). As a result, we have a qualitative description linking the Newtonian and Milgrom regimes: the ellipticity of the potential generated by the stars in the region where Newtonian physics applies serves as an upper limit to the ellipticity at larger distances because the potential must become rounder with increasing distance, albeit more slowly in the MOND regime.

In order to set a realistic upper bound on the potential shapes, we need to properly define the "Newtonian Regime". Milgrom (1986) defines the transition radius $r_t \equiv (GM/a_0)^{1/2}$ between the Newton and Milgrom regions where M is taken to be the total mass of the bound system. In his review, Sanders (1990; Begeman, Broeils, & Sanders 1991) shows that $a_0 \approx 10^{-8}$ cm^2 s^{-1} ($H_0 = 75$ km s^{-1} Mpc^{-1}) in order to explain the flat rotation curves of spiral galaxies. Assuming that the stars constitute the only mass in NGC 720, then $r_t \sim 12$ kpc, where we have used $10^{11} M_\odot$ (cf. §2.5.1) for the stellar mass and a distance of 21 Mpc ($H_0 = 75$ km s^{-1} Mpc^{-1}). This transition distance is consistent with previous estimates which place r_t between 10 and 20 kpc (cf. Sanders 1990; Liboff 1992). Expressing r_t in arcseconds, we have in the context of MOND that the Newtonian regime applies for $r < r_t = 120''$.

The analysis of the previous section (§2.3.2) may be carried over in totality because the relevant X-ray isophotes have semi-major axes $a \sim 100''$; i.e. our geometrical

discussion lay entirely in the Newtonian regime. In fact, our analysis applies even when restricted to a smaller region where presumably the Newtonian approximation is even a better description. If we use $a = 30''$ (3 kpc), for example, as a reference, the projected ellipticity of the stellar potential is 0.13 (cf. Table 6). This value is already rounder than the X-ray isophotes at $a = 105''$ and the discrepancy must be amplified for the stellar isopotential at $a = 105''$ since the ellipticity of the MOND potential must decrease with distance. We conclude that *MOND does not obviate the need for dark matter because the stellar potential is already too round to explain the observed flattening of the X-ray isophotes in the region where Newtonian physics would still apply.*

We may also examine MOND without reference to the actual value of a_0. Equation (2.12) may be expressed in terms of the Newtonian field $\vec{g}_N = -\nabla\Phi_N$,

$$\mu(g_M/a_0)\vec{g}_M = \vec{g}_N + \nabla \times \vec{h} \tag{2.14}$$

where $\vec{g}_M = -\nabla\Phi_M$ is the MOND gravitational field, and $\vec{h}$ is an unspecified field (Bekenstein & Milgrom 1984). In order to satisfy the basic assumptions of MOND expressed by equations (2.10) and (2.11), the curl term in equation (2.14) must be small with respect to $\vec{g}_N$; Bekenstein & Milgrom do show that $\nabla \times \vec{h}$ decreases faster than $\vec{g}_N$ at large distances. For systems possessing a high degree of symmetry (e.g., spherical, planer, and cylindrical), the curl term vanishes exactly. Hence, $\mu(g_M/a_0)\vec{g}_M \approx \vec{g}_N$ must be a good approximation for an arbitrary system if indeed the field equation is to reproduce the basic tenets of MOND and connect appropriately to Newtonian mechanics.

Equation (2.14) implies that for a surface where $g_N = constant$, g_M must also be nearly constant, and thus $\vec{g}_M/\vec{g}_N$ is also constant; i.e. surfaces of constant acceleration in MOND are approximately surfaces of constant acceleration in Newtonian gravitation. Applying this approximation of MOND to the stellar matter distribution of NGC 720 yields the same isopotential shapes derived for the Newtonian case discussed in §2.3.2; we are currently examining numerical solutions of the field

equation to obtain shape constraints on the MOND potential to arbitrary accuracy (Bertschinger, Buote, & Canizares 1995, in preparation). *To the accuracy implied by taking* $\mu(g/a_0)\vec{g} \approx \vec{g}_N$, *MOND cannot account for the observed flattening of the X-ray isophotes without invoking the existence of dark matter, independent of the value of* a_0

2.4 Total Gravitating Matter Distribution

2.4.1 Model

We investigate how the the the morphology of the X-ray gas constrains the structure of the total galaxian mass. Except for some minor improvements, we employ the technique described by Buote & Canizares (1992; Buote 1992) which involves four principal steps: (1) modeling the gravitational potential, (2) "filling" the potential well with hot, X-ray emitting gas, (3) projecting the emission onto the plane of the sky, and (4) convolving the emission with the PSPC PSF to compare to observations.

We assume the gross structure of the mass is adequately described by a single ellipsoid of constant shape and orientation; in §2.5 the contributions from the stars, X-ray gas, and dark matter will be analyzed separately; in a future paper we will explore the effects of other types of mass models. We consider mass densities of both Ferrers (cf. Chandrasekhar 1969) and Hernquist (1990) types. For an ellipsoid having semi-axes a_i, the Ferrers (i.e. power-law) density has the dimensionless form,

$$\tilde{\rho}_F(\vec{x}) = \left[\left(\frac{a_0}{a_3}\right)^2 + m^2\right]^{-n}, \qquad m^2 = \sum_{i=1}^{3} \frac{x_i^2}{a_i^2}, \tag{2.15}$$

where a_0 is the core parameter, a_3 is the semi-major axis, and the dimensionless number m defines the equation of a homoeoid between the origin ($m = 0$) and the boundary ($m = 1$) of the ellipsoid. As discussed in Binney & Tremaine (1987), power-law densities having $2 < 2n < 3$ are suitable approximations of the mass and light profiles of many galaxies. Applying the notation of equation (2.15), the dimensionless

Hernquist (1990) density becomes,

$$\tilde{\rho}_H(\vec{x}) = m^{-1}\left[\frac{a_0}{a_3} + m\right]^{-3}, \tag{2.16}$$

where the ellipsoidal surface enclosing half of the mass is defined by $m_{1/2} = (1 + \sqrt{2})a_0/a_3$ (Hernquist 1992) for a mass distribution extending throughout all space; equation (2.16) gives rise to an excellent approximation of the de Vaucouleurs $R^{1/4}$ law. In order to limit the number of free parameters in our model, we consider axisymmetric ellipsoids. The oblate spheroid has $a_1 = a_3$ and $a_2 = (1 - \epsilon)a_3$, where ϵ is the ellipticity of the isodensity surfaces in the (x_1, x_2) and (x_2, x_3) planes. For the prolate case, $a_1 = a_2 = (1 - \epsilon)a_3$, where ϵ is now the ellipticity in the (x_1, x_3) and (x_2, x_3) planes. By generating both oblate and prolate models we bracket the triaxial case (Binney & Strimple 1978).

The gravitational potential generated by these densities is a complicated function requiring numerical evaluation; for a discussion of ellipsoidal potentials see Chandrasekhar (1969) and Binney & Tremaine (1987). The potential of an ellipsoidal mass with a finite outer boundary may be written as,

$$\Phi_\alpha(\vec{x}) = -\frac{GM}{S_\alpha}\phi_\alpha(\vec{x}), \tag{2.17}$$

where $\alpha = F$ refers to a Ferrers density and $\alpha = H$ refers to the Hernquist density, G is Newton's constant, and M is the total ellipsoidal mass; S_α is a dimensionless number related to the mass,

$$S_\alpha = 4\int_0^1 \tilde{\rho}_\alpha(m^2)m^2 dm, \tag{2.18}$$

where $\tilde{\rho}_\alpha$ refers to either equation (2.15) or (2.16). The function $\phi(\vec{x})$ has the dimen-

sions of inverse length and for the Ferrers density has the form,

$$\phi_F(\vec{x}) = \int_\lambda^\infty \frac{du}{\Delta} \begin{cases} \log\left[\frac{(a_0/a_3)^2+1}{(a_0/a_3)^2+m^2(u)}\right] & n=1 \\ \frac{1}{1-n}\left[\left(\left(\frac{a_0}{a_3}\right)^2+1\right)^{1-n} - \left(\left(\frac{a_0}{a_3}\right)^2+m^2(u)\right)^{1-n}\right] & n\neq 1 \end{cases}, \quad (2.19)$$

where

$$\Delta^2 = \prod_{i=1}^{3}(a_i^2+u), \qquad m^2(u) = \sum_{i=1}^{3}\frac{x_i^2}{a_i^2+u}, \quad (2.20)$$

and λ is the ellipsoidal coordinate of the point $\vec{x} = (x_1, x_2, x_3)$; λ is defined so that $m^2(\lambda) = 1$ for $\vec{x}$ exterior to the bounding ellipsoid, and $\lambda = 0$ for $\vec{x}$ interior to the bounding ellipsoid. The expression for $\phi(\vec{x})$ using the Hernquist density is,

$$\phi_H(\vec{x}) = \int_\lambda^\infty \frac{du}{\Delta}\left[\left(\frac{a_0}{a_3}+m(u)\right)^{-2} - \left(\frac{a_0}{a_3}+1\right)^{-2}\right]. \quad (2.21)$$

By normalizing Φ (eq. [2.17]) to its central value, we generate potential families of varying scale (a_0) and shape (ϵ).

The potential is then "filled" with hot, X-ray emitting gas by making the fundamental assumption that the gas is in hydrostatic equilibrium with the underlying gravitational potential Φ (cf. §2.3.1). If the gas is isothermal and obeys an ideal gas equation of state, then the equation of hydrostatic equilibrium may be solved exactly to give,

$$\rho_{gas}(\vec{x}) = e^{[1-\Phi(\vec{x})]\Gamma}, \qquad \Gamma = \frac{\mu m_p \Phi_0}{k_B T_{gas}}, \quad (2.22)$$

where ρ_{gas} and Φ are normalized to their central values $\rho_{gas}(0)$ and Φ_0, μ is the mean atomic weight, m_p is the proton mass, k_B is Boltzmann's constant, and T_{gas} is the gas temperature. For a given potential shape, Γ is well constrained by the radial profile of the X-ray surface brightness; i.e. we do not require knowledge of either the gas temperature (T_{gas}) or the depth of the potential (Φ_0), and therefore the mass of the galaxy. In fact, results concerning the shape of the potential are not particularly sensitive to the assumption of isothermality because the PSPC is relatively insensitive to the range of T_{gas} implied by the the galaxy spectrum (cf. §2.2.2 and §2.3.1).

We test the effects of possible temperature gradients on the shape measurements. First, we consider a linear perturbation to the isothermal case,

$$T(a) = T_0 \left(1 + \frac{a}{a_s}\delta\right), \tag{2.23}$$

where $a = ma_3$ is the elliptical radius, a_s is an appropriate scale length and δ is a free parameter. For δ sufficiently small, the equation for ρ_{gas} is the same as (2.22) except that T_{gas} in Γ is replaced with (2.23). Second, we consider a polytropic relation, $p_{gas} = K\rho_{gas}^{\gamma}$ ($K = constant$), which yields upon substitution into the hydrostatic equilibrium equation,

$$\rho_{gas} = \left[\frac{\gamma - 1}{\gamma}(\Phi - 1)\,\Gamma + 1\right]^{\frac{1}{\gamma - 1}}; \tag{2.24}$$

where ρ_{gas} and Φ are normalized to their central values, and $\Gamma = |\Phi_0|/K\rho_{gas}^{\gamma-1}(0)$. If in addition the gas is assumed to be ideal, then $\Gamma = \mu m_p|\Phi_0|/k_B T_{gas}(0)$, and the temperature is simply proportional to the expression within the brackets of equation (2.24).

We have shown in §2.3.1 that the X-ray emission of the gas is accurately represented by $\rho_{gas}^2 \times$(weak function of temperature). Hence, the surface brightness of the gas may now be constructed by simply integrating ρ_{gas}^2 along the line of sight,

$$\Sigma_X(y,z) \propto \int \rho_{gas}^2 dx, \tag{2.25}$$

where the $y - z$ plane coincides with the sky. This scheme assumes that the symmetry axis of the spheroid lies in the plane of the sky. Given the observed flattening of the stellar distribution of NGC 720, we believe that a substantial inclination of the symmetry axis is unlikely because (1) the observed number of galaxies flatter than NGC 720 is relatively small (Fasano & Vio 1991; Lambas, Maddox, & Loveday 1992; Ryden 1992, 1991), (2) galaxies substantially flatter than NGC 720, and not rotationally supported, are dynamically unstable (Merrit & Stiavelli 1990; Merrit & Hernquist 1991), and (3) dynamical studies of NGC 720 by Binney, Davies, & Illingworth (1990)

and van der Marel (1991) suggest that the galaxy is nearly edge-on. Furthermore, we are not sensitive to small inclination angles (cf. Binney & Strimple 1978; Fabricant, Rybicki, & Gorenstein 1984; and Buote & Canizares 1992). The final step consists of convolving $\Sigma_X(y,z)$ with the PSPC PSF described in §2.2.1, and comparing the result to the PSPC image.

2.4.2 Shape of the Total Matter

Our procedure to determine the shape of the total matter begins by specifying the semi-major axis length (a_3) of the spheroid. Then, for a given total matter ellipticity (ϵ_{tot}) we generate surface brightness maps for any values of a_0 and Γ; here we have assumed the isothermal gas solution (eq. [2.22]). Using a χ^2 fit to compare the radial profile of the model image to the data, we obtain the 90% confidence interval (a_0, Γ) defined by those models having $\chi^2 \leq \chi^2_{min} + 4.61$; note that the models with temperature gradients have three interesting parameters (e.g., a_0, Γ, δ) and the corresponding $\Delta\chi^2 = 6.25$ to determine the 90% confidence level. Within this 90% interval, we compute the minimum and maximum ellipticities of the model surface brightness $(\epsilon^{min}_{model}, \epsilon^{max}_{model})$ using the iterative moment technique as described in §2.2.1 for an elliptical aperture having semi-major axis 90″. The upper limit for ϵ_{tot} is obtained by finding the smallest value of ϵ_{tot} such that $\epsilon^{min}_{model} > \epsilon^{max}_{data}$ in its 90% confidence interval, where ϵ^{max}_{data} is the 90% confidence upper limit on ϵ_M from Table 3. In the same manner, a lower limit is obtained by finding the largest value of ϵ_{tot} such that $\epsilon^{max}_{model} < \epsilon^{min}_{data}$. As we discuss in §2.6, ϵ_{tot} is in effect constrained only out to distances where ϵ_{data} is well determined.

We list in Table 8 the results for the isothermal gas solution (eq. [2.22]) assuming $a_3 = 450''$; the fit results of a typical model are shown in Figure 8. The $\rho \propto r^{-2}$ and Hernquist density distributions yield excellent fits to the X-ray surface brightness while $\rho \propto r^{-3}$ is too steep to adequately reproduce the data. Each of the density profiles yields very large ellipticities for the gravitating matter with lower limits only marginally consistent with the maximum stellar isophote ellipticity of ~ 0.45. For smaller a_3, the quality of the fits diminishes for each density model, which sets a lower

limit on a_3. We define the fits to be unacceptable if the probability that χ^2 should exceed the measured value of χ^2_{min} by chance is less than 10%. In this manner we obtain lower limits on a_3 of 225″ and 260″ for the oblate and prolate ($\rho \sim r^{-2}$) cases respectively; there is no upper bound. For $a_{3min} < a_3 < 450''$, the ϵ_{tot} limits change by less than 0.01.

The results for the linearly perturbed isothermal models (eq. [2.23]) agree very well with the isothermal results. The best-fit values for the δ parameter are negative and have typical magnitudes ~ 0.06; the scale length a_s is set to 400″ in all the fits. From consideration of only the fits to the radial profile, we obtain 90% confidence limits (oblate models) of $\delta = -0.06^{+0.13}_{-0.14}$ and $\epsilon_{tot} = 0.51 - 0.79$; i.e. these models have larger parameter spaces than the isothermal models and bracket the isothermal results. However, by considering the temperature gradients implied by the expanded parameter space we may eliminate those models inconsistent with the PSPC spectrum (§2.2.2). That is, we compute emission-weighted temperatures of the models in the $0'' - 60''$ and $120'' - 400''$ regions and then simulate PSPC Raymond-Smith spectra as described in §2.2.2. These simulated spectra are then compared to the allowed gradients implied by the K-S results for the actual data in §2.2.2. When restricting the parameter spaces to be consistent with the K-S tests, we obtain results almost identical to the isothermal case. Although our models do not account for the reduction in central temperature due to a possible cooling flow, the comparison should not be greatly affected since we average over a large region. These same results apply to the r^{-3} and Hernquist models.

The polytropic equation equation of state (eq. [2.24]) yields results that are essentially identical to the linearly perturbed isothermal models. For the $\rho \sim r^{-2}$ model, the polytropic indices derived from the fits span the range $\gamma = 1.06^{+0.17}_{-0.20}$ for oblate models and $\gamma = 1.10^{+0.18}_{-0.19}$ for prolate models (90% confidence); the ellipticities also have a larger range than the isothermal case: $\epsilon_{tot} = 0.50 - 0.77$ for oblate models and $\epsilon_{tot} = 0.46 - 0.69$ for prolate models. However, just as with the linear temperature model, the constraints from K-S tests eliminate those models which differ significantly from the isothermal case. As a result, the polytropic models agree very well with the

isothermal solution. Again, these same results apply to the r^{-3} and Hernquist models.

2.4.3 Estimate of the Total Matter

Equation (2.17) and the definition of Γ (eq. [2.22]) combine to give an expression for the total mass,

$$M_{tot} = \frac{S_\alpha}{G\phi_\alpha(0)} \left(\frac{k_B T_{gas}}{\mu m_p} \right) \Gamma, \tag{2.26}$$

where as before α refers to either a Ferrers or Hernquist mass profile, and ϕ is evaluated at the center of the spheroid. Using the 90% confidence results from Table 8 with the above equation, we list in Table 9 the total masses (M_{tot}) and the corresponding values of $\Upsilon_B = M_{tot}/L_B$ in solar units for both the $\rho \sim r^{-2}$ and Hernquist densities; the B-band luminosity $L_B = 2.2 \times 10^{10} h_{80}^{-2} L_\odot$ is obtained by scaling $B_T = 11.15$ from Burstein et al. (1987) to $D = 20 h_{80}$ Mpc; also listed are $\rho \sim r^{-2}$ results assuming the minimum acceptable semi-major axis length for the total matter spheroid. There is no significant difference in M_{tot} for the $\rho \sim r^{-2}$ and Hernquist densities of the same a_3. However, M_{tot} is systematically less for smaller a_3 because the density profile is essentially the same for all the cases but the total spheroidal volume is not. In Figure 9 we plot the integrated mass ($\rho_{tot} \sim r^{-2}$) interior to a spheroid of semi-major axis $a < a_3$, where a is the elliptical radius defined by $a = m a_3$ and a_3 is the spheroid having mass M_{tot}. As expected, the masses for $a_3 = 450''$ and $a_3 = 225''$ demonstrate good agreement at $a = 225''$ although the $a_3 = 450''$ has systematically more mass for small a.

Assuming a stellar $\Upsilon_B \sim 7 \Upsilon_\odot$ (§2.5.1), and neglecting the mass of the gas (i.e. $M_{tot} = M_{stars} + M_{DM}$, cf. §2.5.2), we obtain 90% confidence limits on the ratio of dark matter to stellar matter, for both oblate and prolate $\rho_{tot} \sim r^{-2}$ models, of $M_{DM}/M_{stars} = 4 - 9$ at $a_3 = 450''$ and $M_{DM}/M_{stars} = 3 - 5$ at the minimum a_3; note that these values may be systematically low due to the uncertainty in Υ_B for the stars described in §2.5.1. We are unable to set an upper bound on the mass because a_3 is not constrained by the data, but we obtain a 90% confidence lower bound $\Upsilon_B > 20 h_{80}^{-1} \Upsilon_\odot$ using the prolate $a_3 = 260''$ models which have the minimum

acceptable value of a_3 (see above).

TFC estimate the binding mass of NGC 720 by inferring the X-ray gas density from deprojecting the spherical King function (eq. [2.3]) and then employing the equation of hydrostatic equilibrium (eq. [2.1]). Assuming the gas is isothermal with temperatures consistent with our single-temperature models in §2.2.2, TFC find $M_{tot} \sim 6 \times 10^{11} h_{80} M_{\odot}$ at $r = 240''$, in excellent agreement with our values at that distance. Binney, Davies, & Illingworth (1990; also van der Marel 1992) utilize R-band surface photometry and extensive spectroscopic data to generate axisymmetric mass models for NGC 720. Within $\sim 60''$, Binney et. al. obtain $\Upsilon_B < 17.2$ scaled to $D = 20 h_{80}$ Mpc, which is consistent with the values in Figure 9. They also determine that a spatially constant value of Υ_B is consistent with their models; we will address this issue in the following section.

Franx (1993) shows that simple models of elliptical galaxies with massive halos satisfy a Tully-Fisher relation provided $v_c/\sigma_0 \sim 1.38$, where v_c is the maximum circular velocity of the halo and σ_0 is the observed central velocity dispersion. We may compute this quantity directly from our models. In cylindrical coordinates, the circular velocity for an oblate spheroid is,

$$v_c^2(R) = R \frac{\partial \Phi(R,z)}{\partial R}\bigg|_{z=0} \tag{2.27}$$

$$= \frac{4GM}{S_\alpha} \int_0^{R/a_3} \frac{\tilde{\rho}_\alpha(m^2) m^2 dm}{\sqrt{R^2 - e^2 a_3^2 m^2}}, \tag{2.28}$$

where S_α and $\tilde{\rho}_\alpha$ are defined by equation (2.18), $e = \sqrt{1-q^2}$ is the eccentricity, and in the notation of §2.4.1, $R^2 = x_1^2 + x_3^2$ and $z = x_2$. Hence, we may compute v_c/σ_0 using the total masses derived above; in principle, $v_c/\sigma_0 \sim 1.38$ may be used to constrain the mass as well. By using the previously derived total masses (90% confidence) for $\rho \sim r^{-2}$ and $a_3 = 450''$, we obtain $v_c(a_3) = (327-409)$ km s^{-1} and $v_c/\sigma_0 = 1.26-1.57$, where $\sigma_0 = 260$ km s^{-1} (Binney et al. 1990). For the models having $a_3 = 225''$, we obtain $v_c(a_3) = (351-429)$ km s^{-1} and $v_c/\sigma_0 = 1.35-1.65$. Therefore our potentials derived from analysis of the X-ray gas yield v_c and v_c/σ_0 consistent with the models

of Franx (1993), the agreement being better for the models having larger a_3.

2.5 Dark Matter Distribution

We utilize knowledge of the observed stellar and X-ray gas distributions to determine the distribution of dark matter. The total gravitational potential of the galaxy is simply,

$$\Phi = \Phi_{stars} + \Phi_{gas} + \Phi_{DM}, \tag{2.29}$$

where Φ_{stars}, Φ_{gas}, and Φ_{DM} are respectively the potentials of the visible stellar distribution, the X-ray emitting gas, and the dark matter. We would like to emphasize that Φ_{stars} is simply the potential inferred directly from the optical light (i.e. constant mass-to-light ratio model having mass of visible stars), Φ_{gas} is inferred directly from the observed X-rays, and Φ_{DM} is anything else – we do not assume anything about the composition of the dark matter, only that it is distributed differently from the visible stars and X-rays. In the notation of equation (2.17) we can express the above potential as,

$$\Phi = -GM_{stars}\left[\frac{\phi_{stars}}{S_{stars}} + \frac{\phi_{gas}}{S_{gas}}\left(\frac{M_{gas}}{M_{stars}}\right) + \frac{\phi_{DM}}{S_{DM}}\left(\frac{M_{DM}}{M_{stars}}\right)\right]. \tag{2.30}$$

Since Φ normalized to its central value is all that is necessary to constrain its shape, the masses enter only in terms of ratios to M_{stars}. As we show below, the ratio M_{gas}/M_{stars} is small for reasonable values of M_{stars}. Hence, the only free parameters of importance are those associated with the shape of the dark matter and the ratio M_{DM}/M_{stars}.

We emphasize that determination of M_{DM}/M_{stars} by fits to the X-ray radial profile is independent of the distance to the galaxy. By comparing the total mass obtained from this method to the mass derived from the distance-dependent equation (2.26), one can in principle constrain the distance to the galaxy; of course, this method will depend to some extent on the functional forms assumed for the three mass components. Unfortunately the PSPC constraints on $T(r)$ are still not precise enough to

set strong constraints on the mass. We must await instruments with superior spatial and spectral resolution (e.g., AXAF) to determine the viability of this method as a distance indicator.

2.5.1 Stellar Mass

We estimate the stellar mass density (ρ_{stars}) by assuming that it is proportional to the stellar light. Comprehensive major-axis R-band surface photometry data exists in the literature for NGC 720 (see references in §2.2.1) allowing us to examine data spanning the whole galaxy; i.e. Lauer (1985) concentrates on the inner 5″ of the galaxy; Jedrzejewski, Davies, & Illingworth (1987), who like other authors, publish data out to $\sim 60''$; and Peletier et al. (1990) who publish data for NGC 720 extending out to $\sim 120''$; see Peletier et. al. (1990) for a discussion regarding the consistency of these data sets.

For simplicity, we fit functions to the surface brightness data that are projections of either the Ferrers or Hernquist models (§2.4.1). Since our models require that the mass be bounded (i.e. $0 \leq m \leq 1$), we have to arbitrarily assign an edge to the stellar matter; we also assume the galaxy is not inclined along the line of sight (cf. §2.4.1). The projection of the Ferrers model proceeds by considering an oblate spheroid having semi-major axes a_x, a_y and semi-minor axis $a_z = qa_x$, where q is the axial ratio, and the (y, z) plane is the sky plane. The luminosity density for the Ferrers model is then $j_F \propto (a^2 + x^2 + y^2 + z^2/q^2)^{-n}$. Since we fit only the surface brightness data on the projected major axis ($z = 0$), j_F only depends on $r = \sqrt{x^2 + y^2}$. By exploiting the circular symmetry in the plane in the same manner that is done for spherical systems (cf. Binney & Tremaine 1987, §2.1 (d)), we obtain the projected luminosity,

$$I_F(R) \propto \left[1 + \left(\frac{R}{a}\right)^2\right]^{n-1/2} \int_0^B \frac{du}{(1+u^2)^n}, \qquad B = \left(\frac{a_3^2 - R^2}{R^2 + a^2}\right)^{1/2}, \qquad (2.31)$$

where R is the projected radius, $a_3 = a_x = a_y$ is the edge of the stellar matter, a, and n are free parameters; note that q is not constrained by this method. By fitting I_F to the major axis surface brightness we obtain j_F, from which follows $\rho_{stars} \propto j_F$.

For the projected Hernquist density, we just use the de Vaucouleurs $R^{1/4}$ Law. We assume 2% uncertainties for all the data sets

Neither of the models fits the surface brightness with high accuracy over the whole galaxy. Generally I_F is an excellent description of both the inner $\sim 60''$ where $n \sim 1.25$, and outside $60''$ where $n \sim 1.5$. Fitting the whole galaxy, in contrast, yields a marginal result that is a good representation of the core, but slightly too flat in the outskirts. The $R^{1/4}$ Law characterizes well the outer regions ($\gtrsim 60''$) of the galaxy, but is a terrible fit in the interior. We choose to employ a single power law over the entire galaxy because (1) most of the light is concentrated in the regions where I_F is a very accurate description of the surface brightness, and (2) the increased accuracy of a more sophisticated model (e.g., a smooth joining of the Ferrers density in the interior to the Hernquist density in the exterior region) is not justified for modeling of the X-ray data. Since the fitted values of a and n depend to some extent on the choice of a_3, we examine the effects of a_3 varying between the minimum $120''$ and ∞. Over this range the best-fit a and n change by less than 10%, where $a_3 = 225''$ yields essentially intermediate parameter values. Upon examination of the three data sets with a_3 set to $225''$, we adopt $a = 4''$ and $n = 1.3$. Thus, we model the stellar matter as an oblate spheroid having the density,

$$\rho_{stars} \propto \left[\left(\frac{4}{225}\right)^2 + m^2\right]^{-1.3}, \tag{2.32}$$

where m is the ellipsoidal parameter defined by equation (2.15). From consideration of the R-band isophote shapes we set $\epsilon_{stars} = 1 - q = 0.40$.

In order to completely specify ρ_{stars} we must determine the total stellar mass. Ideally, we would like to assign to M_{stars} the mass associated with the visible stars. Then we could identify M_{DM}/M_{stars} as the ratio of dark matter to stellar matter. Unfortunately, the stellar mass estimates of ellipticals derived from population synthesis techniques (e.g., Pickles 1985; Bacon 1985; Peletier 1989) are very uncertain and are generally modeled to agree with dynamical estimates. Since dynamical masses only yield total masses, the population synthesis estimates of the visible stellar matter may

actually contain significant amounts of dark matter. The population synthesis studies generally find that $\Upsilon_B \sim 7\Upsilon_\odot$ for the stellar content of ellipticals, independent of absolute magnitude. Since $B-R$ is essentially constant across NGC 720 (Peletier et al. 1989), the shape of ρ_{stars} in R and B may be assumed equal. Hence, the above mass-to-light ratio translates to a stellar mass $M_{stars} \sim 1.5 \times 10^{11} h_{80} M_\odot$ for NGC 720, where we have used L_B as computed in §2.4.3. Note that since this estimate of the stellar mass may contain a significant contribution of dark matter, we may underestimate the mass in dark matter.

2.5.2 X-ray Gas Mass

Neglecting the ellipticity of the gas, the X-ray surface brightness is accurately parameterized by the King function (eq. [2.3]). By taking $\beta = 0.50$, deprojection of the King function yields the simple expression for the X-ray luminosity density,

$$j_{gas}(r) = \frac{I_0}{2a_X}\left[1+\left(\frac{r}{a_X}\right)^2\right]^{-3/2}, \tag{2.33}$$

where I_0 is the surface brightness evaluated at $r = 0$ and $a_X = 16''$ is the core radius. We relate j_{gas} to the gas density using equation (2.9),

$$\rho_{gas} = \left(\frac{\mu^2 m_p^2 I_0}{0.44 a_X \Lambda_{PSPC}(T_{gas})}\right)^{1/2}\left[1+\left(\frac{m a_{3X}}{a_X}\right)^2\right]^{-3/4}, \tag{2.34}$$

where we have set $a_{3X} = 375''$ (cf. §2.2.1); and in analogy with ρ_{stars} we have expressed ρ_{gas} in terms of the dimensionless ellipsoidal parameter m (cf. eq. [2.15]). Although we have derived the radial variation of ρ_{gas} assuming spherical symmetry, we set $\epsilon_{gas} = 0.25$ in the models to reflect the shape of the X-ray isophotes. As we show below, the precise form for ρ_{gas} is not particularly important in the models since M_{gas}/M_{stars} is small.

We obtain the mass of the gas by integrating equation (2.34). For simplicity, and because the isophote shapes are not well constrained for distances greater than $\sim 105''$, we assume spherical symmetry for estimation of M_{gas}; this assumption will cause us to

overestimate the mass by $\sim 25\%$ if the gas is intrinsically oblate with constant $\epsilon_{gas} = 0.25$ out to a_{3X}. Using the single-temperature 90% confidence range for T_{gas} (cf. Table 5), we list in Table 10 values of M_{gas}, the volume-averaged particle density ($\overline{n}$), and its associated cooling time ($\overline{\tau}$), all computed within $a_{3X} = 375''$; also listed are the best-fit results for the two-temperature spectrum with solar abundances having emission-weighted temperature 0.74 keV. To facilitate comparison with TFC, we also list these parameters computed within $r = 210''$. TFC, who apply a different technique and assume a 1 keV spectrum with solar abundances, obtain best-fit estimates (scaled to $D = 20$ Mpc) of $M_{gas} = 1.2 \times 10^9 M_\odot$, $\overline{n} = 1.1 \times 10^{-3}$ cm^{-3}, and $\overline{\tau} = 2.9 \times 10^9$ yr, in good agreement with our values within TFC's considerable uncertainties.

These values of M_{gas} imply $M_{gas}/M_{stars} \lesssim 1/20$, where M_{stars} was estimated in the previous section; i.e. the influence of the gas on the total potential of the galaxy is negligible. Nevertheless, we included the gas in our models (typically setting $M_{gas}/M_{stars} = 1/50$) and determined that not until $M_{gas}/M_{stars} \sim 1$ does this ratio begin to significantly influence the derived dark matter shapes and masses; i.e. the self-gravity of the gas is not dynamically important.

2.5.3 Results

Having specified ρ_{stars}, ρ_{gas}, and M_{gas}/M_{stars}, the only remaining quantities required to determine the total gravitational potential (eq. [2.30]) are the dark matter shape parameters a_3, ϵ_{DM}, a_0, and the mass ratio M_{DM}/M_{stars}. For a given value of M_{DM}/M_{stars}, the limits on ϵ_{DM} are obtained in the same manner as in §2.4. Because of the stringent constraints placed on temperature gradients by the K-S tests (cf. §2.4.2) we restrict ourselves to the isothermal case; any small uncertainties due to temperature gradients will be outweighed by systematic effects resulting from our specific choice of mass models. As a result we employ the isothermal expression (eq. [2.22]) for ρ_{gas}. For simplicity we consider only oblate forms for the stars, gas, and dark matter. In the following section we discuss the position angle offset of the optical and X-ray distributions.

First we examine dark matter having $\rho_{DM} \sim r^{-2}$ and $a_3 = 450''$. In Table 11

we list the results of our fits for several values of M_{DM}/M_{stars}. The galaxy without any dark matter is immediately ruled out because $\rho_{stars} + \rho_{gas}$ alone produces an X-ray surface brightness far too steep to account for the data (cf. Figure 10); we mention that polytropic models of the stellar mass will yield acceptable fits to the X-ray surface brightness only for large polytropic indices ($\gamma \sim 1.5$) that imply large temperature gradients that are ruled out by the PSPC spectrum (cf. §2.2.2). For $M_{DM}/M_{stars} > 25$, the models highly resemble the single-component case; i.e. the model surface brightness fits the data beautifully and exhibits ϵ_{DM} ranges virtually identical to ϵ_{tot} in Table 8. For smaller values of M_{DM}/M_{stars}, the fits deteriorate while the ϵ_{DM} limits remain nearly constant in width but are systematically shifted upwards by $\epsilon \sim 0.02$. However, the core parameter values increase with decreasing mass ratio in order to flatten out the radial profile which is becoming steeper due to the increasing influence of ρ_{stars}. By employing the same criteria used in §2.4.2 for determining the acceptability of fits, we find that for $a_3 = 450''$, $M_{DM}/M_{stars} > 7$ (90% confidence), independent of the distance to the galaxy or the gas temperature; we show in Figure 10 the fit results of a typical model. It then follows that $M_{DM} > 1.1 \times 10^{12} h_{80} M_{\odot}$ and $M_{tot} > 1.2 \times 10^{12} h_{80} M_{\odot}$ using the value for M_{stars} adopted in §2.5.1. As with the total matter, the fitted parameters do not change substantially over the allowed ranges of $a_3 > a_{3min} = 225''$; e.g., the ϵ_{DM} limits shift systematically higher by ~ 0.02 for $a_3 = 225''$. However, because of the smaller volume the minimum dark mass ratio falls to $M_{DM}/M_{stars} = 4$ for $a_3 = 225''$. We thus conclude that $M_{DM}/M_{stars} \geq 4$ is a firm lower limit, although visual examination of the fits to the radial profile suggest that dark matter at least ~ 10 times the stellar mass yields a more accurate description of the data; we mention that the models with temperature gradients give the same results as with the single-component models (cf. §2.4.2). The lower limit for the mass derived from M_{DM}/M_{stars} is marginally consistent with the upper end of the confidence interval for the corresponding isothermal M_{tot} in Table 9. This slight discrepancy could be accounted for if the gas is really multi-temperature, or if the galaxy is more distant than 20 Mpc, or if our chosen mass models are not adequate descriptions for the galaxy.

The results for ρ_{DM} having the Hernquist form closely parallel the $\rho_{DM} \sim r^{-2}$ behavior; i.e. for $M_{DM}/M_{stars} > 25$ the total matter results of §2.4.2 are returned very accurately. Judging by the quality of the fits, the minimum allowed mass ratio for $a_3 = 450''$ is 9 and the ϵ_{DM} limits change less than ~ 0.01 over the range of M_{DM}/M_{stars}. For mass ratios decreasing below 25 the values of a_0 increase substantially, becoming equal to and exceeding a_3 for $M_{DM}/M_{stars} \leq 10$. Such large values for a_0 indicate that the r^{-4} regime of the Hernquist density is being suppressed, thus suggesting that an intrinsic profile flatter than the Hernquist form is a more natural description of the dark matter.

We plot in Figure 11(a) the mass of stars, gas, and dark matter as a function of $a = ma_3$ for $\rho_{DM} \sim r^{-2}$ and $a_3 = 450''$ assuming $M_{DM}/M_{stars} = 10$; the plot is normalized to the value of M_{stars} from §2.5.1. For comparison we plot in Figure 11(b) $\Upsilon_B(a) = M_{tot}(a)/L_B(a)$, where $M_{tot}(a) = M_{DM}(a) + M_{stars}(a) + M_{gas}(a)$ is the total mass within a, and $L_B(a) = \Upsilon_{Bstars} M_{stars}(a)$, where $\Upsilon_{Bstars} \sim 7\Upsilon_\odot$ from §2.5.1. The stellar mass dominates the dark matter within $\sim 20''$, but M_{DM}/M_{stars} increases quickly to 1 at $\sim 50''$ corresponding to the optical effective radius ($R_e = 52''$, Burstein et al. 1987). Exterior to R_e the dark matter prevails.

This behavior of Υ_B is consistent with recent optical studies. Both Binney et. al. (1990) and van der Marel (1991) obtain a nearly constant value for Υ_B in the inner regions of NGC 720; in addition, van der Marel concludes from his study of NGC 720 and 36 other bright ellipticals that Υ is generally not constant in the outermost regions of these ellipticals. This description for $\Upsilon_B(a)$ is consistent with that inferred from other stellar kinematic data (e.g., in de Zeeuw & Franx 1991). More recently, using a two-component model of stars + dark matter, Saglia, Bertin, & Stiavelli (1992; Bertin, Saglia, & Stiavelli 1992) conclude from stellar dynamical analyses of 10 bright round ellipticals, that generally the amount of dark matter inside an effective radius (R_e) is of order the stellar mass; typically $\Upsilon_B \sim 7\Upsilon_\odot$ for the stars and $\Upsilon_B \sim 12\Upsilon_\odot$ for the total mass. The analysis of Saglia et al. underestimates the mass if those galaxies, round in projection, are actually flattened along the line-of-sight. Our results for Υ_B obtained by analyzing X-ray data of NGC 720 agree with these studies.

2.6 Discussion

The procedures developed in §2.4 and §2.5 to measure the ellipticity of the total gravitating matter and the dark matter both assume a mass ellipsoid of constant shape and orientation. However, the derived shapes are certain only out to distances where the X-ray isophote shapes are well determined. In Figure 12 we illustrate this effect by plotting ellipticity as a function of $a = ma_3$ for the X-ray surface brightness data (cf. Table 3) and a typical single-component matter model. The ellipticity of the data and model show excellent agreement for $a \leq 105''$ with the exception of $a = 60''$; presumably the $a = 60''$ discrepancy is due to the systematic errors discussed in §2.2.1 since the dip is not observed from the results of the isophote fitting. For $a > 105''$, the ellipticities of the model exceed the data which may result from either a real decrease in ellipticity of the gas or to a measurement error due to systematic errors in the computation of ϵ_M from the data; i.e, the systematic errors discussed in §2.2.1 become more serious as the S/N decreases as does the importance of the background and any other environmental effects. As a result of this uncertainty in the data, our constraints on the shape of the total matter and dark matter are strictly valid only out to $a = 105''$. The minimum acceptable $a_3 = 225''$ is quite insensitive to the relatively small ellipticities of the X-ray isophotes since it is determined from fits to the azimuthally-averaged radial profile. Because the dark matter may be significantly rounder than our models for $a > 105''$ the models may underestimate the total mass by as much as a factor of 2. It would be useful to compare the results for constant shape ellipsoids to models possessing a slow radial variation of ellipticity (e.g., Stäckel potentials); we will explore the effects of different mass models in a future paper. In any event, we must await future missions (i.e. AXAF) with increased sensitivity to obtain precise measurements of the outer X-ray isophotes and thus determine the shape of the dark matter for larger distances.

The misalignment of the projected major axes of the gas and stars is intriguing. We argue in §2.3.2 that if there were no dark matter, and the stellar ellipsoid is axisymmetric, then the major axes should be aligned. Triaxiality could be the source

of such an offset which we will explore in a future paper which will include a ROSAT HRI observation of NGC 720. Another possibility is that the gas and stars are both axisymmetric (e.g., both are oblate) but their axes are not aligned. If indeed the mass in the interior of the galaxy is dominated by the stars as suggested by our models §2.5.3, we would expect the isophote major axes to gradually align themselves with the stellar matter as the radius decreases. We investigated the effects of such a misalignment for the $M_{DM}/M_{stars} = 7$ models of the previous section. We find that the requirement that the models reproduce the observed position angle offset does not increase the required amount of dark matter. This is simply an effect of the PSPC point spread function smearing out the inner 30″ where the stellar potential and any corresponding position angle twists become important. The superior resolution of the HRI should enhance our understanding of these issues.

A misalingment of the three-dimensional gas and stellar distributions will also have implications for theories of galaxy formation. In their simulations of hierarchical galaxy formation including gas dynamics, Katz & Gunn (1991) produce objects resembling spiral galaxies where the disk transfers more than 50% of its original angular momentum to the dark halo and forms at an angle of $\sim 30°$. Similar inclinations of the dark halo and stellar matter are observed in related simulations for galaxies of different Hubble types (Neal Katz 1993, private communication).

We have discussed in §2.3.1 how the interpretation of the shapes of the X-ray isophotes could be clouded if the gas is actually a multi-phase medium. However, it is also possible that in the very center, where the emission from the cold clumps dominate, the shape of the radial profile of the X-ray surface brightness could be distorted by a central peak; e.g., the excess emission due to a cooling flow. With regards to the derived ellipticity of the total matter, our models do not appear to be overly sensitive to the local details of the radial profile. Hence we conclude that the fine details of the state of the gas do not affect the shape determination; the fitted parameters a_0 and Γ are more sensitive, but typically do not vary by more than $\sim 50\%$.

The shape of the flattened halo we measure for NGC 720 appears to be consistent

with standard dissipationless collapse scenarios in a Cold Dark Matter (CDM) universe (Frenk et al. 1988; Katz 1991; Dubinski & Carlberg 1991; Franx, Illingworth, & de Zeeuw 1991; Warren, Quinn, Salmon, & Zurek 1992; cf. Silk & Wyse 1993 for a review). Generally these simulations produce halos which are, on average, flatter than the stellar population with a mean ellipticity ~ 0.50. In addition, the simulations of Dubinski & Carlberg (1992) do not produce halos flatter than $\epsilon \sim 0.60$ which happens to be approximately the mean ϵ of our results. It is also interesting to note that Dubinski & Carlberg (1992) find that their halos are fitted extremely well by a Hernquist density with an extremely small core. These results are also reproduced when dissipation is included in the simulations (Dubinski 1994). This is certainly not true for our models, although the core radii that we derive may be contaminated by the presence of a cooling flow in the innermost region (see above).

Until recently, the evidence for dark matter in normal ellipticals was quite weak (for reviews see Kent 1990; de Zeeuw & Franx 1991; Ashman 1992). Specifically, optical studies of normal ellipticals are generally confined to within $\sim R_e$ where the potential is likely to be dominated by the stars. And the masses of the few galaxies possessing rotation curves calculated from H I emission are uncertain because of uncertainty regarding the shape of the gas orbits. Even the previous X-ray studies of normal ellipticals with *Einstein* (e.g., TFC) have been very uncertain due to the poor constraints on $T(r)$. Recently Saglia et. al. (1993), having obtained accurate velocity dispersions for several ellipticals out to distances greater than $\sim (1-2)R_e$, find strong evidence for dark matter. Maoz & Rix (1993) deduce from observed gravitational lensing statistics that early-type galaxies have dark halos with typical velocity dispersions $\sigma^* > 270$ km s^{-1} for an L^* galaxy. From analysis of the polar ring galaxy NGC 4650, Sackett & Sparke (1991) conclude that there exists a dark matter halo with ellipticity ~ 0.60, although with considerable uncertainty. Recent studies of the Galactic halo and the halos of other late-type galaxies show evidence for triaxiality (Franx & de Zeeuw 1992; Kuijken & Tremaine 1993). All of these findings are consistent with our results.

In contrast, analyzing the dynamics of planetary nebulae extending out to $3.5R_e$

in the E0 galaxy NGC 3379, Ciardullo, Jacoby, & Dejonghe (1993) conclude that simple models having a constant mass-to-light ratio fit the data adequately without the need for dark matter. However, they do not demonstrate that dark matter models are inconsistent with their data; e.g., a massive dark matter halo model with anisotropic velocity dispersion. In addition to the possible environmental effects discussed by the authors to explain the "missing" dark matter, the spherical geometry of the stars may represent additional uncertainty. For example, Saglia et al. (1992) employ sophisticated two-component dynamical models to analyze the mass distributions for several bright ellipticals (cf. §2.5.3). They caution the reader that their "method seems to underestimate the amount of dark matter present" for intrinsically non-spherical objects seen round in projection. Hence, if NGC 3379 is significantly flattened along the line of sight, Ciardullo et al. likely underestimate the mass of the galaxy. We believe that Ciardullo et al.'s result does not contradict increasing evidence that ellipticals contain large amounts of dark matter.

2.7 Conclusion

We have described (1) a new test for dark matter and alternate theories of gravitation based on the relative geometries of the X-ray and optical surface brightness distributions and an assumed form for the gravitational potential of the optical light, (2) a technique to measure the shapes of the total gravitating matter and dark matter in an ellipsoidal system which is insensitive to the precise value of the temperature of the gas and to modest temperature gradients, and (3) a method to determine the ratio of dark mass to stellar mass (when the self-gravitation of the gas may be ignored) that is dependent on the functional forms for the visible star, gas, and dark mass but independent of the distance to the galaxy or the gas temperature.

We have applied these techniques to X-ray surface brightness data from the ROSAT PSPC of the flattened elliptical galaxy NGC 720. NGC 720 was selected because its flattened stellar distribution ($\epsilon \sim 0.40$) reduces possibilities of significant projection effects, and its large degree of isolation from other large galaxies suggests

that the gas is not distorted by environmental effects.

We draw the following conclusions:

1. We compute the ellipticities of the X-ray surface brightness by essentially taking quadrupole moments of the count distribution. The X-ray isophotes are elongated, having $\epsilon \sim 0.25$ for semi-major axis $a \sim 100''$. The major axes of the optical and X-ray isophotes are misaligned by $\sim 30°$

2. The gas does not exhibit either significant radial or azimuthal temperature gradients. A single-temperature (~ 0.6 keV) Raymond-Smith plasma with subsolar heavy element abundances is a good fit to the data; a two-temperature model (0.5 and 1.1 keV) with solar abundances describes the data just as well.

3. Considering only the relative geometries of the X-ray and optical surface brightness distributions and an assumed form for the potential of the optical light, *we conclude that matter distributed like the optical light cannot produce the observed ellipticities of the X-ray isophotes,* independent of the pressure and temperature of the gas and the value of the stellar mass. This conclusion assumes the conditions of quasi-hydrostatic equilibrium; i.e the shapes of the three-dimensional gas density trace the three-dimensional gravitational potential. We discuss the viability of this assumption in §2.3.1. Since this analysis is confined to the region where Milgrom's Modification of Newtonian Dynamics (MOND) predicts Newton's laws to apply, *we conclude that MOND does not eliminate the need for dark matter in NGC 720.*

4. Employing essentially the technique of Buote & Canizares (1992; Buote 1992) we use the *shape* of the X-ray surface brightness to constrain the *shape* of the total gravitating matter. The total matter is modeled as an oblate or prolate spheroid of constant shape and orientation having either a Ferrers ($\rho \sim r^{-n}$) or Hernquist density. Assuming the X-ray gas is in hydrostatic equilibrium with the potential generated by this mass, we construct a model X-ray gas distribution.

5. We determine the ellipticity of the total gravitating matter to be $\epsilon \sim 0.50 - 0.70$. Using the single-temperature model we estimate a total mass $(0.41 - 1.4) \times 10^{12} h_{80} M_{\odot}$ interior to a spheroid having semi-major axis ranging from $21.8 - 43.6 h_{80}$ kpc. Ferrers densities as steep as r^{-3} do not fit the data, but the r^{-2} and Hernquist models yield excellent fits.

6. We estimate the mass distributions of the stars and the gas by deprojecting their observed major-axis surface brightness profiles. We then fit the dark matter directly and find shapes in good agreement with those derived for the total matter. These fits yield a distance-independent and temperature-independent measurement of the ratio of dark mass to stellar mass M_{DM}/M_{stars}, but it is dependent on the models assumed for the three mass components of the galaxy. We estimate at minimum $M_{DM}/M_{stars} \geq 4$ interior to a spheroid of semi-major axis $21.8 h_{80}$ kpc corresponding to a total mass $(8.0 \times 10^{11} h_{80} M_{\odot})$ slightly greater than that derived from the single-temperature models at $D = 20 h_{80}$ Mpc $(4.1 - 7.5 \times 10^{11} h_{80} M_{\odot})$. More plausible values are $M_{DM}/M_{stars} \sim 10$ out to $\sim 30 h_{80}$ Mpc. The estimates for M_{DM}/M_{stars} may be lower than in reality since M_{stars} may contain a significant portion of dark matter.

Similar studies need to be performed on other galaxies in various environments to determine whether a flattened halo is a general property of ellipticals. In addition, the new proposed test for dark matter and alternate theories of gravitation needs to be applied to other galaxies (and perhaps clusters of galaxies) in order to ascertain the generality of our conclusions regarding MOND.

We are indebted to Paul Schechter and James Binney for suggesting the importance of studying X-ray properties of flattened ellipticals. Special thanks are given to an anonymous referee for his/her careful reading of the manuscript and whose many suggestions greatly improved the content and presentation of the paper. We express sincere gratitude to James Binney, Mordehai Milgrom, and Scott Tremaine for their careful reading of the manuscript and for several valid criticisms, particularly raising the issue of gas rotation. We would also like to thank Marijn Franx for

clarifying aspects of his Tully-Fisher relation for ellipticals. We gratefully acknowledge Christopher Becker, Edmund Bertschinger, Giuseppina Fabbiano, Eric Gaidos, Neal Katz, Eugene Magnier, and Paul Schechter for insightful discussions, Jonathon Woo for assistance with XSPEC, and the friendly people of hotseat@cfa.harvard.edu (especially Kathy Manning) who cheerfully answered our many questions regarding PROS. We thank John Tonry for providing us with his χ^2 minimization programs. We also acknowledge use of the SIMBAD data base. Supported in part by NASA grant NAG5-1656, NASGW-2681 (through subcontract SVSV2-62002 from Smithsonian Astrophysical Observatory), and NAS8-38249.

A. Analytical Calculation of $\Delta\epsilon_M$ and $\Delta\theta_M$

We derive the statistical uncertainty of the ellipticity and position angle for the iterative moment technique described in §2.2.1. Recall that ϵ_M and θ_M are complicated functions of the moments μ_{mn} (eq. [2.4]) which are themselves weighted averages over the whole aperture. Since the photon fluctuations from pixel to pixel are uncorrelated, we have for the variance in ellipticity, $(\Delta\epsilon_M)^2$, and position angle, $(\Delta\theta_M)^2$,

$$(\Delta\epsilon_M)^2 = \sum_{i=1}^{P} \left(\frac{\partial\epsilon_M}{\partial n_i}\right)^2 \sigma_{n_i}^2 \quad \text{and} \quad (\Delta\theta_M)^2 = \sum_{i=1}^{P} \left(\frac{\partial\theta_M}{\partial n_i}\right)^2 \sigma_{n_i}^2, \tag{A1}$$

where $N = \sum_{i=1}^{P} n_i$ is the total number of pixels in the aperture considered, and $\sigma_{n_i}^2$ is the variance of the counts, n_i, in the i'th pixel: for Poisson statistics, $\sigma_{n_i}^2 = n_i$. We begin by expressing ϵ_M (eq. [2.5]) and θ_M (eq. [2.6]) in terms of the moments μ_{mn}. Solving equation (2.7) for $\Lambda_\pm$ yields,

$$\Lambda_\pm = \left(\frac{-b \pm \sqrt{b^2 - 4c}}{2}\right)^{1/2}, \tag{A2}$$

where $b = -(\mu_{02} + \mu_{20})$ and $c = \mu_{02}\mu_{20} - \mu_{11}^2$. The moments from equation (2.4) take the explicit form:

$$\mu_{02} = \frac{1}{N}\sum_i n_i Y_i^2 - \left(\frac{1}{N}\sum_i n_i Y_i\right)^2, \tag{A3}$$

$$\mu_{20} = \frac{1}{N}\sum_i n_i X_i^2 - \left(\frac{1}{N}\sum_i n_i X_i\right)^2, \tag{A4}$$

$$\mu_{11} = \frac{1}{N}\sum_i n_i X_i Y_i - \frac{1}{N^2}\sum_i n_i X_i \sum_i n_i Y_i, \tag{A5}$$

where we have suppressed the upper limit, P, on the summations in the interest of compact notation. In practice we set $X_i \equiv x_i - \bar{x}_i$ and $Y_i \equiv y_i - \bar{y}_i$; in the following we will neglect the derivatives of the additional centroid terms since they contribute terms that are of order $\frac{1}{N}$ with respect to the other undifferentiated terms. Since N is a large number (> 100) for all our apertures, we may safely neglect this contribution.

Substituting $\Lambda_\pm$ into the expressions for ϵ_M and θ_M and taking the derivative with respect to n_i gives,

$$\frac{\partial \epsilon_M}{\partial n_i} = \left(b + \sqrt{b^2 - 4c}\right)\left(\frac{1}{4c^{3/2}}\frac{\partial c}{\partial n_i}\right) - \frac{1}{2\sqrt{c}}\left(\frac{\partial b}{\partial n_i} + \frac{b\partial b/\partial n_i - 2\partial c/\partial n_i}{\sqrt{b^2 - 4c}}\right), \tag{A6}$$

$$\frac{\partial \theta_M}{\partial n_i} = \left[1 + \left(\frac{\mu_{11}}{\Lambda_+^2 - \mu_{02}}\right)^2\right]^{-1}\left\{\frac{\partial \mu_{11}/\partial n_i}{\Lambda_+^2 - \mu_{02}} - \frac{\mu_{11}}{(\Lambda_+^2 - \mu_{02})^2}\left[\frac{\partial \Lambda_+^2}{\partial n_i} - \frac{\partial \mu_{02}}{\partial n_i}\right]\right\} \tag{A7}$$

where

$$\frac{\partial \Lambda_+}{\partial n_i} = 2^{-3/2}\left(-b + \sqrt{b^2 - 4c}\right)^{-1/2}\left[-\frac{\partial b}{\partial n_i} + \frac{b\partial b/\partial n_i - 2\partial c/\partial n_i}{\sqrt{b^2 - 4c}}\right], \tag{A8}$$

where the derivatives of b and c follow straightforwardly from their above definitions. All that now remains is to compute the derivatives of the moments. Keeping terms only to order $1/N$ we find:

$$\frac{\partial \mu_{02}}{\partial n_i} = \frac{1}{N}Y_i^2 - \frac{2}{N}Y_i\left(\frac{1}{N}\sum_k n_k Y_k\right), \tag{A9}$$

$$\frac{\partial \mu_{20}}{\partial n_i} = \frac{1}{N}X_i^2 - \frac{2}{N}X_i\left(\frac{1}{N}\sum_k n_k X_k\right), \tag{A10}$$

$$\frac{\partial \mu_{11}}{\partial n_i} = \frac{1}{N} X_i Y_i - \frac{1}{N} X_i \left(\frac{1}{N} \sum_k n_k X_k \right) - \frac{1}{N} Y_i \left(\frac{1}{N} \sum_k n_k Y_k \right). \quad \text{(A11)}$$

By substituting the expressions for $\partial \epsilon_M / \partial n_i$ and $\partial \theta_M / \partial n_i$ into equation (A1) , one obtains the 68% confidence statistical uncertainties $\Delta \epsilon_M$ and $\Delta \theta_M$. Multiplying these 68% errors by $\sqrt{2.71}$ gives 90% error estimates. We have verified the reliability of these uncertainty estimates through the Monte Carlo simulations described in §2.2.1.

B. Projections of Non-Similar Spheroids

There is a paucity of simple, yet flexible, analytic models for non-similar spheroids. By flexible we mean that the models extant in the literature generally do not allow one to easily impose a specific ellipticity function ($\epsilon(r), r = \sqrt{x^2 + y^2 + z^2}$) on the model; e.g. Stäckel models (e.g., Dejonghe & de Zeeuw 1988), models consisting of a multipole decomposition into monopole and quadrupole terms (e.g., Kochanek 1991), and models constructed by adding individual homoeoids of varying axial ratio (Schramm 1994). In addition, the first two of these models are not exactly spheroidal. In order to achieve the desired flexibility, we prefer to generalize the similar spheroid case by considering functions stratified on surfaces of constant

$$\xi^2 = x^2 + y^2 + z^2/q^2, \quad \text{(B12)}$$

where $q = q(r)$ is the radially-varying axial ratio. These surfaces, like the previously mentioned examples, are not true spheroids. However they are good approximations to spheroids for reasonable $q(r)$, their deviations being characterized by slight " boxyness". Hence, in these models $q < 1$ corresponds to an oblate pseudo spheroid, $q > 1$ corresponds to a prolate pseudo spheroid.

We are ultimately interested in functions that represent the X-ray gas volume emissivities and gravitational potentials of elliptical galaxies. It follows that we may restrict ourselves to functions whose radial dependence is not flatter than $\log \xi$ (corresponding to flattest reasonable potentials) and not steeper than ξ^{-4} (corresponding

to volume densities appropriate to the outer regions of a de Vaucouleurs Law). We also demand that our functions possess ellipticity ($\epsilon = 1 - q$) gradients that are typical of assumed potentials in elliptical galaxies (cf. Figure 2-13 in Binney & Tremaine 1987). Such ellipticities are smooth and monotonically decreasing, and have central ellipticity no greater than $\epsilon \sim 0.40$ corresponding to E6 galaxies.

A simple parametrization of the ellipticity of the pseudo spheroids that qualitatively obeys these restrictions is given conveniently by,

$$\epsilon(r) = \frac{2\epsilon_c}{1 + r/r_c}, \tag{B13}$$

where $\epsilon_c = \epsilon(r_c) = \epsilon(0)/2$. For $r \gg r_c$, $\epsilon(r) \sim r^{-1}$ which is somewhat steeper than the gradients of the assumed theoretical potentials. We desire this behavior since our intent is to study the effects of ellipticity gradients of a three dimensional distribution on the ellipticities of the contours of its projection. The projections of the pseudo spheroids with $\epsilon(r)$ should exhibit the maximum deviations from the similar spheroid case expected of ellipticity gradients consistent with the above restrictions.

We consider the functions $\log(a_0^2 + \xi^2)$ and $(a_0^2 + \xi^2)^{-2}$ with $q(r) = 1 - \epsilon(r)$ as given above, where a_0 is the core parameter. We assume a_0 is the same for both functions because the core parameter should be very similar for the potential and X-ray emissivity under the conditions of hydrostatic equilibrium and reasonably small temperature gradients (eq. [2.1]). Moreover, for steep (negative) temperature gradients a_0 of the mass (and potential) may be significantly smaller than that of the gas. This has the effect of steepening the radial slope of the inner part of the potential, thus bringing the radial slope into slightly better agreement with the steeper gas emissivity; i.e. steep negative temperature gradients will give smaller core parameters for the potential that yield projected ellipticity deviations smaller than in the isothermal case. We set $\epsilon_c = 0.20$ so the model potentials will include the flattest potentials expected for ellipticals; also, smaller values of ϵ_c reflect more spherical objects whose axial ratios are less sensitive to projection. There are three distinct regimes that characterize the behavior of these pseudo spheroids: (1) $a_0 \gg r_c$, (2) $a_0 \sim r_c$, and

(3) $a_0 \ll r_c$. In Figure 13 we plot the projections of these functions (edge-on) in each regime; i.e. $a_0 = r_c/10$, $a_0 = r_c$, and $a_0 = 10r_c$. The figures show a consistent picture of the difference in ellipticity ($\Delta\epsilon$) of the logarithmic and r^{-4} projections. First, the logarithmic function projects to contours that are noticeably rounder than the r^{-4} and the three dimensional ellipticity. This effect arises because contributions from the rounder, outermost three dimensional surfaces to the projection are more important to the flat logarithmic function than the steep r^{-4} model. We also observe the anticipated correlation between the magnitude of $\Delta\epsilon$ and the gradient in $\epsilon(r)$; i.e. the steeper the gradient in ellipticity, the larger is $\Delta\epsilon$. However, in all regimes $\Delta\epsilon \lesssim 0.04$ for $a > a_0$ and never exceeds 0.06 for all a; these results are identical for the oblate and prolate pseudo spheroids. Thus, assuming quasi-hydrostatic equilibrium in elliptical galaxies, *the shapes of the X-ray isophotes and the projected potentials are approximately the same, with maximum deviations of* $\Delta\epsilon \lesssim 0.04$ *outside of the core region.* For two functions not having such disparate radial slopes and/or flatter ellipticity profiles, the discrepancy in projected ellipticities will be significantly smaller. We illustrate this point with a concrete example applied to NGC 720.

Suppose the only significant mass component in NGC 720 is that due to the visible stars. Then quasi-hydrostatic equilibrium requires that the three dimensional X-ray gas emissivity (j_{gas}) has the same three dimensional contours as the gravitational potential generated by the visible stars (Φ_{stars}). As we discuss in §2.5.1, the visible star density is reasonably approximated by an oblate spheroid with radial dependence $\rho_{stars} \sim r^{-2.6}$ and $\epsilon = 0.40$. This density yields a potential that approximately behaves as $\Phi_{stars} \sim r^{-0.6}$; its contours are moderately flattened at the center ($\epsilon \sim 0.20$) and become monotonically rounder with distance. In §2.5.2 we show that $j_{gas} \sim r^{-3}$, with a core parameter $a_0 = 16''$.

We now examine the projections of Φ_{stars} and j_{gas}. We parametrize the emissivity as a pseudo spheroid $j_{gas} \propto (a_0^2 + \xi^2)^{-3/2}$, where we assign the $\epsilon(r)$ associated with Φ_{stars}. In order to make a consistent comparison, we also employ the pseudo spheroid construction for Φ_{stars}. That is, after computing Φ_{stars} numerically, we fit the ellipticity profile ($\epsilon(r)$) along the major axis. An acceptable fit is obtained us-

ing a function consisting of products of equation (B13) with additional parameters: $\epsilon(r) \propto (1 + (r/r_c)^a)^{-1}(1 + (r/r_d)^b)^{-1}$, where r_c, r_d, a, and b are free parameters. In Figure 14 (a) we plot this fitted $\epsilon(r)$ and the exact ellipticity profile of Φ_{stars} obtained numerically. The fitted function yields a good qualitative representation of the three dimensional potential ellipticity.

Using this $\epsilon(r)$, we then construct $\Phi_{stars} \propto (a_0^2 + \xi^2)^{-0.3}$, where $a_0 = 16''$; note the results are not sensitive to the precise choice of a_0 (see above). In Figure 14 (b) we show the results of the projections for oblate spheroids (the prolate case gives the same qualitative results as is expected since we are dealing with relatively small ellipticities); note that the integration is performed only within a spheroid having a major axis of 400″, that being the extent of the X-ray gas. For comparison we plot in Figure 14 (a) the projection of Φ_{stars} obtained from direct numerical calculation. Notice that our approximation to $\epsilon(r)$ is slightly steeper than the exact case and that the exact projected ellipticities deviate less from the three dimensional ellipticities than for the pseudo spheroid case because the exact case is more closely related to a similar spheroid. As for the pseudo spheroids, the agreement between the projected potential and the projected emissivity is excellent, the maximum deviation being $\Delta\epsilon \sim 0.02$. This value is less than the statistical uncertainty in the measured values of ellipticity of the X-ray isophotes (§2.2.1). Thus quasi-hydrostatic equilibrium implies that *if the stars are the dominant contribution to the gravitational potential in NGC 720, then the PSPC X-ray isophotes and projected potential contours have virtually identical shapes.*

Table 1: ROSAT Observation of NGC 720

ROSAT Seq, No.	Date Obs,	R.A.;[a] Dec	R.A.[b] Dec	Exposure (s)	Flux[c] (erg cm^{-2} s^{-1})
rp600005	Jan., 92	$1^h53^m00^s.4$	$1^h53^m00^s.0$;	23108	9.76×10^{-13}
		$-13°44'18''$	$-13°44'20''$		8.52×10^{-13}

[a]Optical center from Dressler, Schechter, & Rose (1986) precessed to J2000 coordinates.

[b]X-ray centroid (J2000) computed in this paper.

[c]Computed in 400″ radius circle for energy range 0.2 - 2.4 keV; 0.4 - 2.4 keV.

Table 2: Fits to King Function

	Best Fit a_x (arcsec)	90% Range	Best Fit β	90% Range	χ^2_{min}	dof	R (arcsec)
BC	16.0	12.0 - 20.7	0.51	0.49 - 0.53	15.6	22	375
TFC*	3	< 37	0.45	0.40 - 0.50	12.9	8	495

*Energy range 0.2 - 4 keV.

Table 3: X-ray Ellipticities

a[a]	ϵ_M[c]	$\Delta\epsilon_M$[c]	cts[d]	a_{in}[e]	r[b]	ϵ_M[f]	$\Delta\epsilon_M$[f]	cts[d]	ϵ_{iso}[g]	$\Delta\epsilon_{iso}$[g]	ϵ_{opt}[h]
30	0.08	0.06	476						0.08	0.08	0.42
45	0.13	0.05	689						0.16	0.09	0.44
60	0.09	0.05	871	30	57	0.11	0.06	398	0.18	0.08	0.48
75	0.20	0.05	953	45	66	0.23	0.06	306	0.24	0.14	0.46
90	0.25	0.05	1011	60	74	0.32	0.09	229	0.36	0.09	0.46
105	0.25	0.05	1090	75	87	0.32	0.09	146	0.22	0.14	0.44
120	0.13	0.06	1184								0.44
135	0.15	0.07	1219								
150	0.16	0.08	1223	105	140	0.13[i]	0.07[i]	279[i]			
225	201	0.20[i]	0.05[i]	1774[i]	150	200	0.21[i]	0.09[i]			

[a]Semi-major axis of aperture in arcseconds.

[c]Computed with an elliptical aperture containing all counts interior to a (5″ pixels); $\Delta\epsilon_M$ represents 90% confidence statistical uncertainties.

[d]Counts interior to aperture (0.4 – 2.4) keV.

[e]Inner semi-major axis of annular aperture in arcseconds.

[f]Computed with elliptical annular aperture between a and a_{in} (5″ pixels); $\Delta\epsilon_M$ represents 90% confidence statistical uncertainties.

[g]Results from fitting ellipses to the X-ray isophotes; $\Delta\epsilon_{iso}$ represents 68% confidence statistical uncertainties.

[h]R – band optical ellipticities taken from Peletier et al. (1989).

[i]Computed from image with 15″ pixels.

Table 4: X-ray Position Angles (N through E)

a[a]	r[b]	θ_M[c]	$\Delta\theta_M$[c]	a_{in}[d]	r[b]	θ_M[e]	$\Delta\theta_M$[e]	r[b]	θ_{iso}[f]	$\Delta\theta_{iso}$[f]	θ_{opt}[g]
30	29	83	24					29	119	28	142
45	42	125	12					41	126	18	142
60	57	118	17	30	57	116	17	54	109	14	141
75	67	111	7	45	66	106	9	59	112	19	142
90	78	113	6	60	74	116	8	73	115	9	144
105	91	116	6	75	87	120	10	93	112	21	144
120	112	117	15								136
135	124	102	14								
150	137	102	15	105	140	104[h]	18[h]				
225	201	107[h]	8[h]	150	200	124[h]	15[h]				

[a]Semi-major axis of aperture in arcseconds

[b]Effective radius of aperture $r = (ab)^{1/2}$, where $b = (1 - \epsilon)a$.

[c]Position angle (degrees) computed with an elliptical aperture containing all counts interior to a (5″ pixels); $\Delta\theta_M$ represents 90% confidence statistical uncertainties.

[d]Inner semi-major axis of annular aperture in arcseconds.

[e]Position angle computed with elliptical annular aperture between a and a_{in} (5″ pixels); $\Delta\theta_M$ represents 90% confidence statistical uncertainties.

[f]Results from fitting ellipses to the X-ray isophotes; position angle in degrees and $\Delta\theta_{iso}$ represents 68% confidence statistical uncertainties.

[g]R – band optical position angles (degrees) taken from Peletier et al. (1989).

[h]Computed from image with 15″ pixels.

Table 5: Spectral Data and Fit Results

Region	Model	χ^2_{min}	dof*	N_H cm^{-2}	Abun (% solar)	T (keV)
0″- 400″	$1T$†	25.1	25	$(0.1 - 3.2) \times 10^{20}$	8 - 60	0.48 - 0.69
0″- 400″	$2T$‡	24.0	24	4×10^{19}	100	(0.44, 1.1)
0″- 60″	$1T$	21.3	18	$(0.5 - 2) \times 10^{20}$	10 - 40	0.5 - 0.7
120″- 400″	$1T$	10.2	12	$< 4 \times 10^{20}$	1 - 80	0.4 - 0.8
(A)	$1T$	15.6	16	$< 2 \times 10^{20}$	10 - 80	0.5 - 0.7
(B)	$1T$	20.0	17	$(1 - 4) \times 10^{20}$	5 - 25	0.5 - 0.7

*Degrees of freedom. The energy ranges are: (0.2 - 2.4) keV for 0″- 400″; (0.2 - 1.7) keV for 0″- 60″; (0.2 - 0.28, 0.4 - 1.4) keV for 120″- 400″; (0.2 - 0.37, 0.4 - 1.6) keV for (A); and (0.2 - 1.5, 1.6 - 1.7) keV for (B).

† Single-temperature Raymond-Smith model. 90% confidence estimates for parameters are shown for 0″- 400″, 68% confidence for the others.

‡Two-temperature Raymond-Smith model with abundances fixed at 100% solar. Only the best-fit values are displayed.

Table 6: Oblate Stellar Equipotential Ellipticities

a		ϵ_{pot}			$\epsilon_{isophote}$
(arcsec)	ϵ_x	3-D	2-D	$\langle$2-D$\rangle_{PSPC}$	$\langle$2-D$\rangle_{PSPC}$
30	0.02 - 0.14	0.13	0.13	0.11	0.06
45	0.08 - 0.18	0.12	0.12	0.11	0.09
60	0.04 - 0.14	0.11	0.11	0.11	0.10
75	0.15 - 0.25	0.11	0.11	0.10	0.10
90	0.20 - 0.30	0.11	0.10	0.10	0.10
105	0.20 - 0.30	0.10	0.10	0.10	0.10
120	0.07 - 0.19	0.10	0.10	0.09	0.10
135	0.08 - 0.22	0.10	0.09	0.09	0.09
150	0.08 - 0.24	0.10	0.09	0.09	0.09
225	0.15 - 0.25	0.07	0.05	0.05	0.05

Note. — Ellipticities listed as a function of semi-major axis a. ϵ_x are the 90% limits for ϵ_M computed for the X-ray image in Table 3. ϵ_{pot} is the ellipticity of the stellar isopotentials in three dimensions (3-D), 2-D (i.e. projected along the line of sight), and 2-D convolved with the PSF of the PSPC. $\epsilon_{isophote}$ is the expected ellipticity of the isophotes if the gas is an isothermal ideal gas (i.e. contours of constant projected ρ^2_{gas}; cf. Table 11).

Table 7: Monte Carlo Ellipticities

a	Oblate			Prolate		
(arcsec)	$\bar{\epsilon}_M$	90%	99%	$\bar{\epsilon}_M$	90%	99%
30	0.07	0.00 - 0.13	0.00 - 0.24	0.10	0.00 - 0.22	0.00 - 0.37
45	0.08	0.00 - 0.15	0.00 - 0.20	0.10	0.00 - 0.19	0.00 - 0.29
60	0.09	0.00 - 0.15	0.00 - 0.22	0.10	0.00 - 0.19	0.00 - 0.27
75	0.10	0.01 - 0.17	0.00 - 0.23	0.11	0.01 - 0.19	0.00 - 0.25
90	0.10	0.01 - 0.18	0.00 - 0.24	0.11	0.01 - 0.19	0.00 - 0.25
105	0.10	0.00 - 0.19	0.00 - 0.25	0.11	0.01 - 0.20	0.00 - 0.25
120	0.11	0.01 - 0.20	0.00 - 0.26	0.11	0.01 - 0.20	0.00 - 0.25
135	0.11	0.01 - 0.20	0.00 - 0.26	0.11	0.01 - 0.20	0.00 - 0.26

Note. — Results of 1000 Monte Carlo simulations of the constant mass-to-light model. Listed are ellipticities as a function of semi-major axis a computed using the iterative moment technique described in §2.2.1. $\bar{\epsilon}_M$ is the mean value of ϵ_M for all the simulations and 90% and 99% are the corresponding confidence limits

Table 8: Total Gravitating Matter Shape Results (ϵ_{tot})

Density Model	Oblate ϵ_{tot}	Prolate ϵ_{tot}	χ^2_{min} [a]	a_0 (arcsec)[b]	$\lvert\Gamma\rvert$[b]
$\rho \sim r^{-2}$	0.52 - 0.74	0.49 - 0.65	15	6.9 - 14.9	5.63 - 6.14
$\rho \sim r^{-3}$	0.50 - 0.72	0.45 - 0.62	35	32.4 - 49.0	4.83 - 5.09
Hernquist	0.50 - 0.71	0.47 - 0.63	20	133 - 213	5.43 - 5.80

[a]Typical minimum χ^2 (22 dof) for ϵ_{tot} ranges in columns 2 and 3.

[b]90% confidence values for oblate ϵ_{tot} range in column 2.

Table 9: Total Spheroidal Mass†

		Oblate		Prolate	
Model	a_3‡	$M_{tot}(10^{12}M_\odot)$	$\Upsilon_B(\Upsilon_\odot)$	$M_{tot}(10^{12}M_\odot)$	$\Upsilon_B(\Upsilon_\odot)$
$\rho \sim r^{-2}$	450	0.79 - 1.4	35.9 - 62.7	0.61 - 1.1	27.7 - 51.8
$\rho \sim r^{-2}$	(225, 260)*	0.45 - 0.75	20.6 - 34.3	0.41 - 0.73	18.8 - 33.2
Hernquist	450	0.64 - 1.1	28.9 - 51.8	0.54 - 1.0	24.6 - 45.9

†Assuming $D = 20h_{80}$ Mpc.

‡Semi-major axis in arcseconds ($10'' \sim 1$ kpc).

*(oblate, prolate).

Table 10: Total X-ray Gas Mass†

	M_{gas} ($10^9 h_{80}^{5/2} M_\odot$)		$\overline{n}$ ($10^{-3} h_{80}^{-1/2}$ cm^{-3})		$\overline{\tau}$ ($10^9 h_{80}^{1/2}$ yr)	
Model‡	$r = 210''$	$r = 375''$	$r = 210''$	$r = 375''$	$r = 210''$	$r = 375''$
$1T$	2.1 - 3.0	5.9 - 8.2	2.5 - 3.6	0.99 - 1.36	2.8 - 2.9	7.1 - 7.3
$2T$*	1.5	4.0	1.66	0.65	2.0	5.2

†0.4 - 2.4 keV.

‡Consult the spectral models in Table 5.

*We have used the emission-weighted temperature 0.74 keV.

Table 11: Dark Matter Shape Results†

$\frac{M_{DM}}{M_{stars}}$	ϵ_{DM}	χ^2_{min} [a]	a_0 (arcsec)[b]	$\lvert\Gamma\rvert$[b]
100	0.52 - 0.74	14.7 - 15.5	7.7 - 16.4	5.65 - 6.14
50	0.52 - 0.74	14.7 - 15.5	8.7 - 19.4	5.67 - 6.15
25	0.52 - 0.75	14.7 - 15.4	11.0 - 23.1	5.71 - 6.20
10	0.54 - 0.76	15.8 - 16.4	23.8 - 65.1	5.92 - 6.70
8	0.56 - 0.77	20.4 - 24.5	30.3 - 92.1	6.02 - 6.63
7	0.57 - 0.78	28.7 - 35.8	33.1 - 93.9	6.01 - 6.51
0[c]	...	605	...	5.2

†Oblate dark matter model with density, $\rho_{DM} \sim r^{-2}$ and $a_3 = 450''$.

[a]22 degrees of freedom.

[b]90% confidence values over ϵ_{DM} interval in column 2.

[c]Only the best-fit values are listed.

REFERENCES

Aschenbach, B. 1988, Appl.Optics, 27, No. 8, 1404

Ashman, K. M. 1992, PASP, 104, 1119

Bacon, R. 1985, A&A, 143, 84

Begeman, K. G., Broeils, A. H., & Sanders, R. H. 1991, MNRAS, 249, 523

Bekenstein, J., & Milgrom, M. 1984, ApJ, 286, 7

Bertin, G., Saglia, R. P., & Stiavelli, M. 1992, ApJ, 384, 423

Bertola, F., Bettoni, D., Danziger, J., Sadler, E., Sparke, L., & de Zeeuw, T. 1991, ApJ, 373, 369

Binney, J. J. 1985, MNRAS, 212, 769

Binney, J. J., Davies, R. L., & Illingworth, G. D. 1990, ApJ, 361, 78

Binney, J., & Strimple O. 1978, MNRAS, 187, 473

Binney, J., & Tremaine, S. 1987, Galactic Dynamics (Princeton: Princeton Univ. Press)

Blandford, R., & Narayan, R. 1992, ARA&A, 30, 311

Buote, D. A. 1992, M.S. Thesis, Massachusetts Institute of Technology

Buote, D. A., & Canizares, C. R. 1992, ApJ, 400, 385

Buote, D. A., & Tsai, J. C. 1995, ApJ, 439, 29

Burstein, D., Davies, R. L., Dressler, A., Faber, S. M., Stone, R. P. S., Lyndon-Bell, D., Terlevich, R. J., & Wegner, G. 1987, ApJS, 64, 601

Busarello, G., Longo, G., & Feoli, A. 1992, A&A, 262, 52

Canizares, C. R., Fabbiano, G., & Trinchieri, G. 1987, ApJ, 312, 503

Capaccioli, M., Piotto, G., & Rampazzo, R. 1988, AJ, 96, 487

Carter, D., & Metcalfe, N. 1980, MNRAS, 191, 325

Chandrasekhar, S. 1969, Ellipsoidal Figures of Equilibrium (New Haven: Yale Univ. Press)

Ciardullo, R., Jacoby, G., & Dejonghe, H. B. 1993, ApJ, 414, 454

Dejonghe, H., & de Zeeuw, T. 1988, ApJ, 333, 90

de Zeeuw, T., & Franx, M. 1991, ARA&A, 29, 239

Djorgovski, S. G. 1985, Ph.D. Thesis, University of California, Berkeley

Dressler, A., Schechter, P. L., & Rose, J. A. 1986, AJ, 91, 1058

Donnelly, R. H., Faber, S. M., & O'Connell, R. M. 1990, ApJ, 354, 52

Dubinski, J., & Carlberg, R. 1991, ApJ, 378, 496

Dubinski, J. 1994, ApJ, 431, 617

Fabbiano, G. 1989, ARA&A, 27, 87

Fabbiano, G, Kim, D.-W., & Trinchieri, G. 1992, ApJS, 80, 531

Fabian, A. C., Nulsen, P. E. J., & Canizares, C. R. 1991, A&ARev.

Fabricant, D., Lecar, M., & Gorenstein, P. 1980, ApJ, 241, 552

Fabricant, D., Rybicki, F., & Gorenstein, P. 1984, ApJ, 286, 186

Fasano, G., & Vio, R. 1991, MNRAS, 249, 629

Forman, W., Jones, C., & Tucker, W. 1985, ApJ, 293, 102

Franx, M. 1987, MNRAS, 231, 285

Franx, M. 1993, in Galactic Bulges (IAU Symp. 153), ed. H. Dejonghe and H. Habing (Dordrecht: Reidel), in press

Franx, M., Illingworth, G., & de Zeeuw, T. 1991, ApJ, 383, 112

Franx, M., & de Zeeuw 1992, ApJ, 392, 47

Frenk, C. S., White, S. D. M., Davis, M., Efstathiou, G. 1988, ApJ, 327, 507

Gehrels, N. 1986, ApJ, 303, 336

Hasinger, G., Turner, T. J., George, I. M., & Boese, G., 1992, in Legacy, No. 2, November, The Journal of the High Energy Astrophysics Science Archive Research Center (NASA: Goddard Space Flight Center), 77

Hernquist, L. 1990, ApJ, 356, 359

Hernquist, L. 1992, ApJ, 400, 460

Jedrzejewski, R. 1987, MNRAS, 226, 747

Jedrzejewski, R. I., Davies, R. L., & Illingworth 1987, AJ, 94, 1508

Katz, N. 1991, ApJ, 368, 325

Katz, N., & Gunn, J. E. 1991, ApJ, 377, 365

Kent, S. M. 1990, in Evolution of the Universe of Galaxies (ASP conf. vol. 10), ed. R. G. Kron (Provo: Brigham Young Univ. Print Serv.), 109

Kley, W., & Mathews, W. G. 1995, 438, 100

Kochanek, C. S. 1991, ApJ, 373, 354

Kormendy, J., & Knapp, G. R. ed. 1987, in IAU Symp. 117 Dark Matter in the Universe (Dordrecht: Reidel)

Kuijken, K., & Tremaine, S. 1993, preprint

Lambas, D. G., Maddox, S. J., & Loveday, J. 1992, MNRAS, 258, 404

Lauer, T. R. 1985a, ApJS, 57, 473

Lauer, T. R. 1985b, ApJ, 292, 104

Liboff, R. L. 1992, ApJ, 397, L71

Maoz, D., & Rix, H.-W. 1993, ApJ, 416, 425

Mathews, W. G. 1990, ApJ, 354, 468

Merrit, D., & Stiavelli, M. 1990, ApJ, 358, 399

Merrit, D., & Hernquist, L. 1991, ApJ, 376, 439

Mihalas, D., & Binney, J. 1981, Galactic Astronomy (New York: Freeman)

Milgrom, M., 1983a, ApJ, 270, 365

Milgrom, M., 1983b, ApJ, 270, 371

Milgrom, M., 1983c, ApJ, 270, 384

Milgrom, M. 1986, ApJ, 302, 617

Nieto, J.-L., Poulain, P., Davoust, E., & Rosenblatt, P. 1991, A&AS, 88, 559

Peletier, R. F. 1989, Ph.D. Thesis, University of Groningen

Peletier, R. F., Davies, R. L., Illingworth, G. D., Davis, L. E., Cawson, M. 1990, AJ, 100, 1091

Pickles, A. J. 1985, ApJ, 296, 340

Pfeffermann, E. et al., 1987, Proc. SPIE, 733, 519

Raymond, J. C., & Smith, B. W. 1977, ApJS, 35, 419

Refsdal, S., & Surdej, J 1994, Rept. Prog. Phys., in press

Ryden, B. S. 1991, MNRAS, 253, 743

Ryden, B. S. 1992, ApJ, 396, 445

Sackett, P., & Sparke, L. S. 1993, ApJ, 361, 408

Saglia, R. P., Bertin, G., & Stiavelli, M. 1992, ApJ, 384, 433

Saglia, R. P., et al. 1993, ApJ, 403, 567

Sanders, R. H. 1990, A&ARev., 2, 1

Sarazin, C. L. 1986, Rev. Mod. Phys., 58, 1

Schechter, P. L. 1987, in Structure and Dynamics of Elliptical Galaxies (IAU Symp. 127), ed. T. de Zeeuw (Dordrecht: Reidel), 217

Schramm, T. 1994, A&A, in press

Serlemitsos, P. J., Loewenstein, M., Mushotsky, R. F., Marshall, F. E., & Petre, R. 1993, ApJ, 413, 518

Silk, J., & Wyse, R. F. G. 1993, Phys. Reports, in press

Snowden, S. L., Plucinsky, P. P., Briel, U., Hasinger, G., & Pfeffermann, E. 1992, ApJ, 393, 819

Soucail, G. 1992, in Clusters and Superclusters of Galaxies (NATO ASI Series C. vol. 366), ed. A. C. Fabian (Dordrecht / Boston / London: Kluwer), 199

Sparks, W. B., Wall, J. V., Jorden, P. R., Thorne, D. J., & van Breda, I. 1991, ApJS, 76, 471

Stark, A. A. 1977, ApJ, 213, 368

Stark, A. A., et al. 1992, ApJS, 79, 77

Strimple, O., & Binney, J. 1978, MNRAS, 188, 883

Thomas, P. 1988, MNRAS, 235, 315

Thomas, P., Fabian, A. C., & Nulsen, P. E. J. 1987, MNRAS, 228, 973

Tonry, J. L., Ajhar, E. A., & Luppino, G. A. 1990, AJ, 100, 1416

Trimble, V. 1987, ARA&A, 25, 425

Trinchieri, G., Fabbiano, G., & Canizares, C., 1986, ApJ, 310, 637 (TFC)

Trumpler, R. J., & Weaver, H. F. 1953, Statistical Astronomy, (Berkeley: Univ. California Press)

Tsai, J. C. 1994, ApJ, in press

Tsai, J. C., Katz, N., & Bertschinger, E. 1994, ApJ, in press

Warren, M. S., Quinn, P. J., Salmon, J. K., & Zurek, W. H. 1992, ApJ, 399, 405

White, J. 1987, B.S. Thesis, Massachusetts Institute of Technology

White, J., & Canizares, C. 1987, BAAS, 19, 682

van der Marel, R. P. 1991, MNRAS, 253, 710

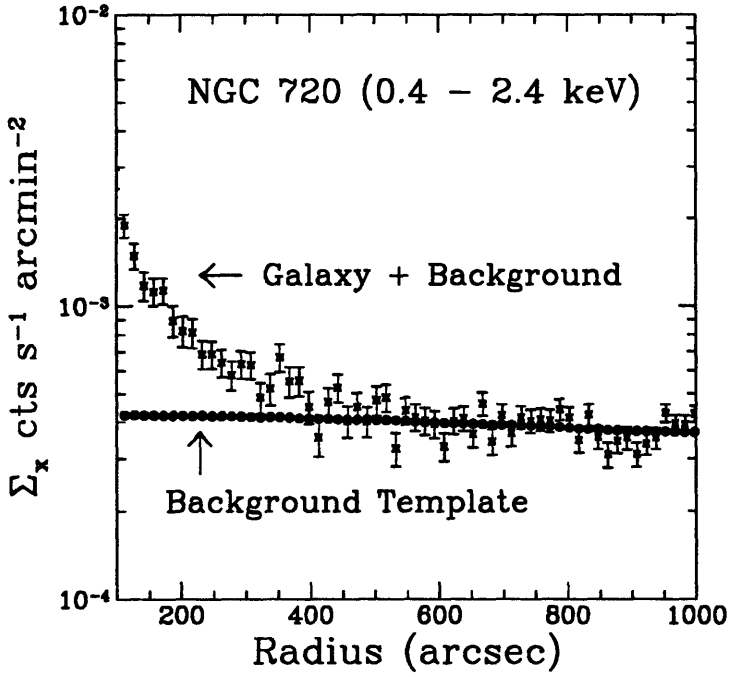

Fig. 1.—
Azimuthally-averaged radial profile (15″ bins) of the image and the background template both corrected for the effects of exposure variations, vignetting, and embedded point sources.

Fig. 2.—
Contour map of the X-ray surface brightness of the elliptical galaxy NGC 720; the contours are separated by a factor of 2 in intensity and the units are 15″ pixels The image has been corrected for the effects of exposure variations, vignetting, embedded point sources, and background; the point sources have simply been removed from the image thus causing some of the apparent asymmetries for radii greater than about 150″; e.g. the isolated contour in the upper right. The image has been smoothed for visual clarity with a Gaussian of $\sigma = 11.25''$, although the image used for analysis is not smoothed in any manner.

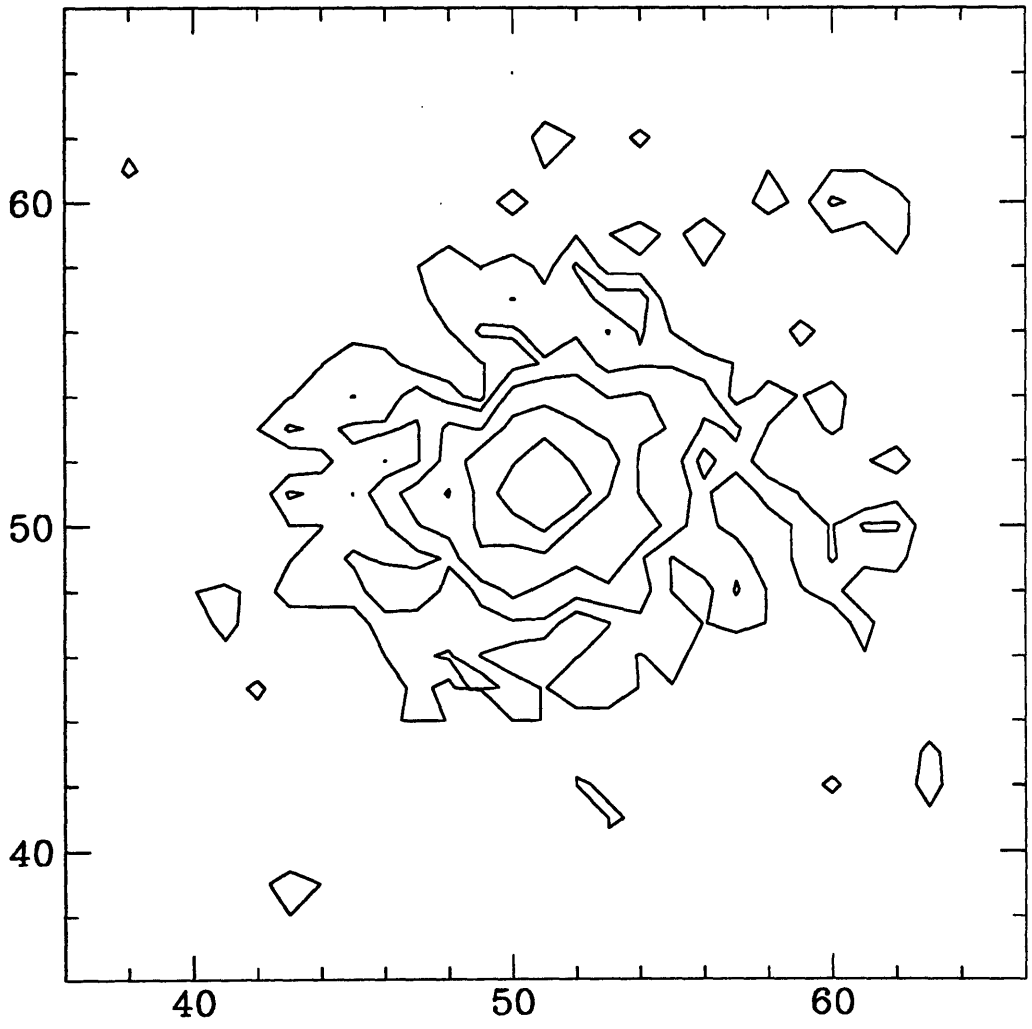

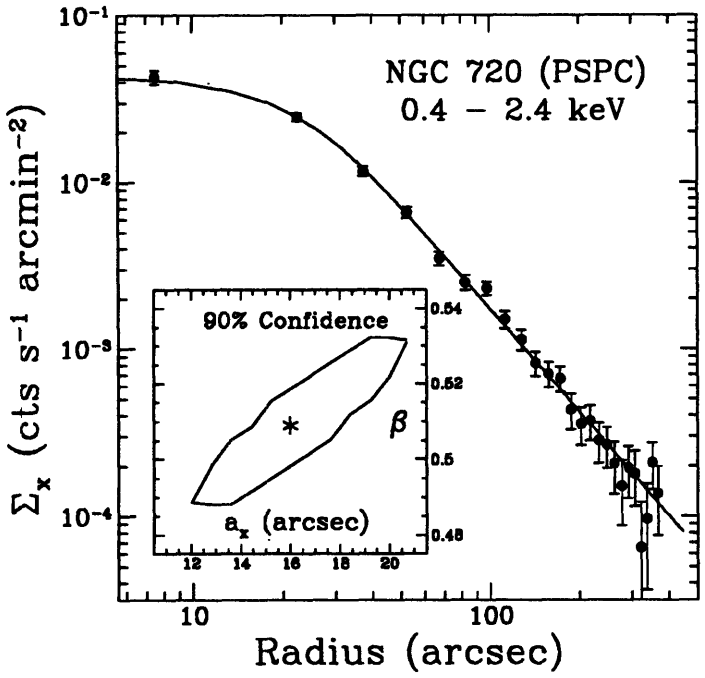

Fig. 3.—
The azimuthally-averaged radial profile of the reduced image, the best-fit King model, and the 90% confidence estimates of the fitted King parameters.

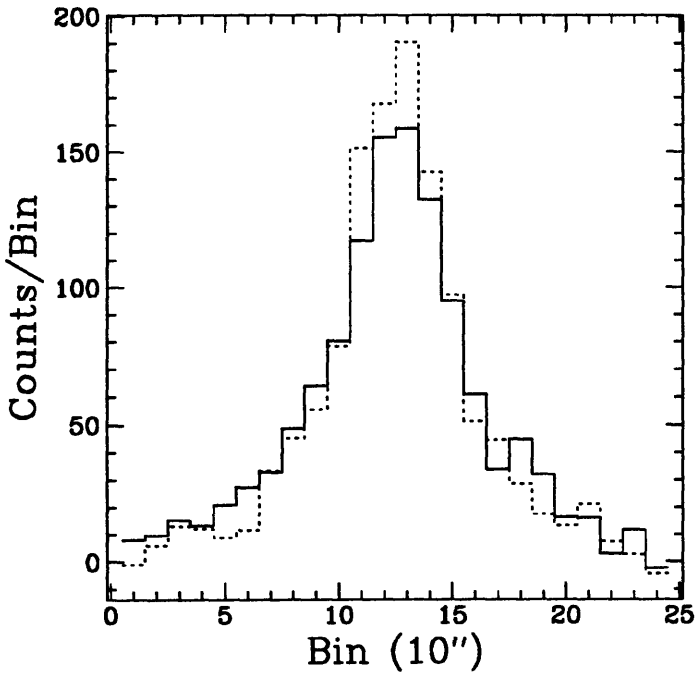

Fig. 4.—
One-dimensional projections of the image in a 240″ box along the major axis (solid) and the minor axis (dotted).

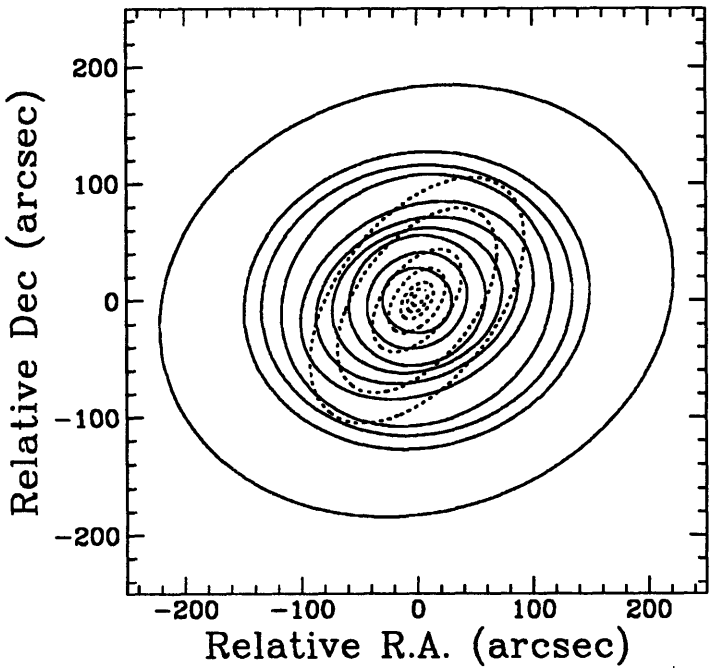

Fig. 5.—
X-ray contours (solid) having $\epsilon = \epsilon_M$ computed for the circular aperture (Table 3, column 3) and the R-band isophotes (dotted) from Peletier et al. (1989). The X-ray contours are separated by factors of $\sim 1.2 - 1.7$ in intensity and the optical contours are separated by 1 mag arcsec^{-2}.

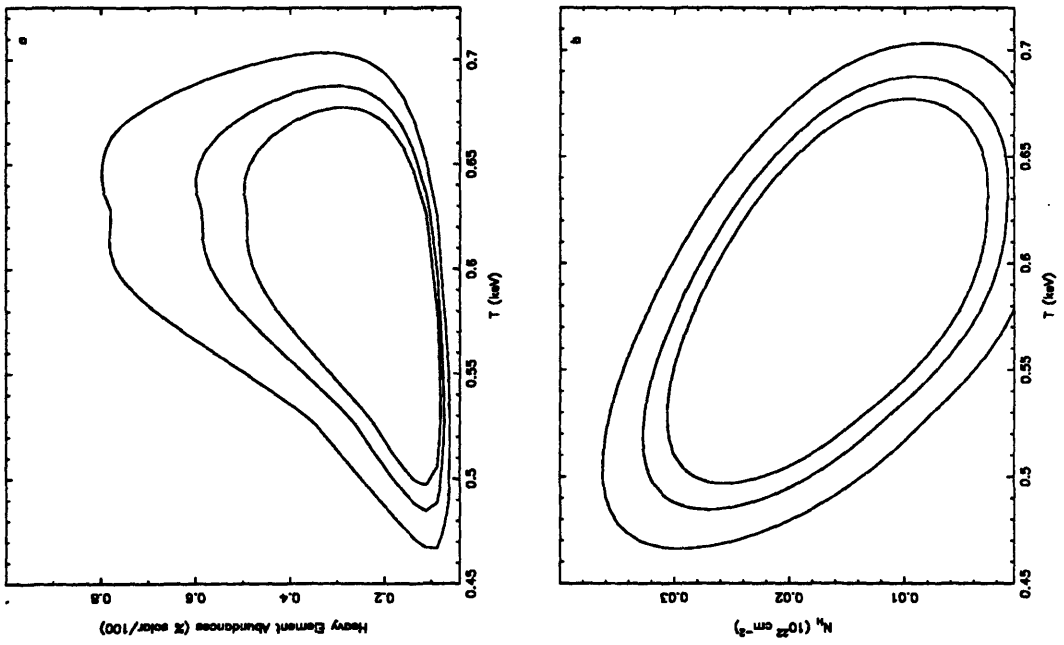

Fig. 6.—
90%, 95%, and 99% confidence contours ($0'' - 400''$; 0.2 - 2.4 keV) for (a) abundances vs. T and (b) Hydrogen column density vs. T.

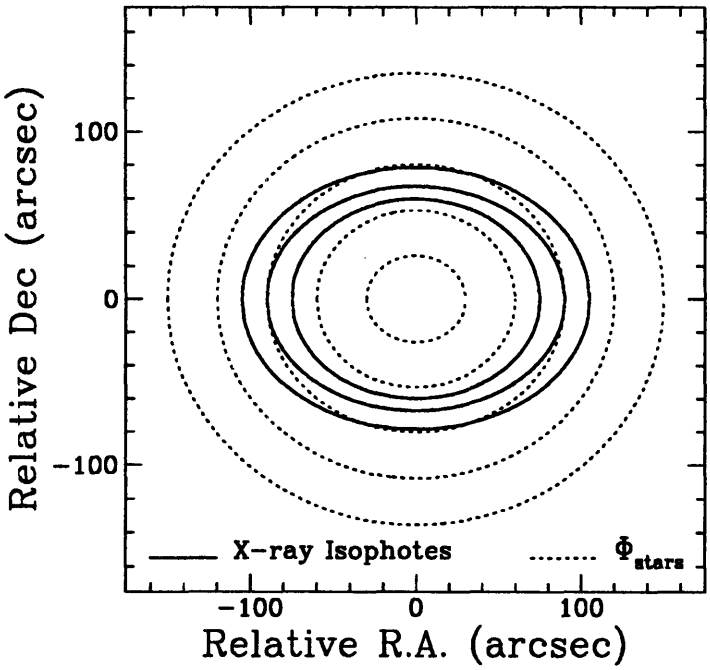

Fig. 7.—
Gravitational potential projected onto the plane of the sky (dotted) generated by mass distributed like the stars; the ellipticities are those of 2-D ϵ_{pot} in Table 6. For comparison, the most distant X-ray isophotes whose shapes are very accurately determined are also plotted as perfect ellipses (solid). The relative position angle offset of the X-ray and optical isophotes is suppressed.

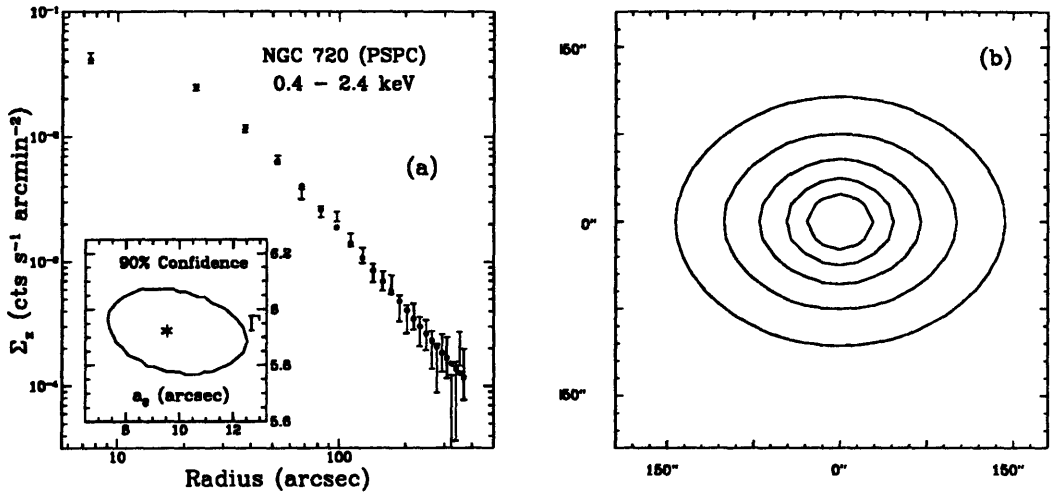

Fig. 8.—
(a) Radial profile of a typical model (filled circles) consistent with the data (error bars); the model displayed is oblate and has $\rho_{tot} \sim r^{-2}$, $a_3 = 450''$, $\epsilon_{tot} = 0.60$, $a_0 = 9.5''$, $\Gamma = 5.92$, and $\chi^2_{min} = 14.8$. The 90% confidence contour and the best-fit values are displayed in the inset.

(b) X-ray isophotes for the best-fit model ($375'' \times 375''$) separated by a factor of 2 in intensity.

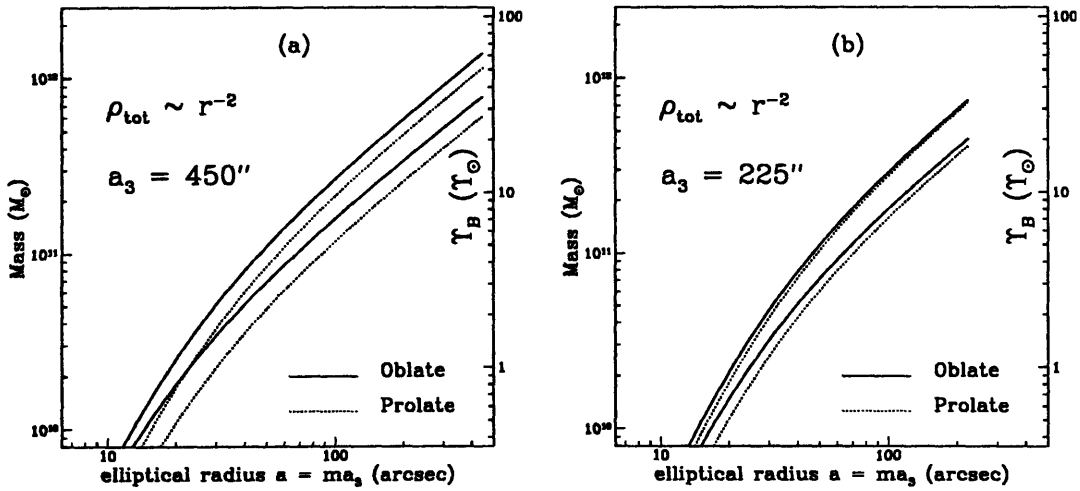

Fig. 9.—
Upper and lower solid (dashed) curves show 90% confidence limits of the integrated mass as a function of elliptical radius for the galaxy modeled as a single oblate (prolate) ellipsoid having $\rho_{tot} \sim r^{-2}$ and semi-major axis (a) $a_3 = 450''$ and (b) $a_3 = 225''$

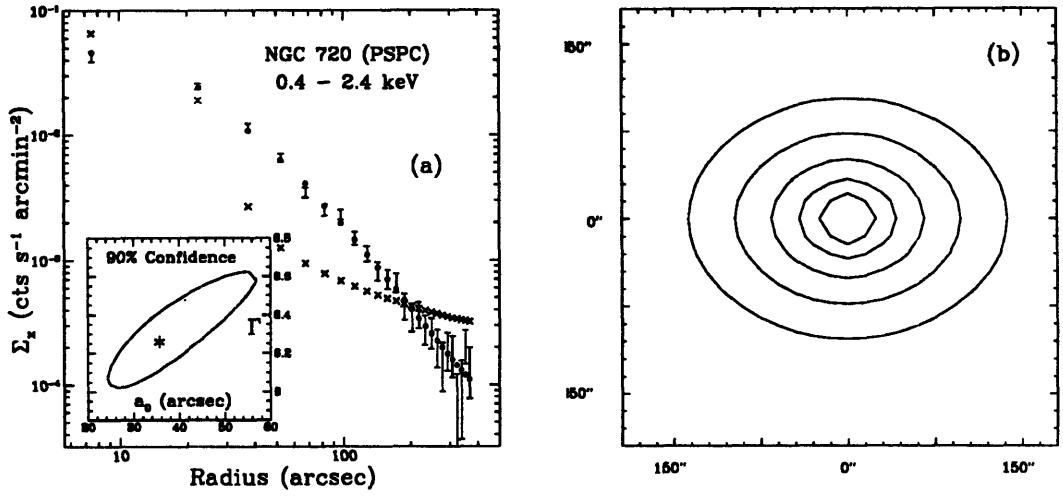

Fig. 10.—
(a) Radial profile of (1) the model without dark matter (crosses) and (2) a typical model (filled circles) consistent with the data (error bars): $\epsilon_{DM} = 0.60$, $a_3 = 450''$, $M_{DM} = 10 M_{stars}$, $M_{gas} = M_{stars}/50$, and $M_{stars} = \Upsilon_B L_B = 1.6 \times 10^{11} M_\odot$, where $\Upsilon_B \sim 7 \Upsilon_\odot$ is the B-band mass-to-light ratio of the stellar matter in solar units. The 90% confidence contour and the best-fit values are displayed in the inset.

(b) X-ray isophotes for the best-fit model ($375'' \times 375''$) separated by a factor of 2 in intensity.

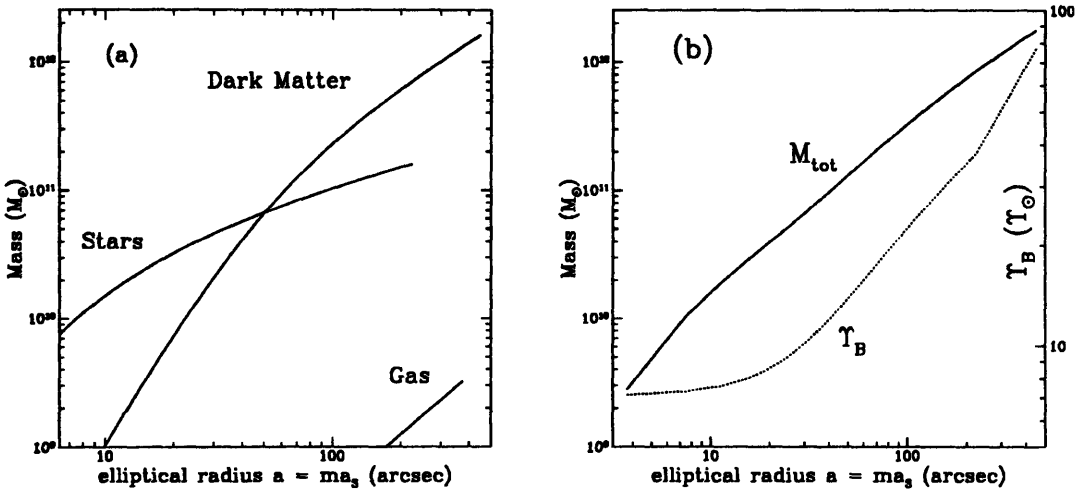

Fig. 11.—
(a) Integrated mass as a function of elliptical radius for the dark matter, stars, and gas corresponding to the model of Figure 10. Interior to $\sim 50''$ (which is the radius enclosing half the light) M_{stars} dominates M_{DM} while the opposite is true for larger distances. The self-gravitation of the gas is not important anywhere in the galaxy.

(b) Here we show the total mass for this model and the corresponding Υ_B as a function of ellipsoidal radius. Υ_B is very nearly constant inside of $10''$ but increases substantially for $a > 20''$. Note that the "kink" in Υ_B at $a = 225''$ occurs where we assign the discrete edge to the stellar mass; this can be made smooth by adding an exponential cutoff.

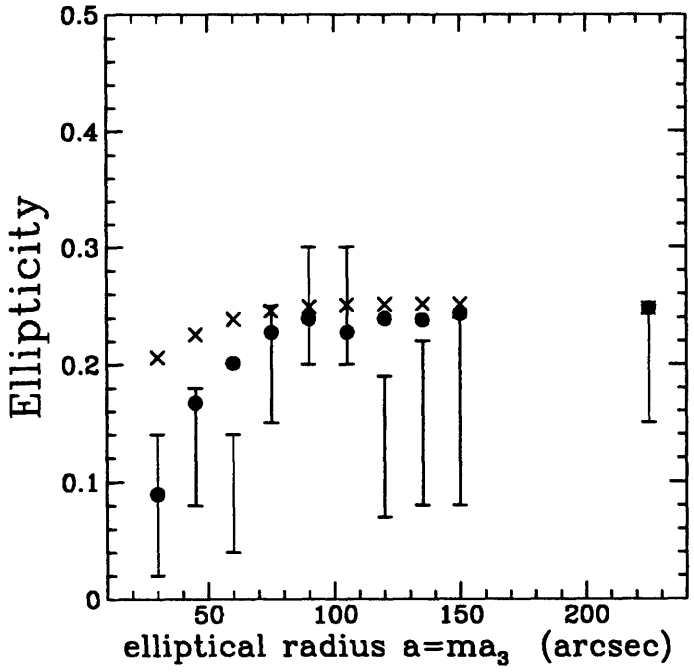

Fig. 12.—
Shown are the results of computing ϵ_M in an elliptical aperture of semi-major axis a (filled circles) and the actual ellipticity of the isophote at a (crosses) for the total mass model in Figure 8; also displayed is ϵ_M computed from the data listed in Table 3 (error bars).

Fig. 13.—
Shown are the results of the projection (edge-on) of the pseudo oblate spheroids discussed in Appendix B. for the three regimes (a), (b), and (c) of interest. We plot the ϵ of (1) the three dimensional surfaces (i.e. $\epsilon(r)$, small dashes), (2) the projection of $(a_0^2+\xi^2)^{-2}$ (big dashes), (3) the projection of $\log(a_0^2+\xi^2)$ (solid line), and (4) the difference in ellipticity of (2) and (3) (dot-dash).

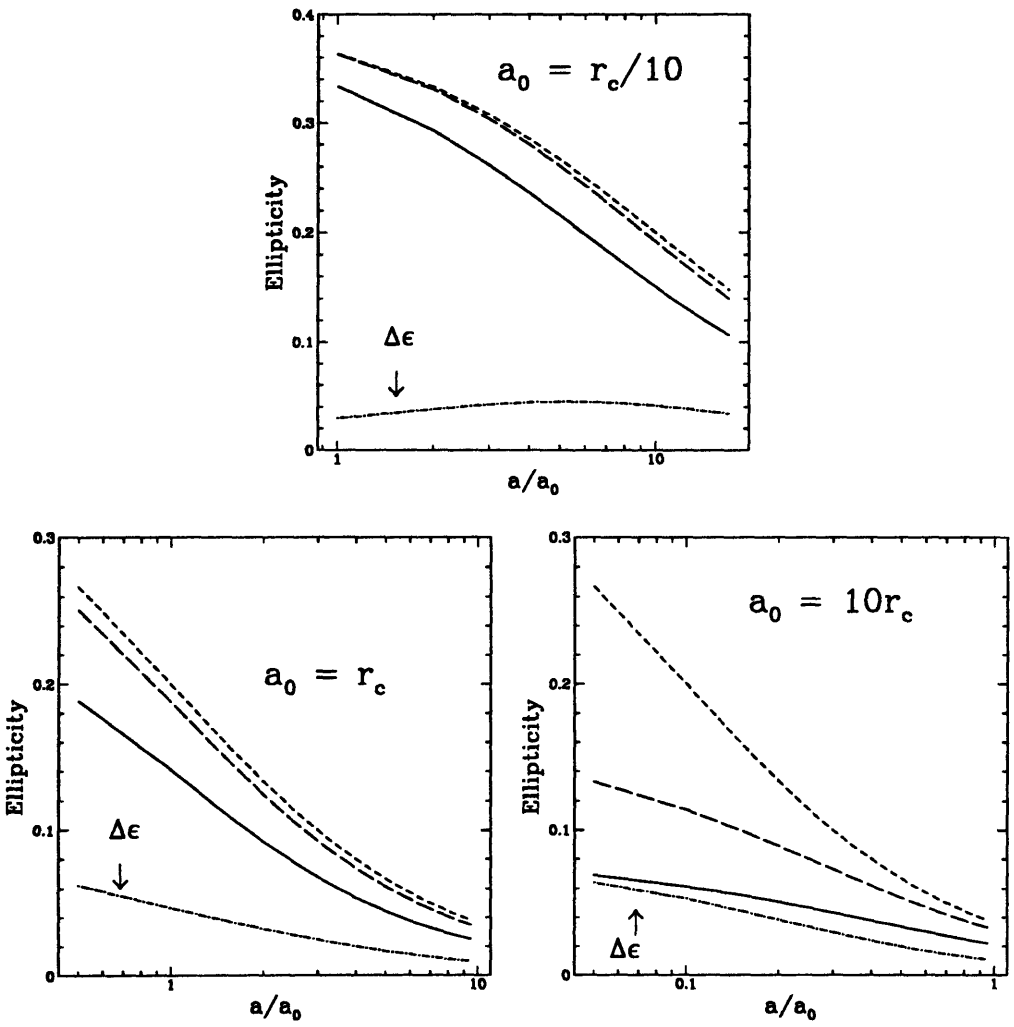

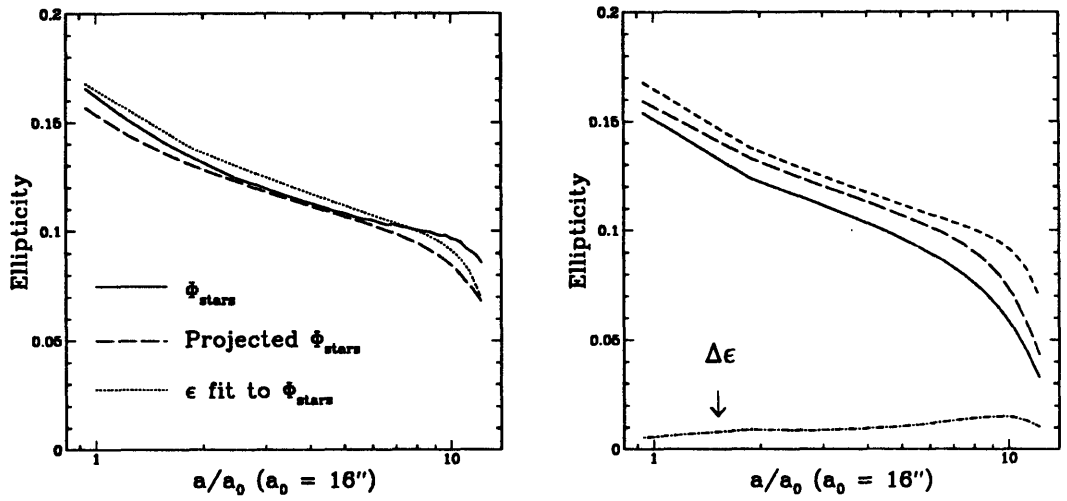

Fig. 14.—
(a) Major-axis ellipticity profile of model for Φ_{stars} (solid line) and its edge-on projection (dashes). The fit to the three-dimensional ellipticity that is used for the ensuing pseudo spheroid comparison is given by the dotted line.
(b) Results of the edge-on projections of the pseudo oblate spheroids discussed in Appendix B. corresponding to the gas emissivity (big dashes) and stellar gravitational potential of NGC 720 (solid line). The small dashes represent the approximation to the three dimensional ellipticity (see (a)) of the stellar potential and $\Delta\epsilon$ is the ellipticity difference of the projections.

Chapter 3

X-ray Constraints on the Intrinsic Shape of the Lenticular Galaxy NGC 1332

In our companion study to NGC 720 we analyzed ROSAT PSPC X-ray data for the E7/S0 galaxy NGC 1332 for the purpose of constraining its intrinsic shape. Although the quality of the observation for NGC 1332 did not allow us to obtain as robust constraints as we did for NGC 720, we used this opportunity to explore in detail the effects of gas rotation, emission from discrete galactic sources, and a variety of models for the dark matter distribution on measurements of the intrinsic shape of the galaxy. Moreover, we noticed that the "geometric" test for dark matter introduced in the previous chapter in principle allows for a non-parametric test for whether mass follows light in a galaxy; hence, this is perhaps the cleanest means to test for dark matter in ellipticals. Detailed analysis of the mass distribution following Buote & Canizares gives constraints on the ellipticity of the underlying mass of $\epsilon_{mass} = 0.47-0.72(0.31-0.83)$ at 68% (90%) confidence for isothermal and polytropic models. The total mass of the isothermal models within $a = 43.6$ kpc ($D = 20h_{80}^{-1}$ Mpc) is $M_{tot} = (0.38-1.7)\times 10^{12}M_{\odot}$ (90% confidence) corresponding to total blue mass-to-light ratio $\Upsilon_B = (31.9-143)\Upsilon_{\odot}$; polytropic models yield mass ranges larger by a factor of ~ 2 due to the uncertainty in the temperature profile. Similar results are

obtained when the dark matter is fit directly using the known distributions of the stars and gas. When possible rotation of the gas and emission from discrete sources are included flattened mass distributions are still required, although the constraints on ϵ_{mass}, but not the total mass, are substantially weakened.

3.1 Introduction

The distribution of intrinsic shapes of galactic halos is of cosmological importance since it can be predicted from cosmological N-body simulations. Cold Dark Matter (CDM) simulations predict dark halos that are flatter ($\epsilon \sim 0.5$) than inferred from analysis of observed optical isophotes ($\epsilon \sim 0.3$) of ellipticals (e.g., Dubinski & Carlberg 1991; Dubinski 1994); the distribution of the shapes of halos in CDM simulations appears to be insensitive to the power spectrum (Frenk et al. 1988; Efstathiou et al. 1988). Since the observed stars may not trace the shape of the dark mass, this is not necessarily a discrepancy: the shape of the total gravitating matter is required to compare to the simulations. Unfortunately, reliable constraints on the shapes of dark halos exist for only a few galaxies (Sackett et al. 1994). The uncertainty in the shape of the stellar velocity dispersion tensor has hindered optical methods to measure the dark matter distribution in early-type galaxies. In fact, the need for any dark matter in early-type galaxies has not been definitively established from optical data (Kent 1990; de Zeeuw & Franx 1991; Ashman 1992; although see Saglia et al. 1993). Measuring the intrinsic shapes of early-type galaxies using the observed velocity profiles may eventually enable robust constraints from optical data (Statler 1994).

Perhaps the most powerful probe of the intrinsic shapes of early-type galaxies is the hot, X-ray–emitting gas because the dispersion tensor of the gas should be isotropic (e.g., Sarazin 1986). The full potential of X-ray analysis for determining the shapes of dark halos has not yet been achieved primarily because instruments on board previous X-ray satellites lacked the spatial resolution to accurately measure the shapes of the X-ray isophotes (White & Canizares 1987; White 1987). Recently,

Buote & Canizares (1994; hereafter BC94) used the higher resolution X-ray data of the ROSAT PSPC ($FWHM \sim 30''$) to constrain the shape of the E4 galaxy NGC 720. By assuming the X-rays are due to hot gas in hydrostatic equilibrium with the galactic potential, BC94 obtained for the halo ellipticity, $\epsilon = 0.46 - 0.74$ (90% confidence), which is mostly insensitive to the poorly determined temperature profile of the gas. In addition, BC94 introduced an X-ray test for dark matter in early-type galaxies that is completely independent of the temperature profile of the gas and, in principle, without requiring any model fitting; we elucidate the robust nature of the test (§3.5.1). Moreover, this geometric test may be applied to test alternate gravity theories like MOND.

This "geometric" test is especially relevant considering that the lack of high quality, spatially resolved temperature profiles for most early-type galaxies has rendered inconclusive previous X-ray studies of dark matter (e.g., Fabbiano 1989). Even for those galaxies now possessing high quality, spatially resolved spectra from ROSAT, the translation of these spectra into temperature profiles using standard spectral models is still uncertain (e.g., Trinchieri et al. 1994). This uncertainty in interpreting temperatures may be resolved with X-ray data from ASCA (Tanaka et al. 1994). Although the poor spatial resolution of ASCA inhibits measurements of temperature profiles, the superior spectral resolution allows for model-independent determination of mean galactic temperatures from line ratios that provides preliminary evidence for dark matter in three bright ellipticals in Virgo (Awaki et al. 1994). Since establishing the firm existence of dark matter in early-type galaxies is of vital consequence to cosmological theories of structure formation (e.g., Ashman 1992; Silk & Wyse 1993), an X-ray method to detect dark matter that takes advantage of the high quality spatial data of current X-ray satellites but does not require detailed temperature information is of great utility; note that methods to map the projected mass density of individual galaxies with weak gravitational lensing (Kaiser & Squires 1993) are impractical because the angle subtended by galactic halos at the redshifts required for significant lensing effect contains too few background galaxies for an adequate signal; however, it may be possible to usefully probe the outer portions of galactic halos with this

method (i.e. $r \gtrsim 100$ kpc).

In this paper we analyze ROSAT PSPC data for the S0 galaxy NGC 1332 which, along with NGC 720, is especially suited for X-ray analysis of its intrinsic shape. NGC 1332 is quite elongated in the optical ($\epsilon \sim 0.43$), a desirable property to reduce the likelihood of substantial projection effects. If, in addition, the elongation in the optical is correlated to intrinsic elongation of the underlying mass, then the gravitational potential, hence the X-ray isophotes, should exhibit noticeable flattening. Located in a poor cluster (the Eridanus group, Willmer et al. 1989), NGC 1332 is relatively isolated from other large galaxies. Isolation is desirable so that the gas is not distorted by ram-pressure or tidal effects (Schechter 1987). The X-ray emission of NGC 1332 extends to over 7′ on the sky, thus providing many pixels of angular resolution. Considering the desired elongation, isolation, and angular sizes, NGC 1332, along with NGC 720, possess the largest X-ray fluxes of normal early-type galaxies observed with *Einstein* (Fabbiano, Kim, & Trinchieri 1992) that are likely to be dominated by emission from hot gas (Kim, Fabbiano, & Trinchieri 1992).

We explore in detail in this paper many of the fundamental assumptions underlying X-ray analysis of the intrinsic shapes and radial mass distributions in early-type galaxies to provide a reference for future investigators. These issues were discussed in our study of NGC 720 (BC94), but the peculiarities of that galaxy did not require detailed investigation of these issues (e.g., position-angle offset in NGC 720 argues against substantial emission from discrete sources). The paper is organized as follows. In §3.2 we discuss spatial analysis of the ROSAT X-ray data. In §3.3 we discuss spatial analysis of I-band observations of NGC 1332. Spectral analysis of the X-ray data is presented in §3.4. In §3.5 we clarify the geometric test for dark matter and apply it to NGC 1332. Detailed analysis of the composite mass distribution and the dark matter are presented in §§3.6 and 3.7. We discuss the implications of our results in §3.8 and present our conclusions in §3.9.

3.2 Spatial Analysis of the X-ray data

NGC 1332 was observed for 25.6 ks on August 13-14, 1991 with the Position Sensitive Proportional Counter (PSPC) on board ROSAT (Trümper 1983). For a description of the ROSAT X-ray telescope see Aschenbach (1988) and for a description of the PSPC see Pfeffermann et al. (1987). Table 1 summarizes the details of the observation.

In relation to optical images of nearby early-type galaxies, X-ray images generally have much lower signal-to-noise (S/N). The relatively noisy X-ray data thus allows only useful aggregate constraints of the radial and azimuthal shape of the surface brightness, whereas the detailed two-dimensional surface brightness of an optical image of a typical early-type galaxy may be usefully analyzed with elliptical isophote fitting (e.g., Jedrzejewski 1987). As a result, we analyze the radial profile of the X-ray surface brightness in azimuthally averaged circular annuli (§3.2.2) and the ellipticity in elliptical apertures of increasing size (§3.2.3).

The distance to NGC 1332 has been determined by several different methods, including Hubble-flow analysis $D = 19.0$ Mpc (e.g., in Canizares, Fabbiano, & Trinchieri 1987), $D_n - \sigma$, which gives 24.1 Mpc (Donnelly, Faber, & O'Connell 1990), and surface brightness fluctuations, 20.1 Mpc (J. Tonry 1994, private communication); each distance we have scaled to $H_0 = 80h_{80}$ km s^{-1} Mpc^{-1}. For this paper we adopt $D = 20h_{80}^{-1}$ Mpc for the distance to NGC 1332; at this distance $1'' \sim 0.1$ kpc.

3.2.1 Image Reduction

To prepare the X-ray image for spatial analysis we (1) excluded time intervals where the background was anomalously high, (2) corrected for exposure variations and telescopic vignetting, (3) identified and removed point sources embedded in the galactic continuum emission, and (4) subtracted the background. Steps (1) and (2) as well as the identification of point sources were performed using the standard IRAF-PROS software.

ROSAT pointed observations are partitioned into many short exposures to maximize efficiency. Unlike NGC 720 the light curve for NGC 1332 shows several spikes,

all of which occur at the beginning and/or end of the individual exposures; these mostly represent scattered solar radiation. We identified the affected time intervals by extracting the emission in a 300″ radius of the galaxy with embedded point sources masked out (see below) and then binning the observation into 100 time bins to improve S/N. Judging by "eye" we excluded all time bins with count rate ≥ 0.9 counts per second. The resulting image has 21141s of accepted observing time.

We rebinned the PSPC image of NGC 1332 into 5″ pixels corresponding to a total 1536×1536 field of pixels, which proved to optimize S/N and bin-size requirements for computing the ellipticity in §3.2.3 (see BC94). Only data from the hard band (0.4−2.4 keV) were used in order to minimize contamination from the X-ray background and the blurring due to the point spread function (PSF) of the PSPC (see §3.2.2).

The flat-field correction for NGC 1332 is particularly important because the galaxy center is 7′ off-axis, just where vignetting becomes important for the PSPC. We divided the image by the exposure map provided with the observation which corrects for both exposure variations across the field and for vignetting; note the exposure map is a factor of six coarser than our chosen pixel scale. In principle this correction depends on the energy of each individual photon, but for energies above 0.2 keV the energy dependence is small and we neglect it (Snowden et al. 1994). In Figure 1 (a) we show contours of the flat-field corrected image of NGC 1332.

The next steps to prepare the image for analysis are to identify and remove point sources embedded in the continuum emission of the galaxy. We identify sources in the field using the results from the Standard Analysis System Software (SASS) provided with the observation; SASS employs a maximum-likelihood algorithm which is explained in the *detect* package in PROS. Since, however, the software has difficulty identifying sources embedded in a continuum, we identified one source "by eye" located within $\sim 1'$ of the galaxy center in addition to the SASS sources. In all we identified five embedded sources lying in a $15' \times 15'$ box centered on the galaxy; this includes the entire region of significant galaxy emission (§3.2.2). The positions of the identified sources are listed in Table 2.

In order to limit the introduction of spurious features into the image shape param-

eters (§3.2.3), it is vital to remove the effects of the embedded sources on the galactic continuum emission. Contamination due to embedded sources is especially problematic when the continuum is nearly circular or has low S/N; a significant distortion will generate a preferred direction and non-zero ellipticity. We remove the embedded sources by "symmetric substitution" which is particularly suited to our analysis of the intrinsic shape of the underlying mass (see Buote & Tsai 1995a for a discussion of this technique). In essence, we replace a particular source with the continuum emission in the regions obtained by reflecting the source over the symmetry axes of the image.

We obtained the symmetry axes from the source-free region $r \leq 45''$ using the iterative moment technique described in §3.2.3. The position angle (PA) so obtained is 132° N-E and we found that the ellipticity profiles do not appreciably differ for symmetry axes within the 90% confidence limits $111° - 152°$. We decided to set the orientation of the symmetry axes to the optical $PA = 115^{\circ}$ (§3.3) because it is much more precisely determined and it is within the uncertainties of X-ray PA. We display in Figure 1 (b) the central portion of the image of NGC 1332 with the sources removed.

Finally, we computed the background from examination of the azimuthally averaged radial profile; in Figure 2 we show the radial profile binned in 30″ circular bins. Since the galactic emission only extends to $\sim 250''$ from the center a mean background level is sufficient; i.e. the cosmic X-ray background should not vary significantly over the galaxy. Computing the mean background in an annulus extending from $350'' - 400''$ centered on the galaxy centroid (§3.2.2) we obtained a mean background count rate of 3.22×10^{-4} counts s^{-1} arcmin^{-2}. Note that we will subsequently subtract the background for construction of the radial profile (§3.2.2) but not for computation of the ellipticity (§3.2.3).

3.2.2 Radial Profile

After subtracting the background, we constructed the radial profile following BC94. That is, we first computed the centroid of the X-ray emission in a circle of radius 90″

which contains $\sim 75\%$ of the galaxy counts. An initial guess for the center was selected by "eye" and then iterated until the centroid changed by less than 0.1 pixels. We also investigated the effect of choosing different-sized radii for the circle and find that centroid position varies by < 0.5 pixels for radii $\leq 110''$. The centroid value is listed in Table 1. We binned the radial profile such that each circular bin has $S/N \geq 2.5$. This corresponds to $5''$ bins from $r = 0'' - 15''$, $15''$ bins from $r = 15'' - 105''$, and $45''$ bins from $r = 105'' - 285''$; we do not find an appreciable gain in S/N when the circular annuli are replaced with elliptical annuli consistent with the shapes and orientations obtained in §3.2.3. The background-subtracted radial profile is displayed in Figure 3.

The PSPC off-axis PSF described by Hasinger et al. (1993; updated May 1994) depends on both the energy of the incident photon and the off-axis position. We adopted a mean value for the energy by taking a counts-weighted average of the spectrum (§3.4) in the hard band (0.4-2.4 keV) which yielded $\langle E \rangle = 0.82 \pm 0.36$ keV. We set the position of the PSF at the centroid of the galaxy emission which lies off-axis $\theta = 7.25'$ to the West. In Figure 3 we plot the PSF with these parameters adjusting the normalization to give a best fit to the radial profile. The PSF is too flat in the core to describe the emission of NGC 1332, even if it is a point source. The PSF is still too flat if we set $\langle E \rangle = 1.1$ keV, the energy that effectively minimizes the width of the PSF and is consistent with the PSPC spectrum (see Figure 3). By demanding that the inner $60''$ of the radial profile be fit well by the β model (see below) we decided to use the PSF of Hasinger et al. evaluated at $\langle E \rangle = 1.1$ keV and $\theta = 5'$. We arrived at this choice as a compromise between obtaining a best fit and wanting to stay close to the real off-axis position of NGC1332. We plot this PSF in Figure 3.

A convenient parametrization of the X-ray radial profiles of early-type galaxies is the β model (Cavaliere & Fusco-Femiano 1976; Forman, Jones, & Tucker 1985; Trinchieri, Fabbiano, & Canizares 1986),

$$\Sigma_X(R) \propto \left[1 + \left(\frac{R}{a_X}\right)^2\right]^{-3\beta+1/2}, \tag{3.1}$$

where a_X and β are free parameters. The β model is useful as (1) a benchmark for comparison of $\Sigma(R)$ to other galaxies and (2) an analytic parametrization for computing the gas mass (§3.7.2). In order to obtain physical constraints on the parameters a_X and β, we convolved Σ_X with the PSPC PSF (as described above) and performed a χ^2 fit to the radial profile; note the fitted parameters a_X and β vary by less than 50% and 5% respectively over the entire range of PSFs considered above.

To make a fair comparison between model and data we evaluated the β model convolved with the PSF on a grid of 5″ pixels similar to the real image. We computed the radial profile binned as above and then performed a χ^2 fit between the model radial profile and that of the data. The best-fit model is shown in Figure 4 and the confidence limits in Table 3.

We will find it convenient to analyze the radial profile without the three bins from $0'' - 15''$ (§3.6.2). For this case we rebinned the image into 15″ pixels and computed the radial profile as before, except that the inner 15″ is now one bin. We plot the best-fit model (as above) in Figure 4 and give the confidence limits of the parameters in Table 3.

3.2.3 Ellipticity of the X-ray Surface Brightness

Methods and Results

Like NGC 720, NGC 1332 has many fewer counts (~ 1000 for $r \lesssim 100''$) than typical optical images of nearby ellipticals. As a result, we can only hope to measure with any precision the aggregate elongation of the X-ray surface brightness in a large aperture. The iterative moment technique introduced by Carter & Metcalfe (1980) is particularly suited to measuring aggregate shapes; see BC94 for specific application to X-ray images. In essence this technique entails computing the analog of the two-dimensional moments of inertia arrived at by iterating an initially circular region; the square root of the ratio of the principal moments is the axial ratio and the orientation of the principal moments yields the position angle. The parameters obtained from this method, ϵ_M and θ_M, are good estimates of the ellipticity (ϵ) and position angle

(θ) of an intrinsic elliptical distribution of constant shape and orientation. For a more complex intrinsic shape distribution, ϵ_M and θ_M are average values weighted heavily by the outer parts of the region.

BC94 found that the uncertainties on ϵ_M and θ_M obtained from Monte Carlo experiments were characterized well by their analytical estimates, $\Delta\epsilon_M$ and $\Delta\theta_M$, computed from simple propagation of Poissonian errors (see appendix A of BC94). For NGC 720, however, the X-ray emission is more extended and the S/N is much larger than for the NGC 1332 PSPC data. We find, thus, that the analytic statistical error estimates generally underestimate the uncertainties for NGC 1332. As a result, we estimated the uncertainties by simulating β models having the best-fit a_X and β obtained in §3.2.2 but also have a constant ellipticity and orientation; we implemented this by replacing $R = \sqrt{x^2 + y^2}$ with the elliptical radius $\sqrt{x^2 + y^2/q^2}$, where q is the constant axial ratio. These models were scaled to have the same number of counts as the background-subtracted PSPC image of NGC 1332; then a uniform background (scaled to the PSPC observation) and Poisson noise was added. Since ϵ_M is unaffected by a uniform background (see Carter & Metcalfe 1980) we did not then subtract an estimate for the background. We performed 1000 simulations each for a suite of ellipticities; note that we do not include the PSF in these simulations – the PSF is taken into account in our models in later sections.

To determine the confidence intervals on the measured ϵ_M we proceed as follows; for now we focus our attention on the 90% confidence limit for a particular aperture size. We arrange the results of the 1000 simulations for a given input ϵ_x into ascending order of measured ellipticity ϵ_M; i.e. $\epsilon_M^1 < \epsilon_M^2 < \cdots < \epsilon_M^{1000}$. The 90% upper limit for this model is defined to be the value of ϵ_M corresponding to the $0.9 \times 1000 = 900$th value of ϵ_M in the ordered array; i.e. ϵ_M^{900}. The 90% confidence lower limit of the real data is given by the model with input ϵ_x whose ϵ_M^{900} just equals the measured value of ϵ_M from the real image (see below). Similarly, the 90% confidence upper limit of the real data is given by the model with input ϵ_x whose ϵ_M^{100} just equals the measured value of ϵ_M from the real image. The same procedure applies to different confidence limits and aperture sizes.

We estimated the confidence limits for the position angles θ_M from the model having $\epsilon_x = \epsilon_M$ of the data for the specific aperture size. We define, for example, the 90% confidence limits to be $(\theta_M^{50}, \theta_M^{950})$; the other confidence limits are defined similarly. This procedure is not the most rigorous means to determine the uncertainties on θ_M because the value of ϵ_M in each simulation is not equal to ϵ_x. Since, however, we do not use θ_M in our modeling (§3.6) the estimates are sufficient for our purposes.

In addition to the iterative moments, we also parametrized the shape of the X-ray surface brightness by fitting perfect ellipses to the isophotes following Jedrzejewski (1987; implemented with the *ellipse* task in the IRAF-STSDAS software). This method has the advantage that the computed parameters for ellipticity (ϵ_{iso}) and position angle (θ_{iso}) correspond to an elliptical isophote at a specific radius and thus may provide a more accurate representation of the radial variation in shape and orientation of the surface brightness. Unfortunately this technique, which was developed to study slight departures of optical isophotes from true ellipses, has the disadvantage of having larger statistical uncertainties than the iterative moments; i.e. as applied in STSDAS, the counts associated with fitting an isophote are only a small fraction of those present in the elliptical apertures used to compute the iterative moments. To improve the S/N we rebinned the image into 15″ pixels for the ellipse fitting.

We list the results for ϵ_M and ϵ_{iso} in Table 4 and the results for θ_M and θ_{iso} in Table 5; note that the ellipticities in Table 4 include the blurring due to the PSPC PSF (which we will account for in our models in the later sections) and the background, since (as mentioned above) ϵ_M is unaffected by a uniform background; also, only 68% confidence limits are given for the results from isophote fitting. The ellipticities for the two methods agree within their considerable uncertainties at all radii. As expected, the iterative moment results are determined more precisely. At the 90% confidence level, ϵ_M is consistent at all radii, although at 68% confidence the innermost $a \leq 30''$ and outermost $r \geq 135''$ are rounder than the intermediate radii; this simply reflects the blurring due to the PSF for the inner isophotes and the low S/N in the outer isophotes which do not allow the iterative moment method to iterate much past its initial guess of a circle.

The most accurately determined values for ϵ_M are for $a \sim 75'' - 90''$ giving $\epsilon_M = 0.10-0.27$ at 90% confidence. These results are similar to those for NGC 720 obtained by BC94 where at the aperture sizes $a = 90''$, $\epsilon_M = 0.20 - 0.30$ at 90% confidence. Unlike NGC 720, there is no evidence for significant elongation at large radii (i.e. $a \geq 90''$) because of the sharp falloff in S/N at those radii in NGC 1332.

There is no evidence for position angle twists at the 90% confidence level. As a result we define the X-ray position angle, θ_X, at the radii where ϵ_M and θ_M are best-determined; i.e. $a \sim 75'' - 90''$. The mean value of θ_M agrees well with the optical position angle (see §3.3) of 115°. Thus we define $\theta_X \equiv \theta_{opt} = 115°$.

Search for Unresolved Sources

Following BC94 we investigated the possibility that the measured values of ellipticities and position angles are due to unresolved point sources embedded in the galactic emission; note Buote & Tsai (1995b) use simulations to show that the effects of unresolved point sources in ROSAT PSPC images of galaxy clusters on measurements of surface brightness shape parameters are generally comparable to or less than the Poisson noise. To search for unresolved sources, we examined (1) the centroid variation with radius, (2) the symmetry of surface brightness, (3) subtraction of a model for the galaxy continuum, and (4) one-dimensional projections along the major and minor axes.

Methods (1), (3), and (4) yield null results. The centroids for both the iterative moments and the isophote fitting varied by less than 0.5 pixels (i.e. 2.5″) for $a \leq 150''$. For (3) we used the results of the isophote fits to construct a model for the surface brightness within $r = 100''$ (see *bmodel* task in IRAF-STSDAS) and then subtracted the model from the image. The residuals showed no statistically significant fluctuations except at the center $r < 30''$ where the model is a poor fit to the data (i.e. model is too flat). For (4), we examined one-dimensional projections of the X-rays along the major and minor axes in boxes of width 150″, 200″, and 250″. In each case there were no statistically significant asymmetries.

Method (2) yielded possible evidence for asymmetries. We considered the surface

brightness in a coordinate system where the $x-$axis was aligned with θ_X. We constructed an image from the first quadrant by reflecting it over the x and y axes; we did the same for the other quadrants to give four images, one derived from each quadrant. If the X-rays possess elliptical symmetry each of these images should possess the same shape. On computing ϵ_M from these images we found that the values were quite different for the different quadrants. For apertures $a = 75'' - 90''$, we obtained $\epsilon_M \sim 0.15$ for the first and fourth quadrants and $\epsilon_M \sim 0.30$ for the second and third quadrants. Judging from the Monte Carlo error estimates in §3.2.3 these values are certainly consistent within their 90% confidence values. Of course, it is difficult to precisely ascertain the significance of these values because each quadrant only has a fraction of the counts we have now given it for the whole image. We conclude that asymmetries are consistent with the data, but are not demanded statistically by the data.

3.3 Spatial Analysis of the Optical data

In later sections we require a mass model for NGC 1332 obtained from assuming a constant mass-to-light ratio. Hence, on August 25, 1992 we obtained a 250s I-band exposure of NGC 1332 with the 1.3m McGraw-Hill telescope at the Michigan-Dartmouth-MIT observatory (MDM). The image was recorded on the Thomson CCD which has a 400 × 576 field of 0.5″ pixels. From stars in the field we estimated the seeing to be 2.0″ FWHM.

We reduced the image using the IRAF-NOAO software. First, we subtracted a constant bias level computed from un-illuminated columns at the edge of the chip. The image was flattened using the average of a suite of sky flats (see Haimen et al. 1994). Next, we subtracted a constant sky value. Finally, we fitted elliptical isophotes as described in §3.2.3.

In addition to this short-exposure observation which emphasizes the core of the galaxy, we also obtained two-dimensional isophotal photometry for a deep exposure of NGC 1332 (J. Tonry 1995, private communication). This 900s I-band exposure was

taken on October 10, 1991 with the 4m reflector at CTIO in fair seeing conditions (1.41″ FWHM). Although this image is especially suited to analysis of the outer regions of the galaxy, the core ($r \lesssim 5''$) is unfortunately saturated.

In Table 6 we list the ellipticities and position angles for the two data sets; note that two-dimensional isophotal surface photometry has not been published in the literature for NGC 1332. The data sets agree quite well within the uncertainties computed for the MDM data; we do not have uncertainties for the Tonry observation. The isophotes are round near the center $a \lesssim 5''$ where the PSF dominates and become increasingly elongated with distance from the center eventually reaching $\epsilon_{opt} \sim 0.70$ at $a \sim 75''$. The position angles are quite steady at $\theta_{opt} \sim 115°$ over most of the radii observed, but for $a < 2''$ for the MDM data and $a > 130''$ for the Tonry data there may be significant twists. The outer twist in the Tonry data may be due to its dwarf companion NGC 1331; the inner twist is not quantifiable due to the seeing.

We combined the major-axis intensity profiles from the two data sets by minimizing the deviations in their overlapping data points; the ellipticity profiles were taken to be those of the MDM data for $a \leq 75''$ and the Tonry data for $a > 75''$. In Figure 5 we plot the combined major-axis intensity profile for the two data sets. The intensity-weighted average ellipticity over the listed radii is $\langle \epsilon_I \rangle = 0.43$, which is necessarily affected to some extent by the blurring of the inner isophotes by the PSF.

The intensity profile exhibits two breaks: one near $a = 1''$ resulting from the MDM PSF and one near $a = 40''$ where apparently the light profile of the disk becomes important. We parametrized the major-axis profile using a simple bulge + disk model consisting of a De Vaucouleurs bulge and an exponential disk,

$$\Sigma_I(R) \propto \exp\left(-7.67\left[(R/R_e)^{1/4} - 0.5\right]\right) + C \exp\left(\frac{-R}{R_d}\right), \qquad (3.2)$$

where the best-fit parameters are the effective radius, $R_e = 25''$, the disk scale length, $R_d = 33''$, and a relative normalization parameter $C = 2.6$; these parameters were obtained by fitting the bulge + disk model convolved with the PSF of the MDM observation taken to be a Gaussian ($\sigma = 0.85''$). We plot this model in Figure 5;

also plotted are the results of a single De Vaucouleurs Law fit to the whole profile ($R_e = 55''$) that will prove more convenient for analytic modeling.

We investigated whether the optical surface brightness profile is consistent with the X-ray emission by fitting the bulge + disk model to the X-ray radial profile (§3.2.2). We constructed a two-dimensional optical model by replacing $R = \sqrt{x^2 + y^2}$ with the elliptical radius $\sqrt{x^2 + y^2/q^2}$ in equation (3.2), where $q = q(R)$ is the axial ratio of the optical isophote at major-axis position $x = R$; note we interpolate between the discrete values listed in Table 6. Following our procedure for the β model in §3.2.2, we convolved the elliptical bulge + disk model with the PSPC PSF and evaluated it on a grid of $5''$ pixels. Then the radial profile is computed in the same manner as for the X-ray data and is compared to the X-ray radial profile. We only needed to rescale the optical profile since all of the parameters are fixed to the optical values. The result is shown in Figure 5 – $\chi^2 = 190$ for 11 degrees of freedom. The poor fit clearly demonstrates that a large fraction of the X-ray emission must not be distributed like the optical light.

We also used the above model evaluated on a grid of $5''$ pixels and convolved with the PSPC PSF to give the range of ϵ_M expected if the X-ray gas follows the optical light. Following the procedure of §3.2.3 we computed ϵ_M for 1000 Monte Carlo simulations. For $a \leq 90''$, the 90% lower limits for ϵ_M (i.e. ϵ_M^{100}) generated by the optical model generally agree with the X-ray values in Table 4. However, at larger radii the optical model predicts ϵ_M larger than observed at $> 95\%$ confidence.

3.4 Spectral Analysis of the X-ray data

The ROSAT PSPC has 256 PI bins spanning the energy range 0.1 - 2.4 keV. Only four groups of bins, however, are resolved in energy. Since NGC 1332 was observed in August, 1991, we used the response matrix and off-axis parameters appropriate to AO1 observations; we always excluded PI bins 1-10 and 224-256 from analysis due to calibration uncertainties (ROSAT Status Report # 78). We extracted the source spectrum using the IRAF-PROS software.

First, we analyzed the reduced image (§3.2) to determine the optimal region to extract the source. After experimenting with circles of different radii centered on the galaxy centroid (§3.2.2), we selected $R = 120''$ as that radius which optimized the S/N of the background-subtracted emission. We extracted the spectrum in this region using the full-scale PSPC image (15360×15360 field of $0.5''$ pixels) corrected only for bad time intervals and embedded point sources; note the sources were simply masked out, not symmetrically substituted (§3.2). The background level was computed in an annulus $R = 350'' - 400''$ and then subtracted from the extracted spectrum after correcting for telescopic vignetting. To improve S/N we rebinned (using *grpha* in FTOOLS) the resulting spectrum into 15 spectral bins each having > 20 counts. With XSPEC, we fit the background-subtracted spectrum to a single-temperature ($1T$) optically thin plasma incorporating thermal bremsstrahlung and line emission (Raymond & Smith 1977; updated to 1992 version) with Galactic absorption. The temperature, metallicity, hydrogen column density, and emission normalization were free parameters in the fits.

Table 5 summarizes the spectral data and fit results. The Raymond-Smith $1T$ model fits the data quite well. The 68% and 90% confidence levels for the three interesting parameters (temperature, abundances, and N_H) are determined by the contours of constant $\chi^2_{min}+$ 3.53 and 6.25 respectively; these contours are plotted in Figure 6. The constraints on $N_H = (0.083 - 4.7) \times 10^{20}$ cm^{-2} (90% confidence) are consistent with the galactic column density $N_H = 2.2 \times 10^{20}$ cm^{-2} (Stark et al. 1992). The abundances, where He was fixed at its cosmic value and the heavy element abundances have relative abundances fixed at solar, are not well determined, but the temperature is constrained to about a factor of 2. Like BC94 find for NGC 720, we find that two-temperature models having abundances fixed at solar fit the spectrum equally well.

We investigated the presence of temperature gradients by employing the same fitting procedure and single-temperature models as above. For examination of radial gradients we partitioned the $120''$ region into an inner circle ($30''$) and an outer annulus ($30''$ - $120''$) each possessing roughly the same S/N; although the $r = 30''$ region is only

slightly larger than the size of the PSF and thus undoubtedly has some correlation with the outer region, the constraints on the temperature gradient are hardly affected by selecting a larger inner circle – the outer region becomes more unconstrained because of the corresponding decrease in size and thus S/N. In addition, we needed to rebin the spectrum into only 8 channels to obtain acceptable S/N in each bin. The results of the fit are listed in Table 5 with only 68% confidence estimates because of the greater uncertainty due to the smaller number of counts in each region. From consideration of the 68% confidence extremes, we constrain the gradient to be $-0.55 < \left(\frac{d\ln T_{gas}}{d\ln R}\right) < 0.64$ ($\sim$ 95% confidence), where we have taken intensity-weighted values of R for each of the regions. If we fix N_H to its Galactic value, we obtain $-0.45 < \left(\frac{d\ln T_{gas}}{d\ln R}\right) < 0.49$ at $\sim$ 95% confidence.

In order to set more stringent limits on radial temperature gradients, we applied a Kolmogorov-Smirnov (K-S) test to the spectra of the two regions. Since the K-S test is intended for analysis of un-binned data, we used the full-scale spectrum consisting of 256 PI bins (with bins 1-10 and 224-256 excluded as above). In addition, since our spectra contained fractional counts (due to background subtraction) we rounded off fractions to the nearest whole number; this rounding off was especially important because after the background was subtracted the many bins that had had only one count then had slightly less $\sim$ 0.9 which would be unfairly eliminated by simply truncating the fractions.

The results of the K-S tests depended on the energy range examined. When channels $\lesssim$ 0.2 keV were included, we obtained probabilities $P_{KS} \ll 1\%$ that the two regions are derived from the same population. However, the X-ray background contribution is largest in the low-energy bins and, because it covers a larger area, the outer region certainly suffers more contamination from errors in the background determination than the inner region; i.e. as a result of imperfect background subtraction the background in each region is a different proportion of the total spectrum which necessarily affects the shape of the cumulative probability distribution responsible for P_{KS}. To reduce background contamination we restricted analysis to the hard band (0.4 - 2.0 keV). We found then that $P_{KS} = 40\%$ for energies 0.4 - 2.0 keV and that

P_{KS} varied by $\lesssim 10\%$ for other nearby cuts of energy; e.g., $P_{KS} = 34\%$ (0.3 - 2.0 keV) and $P_{KS} = 29\%$ (0.5 - 2.0 keV).

As we found for NGC 720 (BC94), this large probability serves as a discriminator for models with steep temperature gradients under the assumption that differences in the spectra of the two regions are due primarily to differences in temperature. To see how sensitive such a test would be for detecting a real temperature gradient we simulated Raymond-Smith spectra (with XSPEC) with statistics appropriate for the PSPC observation of NGC 1332; in each region (i.e. $R = 0'' - 30''$ and $R = 30'' - 120''$) the simulated spectra have Galactic N_H and 50% metallicities but different temperatures. We found that for a temperature in the inner region of $T_{in} = 0.60$ keV and an outer region temperature of $T_{out} = 0.50$ keV, $P_{KS} = 37\%$. The probability fell to $P_{KS} = 15\%$ for $T_{in} = 0.60$ and $T_{out} = 0.45$. However, for a slightly larger gradient (i.e. $T_{in} = 0.65$ keV, $T_{out} = 0.40$ keV), the probability dipped below 1%; this held for other T_{in} and T_{out} between $0.4 - 1.0$ keV. We defined spectral models to be inconsistent with the data if $P_{KS} < 1\%$. With this criterion, we determined that for reasonable temperature ranges (i.e. $0.4 - 1$ keV), the temperature gradient is constrained to be $\left|\frac{d \ln T_{gas}}{d \ln R}\right| < 0.35$. Hence, we find no evidence for radial temperature variations, but the PSPC spectrum cannot rule out sizeable gradients.

Following BC94 we also tested for azimuthal gradients by slicing the 120″ circle into 4 equal wedges of 90°. We defined the edges of the wedges with respect to the major axis to be (1) −45° to +45°, (2) +45° to +135°, (3) +135° to +225°, and (4) +225° to −45°; the major axis was taken along P.A. 115°. We grouped wedges (2) and (4) into a region denoted (A) and regions (1) and (3) were grouped into region (B) in order to improve the S/N. The results of the fits for these regions are listed in Table 5. A K-S test of (A) and (B) (0.1 - 0.3 keV bins omitted) yields a probability of 50% that the two regions are derived from the same population. Hence we find no evidence for a temperature gradient between (A) and (B).

Finally, we considered a possible contribution to the emission from discrete sources in the galaxy. We modeled the spectrum of discrete emission by (1) a power law, (2) a $T = 8$ keV Bremsstrahlung component, and (3) a $T = 8$ keV Raymond-Smith plasma

with Galactic N_H and 50% metallicities. None of these spectra alone fit the PSPC spectrum very well and can be ruled out as the dominant component of the X-ray emission (see Table 5); this is consistent with the poor fit of the optical radial profile to the X-ray radial profile in §3.3. However, the PSPC data cannot precisely constrain the relative flux of the hot gas and discrete components; i.e. equal contributions of hot gas and discrete emission are allowed by the spectrum. We discuss the implications of emission from discrete sources in §§3.5.2, 3.6.2, and 3.6.3.

3.5 Geometric Test for Dark Matter: Clarification and Applications

3.5.1 Theory

Here we clarify the test for dark matter in early-type galaxies introduced by BC94 that employs only the observed optical and X-ray surface brightness distributions of the galaxies and is completely independent of the temperature profile of the gas. We now show that this geometric test in principle allows for a model-independent test for whether mass traces light in a galaxy. More generally, any mass distribution may be tested for consistency with the X-ray data. First, the arguments of BC94 are summarized.

The fundamental assumption of the geometric test is that the X-ray emission may be approximated as due to hot gas in quasi-hydrostatic equilibrium with the underlying gravitational potential of the galaxy,

$$\nabla p_{gas} = -\rho_{gas} \nabla \Phi, \tag{3.3}$$

where ρ_{gas} is the gas density, Φ is the gravitational potential of the galaxy, and p_{gas} is the gas pressure. By "quasi" we mean that any streaming and rotation present must be unimportant with respect to the thermal pressure and gravitational potential energy of the galaxy. It is simple, however, to incorporate any measured rotation of

the gas by replacing Φ with the appropriate effective potential Φ_{eff}.

The hydrostatic equation generically requires that Φ, ρ_{gas}, and p_{gas} are all stratified on the same constant surfaces in three dimensions. With the additional assumption of a single-phase gas, the temperature, T_{gas}, must also share the same constant surfaces. In order to prove this property, we take the the curl of equation (3.3) and obtain $\nabla\rho_{gas} \times \nabla\Phi = 0$; i.e. ρ_{gas} and Φ have parallel normal vectors which means that ρ_{gas} and Φ are stratified on the same constant surfaces in three dimensions. If we instead divide equation (3.3) by ρ_{gas} and take the curl we obtain (after some rearranging) that $\nabla\rho_{gas} \times \nabla p_{gas} = 0$; i.e. ρ_{gas} and p_{gas} share the same constant surfaces in three dimensions. If $p_{gas} = p_{gas}(\rho_{gas}, T_{gas})$ it follows that on surfaces where ρ_{gas} is constant, T_{gas} must also be constant. Hence the hydrostatic equation alone demands that Φ, ρ_{gas}, p_{gas}, and T_{gas} all share the same constant surfaces in three dimensions. Note that no assumption about the form of the pressure or temperature is required for this property except that the gas is adequately described by a single phase; also note that an ideal gas need not be assumed as in BC94.

The important observable quantity, the gas volume emissivity, is also stratified on the same constant surfaces because it is a function only of the gas density and temperature: $j_{gas} \propto \rho_{gas}^2 \Lambda_{PSPC}(T_{gas})$, where Λ_{PSPC} is the plasma emissivity convolved with the spectral response of the PSPC; Λ_{PSPC} is only a weak function of T_{gas} and the metallicity of the gas (e.g., the poor constraints on these parameters obtained for NGC 4636 by Trinchieri et al. 1994). Hence j_{gas} and Φ trace exactly the same shape in three dimensions, regardless of the temperature profile of the gas; note that if the gas is rotating, j_{gas} traces the same shape as Φ_{eff}. This correspondence between the shapes of j_{gas} and Φ is the basis for the geometric test for dark matter.

We now depart from the presentation of BC94 (§3.1) who discussed the qualitative similarity between the shapes of the contours of the projected potential and the X-ray isophotes. Instead we clarify and extend the procedure employed in §3.2 of BC94 to test whether the optical light traces the underlying mass. In BC94 we implied that such a comparison was qualitative, now we show that the comparison is rigorous.

To ascertain whether light traces mass we first obtain Φ from the optical surface

brightness distribution Σ_L. We make the assumption that the three-dimensional luminosity density, j_L, is axisymmetric with its symmetry axis inclined by angle i with respect to the line of sight. With the additional general assumption that j_L may be represented as a finite series of spherical harmonics, Palmer (1994) has shown that j_L may be uniquely and analytically deprojected from Σ_L. For mass tracing light the mass density is just $\rho_L \propto j_L$ and the corresponding potential Φ_L follows from Poisson's equation. Setting $\Phi = \Phi_L$ we have the potential under the assumption mass traces light. By applying the same assumptions for j_L to j_{gas}, then j_{gas} may be uniquely and analytically deprojected from the X-ray surface brightness Σ_X. If Φ and j_{gas} trace the same shape , then mass tracing light is a suitable description of the galaxy. *Inconsistency of the shapes of Φ and j_{gas} signals the presence of dark matter, independent of the temperature profile of the gas and without requiring any model fitting.*

Apart from the fundamental assumption of hydrostatic equilibrium, the few additional assumptions of this geometrical test for dark matter are not restrictive. First, by examining both oblate and prolate axisymmetric deprojections, one necessarily brackets the full range of ellipticities of triaxial galaxies. Second, the unknown inclination angle must be the same for Φ and j_{gas} if mass traces light. Since an inclined axisymmetric galaxy is necessarily rounder in projection than when viewed edge-on, deprojection assuming $i = 90°$ will yield Φ and j_{gas} rounder than the true values. This serves only to make any deviations in the shapes of Φ and j_{gas} more difficult to observe. Third, the assumption that j_{gas} and j_L be represented as a finite series of spherical harmonics should bracket most physical cases of interest. Finally, the assumption of a single, dominant gas phase should be a good description except in the regions of a strong cooling flow (Thomas, Fabian, & Nulsen 1987; Tsai 1994).

The standard X-ray method for analyzing the mass distribution in early-type galaxies utilizes the spherically-symmetric solution of equation (3.3) for a single-phase ideal gas (for a review see Fabbiano 1989). This method emphasizes the radial mass distribution and suppresses any information contained in the shapes of the X-ray isophotes. The mass within a radius r for this solution is expressed in terms of

$d\log\rho_{gas}/d\log r$, $T_{gas}(r)$, and $d\log T_{gas}/d\log r$. As a result, employing this solution requires detailed information on the intrinsic temperature profile of the gas. Moreover, since ρ_{gas} appears explicitly it must be disentangled from the observed surface brightness (Σ_X) assuming knowledge of the plasma emissivity Λ_{PSPC} of the gas. In contrast, the geometric test proposed by BC94, which emphasizes the elongation of the mass, requires only j_{gas} and hence does not depend on knowledge of the temperature profile or the plasma emissivity of the gas. (Note that this test does *not* give any information regarding the radial mass distribution, although it can give the ratio of dark matter to luminous matter.)

BC94 performed the geometric test for dark matter on NGC 720 similar in concept, but different in implementation, to what we have described above. The spatial resolution of the PSPC ($FWHM \sim 30''$) does not warrant detailed deprojection of Σ_X on scales much smaller than $30''$. Since the isophotes of interest for BC94 lie at $\sim 100''$ and the PSPC image of NGC 720 has relatively low S/N ($\sim$ 1500 counts), we opted for a coarser comparison of Φ and j_{gas}. BC94 deprojected Σ_L to obtain j_L by fitting a simple model to the major-axis of Σ_L and assigning to j_L the ellipticity of the flattest isophotes of Σ_L. By assuming mass follows light BC94 computed Φ_L from j_L. Invoking hydrostatic equilibrium, they assigned the ellipticity profile of Φ_L to j_{gas}. They then used a simple parametrization of j_{gas} as a spheroid having ellipticity varying with radius to generate the corresponding Σ_X consistent with the PSPC radial profile. Finally, the ellipticity of this Σ_X consistent with Φ_L was compared to the ellipticity of the data. By performing 1000 Monte Carlo realizations of Σ_X BC94 concluded that the X-ray isophotes generated assuming mass traces light are rounder than the observed isophotes at the 99% confidence level. Note that BC94 implied that the comparison was uncertain due to projection effects whereas we have shown here that the comparison is in fact more robust.

3.5.2 Application

Because the important apertures ($a \sim 80''$) for comparison of ϵ_M lie nearer to the center for NGC 1332 than for NGC 720 ($a \sim 100''$) and the PSPC image of NGC 1332

has even lower S/N than that of NGC 720, we apply the geometric test using simple parametrizations of Σ_L and Σ_X following BC94. Moreover we address the effects of possible rotation of the gas and contamination of the X-ray emission due to discrete sources in the galaxy. We assume that a single-phase gas adequately describes the bulk emission.

Before embarking on the robust geometrical test, we obtain a useful qualitative picture by comparing the shapes of the X-ray isophotes (§3.2.3) to the contours of constant projected potential for a constant M/L model. BC94 showed that for a wide class of physical models the ellipticities of the projected potential and X-ray isophotes should agree to within $\Delta\epsilon \lesssim 0.04$. We obtain ρ_L by deprojecting the single De Vaucouleurs profile obtained from §3.3 approximated by a Hernquist profile (see §3.6.2). Applying Poisson's equation we obtain the potential Φ_L. Listed in Table 8 are the ellipticities of the isopotential surfaces of Φ_L, its projection onto the sky assuming oblate symmetry, and its projection convolved with the PSPC PSF. We also show in Table 8 the ellipticities of the X-ray isophotes predicted by explicit solution of the hydrostatic equation for an isothermal ideal gas (see §3.7.3).

For semi-major axes $75'' - 90''$, those being the apertures for which ϵ_M is best determined, the projected potential convolved with the PSPC PSF and the isothermal model have ellipticities about 0.10. These values are inconsistent with the measured lower limits for ϵ_M at 68% confidence but marginally consistent at 90% confidence. For prolate constant M/L models the ellipticities are virtually identical because the distinction between prolate and oblate spheroids for such small ellipticities is negligible. Considering the uncertainty $\Delta\epsilon \lesssim 0.04$ for comparing the projected potential and X-ray isophotes (BC94) the stellar mass model appears inconsistent at the 68% confidence level on ϵ_M, but consistent at 90% confidence.

We make this comparison robust following the procedure of BC94 discussed at the end of §3.5.1. Our model for Φ_L is the same as previously discussed. We follow BC94 and parametrize j_{gas} by the pseudo-spheroids discussed in Appendix B of BC94:

These spheroids are a function of,

$$\zeta^2 = x^2 + y^2 + z^2/q(r)^2, \tag{3.4}$$

where $q = q(r) = 1 - \epsilon(r)$ is the radially varying axial ratio with $r^2 = x^2 + y^2 + z^2$; such models are very similar to those introduced by Ryden (1990). We parametrize the emissivity by a power law, $j_{gas} \propto (R_c^2 + \zeta^2)^{-n}$, with core radius R_c and slope parameter n. The surface brightness generated by this parametrization, Σ_X^{param}, is computed by integrating j_{gas} along the line of sight and then convolving with the PSPC PSF. We determine R_c and n by fitting the radial profile of Σ_X^{param} to Σ_X as discussed in §3.2.2; the best-fit parameters are $R_c = 0.6''$ and $n = 1.38$. Then Poisson counts and a uniform background are added to the image appropriate for the NGC 1332 PSPC observation; we do not bother to then subtract a background estimate because it does not affect computation of ϵ_M (see §3.2.3).

In Table 9 we list the upper limits on ϵ_M for 1000 simulations for both oblate and prolate deprojections; e.g., 90% upper limit is ϵ_M^{900} (see §3.2.3). For both cases, just like the qualitative comparison made above, the assumption of mass tracing light yields ϵ_M values inconsistent with the data at the 68% confidence level and marginally consistent at the 90% level. In Figure 7 we plot the mean ϵ_M from the oblate simulations superposed on ϵ_M measured from the data. Clearly it is imperative to obtain higher S/N data to determine whether there is a real discrepancy.

Rotation

In the previous discussion we have neglected possible rotation of the gas. The PSPC, of course, does not have the spectral resolution or sensitivity to detect rotation so we must resort to indirect arguments to estimate its effects (see BC94 for a discussion). Since the gas mass of NGC 1332 is only a small fraction of the stellar mass (see §3.7.2) it is consistent with being produced by normal stellar mass loss over $\sim 10^9$ years (Mathews 1990). In such a scenario the gas should have originally rotated in a manner similar to the stars. After being heated by supernovae the gas would expand,

maintaining the same angular momentum of the stars, but with a reduced velocity. In the central regions of a cooling flow, however, the velocity could be driven up above the stellar rotation rate as the gas falls back in to the center (see, e.g., Kley & Mathews 1995). The effect of such rapidly rotating gas resulting from infall cannot be substantial at the relatively large radii $r = 75'' - 90''$ that are of interest to us since only a small fraction of the stellar mass exists at larger radii. We examine the case where the gas rotates like the stars which should serve as a conservative upper limit in light of the above scenario.

Incorporating rotation into our formalism simply entails replacing the gravitational potential in eq. [3.3] with an effective potential $\Phi_{eff} = \Phi - \Phi_{rot}$, where Φ_{rot} is the potential due to rotation. Dressler & Sandage (1983) measured the major-axis rotation curve for NGC 1332 out to $R = 60''$. The velocity profile rises to $R = 20''$ then flattens out to a maximum velocity of $V_{max} = 230$ km s^{-1}. A simple means to incorporate the effect of the gas rotating like the stars is to assume the mean azimuthal rotation, $\bar{v}_\phi$, is a fraction of the circular velocity scaled to the observed V_{max} as follows. For a spherical Hernquist model the circular velocity is $v_c = \sqrt{GMr}/(r + r_c)$, where r is the radius and r_c the core parameter. We take the velocity profile along the major-axis to have this form which becomes $\bar{v}_\phi(R, 0) = 2V_{max}\sqrt{R_c R}/(R_c + R)$, where $V_{max} = \bar{v}_\phi(R_c, 0)$. Replacing R by the spheroidal radius $\sqrt{R^2 + z^2/q^2}$ (with q, the constant axial ratio of the mass, taken to be 0.57 – see §3.3) this velocity profile approximately corresponds to $\Phi_{rot} = 4R_c V_{max}^2/(R_c + \sqrt{R^2 + z^2/q^2})$. Although this relation is not exact, it provides a convenient exploration of the effects of the gas rotating like the stars. To properly normalize Φ_{rot} with respect to Φ we need to specify the total mass. From the results of §3.6.3 we take the mass to be $0.5 \times 10^{12} M_\odot$. For ranges of plausible masses $(0.2 - 0.8) \times 10^{12} M_\odot$ appropriate to the Hernquist model the precise choice of mass is not important.

We list in Table 10 the 68% and 90% upper limits on 1000 simulations of the oblate mass models having the type of rotation just described; we consider only oblate models since minor-axis rotation is rare. Again we focus on semi-major axes $a = 75'' - 90''$ since they are best determined by the data. Even with rotation the

68% confidence upper limits fall below the observed values, although the 90% upper limits are consistent with the data; we note that at the 85% level the $a = 75'' - 90''$ upper limits are just marginally consistent with the data. *Thus rotation of the gas similar in nature to the stars does weaken the need for dark matter based solely on shape alone, but the ellipticities are only about* 10% *larger than the non-rotating case.* This should serve as a conservative upper limit of the effects of rotation if the gas has expanded (due to heating) and conserved angular momentum.

Emission from Discrete Sources

Finally we consider the effects of emission from discrete sources in the galaxy. We model the X-ray surface brightness (Σ_{ds}) due to discrete sources by assuming that $\Sigma_{ds} \propto \Sigma_L$, where Σ_L is the optical surface brightness convolved with the PSPC PSF (see §3.3). Thus in this case our composite model surface brightness is $\Sigma_X = \Sigma_{hg} + \Sigma_{ds}$, where Σ_{hg} is the surface brightness of the hot gas computed in §3.5.2. The relative normalization of the two components is given by F_{ds}/F_{hg} - the ratio of the X-ray fluxes of the two components within $R = 300''$.

In Table 10 we display the results of the simulations for $F_{ds}/F_{hg} = 1/10$ and $1/3$; we consider only oblate models for brevity. For $F_{ds}/F_{hg} = 1/10$ the results essentially reproduce the simulations without discrete emission. For $F_{ds}/F_{hg} = 1/3$ the results essentially reproduce the simulations where the gas is rotating; i.e. discrepancy of X-ray data with mass-follows-light assumption at the 68% level, marginal agreement at the 90% level. Higher quality spectral data could better constrain F_{ds}/F_{hg} and thus allow more robust constraints to be obtained.

To give an impression of the combined effects of rotation and discrete sources we considered the rotating model of §3.5.2 with discrete emission of $F_{ds}/F_{hg} = 1/3$. The combined results are similar to what was found for each of the cases separately (see Table 10). For the aperture $a = 75''$ the simulations give $\epsilon_M = 0.12 - 0.18(0.08 - 0.22)$ at 68%(90%) confidence. It is interesting that the 90% lower limit $\epsilon_M = 0.09$ (i.e. ϵ_M^{100}) for $a = 135''$ is only marginally consistent with the measured value of 0.10; the simulations without rotation or discrete emission have a 90% lower limit of 0.04.

Future observations that accurately determine ϵ_M to large radii will be better able to disentangle the effects of rotation and discrete emission on this geometric test for dark matter.

3.6 Composite Gravitating Matter Distribution

3.6.1 Method

The technique we employ to constrain the shape of the galaxy potential, and hence its mass, from the X-ray image derives from the pioneering work of Binney & Strimple (1978 Strimple & Binney 1979) and is discussed in detail by Buote & Tsai (1995a) and BC94. We refer the reader to these papers for exposition of the modeling procedures we employ in this paper.

We consider the following two families of gravitational potentials:

1. Spheroidal Mass Distributions (SMD): Potentials that are generated by mass distributions stratified on concentric, similar spheroids.

2. Spheroidal Potentials (SP): Potentials that are themselves stratified on concentric, similar spheroids.

Although the SP models have some properties that are undesirable for a physical mass model (i.e. the density may be "peanut-shaped" and possibly somewhere take negative values), the constant shape of the potential and the ellipticity gradient of the mass distribution contrast nicely with the SMDs. The SMD potentials are generated by mass densities $\rho(m)$, where $m^2 = R^2/a^2 + z^2/b^2$, R and z are the conventional cylindrical coordinates, a is the semi-major axis and b the semi-minor axis of the spheroid that bounds the mass; full accounts of SMD potentials are given by Chandrasekhar (1969) and Binney & Tremaine (1987). We consider mass densities having either a Ferrers, $\rho(m) \propto (R_c^2 + a^2m^2)^{-n}$, or Hernquist (1990), $\rho(m) \propto (am)^{-1}(R_c + am)^{-3}$, form; note that $\rho(m) \equiv 0$ outside of the bounding spheroid. The free parameters of the SMD models are the core parameter, R_c, semi-major axis length, a, the ellipticity $\epsilon = 1 - b/a$ of the mass, and the power-law index n.

The SP models are given by $\Phi = \Phi(\xi)$, where $\xi^2 = R^2 + z^2/q_\Phi^2$; q_Φ is the constant axial ratio of the SP such that $q_\Phi < 1$ for oblate and $q_\Phi > 1$ for prolate SPs. In particular, we consider the logarithmic potential of Binney (1981; Binney & Tremaine 1987; also Kuijken & Dubinski 1994), $\Phi(R,z) \propto \log(R_c^2 + \xi^2)$, and the power-law potentials (Evans 1994), $\Phi(R,z) \propto (R_c^2 + \xi^2)^{-n}$. The free parameters for these models are R_c, ϵ_Φ (which is $1 - q_\Phi$ for the oblate models and $1 - 1/q_\Phi$ for prolate models), and n for the power-law models.

Because of the observed elongation of the optical isophotes (see §3.3) the symmetry axis of the mass of NGC 1332 should not be substantially inclined with respect to the sky plane. That is, even if the outer isophotes ($\epsilon \sim 0.70$) have intrinsic ellipticity appropriate to a galactic disk ($\epsilon \sim 0.90$; Binney & Tremaine 1987), then the galaxy can be inclined at most 15° with respect to the sky plane; i.e., $i = 75°$. Hence, we do consider the effects of this moderate inclination angle on the estimates of the intrinsic shape of the galaxy. We also consider the effects of gas rotation and emission from discrete sources in the manner discussed previously (§§3.5.2 and 3.5.2).

3.6.2 Shape of the Composite Mass

We determine the intrinsic shape of the underlying galactic mass by comparing ϵ_M (§3.2.3) and the azimuthally averaged radial profile (§3.2.2) of the PSPC image to those generated by the models (i.e. model ellipticity ϵ_M^{model}). We quantify the elongation of the model surface brightness within semi-major axes $a = 75''$ and $a = 90''$ because they provide the most stringent constraints on ϵ_M. To save CPU time we use $15''$ pixels in the models for computing the radial profiles; these are then compared to the image radial profile having the $15''$ central bin. However, when comparing ellipticities of select models we always use $5''$ pixels. Note that the uncertainty due to the details of the PSF (see §3.2.2) affects mostly determination of R_c; the slope and ellipticity of the surface brightness, especially for $a = 75'' - 90''$, are hardly affected. The total mass, however, is more sensitive (see §3.6.3).

For the SMD models we begin by specifying the semi-major axis (a) of the bounding mass spheroid, the power-law index of the particular mass model (i.e. Ferrers

[$n = 1 - 1.5$] or Hernquist), and the inclination angle (i) of the symmetry axis (i.e. either $i = 90°$ or $i = 75°$). Then for a given ellipticity of the mass we generate model X-ray surface brightness maps for any values of the free parameters associated with the particular solution of the hydrostatic equation; i.e. R_c and Γ for the isothermal case and R_c, γ, and Γ for the polytropic case (see BC94). The procedure is the same for the SP models except that (1) the boundary of the mass is not specified, and (2) the power-law index of the potential (logarithmic or $n = 0.1 - 0.5$) and the ellipticity of the potential (ϵ_Φ) are specified. We determine the confidence limits on the free parameters by performing a χ^2 fit that compares the radial profiles of the model and image. The confidence interval is defined by models having $\chi^2 \leq \chi^2_{min} + \Delta\chi^2$, where $\Delta\chi^2 = (4.61, 6.25)$ for the 90% confidence interval of the isothermal and polytropic cases respectively; $\Delta\chi^2 = (2.30, 3.53)$ and $\Delta\chi^2 = (6.17, 8.02)$ are used for the 68% and 95% confidence limits.

We determine a particular model in these confidence intervals to be consistent with the image if ϵ_M computed from the model in the 75″ and 90″ apertures is consistent with that computed from the image in §3.2.3. The confidence interval used for the radial profile is also used for the ϵ_M – ϵ_M^{model} comparison; e.g., 90% confidence limit on ϵ_{mass} reflects 90% limits on the parameters determined from the radial profile and from ϵ_M.

Mass Traces Light

First we examine again in this more detailed analysis if the hypothesis that mass traces light in the galaxy is consistent with the X-ray data. To estimate the luminosity density, j_L, we deproject the I-band major-axis surface brightness profile (§3.3). For simplicity we use the single De Vaucouleurs Law ($R_e = 55''$) fitted to the major-axis profile. We assign to j_L, and hence to the mass density, ρ, the constant intensity-weighted ellipticity of 0.43. Hence our model for the composite mass density, ρ, is a Hernquist SMD with $R_c = 55''/1.8153$, $a = 300''$, and $\epsilon_{mass} = 0.43$; the choice for a was arbitrary since any $a \gtrsim 150''$ yields similar major-axis surface brightness profiles.

Assuming the gas is isothermal, the constant M/L model is ruled out to high

confidence since it produces an X-ray radial profile that is far steeper than observed; the best-fit yields $\chi^2_{min} = 73$ for 9 degrees of freedom. The polytropic solution, however, is a good fit to the radial profile with best-fit values $\chi^2_{min} = 8.2$ (8 dof), $\gamma = 1.27$, and $\Gamma = 3.79$. Using the same definitions in §3.4, this model produces a sizeable temperature gradient $\frac{d \ln T_{gas}}{d \ln R} = -0.37$ that is marginally inconsistent with the K-S tests in §3.4. The ellipticities generated by the polytropic model (and the isothermal model), $\epsilon_M = 0.09(0.10)$ for apertures $a = 75''(90'')$, are inconsistent with the data at 68% confidence and only marginally consistent at 90% confidence; note the effects of rotation like the stars and emission from discrete sources in the galaxy reduce the discrepancy to the 68% confidence level as found in §3.5.2.

Hence, because of the poor constraints on the temperature profile of the gas and the relatively weak constraints on the shapes of the X-ray isophotes, a constant M/L model is inconsistent with the X-ray data at 68% confidence but marginally consistent at the 90% confidence level. The ellipticities generated by the polytropic and isothermal cases are virtually identical and yield results consistent with the geometric test in §3.5.2. The similarity of the shapes of the isothermal and polytropic models appears to be a generic feature of these models (Strimple & Binney 1979; Fabricant, Rybicki, & Gorenstein 1984; also see appendix B of BC94).

General Mass Models

We list in Table 11 the results for the isothermal SMD models; the semi-major axis of the mass models is set to $a = 450''$ which corresponds to $a = 43.6$ kpc for $D = 20$ Mpc; in Figure 8 we display the results for a typical model. The $\rho \sim r^{-2}$ (i.e. $n = 1$) and Hernquist models yield excellent fits to the X-ray radial profile, but the $\rho \sim r^{-3}$ (i.e. $n = 1.5$) model is too steep to fit the data. The derived ranges of ϵ_{mass} for the $\rho \sim r^{-2}$ and Hernquist models are very similar with $\epsilon_{mass} \gtrsim 0.50$ (68% confidence) marginally inconsistent with the intensity weighted $\epsilon = 0.43$ of the optical isophotes (see §3.3). At 90% confidence this disagreement vanishes since $\epsilon_{mass} \gtrsim 0.30$. Note that the need for a flattened mass distribution is still significant at the 95% confidence level where, e.g., $\epsilon_{mass} = 0.26 - 0.82$ for the oblate $\rho \sim r^{-2}$ model.

These constraints on ϵ_{mass} are not sensitive to the value of a. There is no upper limit on a, but we define a lower limit when models yield χ^2_{min} such that the probability that χ^2 should exceed χ^2_{min} is less than 10%. The value of a_{min} slightly varies over the range of ϵ_{mass}. We estimate $a_{min} = 105''$ ($a_{min} = 120''$) at the lower limit for ϵ_{mass} and $a_{min} = 135''$ ($a_{min} = 135''$) at the upper limit for ϵ_{mass} for oblate (prolate) models at 90% confidence for the $n = 1$ SMD; there is little difference in a_{min} between the SMD models considered. For $a \geq a_{min}$ the constraints on ϵ_{mass} systematically differ by $\lesssim 0.02$.

We examined the effects of inclination by setting $i = 75°$ for the isothermal $\rho \sim r^{-2}$ SMD models having $a = 450''$ (see end of §3.6.1). The 68% and 90% confidence limits for prolate and oblate models are listed in Table 11. The derived ϵ_{mass} constraints are systematically shifted upwards with respect to the $i = 90°$ models by ~ 0.06 for the oblate models and ~ 0.03 for the prolate models.

In Table 11 we list the results for the isothermal SP models; in Figure 9 we display the results of a typical model. The logarithmic and $n \lesssim 0.1$ SP models fit the data well, but models with larger values of n do not; e.g., for the $n = 0.25$ model $\chi^2_{min} \sim 18$. Since the SP models have mass distributions that change shape with radius, we assign an aggregate ellipticity to the SP models by computing the ellipticity obtained from the iterative moments (§3.2.3) in a plane containing the major and minor axes. For values of the aperture semi-major axis $\gtrsim 150''$, ϵ_{mass} is essentially constant because of the small values of R_c. In Table 11 we list the average value of ϵ_{mass} for aperture semi-major axes $\gtrsim 150''$. The logarithmic SP yields ϵ_{mass} constraints very similar to the oblate SMD models. The prolate SP models unlike the SMD models have ϵ_{mass} virtually identical to the oblate models; this is simply a manifestation of the different behavior of the SMD and SP models in projection. The power-law models yield very flat masses with no upper limit for $n \gtrsim 0.1$.

The polytropic models also require flattening of the underlying mass. We obtain similar results for the $\rho \sim r^{-2}$ SMD polytropic model; i.e. at 90% confidence limits $\epsilon_{mass} = 0.33 - 0.80(0.30 - 0.71)$ and $\gamma = 0.73 - 1.38(0.76 - 1.41)$ for oblate (prolate) models with $a = 450''$. The oblate models have corresponding temperature gradi-

ents $\left|\frac{d\ln T_{gas}}{d\ln R}\right| \leq 0.39$ which are essentially consistent with the PSPC spectrum (see §3.4); i.e. even with the additional freedom allowed by temperature gradients, the constraints on ϵ_{mass} are essentially identical to the isothermal case for the $\rho \sim r^{-2}$ SMD model. The polytropic $\rho \sim r^{-3}$ SMD model fits the surface brightness well but requires large polytropic indices $\gamma = 1.24 - 1.89$ (oblate) some of which are unlikely to be present in early-type galaxies. The oblate (prolate) models give a 90% lower limit $\epsilon_{mass} \geq 0.53(0.43)$. For each acceptable $\rho \sim r^{-3}$ SMD model the 90% lower-limit $\gamma \sim 1.25$ implies $\left|\frac{d\ln T_{gas}}{d\ln R}\right| \approx -0.34$ which is only marginally consistent with the spectral constraints in §3.4. The Hernquist polytropic models behave like the $\rho \sim r^{-2}$ models in that they reproduce the isothermal results for ϵ_{mass}, R_c, and Γ in the 90% confidence interval, but the best-fit region of the parameter space has unphysical parameters such as huge values of $R_c \gg a$ and small values of $\gamma < 0.4$; these low values of γ typically imply $\left|\frac{d\ln T_{gas}}{d\ln R}\right| \gtrsim 0.7$ which is inconsistent with the spectral constraints in §3.4. The logarithmic SP model yields $\epsilon_{mass} \geq 0.36$ (90% confidence) with R_c and Γ values comparable to their isothermal ranges, although no upper limit can be set on ϵ_{mass} at 90% confidence. Thus, the presence of possible temperature gradients does not greatly affect the constraints on the intrinsic shape of NGC 1332; even the weak spectral constraints obtained from the PSPC data (§3.4) strongly suggest that ρ is flatter than r^{-3} for the SMD models.

We examined the effects of rotation following our treatment in §3.5.2. In Table 11 we list the results for the oblate Hernquist models ($a = 450''$) having rotation similar to that of the stars. The derived ellipticity ranges are systematically shifted down by $\Delta\epsilon_{mass} \sim 0.15$. However, the need for a flattened halo is still preserved even considering the substantial rotation.

We estimate the effect of emission from discrete sources on ϵ_{mass}. In Table 11 we list the results for the isothermal oblate $\rho \sim r^{-2}$ SMD model of the hot gas with a discrete model (see §3.5.2) in terms for their flux ratio F_{ds}/F_{hg}. Models with $F_{ds}/F_{hg} = 1/2$ (i.e. 1/3 discrete emission, 2/3 hot gas) have the largest discrete contribution that yields acceptable fits to the data; e.g., for $F_{ds}/F_{hg} = 1$, $\chi^2_{min} \sim 49$ for 8 dof – unacceptable models have χ^2_{min} such that the probability that χ^2 should

exceed χ^2_{min} is less than 10%; note also that $F_{ds}/F_{hg} \lesssim 1$ implies discrete fluxes F_{ds} consistent with the L_X/L_B relation for galaxies dominated by emission from discrete sources (see, e.g., Canizares et al. 1987). The upper limit on ϵ_{mass} is virtually unaffected by the presence of discrete emission, but the lower limit is very sensitive; e.g., the lower limit on ϵ_{mass} falls to 0.16 (90% confidence) for $F_{ds}/F_{hg} = 1/2$. Hence, the ability to constrain the shape of the underlying mass is substantially influenced by the possible presence of emission from discrete sources in the galaxy.

Finally, we considered the combined effects of rotation and emission of discrete sources using the rotating model of §3.5.2 with a discrete component such that $F_{ds}/F_{hg} = 1/3$ in analogy to what was done in §3.5.2; the results are presented in Table 11. As expected, the effects of both rotation and discrete emission further weaken, but do not eliminate, the need for a substantially flattened halo.

3.6.3 Estimate of the Composite Mass Profile

Using the models of the previous section together with the results for the PSPC spectrum (§3.4) we compute the total integrated mass of the galaxy; note that (unlike the shape) the procedure to obtain the total mass profile (see, e.g., eq. [26] of BC94) requires detailed knowledge of the temperature profile and thus suffers from the same uncertainties of the traditional spherically-symmetric analysis of the total mass (for a review see Fabbiano 1989). In Table 9 we list the total masses (M_{tot}) and total blue mass-to-light ratios ($\Upsilon_B = M_{tot}/L_B$) for several mass models of the previous section. The total blue luminosity, $L_B = 1.91 \times 10^{10} L_\odot$, is taken from Donnelly et al. (1990) scaled to $D = 20$ Mpc. The 68% and 90% confidence limits reflect the same confidence values for the parameters of the mass models. However, in both cases the 90% confidence limits on the gas temperature are used. Note that the uncertainty in R_c due to PSF calibration (§3.2.2) is less than 50% which typically translates to at most 30% uncertainty in the mass.

The total masses overlap for the all of the models although there are systematic differences between models; e.g., $n = 1$ isothermal SMD models systematically allow for higher masses than the steeper isothermal Hernquist models. The lower bound

on Υ_B is obtained from the a_{min} prolate model which gives $\Upsilon_B = 8.9\Upsilon_\odot$ at 68% confidence and $\Upsilon_B = 7.9\Upsilon_\odot$ at 90% confidence (assuming $D = 20$ Mpc) for the isothermal $n = 1$ SMD models. The 90% lower limits on Υ_B are not very different from $\Upsilon_B \sim 7\Upsilon_\odot$ expected of the stellar population alone (§3.7.1). The effects of possible temperature gradients are substantial for the total mass and yield mass ranges larger than a factor of two over the isothermal case. In Figure 10 we plot the integrated mass profile as a function of spheroidal radius am, where a is the semi-major axis of the spheroid having mass M_{tot}, for two typical SMD models consistent with the fits to the radial profile; we also plot the spherically-averaged mass profile for the isothermal logarithmic SP model. Assuming $\Upsilon_B \sim 7\Upsilon_\odot$ for the stellar population and that the gas mass may be neglected (§3.7.2) we compute the relative fraction of mass in stars (M_{stars}) and dark matter (M_{DM}). For the isothermal $\rho \sim r^{-2}$ SMD models we obtain 90% confidence estimates of $M_{DM}/M_{stars} = 2.9 - 11.1$ for $a = 450''$ and $M_{DM}/M_{stars} = 1.4 - 3.3$ for the minimum acceptable a models.

We examined the effects of gas rotation and emission from discrete sources on determining the integrated mass profile using a series of isothermal Hernquist models listed in Table 9: (1) Hernquist SMD ($a = 450''$), (2) rotation model, (3) Hernquist SMD with discrete component in flux ratio $F_{ds}/F_{hg} = 1/3$, and (4) rotation model plus discrete component in flux ratio $F_{ds}/F_{hg} = 1/3$. The total masses for these models agree to within 30%. The ellipticity constraints for these models, in contrast, vary substantially more than this (see Table 11); e.g., the 90% confidence limits $\epsilon_{mass} = 0.1 - 0.6$ for model (4) and $\epsilon_{mass} = 0.33 - 0.83$ for (1) corresponding to a 40% shift in the mean for the two models. Hence, the X-ray determination of the integrated mass profiles of early-type galaxies are less sensitive to uncertainties due to possible rotation of the gas and emission from discrete sources than the intrinsic shape, ϵ_{mass}.

Finally, we compute the circular velocity (v_c) of these models. Franx (1993) shows that simple models of ellipticals with massive halos satisfy a Tully-Fisher relation when $v_c/\sigma_0 \sim 1.38$, where v_c is the maximum circular velocity of the halo and σ_0 is the observed central velocity dispersion. Dalle Ore et al. (1991) measure $\sigma_0 = 347$ km

s^{-1} for NGC 1332 which has the distinction of having the largest σ_0 in their sample of 79 early-type galaxies. For the $\rho \sim r^{-2}$ SMD models, v_c occurs at a which gives 90% confidence values of $v_c = 278-428$ km s^{-1} and $v_c/\sigma_0 = 0.80-1.23$ for $a = 450''$; at the minimum values of a, $v_c = 313-453$ km s^{-1} (90% confidence) and $v_c/\sigma_0 = 0.90-1.31$. The logarithmic SP model gives 90% confidence values $v_c = 272 - 414$ km s^{-1} and $v_c/\sigma_0 = 0.78-1.20$. These values for v_c/σ_0 are systematically less than the suggested value from Franx (1993), but the large central velocity dispersion for NGC 1332 may suggest that it is an unusual case.

3.7 Dark Matter Distribution

The composite gravitational potential we analyzed in the previous section may be decomposed into its constituents,

$$\Phi = \Phi_{stars} + \Phi_{gas} + \Phi_{DM}, \tag{3.5}$$

where Φ_{stars} is the potential arising from a mass distributed like the light having the total mass of the visible stars, Φ_{gas} is the potential generated by the the mass of the X-ray–emitting gas, and Φ_{DM} is the potential generated by the dark matter. By using the observations to constrain Φ_{stars} and Φ_{gas} we may determine the distribution of dark matter directly. The procedure to constrain Φ is the same as before except now the free parameters are those associated with the shape of Φ_{DM} and the ratio of the mass in dark matter to the mass in visible stars, M_{DM}/M_{stars} (see BC94); note we neglect Φ_{gas} since $M_{gas} \ll M_{stars}$ (see below).

BC94 pointed out that determination of M_{DM}/M_{stars} in this fashion depends only on the relative distribution of stars and dark matter, not the distance to the galaxy. As a result, BC94 suggested (but did not explain) that in principle M_{DM}/M_{stars} could be used a distance indicator. If the stellar mass-to-light ratio, Υ_{stars}, of early-type galaxies is universal, then $M_{stars} = \Upsilon_{stars} L_{stars} \propto D^2$, where D is the distance to the galaxy. For M_{DM}/M_{stars} constrained by fitting to the surface brightness, we may

compute the resulting total mass $M_{fit} = M_{stars} + M_{DM} \propto D^2$. Comparing M_{fit} to $M_{tot} \propto D$ computed in §3.6.3, we have $D \propto M_{fit}/M_{tot}$. Hence for high-quality optical and X-ray data that accurately determine M_{fit} and M_{tot} the distance to the galaxy may in principle be inferred. Unfortunately, the value of Υ_{stars} is at present quite uncertain (see below). In any event, spatial and spectral X-ray data far superior to the PSPC would be required to accurately address, e.g., the issues of temperature gradients, rotation, emission from discrete sources and thus enable examination of the viability of this technique as a distance indicator.

3.7.1 Visible Stellar Mass Distribution

The stellar distribution is just that of the constant M/L model of §3.6.2. Following BC94 we normalized ρ_{stars} by assigning the stars a mass-to-light ratio $\Upsilon_B = 7\Upsilon_\odot$. This value is actually quite uncertain since population synthesis studies give $\Upsilon_B = (1-12)\Upsilon_\odot$ (e.g., Pickels 1985). The uncertainty is reduced by normalizing to dynamical studies of the cores of ellipticals (e.g., Bacon 1985; Peletier 1989). As a result, $\Upsilon_B = 7\Upsilon_\odot$ may overestimate the stellar mass by including a significant amount dark matter. With these uncertainties aside, we obtain a stellar mass $M_{stars} = 1.3 \times 10^{11} M_\odot$ assuming $D = 20$ Mpc.

3.7.2 X-ray Gas Mass Distribution

The radial X-ray surface brightness distribution is well parametrized by the β-model (§3.2.2), but the elongation is not so well determined (§3.2.3). We compute the radial distribution under the assumption of spherical symmetry which should not introduce errors greater than $\sim 25\%$ for plausible ellipticities of the gas (e.g., BC94). Straightforward deprojection of the β-model yields the volume emissivity, j_{gas}. The gas density, $\rho_{gas} \propto \sqrt{j_{gas}}$ (see BC94), is then integrated to get the total gas mass.

We list in Table 13 the gas mass, M_{gas}, the volume-averaged particle density, $\bar{n}$, and its associated cooling time, $\bar{\tau}$, all computed within the gas sphere with radius $r = 300''$; note these values reflect 90% confidence values on a_X, β, and the spectral

parameters of the single-temperature model (§3.4). The 90% confidence range of M_{gas} implies that $M_{gas}/M_{stars} \lesssim 1/100$. For such small values the self-gravitation of the gas may be neglected in eq. [3.5] and hence we ignore Φ_{gas} in the following determination of the dark matter.

3.7.3 Results

For a given value of M_{DM}/M_{stars} the fitting procedure follows that in §3.6.2 where the free parameters are now associated with the dark matter model. Because adding another parameter weakens the already loose constraints on the models, we restrict our discussion to isothermal $\rho \sim r^{-2}$ SMD models for the dark matter. Similarly, we do not discuss the effects of rotation or emission from discrete sources here. We simply wish to obtain an understanding of how the dark matter itself is distributed for some plausible models.

In Table 14 we list the results for several values of M_{DM}/M_{stars} where the semi-major axis of the dark matter has been set to $a = 450''$; note the quality of the fits and isophote shapes for typical models are the same as for the composite case (§3.6.2). For $M_{DM}/M_{stars} > 10$ the dark matter models agree well with the results for the composite mass in §3.6.2. Smaller values of M_{DM}/M_{stars} render the models less constrained. In particular, the upper limit on ϵ_{DM} becomes indeterminate while the lower limit holds firm at about 0.31 (90% confidence). Employing the same criteria of goodness of fit used to constrain a in §3.6.2, we determine a lower limit $M_{DM}/M_{stars} > 3$ for these models having $a = 450''$; the results are not sensitive to large values of a. These values of M_{DM}/M_{stars} are consistent to those obtained using the gas temperature in §3.6.3.

We are unable to set a lower limit on a for the dark matter models because of the extra freedom given by the choice of M_{DM}/M_{stars}. However, for M_{DM}/M_{stars} as small as 2, the lower limit on a is essentially the same as that for the composite mass in §3.6.2 and the shapes are essentially the same as the $a = 450''$ case to within $\sim 10\%$. For smaller M_{DM}/M_{stars} the results are highly uncertain and are, to a large extent, much more sensitive to the precise form of the model for Φ_{stars} than the models with

larger M_{DM}/M_{stars} values.

In Figure 11 we plot the major-axis mass profiles of the stars, gas, and dark matter for a typical model having $M_{DM}/M_{stars} = 10$; the plot is normalized to the value of M_{stars} (§3.7.1). We also plot in Figure 11 the spatially variant Υ_B along the major axis where $\Upsilon_B(ma) = [M_{stars}(ma) + M_{DM}(ma)]/L_B(ma)$, $L_B(ma) = \Upsilon_B^{stars} M_{stars}(ma)$, and $\Upsilon_B^{stars} = 7\Upsilon_\odot$ as given in §3.7.1. At $\sim 10''$, the stellar and dark mass contribute equally. The dark matter rises faster than the stars and dominates the total mass exterior to R_e. This description is similar to what was found for NGC 720 by BC94.

3.8 Discussion

The geometric test for dark matter introduced by BC94 and clarified in this paper (§3.5.1) is the most robust means to test the hypothesis of mass tracing light for flattened, X-ray–bright, early-type galaxies. Optical methods suffer from uncertainty in the shape of the velocity dispersion tensor and thus generally test the mass-follows-light hypothesis by assuming the phase-space distribution function depends only on two integrals of motion (e.g, Binney et al. 1990; van der Marel 1991). Standard X-ray analyses are hindered by poorly determined temperature profiles of the gas (e.g., Fabbiano 1989). Even when the temperature profile could in principle be determined from high quality spatially resolved spectra, interpretation of the spectra in terms of a temperature profile is still uncertain due to questions about the reliability of standard spectral models (Trinchieri et al. 1994). The geometric test only requires knowledge of Σ_X and a few additional unrestrictive assumptions (see §3.5.1). Although ROSAT has accurate maps of Σ_X for only a few galaxies, many more should become available with the superior resolution of the Advanced X-ray Astrophysics Facility (AXAF).

It is important to emphasize that the detailed analysis of the mass distribution in §3.6 and §3.7 inherently depends to some extent on the models used. Only with detailed two-dimensional temperature and surface brightness maps can the potential be usefully determined without parametrizations for Φ and T_{gas}. To determine robustly whether the mass models of §3.6 and §3.7 are consistent with the X-ray data

independent of the poorly constrained temperature distribution, we could use the geometric test discussed in §3.5.1 by replacing Φ_L with the potential derived from the mass models. This approach has the disadvantage that only one model (set of parameters) may be tested at a time.

The relatively poor constraints on the ellipticity of the X-ray isophotes (§3.2.3) are primarily responsible for the large range of acceptable ϵ_{mass}. In Figure 12 (a) we plot ϵ_M as a function of aperture semi-major axis for six typical oblate isothermal models of the composite mass; also plotted are the 90% confidence intervals on ϵ_M computed from the PSPC data (§3.2.3). All of the models produce very similar ϵ_M for $a \lesssim 100''$ where the data is best determined. At larger radii, where the discrepancy between models is most pronounced, ϵ_M is poorly constrained. However, in Figure 12 (b) we plot the true expected isophotal ellipticity of the models; i.e. the ellipticity for a given isophote assuming a very narrow PSF. Now we see that the ϵ profiles are substantially different for the models. For example, the ϵ profile of the Hernquist SMD model falls more steeply than the other models, but adding rotation does flatten it out somewhat; the $n = 1$ SMD and logarithmic SP models have nearly identical profiles outside R_e, but inside the SMD profile increases while that of the SP remains constant. Moreover, the models with a discrete component have a bump in the profiles near R_e not seen in the other models. Hence, isophotal ellipticities computed to better than $\Delta\epsilon \sim 0.02$ over the range $10'' - 200''$ would serve as a powerful discriminator for the mass of the galaxy.

Although the shape of the dark halo in NGC 1332 is uncertain, i.e. ranging from $\epsilon_{mass} = 0.12 - 1$ considering all of the models (90% confidence), if rotation of the gas and emission from discrete sources are indeed negligible then the models suggest $\epsilon_{mass} \sim 0.5 - 0.6$. This degree of flattening for the dark halo is consistent with NGC 720 (BC94) and appears consistent with recent studies of the shapes of dark halos; see Sackett et al. 1994 for a discussion. The flattening is also consistent with results from N-body simulations of dissipationless collapse incorporating the effects of a small dissipational component (Katz & Gunn 1991; Dubinski 1994).

3.9 Conclusion

We have analyzed ROSAT PSPC X-ray data of the S0 galaxy NGC 1332 for the purpose of constraining the intrinsic shape of its underlying mass and presenting a detailed investigation of the uncertainties resulting from the assumptions underlying this type of analysis. Our treatment closely parallels that of BC94 who analyzed the shape of the elliptical galaxy NGC 720 using ROSAT PSPC data. NGC 1332 was selected because, along with NGC 720, it has among the largest known X-ray fluxes from *Einstein* (Fabbiano et. al. 1992) for an early-type galaxy that is elongated in the optical ($\epsilon \sim 0.43$), relatively isolated from other large galaxies, has an angular size ($\sim 7'$) substantially larger than the PSPC PSF, and is likely to be dominated by emission from hot gas (Kim et al. 1992).

The ellipticity of the surface brightness is computed by taking quadrupole moments of the X-ray surface brightness in elliptical apertures of different semi-major axis length. The isophote shapes are best constrained for semi-major axes $a = 75'' - 90''$ where $\epsilon_M = 0.10 - 0.27$ (90% confidence). The position angles of the X-ray isophotes for different a are consistent with each other and the optical value of 115° N-E within the estimated 95% uncertainties.

The spectrum is not well constrained by the PSPC data. A single-temperature plasma with Galactic column density fits the data well, but the temperature and metallicities are not well determined; e.g., $T_{gas} = 0.40 - 0.76$ keV and abundances $= 10\% - 107\%$ solar (90% confidence). Radial temperature gradients are not required by the PSPC spectrum, but large gradients $\left|\frac{d \ln T_{gas}}{d \ln R}\right| < 0.35$ (99% confidence) are consistent with the spectrum. Although simple models for emission from discrete sources in NGC 1332 can be ruled out as the sole source of the X-ray emission, the PSPC spectrum does not tightly constrain the relative flux of hot gas and discrete emission; generally as high as equal fluxes in the two components are allowed by the spectrum.

We clarified the geometric test for dark matter introduced by BC94. Besides a few unrestrictive assumptions, this test allows in principle a model-independent test

for whether mass follows light in the galaxy by making the fundamental assumption that the X-rays result from hot gas in hydrostatic equilibrium with the gravitational potential of the galaxy. By applying a version of this test suitable for the low spatial resolution and low S/N PSPC data for NGC 1332, we find that mass tracing the optical light is not consistent with the X-ray data at the 68% confidence level, but marginally consistent at the 90% level. We considered both the effects of possible rotation of the gas and emission from discrete sources. Following BC94 we assert that the same test may be directly applied to MOND with the same implications, although with weaker significance than NGC 720.

Explicitly solving the equation of hydrostatic equilibrium, we analyzed the shape and profile of the mass using the technique of BC94 (also Buote & Tsai 1995a) derived from the work of Binney & Strimple (1978; Strimple & Binney 1979). By employing a wide class of spheroidal models we constrained the ellipticity of the underlying mass to be $\epsilon_{mass} \sim 0.5-0.7(0.3-0.8)$ at 68% (90%) confidence assuming the rotation of the gas and emission from discrete sources are negligible; a model where the mass traces the optical light is easily ruled out for an isothermal gas, but polytropic models, though inconsistent at the 68% confidence level, are marginally consistent with the data at 90% confidence. Considering the possible effects of rotation of the gas like that of the stars and the effects of emission from discrete sources, the constraints on ϵ_{mass} are weakened considerably. For all the isothermal models considered, the 90% confidence estimate of the total mass out to $a = 450''$ is $M_{tot} = (0.38 - 1.7) \times 10^{12} M_{\odot}$ assuming $D = 20$ Mpc corresponding to blue mass-to-light ratio $\Upsilon_B = (31.9 - 143)\Upsilon_{\odot}$.

We estimated the observed stellar and X-ray mass profiles from their observed surface brightness distributions and then fit the dark matter directly. For models where $M_{DM}/M_{stars} > 10$, the dark matter has the same shape as for the above composite models. For smaller values of M_{DM}/M_{stars} the lower limit on ϵ_{mass} falls by 0.03 but the upper limit is indeterminate (90% confidence). We estimate a lower limit $M_{DM}/M_{stars} > 3$ (90% confidence) assuming the dark matter extends out to $a = 450''$; these results are not sensitive to $a \gtrsim 250''$.

In all, there is marginal evidence for a flattened halo ($\epsilon \approx 0.3-0.8$, 90% confidence)

of dark matter in NGC 1332 consistent with the elongated halo of NGC 720 ($\epsilon \approx 0.5-0.7$, 90% confidence) we found in BC94. The X-ray analysis of NGC 720 and NGC 1332 suggest that the dark matter halos in early-type galaxies are indeed substantially flattened (as also suggested by the analysis of the polar-ring galaxy NGC 4650A by Sackett et al. 1994) in agreement with the predictions of N-body /hydrodynamic simulations (e.g., Dubinski 1994).

We have demonstrated the need for obtaining higher quality spatial and spectral X-ray data to place rigorous constraints on the shape and amount of mass in early-type galaxies. Specifically, (1) the shapes of the X-ray isophotes from the center out to a few optical R_e, (2) the temperature profile of the gas, (3) the flux resulting from discrete sources in the galaxy, and (4) the rotation curve of the gas need to be measured accurately before a truly robust measurement of the shape of the underlying mass can be realized. Although there is no astrophysical instrument on the horizon that will be able to detect rotation of the gas in early-type galaxies, AXAF will greatly improve our understanding of issues (1) - (3).

We acknowledge useful discussions with Eric Gaidos. DAB thanks Eugene Magnier for tutelage in the fine art of optical observing and for providing the flat fields. We thank John Tonry for providing deep I-band surface photometry and a SBF distance for NGC 1332. We appreciate the help of the friendly people at hotseat@cfa.harvard.edu (especially Kathy Manning and Janet De Ponte) for answering questions about PROS and Gail Rohrbach at GSFC for her patient elucidation of the arcane lore of PROS/XSPEC file conversion. We acknowledge use of the SIMBAD data base and the ADS abstract service. Supported in part by grants NAS8-38249 and NASGW-2681 (through subcontract SVSV2-62002 from the Smithsonian Astrophysical Observatory).

Table 1: ROSAT Observation of NGC 1332

ROSAT Sequence Number	Date Observed	R.A., Decl.	Exposure Time (s)	Flux[c] (erg cm^{-2} s^{-1})
rp600006	Aug 13-14, 1991	$3^h26^m17^s, -21°20'09''$[a] $3^h26^m17^s, -21°19'57''$[b]	25,637s	$4.4(3.8) \times 10^{-13}$

[a]Optical center (J2000) from de Vaucouleurs et al. (1991).

[b]X-ray centroid (J2000) computed in this paper.

[c]Computed in 120″ radius circle for energy range 0.1 - 2.4 (0.4 - 2.4) keV.

Table 2: Identified Point Sources

Source #	R.A.	Decl.
1	$3^h26^m14^s$	$-21°21'10''$
2	$3^h26^m06^s$	$-21°20'03''$
3	$3^h26^m02^s$	$-21°17'14''$
4	$3^h26^m36^s$	$-21°17'58''$
5	$3^h26^m43^s$	$-21°15'19''$

Note. — These sources (expressed in J2000 coordinates) were identified and excluded from analysis by either symmetric substitution (§3.2) or masking (§3.4).

Table 3: Fits to the β Model

	Best Fit a_x (arcsec)	90% Range	Best Fit β	90% Range	χ^2_{min}	Degrees of Freedom	R (arcsec)
(1)	0.1	< 1.8	0.47	0.45 - 0.50	15.3	10	285
(2)	0.8	0.004 - 3.4	0.47	0.44 - 0.50	10.2	8	285

Note. — The results of fitting the X-ray radial profile (0.4 - 2.4 keV) to the β-model (§3.2.2) for the inner 15″ consisting of (1) three 5″ bins and (2) 1 bin.

Table 4: X-ray Ellipticities

a (asec)	ϵ_M	68%	90%	95%	99%	cts	ϵ_{iso}	$\Delta\epsilon_{iso}$
30	0.12	0.06 - 0.15	0.00 - 0.22	0.00 - 0.25	0.00 - 0.30	562	0.01	0.08
45	0.17	0.15 - 0.21	0.08 - 0.26	0.03 - 0.28	0.00 - 0.32	694	0.13	0.08
60	0.13	0.08 - 0.15	0.00 - 0.20	0.00 - 0.22	0.00 - 0.26	767	0.26	0.20
75	0.20	0.16 - 0.22	0.10 - 0.27	0.08 - 0.28	0.00 - 0.32	824	0.27	0.10
90	0.19	0.16 - 0.22	0.10 - 0.27	0.08 - 0.28	0.00 - 0.32	869	0.26	0.15
105	0.14	0.10 - 0.16	0.00 - 0.22	0.00 - 0.24	0.00 - 0.28	922		
120	0.13	0.08 - 0.15	0.00 - 0.22	0.00 - 0.24	0.00 - 0.28	953		
135	0.10	0.00 - 0.11	0.00 - 0.18	0.00 - 0.22	0.00 - 0.26	968		

Note. — The values of ϵ_M (and confidence limits) are computed within an aperture of semi-major axis a on the image having 5″ pixels (§3.2.3) with the background included; the counts, however, have the background subtracted. The results from isophote fitting, ϵ_{iso}, are computed on the image with 15″ pixels and the uncertainty, $\Delta\epsilon_{iso}$, reflects 68% confidence error estimates.

Table 5: X-ray Position Angles (N through E)

a (arcsec)	θ_M	68%	90%	95%	99%	θ_{iso}	$\Delta\theta_{iso}$
30	161	138 - 183	120 - 200	107 - 208	82 - 235	177	237
45	132	120 - 147	111 - 152	107 - 157	91 - 167	137	18
60	123	106 - 139	92 - 155	78 - 166	53 - 190	116	23
75	122	113 - 132	106 - 138	104 - 141	96 - 150	111	12
90	111	111 - 121	95 - 128	92 - 133	83 - 147	99	20
105	91	78 - 106	66 - 117	58 - 126	35 - 154		
120	106	88 - 124	68 - 140	52 - 156	28 - 187		
135	118	95 - 144	71 - 167	55 - 185	31 - 202		

Note. — Position angles are prepared in the same manner as the ellipticities in Table 4.

Table 6: *I*-Band Ellipticities and Position Angles

MDM 1.3m					Tonry		
a (arcsec)	ϵ	$\Delta\epsilon$	θ	$\Delta\theta$	a (arcsec)	ϵ	θ
2.0	0.134	0.012	105.6	2.8	12.9	0.354	116.6
2.4	0.164	0.010	109.6	1.9	15.5	0.393	116.6
2.9	0.195	0.007	111.1	1.2	18.7	0.437	116.5
3.5	0.216	0.006	112.8	0.9	22.2	0.487	116.5
4.3	0.230	0.004	114.1	0.6	26.3	0.582	115.8
5.2	0.240	0.005	114.7	0.7	30.9	0.621	115.3
6.3	0.253	0.005	114.9	0.6	36.0	0.617	115.3
7.6	0.274	0.005	115.8	0.7	41.8	0.646	115.0
9.2	0.296	0.007	116.1	0.8	48.2	0.668	114.9
11.1	0.320	0.007	116.2	0.8	55.4	0.679	114.7
13.4	0.350	0.009	116.5	0.9	63.3	0.683	114.7
16.2	0.390	0.013	116.5	1.1	72.1	0.681	114.6
19.7	0.432	0.016	116.3	1.4	81.7	0.673	114.6
23.8	0.478	0.024	116.4	1.9	92.3	0.659	114.5
28.8	0.529	0.027	115.6	2.0	103.8	0.640	114.3
34.8	0.577	0.026	115.3	1.9	116.4	0.615	114.1
42.2	0.626	0.029	114.8	1.9	130.1	0.580	113.4
51.0	0.654	0.019	115.0	1.2	145.1	0.545	112.9
61.7	0.682	0.018	114.7	1.1	161.2	0.505	111.6
74.7	0.688	0.026	114.8	1.6	178.7	0.473	110.1

Table 7: Spectral Data and Fit Results

Region	Model	χ^2_{min}	dof*	N_H (10^{20} cm^{-2})	Abundance (% solar)	T (keV)
0″- 120″	1T†	9.2	11	(0.083 – 4.7)	10 - 107	0.40 - 0.76
0″- 30″	1T	2.1	4	(0.13 – 6.0)	> 21	0.39 - 0.72
30″- 120″	1T	2.3	4	< 4.8	...	0.32 - 1.0
(A)	1T	2.6	4	< 4.8	> 44	0.36 - 0.77
(B)	1T	2.3	4	< 5.7	0.4 - 203	0.38 - 0.84
0″- 120″	(1)‡	34.0	12			
0″- 120″	(2)	27.6	12			
0″- 120″	(3)	66.7	12			

*Degrees of freedom

† Single-temperature Raymond-Smith model. 90% confidence estimates for parameters are shown for 0″- 120″, 68% confidence for the others.

‡Numbers correspond to (1) power law, (2) $T = 8$ keV Bremsstrahlung, and (3) $T = 8$ keV Raymond-Smith plasma models all with interstellar absorption

Table 8: Qualitative Predictions of Mass-Traces-Light

a (arcsec)	ϵ_Φ^{3d}	ϵ_Φ^{2d}	$\langle\epsilon_\Phi^{2d}\rangle_{PSPC}$	$\epsilon_{isothermal}$
30	0.17	0.15	0.13	0.09
45	0.15	0.13	0.12	0.11
60	0.13	0.12	0.10	0.11
75	0.12	0.11	0.09	0.11
90	0.11	0.10	0.09	0.10
105	0.10	0.10	0.08	0.09
120	0.09	0.09	0.07	0.08
135	0.09	0.08	0.07	0.08

Note. — Ellipticities for the oblate mass-traces-light model (see §3.5.2) of the three-dimensional isopotential surfaces (ϵ_Φ^{3d}), the contours of constant projected potential (ϵ_Φ^{2d}), ϵ_Φ^{2d} convolved with the PSPC PSF ($\langle\epsilon_\Phi^{2d}\rangle_{PSPC}$), and the predicted X-ray isophotes assuming an isothermal ideal gas (see §3.6.2).

Table 9: Geometric Test for Dark Matter - ϵ_M^{max} For Simple Case

a		Oblate ϵ_M^{max}		Prolate ϵ_M^{max}	
(arcsec)	ϵ_X	68%	90%	68%	90%
30	0.12	0.09	0.13	0.10	0.13
45	0.17	0.10	0.15	0.11	0.15
60	0.13	0.12	0.17	0.13	0.17
75	0.20	0.14	0.18	0.15	0.19
90	0.19	0.15	0.20	0.16	0.21
105	0.14	0.15	0.21	0.17	0.22
120	0.13	0.16	0.21	0.17	0.23
135	0.10	0.16	0.22	0.17	0.23

Note. — 68% and 90% confidence upper limits on ϵ_M are listed; i.e. ϵ_M^{680} and ϵ_M^{900} as described in §3.2.3. The geometric test assumes the X-rays are due to only hot gas in hydrostatic equilibrium with a potential generated by mass distributed like the optical light. In particular, rotation of the gas and emission from discrete sources are assumed negligible. The X-ray ellipticities (ϵ_X) from Table 4 are listed to facilitate comparison.

Table 10: Geometric Test for Dark Matter - ϵ_M^{max} With Other Considerations

a	Rotation		$F_{ds}/F_{hg} = 1/10$		$F_{ds}/F_{hg} = 1/3$		Rotation + Discrete	
(arcsec)	68%	90%	68%	90%	68%	90%	68%	90%
30	0.10	0.13	0.09	0.12	0.08	0.11	0.08	0.11
45	0.12	0.16	0.10	0.14	0.10	0.14	0.11	0.14
60	0.14	0.19	0.13	0.17	0.13	0.17	0.14	0.18
75	0.17	0.21	0.14	0.19	0.16	0.20	0.18	0.22
90	0.18	0.23	0.16	0.20	0.18	0.23	0.20	0.25
105	0.19	0.24	0.16	0.22	0.19	0.24	0.22	0.26
120	0.19	0.24	0.17	0.22	0.19	0.25	0.23	0.27
135	0.19	0.25	0.17	0.23	0.20	0.26	0.23	0.29

Note. — Upper limits correspond to values of ϵ_M obtained from the geometric test for dark matter as in Table 9 except here the effects of rotation like that of the stars (§3.5.2), emission from discrete sources (§3.5.2), and a combination of both (using $F_{ds}/F_{hg} = 1/3$) are considered.

Table 11: Results for the Shape of the Composite Mass

Mass Model	ϵ_{mass} 68%	ϵ_{mass} 90%	χ^2_{min}	R_c (arcsec)	$\lvert\Gamma\rvert$
Isothermal:					
SMD: $n = 1$, Oblate	0.51 - 0.69	0.34 - 0.80	7.5	2.0 - 5.4	6.51 - 7.45
SMD: $n = 1$, Prolate	0.48 - 0.63	0.32 - 0.71	8.0	2.2 - 7.0	6.02 - 7.24
SMD: $n = 1.5$, Oblate	0.58 - 0.83	0.37 - 0.94	18.0	11.4 - 24.2	5.44 - 5.68
SMD: $n = 1.5$, Prolate	0.52 - 0.70	0.36 - 0.76	18.5	12.4 - 27.3	5.28 - 5.62
SMD: Hernquist, Oblate	0.52 - 0.72	0.33 - 0.83	8.0	71.9 - 105.2	5.74 - 6.23
SMD: Hernquist, Prolate	0.47 - 0.63	0.31 - 0.71	8.5	57.2 - 128.9	5.54 - 6.17
SMD: $n = 1$, $i = 75°$, Oblate	0.57 - 0.75	0.40 - 0.85	7.5	1.7 - 5.0	6.83 - 7.83
SMD: $n = 1$, $i = 75°$, Prolate	0.49 - 0.64	0.33 - 0.72	8.0	1.9 - 6.5	6.38 - 7.67
SP: Logarithmic, Oblate	0.57 - 0.73	0.38 - 0.82	8.3	4.4 - 8.9	5.69 - 6.12
SP: Logarithmic, Prolate	0.57 - 0.73	0.38 - 0.82	8.8	4.5 - 9.5	5.44 - 6.05
SP: $n = 0.1$, Oblate	≥ 0.67	≥ 0.45	10.1	8.3 - 13.7	9.65 - 10.73
SP: $n = 0.1$, Prolate	≥ 0.67	≥ 0.45	10.5	8.4 - 14.3	9.30 - 10.69
Rotation	0.36 - 0.51	0.22 - 0.60	9.5	50.1 - 86.9	5.78 - 6.26
$F_{ds}/F_{hg} = 1/10$	0.49 - 0.69	0.31 - 0.80	7.8	2.4 - 6.7	6.36 - 7.27
$F_{ds}/F_{hg} = 1/5$	0.47 - 0.69	0.26 - 0.80	7.8	3.0 - 9.5	6.25 - 6.98
$F_{ds}/F_{hg} = 1/3$	0.41 - 0.68	0.21 - 0.80	8.0	4.4 - 19.4	5.95 - 6.58
$F_{ds}/F_{hg} = 1/2$	0.35 - 0.62	0.16 - 0.80	11.0	8.8 - 52.3	5.64 - 6.96
Rotation + Discrete	0.26 - 0.45	0.12 - 0.56	7.6	80.2 - 160.0	5.32 - 5.82
Polytropic:					
SMD: $n = 1$, Oblate	0.51 - 0.69	0.33 - 0.80	7.0	0.10 - 12.3	3.70 - 11.9
SMD: $n = 1$, Prolate	0.47 - 0.63	0.30 - 0.71	7.1	0.12 - 11.9	3.48 - 11.1
SMD: $n = 1.5$, Oblate	≥ 0.75	≥ 0.53	7.3	1.0 - 12.0	2.14 - 4.0
SMD: $n = 1.5$, Prolate	≥ 0.63	≥ 0.43	7.4	1.2 - 12.0	2.14 - 4.0

Note. — This is a list of selected models for the composite mass. The listed rotation and discrete models are oblate. χ^2_{min} is the typical value in the 90% confidence interval (8 dof for isothermal models, 7 dof for polytropes). Similarly, R_c and Γ correspond to the 90% confidence limits. For models where only a lower limit for ϵ_{mass} is indicated, the ranges for R_c and Γ are estimates.

Table 12: Composite Mass and Mass-to-Light Ratio

	$M(h_{80}10^{12}M_\odot)$		$\Upsilon_B(h_{80}^{-1}\Upsilon_\odot)$	
Mass Model	68%	90%	68%	90%
Isothermal:				
SMD: $n = 1$, $a = 450''$, Oblate	0.62 - 1.48	0.56 - 1.64	32.4 - 77.5	29.3 - 85.8
SMD: $n = 1$, $a = 450''$, Prolate	0.45 - 1.18	0.38 - 1.44	23.6 - 61.8	19.9 - 75.4
SMD: $n = 1$, $a = min$, Oblate	0.22 - 0.45	0.21 - 0.46	11.5 - 23.6	11.0 - 24.1
SMD: $n = 1$, $a = min$, Prolate	0.17 - 0.41	0.15 - 0.43	8.9 - 21.5	7.9 - 22.5
SMD: Hernquist, $a = 450''$, Oblate	0.32 - 0.78	0.31 - 0.82	16.7 - 40.8	16.2 - 42.9
SMD: Hernquist, $a = 450''$, Prolate	0.27 - 0.59	0.25 - 0.77	14.1 - 30.9	13.1 - 40.3
SP: Logarithmic, $r = 450''$, Oblate	0.78 - 1.71	0.75 - 1.75	40.8 - 89.5	39.2 - 91.6
SP: Logarithmic, $r = 450''$, Prolate	0.76 - 1.68	0.73 - 1.73	39.8 - 87.9	38.2 - 90.6
(Hernquist) $F_{ds}/F_{hg} = 1/3$	0.44 - 1.04	0.41 - 1.12	23.0 - 54.4	21.5 - 58.6
Rotation	0.31 - 0.78	0.29 - 0.83	16.2 - 40.8	15.2 - 43.4
Rotation + Discrete	0.43 - 1.06	0.39 - 1.15	22.5 - 55.5	20.4 - 60.2
Polytropic:				
SMD: $n = 1$, $a = 450''$, Oblate	0.28 - 2.84	0.19 - 3.18	14.6 - 148.6	9.9 - 166.4

Note. — Total integrated masses for selected models. For the SP models the mass is within a sphere of radius r. In all cases the 90% confidence limits on the temperature are used (see Table 7)

Table 13: Total Integrated X-ray Gas Mass

M_{gas}	$\bar{n}$	$\bar{\tau}$
$(10^9 h_{80}^{5/2} M_\odot)$	$(10^{-3} h_{80}^{-1/2} \mathrm{cm}^{-3})$	$(10^{10} h_{80}^{1/2} \mathrm{yr})$
0.69 - 1.81	2.70 - 7.11	0.90 - 1.25

Note. — Quantities represent 90% confidence limits within a sphere of radius 300″ using the results for a single-temperature fit to the PSPC spectrum (Table 7).

Table 14: Dark Matter Shape Results

M_{DM}/M_{stars}	ϵ_{DM}	χ^2_{min}	R_c (arcsec)	$\|\Gamma\|$
50	0.34 - 0.80	8.7	2.2 - 6.1	6.46 - 7.32
25	0.34 - 0.80	8.8	2.5 - 7.0	6.39 - 7.23
10	0.31 - 0.88	9.1	3.5 - 12.4	6.21 - 7.11
5	$\geq$ 0.31	9.2	7.7 - 76.5	6.10 - 7.11
4	$\geq$ 0.31	10.5	8.9 - 61.9	6.00 - 6.75
3	$\geq$ 0.35	17.3	9.2 - 55.2	5.90 - 6.37

Note. — 90% confidence limits on ϵ_{DM}, R_c, and Γ as a function of M_{DM}/M_{stars} for the dark matter modeled as an oblate isothermal SMD with $n = 1$ and $a = 450''$. χ^2_{min} (8 dof) represents the typical minimum χ^2 in the 90% interval. For the models having only a lower limit for ϵ_{DM} the 90% values for R_c and Γ are estimates.

REFERENCES

Aschenbach, B. 1988, Appl.Optics, 27, No. 8, 1404

Ashman, K. M. 1992, PASP, 104, 1119

Awaki et al. 1994, PASJ, 46, L65

Bacon, R. 1985, A&A, 143, 84

Binney, J. J. 1981, MNRAS, 196, 455

Binney, J., & Strimple O. 1978, MNRAS, 187, 473

Binney, J., & Tremaine, S. 1987, Galactic Dynamics (Princeton: Princeton Univ. Press)

Buote, D. A., & Canizares, C. R. 1992, ApJ, 400, 385

Buote, D. A., & Canizares, C. R. 1994, ApJ, 427, 86 (BC94)

Buote, D. A., & Tsai, J. C. 1995a, ApJ, 439, 29

Buote, D. A., & Tsai, J. C. 1995b, ApJ, in press

Canizares, C. R., Fabbiano, G., & Trinchieri, G. 1987, ApJ, 312, 503

Carter, D., & Metcalfe, N. 1980, MNRAS, 191, 325

Cavaliere, A., & Fusco-Femiano, R. 1976, A&A, 49, 137

Chandrasekhar, S. 1969, Ellipsoidal Figures of Equilibrium (New Haven: Yale Univ. Press)

de Zeeuw, T., & Franx, M. 1991, ARA&A, 29, 239

Dalle Ore, Christina, Faber, S. M., Jesús, J., & Stoughton, R. 1991, ApJ, 366, 38

de Vaucouleurs, G., de Vaucouleurs, A., Corwin, H. G., Buta, R. J., Paturel, G., & Fouqué, P. 1991, Third Reference Catalogue of Bright Galaxies, Univ. of Texas Press, Austin

Donnelly, R. H., Faber, S. M., & O'Connell, R. M. 1990, ApJ, 354, 52

Dubinski, J., & Carlberg, R. 1991, ApJ, 378, 496

Dubinski, J. 1994, ApJ, 431, 617

Dressler, A., & Sandage, A. 1983, ApJ, 265, 664

Efstathiou, G., Frenk, C. S., White, S. D. M., & Davis, M. 1988, MNRAS, 235, 715

Evans, N. W. 1994, MNRAS, 267, 333

Fabbiano, G. 1989, ARA&A, 27, 87

Fabbiano, G, Kim, D.-W., & Trinchieri, G. 1992, ApJS, 80, 531

Fabricant, D., Rybicki, F., & Gorenstein, P. 1984, ApJ, 286, 186

Forman, W., Jones, C., & Tucker, W. 1985, ApJ, 293, 102

Franx, M. 1993, in Galactic Bulges (IAU Symp. 153), ed. H. Dejonghe and H. Habing (Dordrecht: Reidel), in press

Frenk, C. S., White, S. D. M., Efstathiou, G., & Davis, M. 1988, ApJ, 327, 507

Haimen, Z., et al. 1994, A&A, 286, 725

Hasinger, G., Turner, T. J., George, I. M., & Boese, G., 1993, MPE/OGIP Calibration Memo CAL/ROS/93-015

Hernquist, L. 1990, ApJ, 356, 359

Jedrzejewski, R. 1987, MNRAS, 226, 747

Kaiser, N., & Squiers, G. 1993, ApJ, 404, 441

Katz, N., & Gunn, J. E. 1991, ApJ, 377, 365

Kent, S. M. 1990, in Evolution of the Universe of Galaxies (ASP conf. vol. 10), ed. R. G. Kron (Provo: Brigham Young Univ. Print Serv.), 109

Kim, D.-W., Fabbiano, G, & Trinchieri, G. 1992, ApJS, 80, 645

Kley, W., & Mathews, W. G. 1995, 438, 100

Kuijken, K., & Dubinski, J. 1994, preprint

Mathews, W. G. 1990, ApJ, 354, 468

Palmer, P. L. 1994, MNRAS, 266, 697

Peletier, R. F. 1989, Ph.D. Thesis, University of Groningen

Pickles, A. J. 1985, ApJ, 296, 340

Pfeffermann, E. et al., 1987, Proc. SPIE, 733, 519

Raymond, J. C., & Smith, B. W. 1977, ApJS, 35, 419

Ryden, B. S. 1990, MNRAS, 244, 341

Sackett, P., Rix, H-W, Jarvis, B. J., & Freeman, K. C. 1994 ApJ, 436, 629

Saglia, R. P., et al. 1993, ApJ, 403, 567

Sanders, R. H. 1990, A&ARev., 2, 1

Sarazin, C. L. 1986, Rev. Mod. Phys., 58, 1

Schechter, P. L. 1987, in Structure and Dynamics of Elliptical Galaxies (IAU Symp. 127), ed. T. de Zeeuw (Dordrecht: Reidel), 217

Silk, J., & Wyse, R. F. G. 1993, Phys. Reports, in press

Snowden, S. L., Plucinsky, P. P., Briel, U., Hasinger, G., & Pfeffermann, E. 1992, ApJ, 393, 819

Stark, A. A., et al. 1992, ApJS, 79, 77

Statler, T. S. 1993, ApJ, 425, 458

Strimple, O., & Binney, J. 1978, MNRAS, 188, 883

Tanaka, Y., Inoue, H., & Holt, S. S. 1994, PASJ, 46, L37

Thomas, P., Fabian, A. C., & Nulsen, P. E. J. 1987, MNRAS, 228, 973

Tonry, J. L., Ajhar, E. A., & Luppino, G. A. 1990, AJ, 100, 1416

Trinchieri, G., Fabbiano, G., & Canizares, C., 1986, ApJ, 310, 637

Trinchieri, G., Kim, D.-W., Fabbiano, G., & Canizares, C., 1994, ApJ, 428, 555

Trümper, J. 1983, Adv. Space Res., 2, 241

Tsai, J. C. 1994, ApJ, 429, 119

White, J. 1987, B.S. Thesis, Massachusetts Institute of Technology

White, J., & Canizares, C. 1987, BAAS, 19, 682

van der Marel, R. P. 1991, MNRAS, 253, 710

Willmer, C. N. A., Focardi, P., Nicolaci Da Costa, L., & Pellegrini, P. S. 1989, AJ, 98, 1531

Fig. 1.—
(a) Contour map of the X-ray surface brightness (0.4 - 2.4 keV) of the Lenticular galaxy NGC 1332 binned into 15″ pixels; the contours are separated by a factor of 2 in intensity and the direction of Celestial North and East are indicated in the plot. The image has been corrected for the effects of exposure variations and telescopic vignetting. The image has been smoothed for visual clarity with a Gaussian of $\sigma = 15.0''$, although the image used for analysis is not smoothed in any manner. (b) Same as Figure (a) except the point sources listed in Table 2 have been removed by symmetric substitution (§3.2)

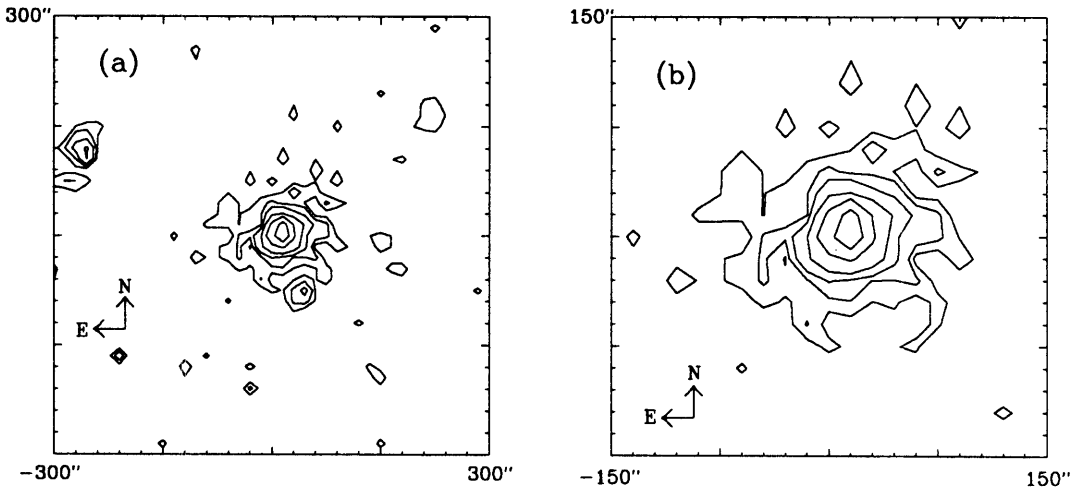

Fig. 2.—
Radial profile (30″ bins) corrected for the exposure variations, vignetting, and embedded point sources. The horizontal line is our estimate of the background level.

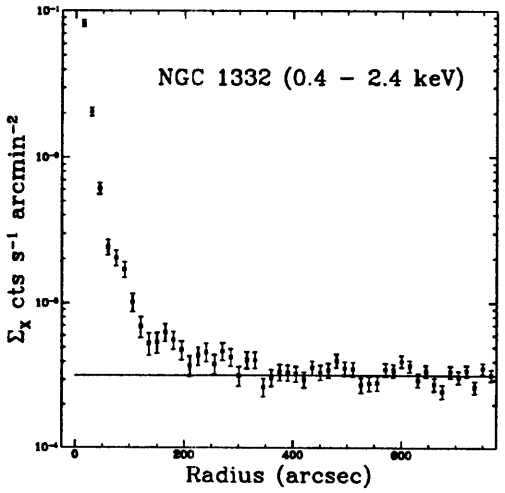

Fig. 3.—
The PSPC background-subtracted radial profile binned in 5″ circular bins from 0″ – 15″, 15″ bins from 15″ – 105″, then 45″ bins to 285″. The midpoint of each bin is use to define its location in the plot. Also shown are representations of the PSPC PSF for (1) $E = 0.818$ keV and $\theta = 7.25'$ (dashed), (2) $E = 1.1$ keV and $\theta = 7.25'$ (dotted), and (3) $E = 1.1$ keV and $\theta = 5'$ (solid).

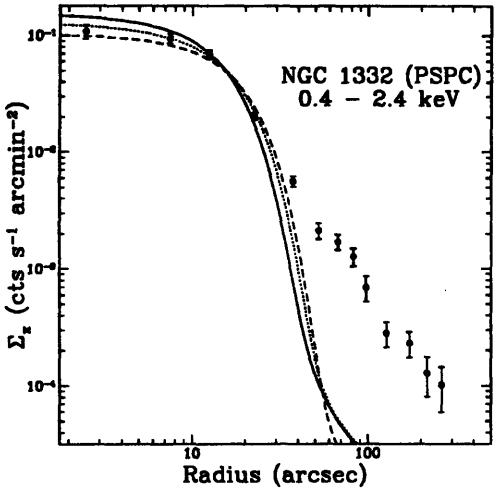

Fig. 4.—
(a) The best-fit β-model (crosses) and the 90% confidence limits on a_X and β fit to the radial profile as in Figure 3. (b) Same as (a) except the inner 15″ has been grouped into one bin.

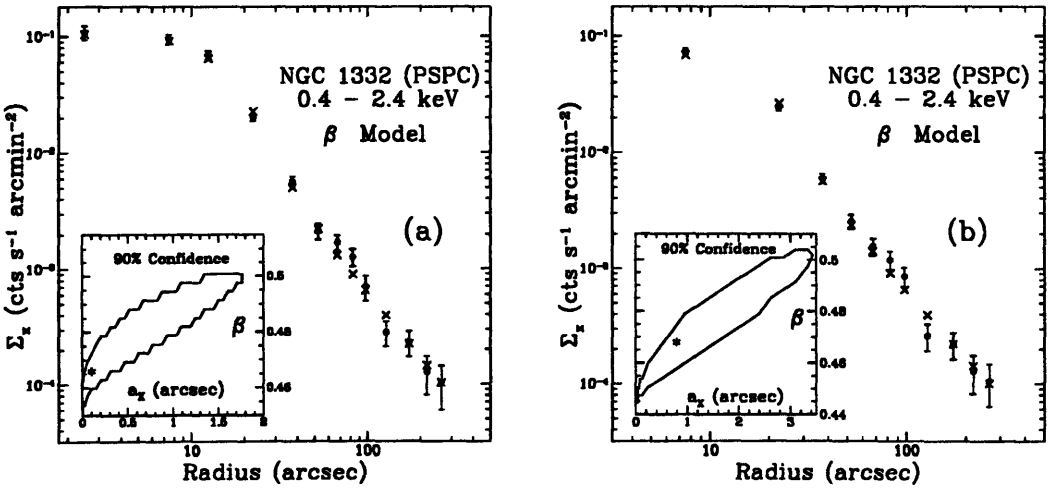

Fig. 5.—
(a) The major-axis I-band profile of the combined MDM 1.3m and Tonry data. The solid line is the best-fit De Vaucouleurs Bulge + Exponential Disk model while the dotted line is the result of fitting a single De Vaucouleurs model. (b) The best-fit De Vaucouleurs Bulge + Exponential Disk model (crosses) of the I-band major-axis profile convolved with the PSPC PSF and fitted to the PSPC radial profile prepared as in Figure 3.

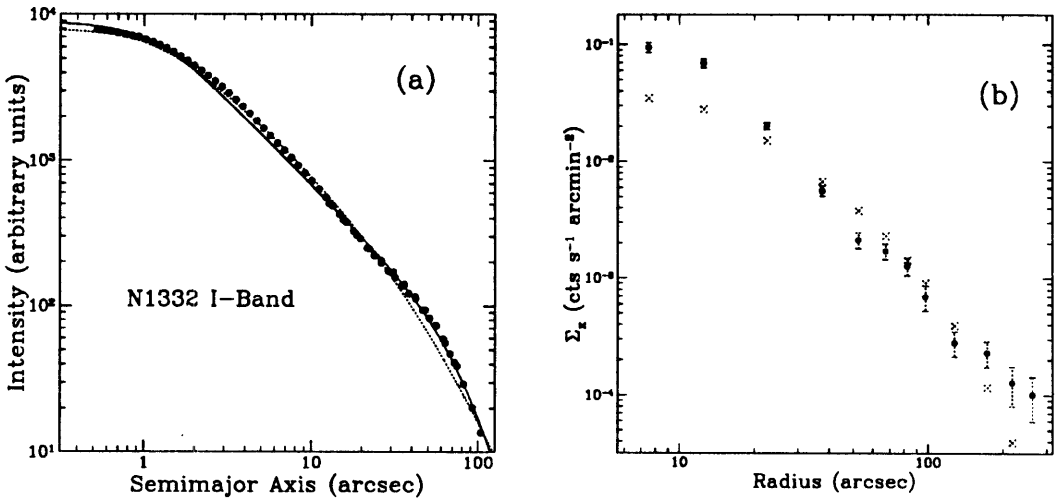

Fig. 6.—
68% and 90% confidence contours for (a) Hydrogen column density vs. T and (b) abundances vs. T deduced from fitting a single-temperature Raymond-Smith plasma to the PSPC spectrum ($0'' - 120''$).

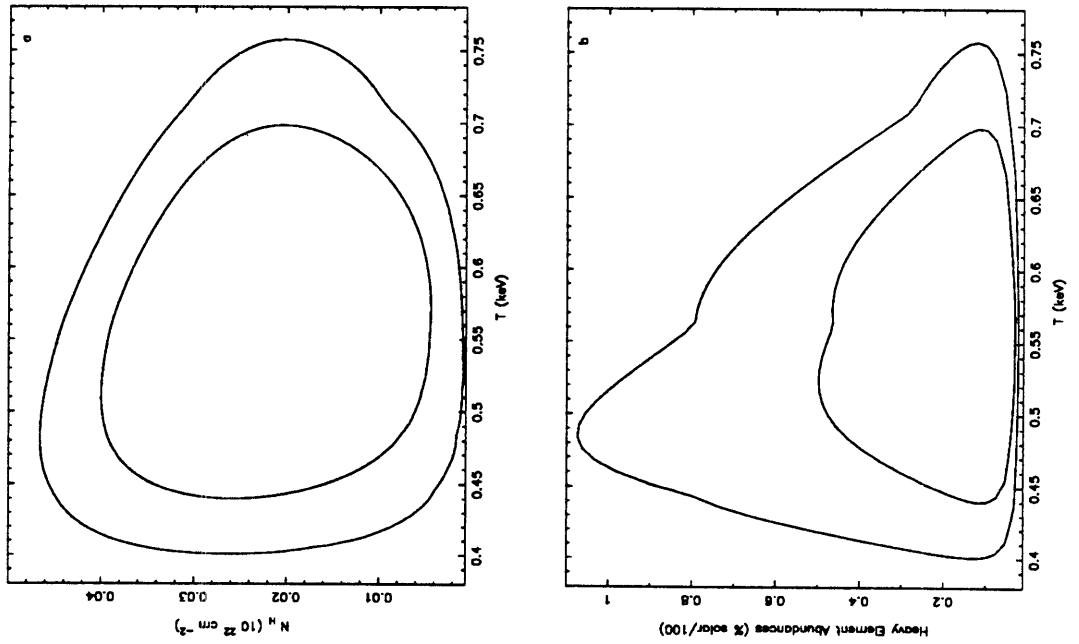

Fig. 7.—
The dotted lines are the mean values of ϵ_M (plotted as perfect ellipses) for the X-ray surface brightness predicted from the geometric test for dark matter (i.e. mass follows light) assuming oblate symmetry; i.e. mean values of 1000 simulations. The solid lines are the observed ϵ_M (§3.2.3) for $a = 75'' - 90''$.

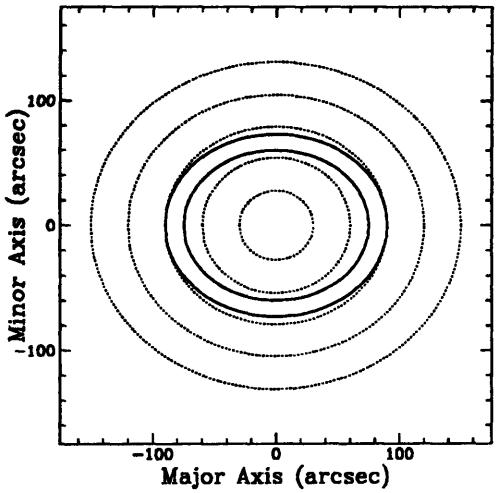

Fig. 8.—
(a) Radial profile of a typical isothermal SMD model (filled circles) consistent with the PSPC data (error bars). The model displayed is an oblate Hernquist SMD with $a = 450''$ and $\epsilon_{mass} = 0.60$. The best-fit parameters are $R_c = 72.8''$, $\Gamma = 5.95$, and $\chi^2_{min} = 10.0$. The 90% confidence contour and the best-fit parameter values are displayed in the inset. (b) X-ray isophotes for the best-fit model separated by a factor of 2 in intensity.

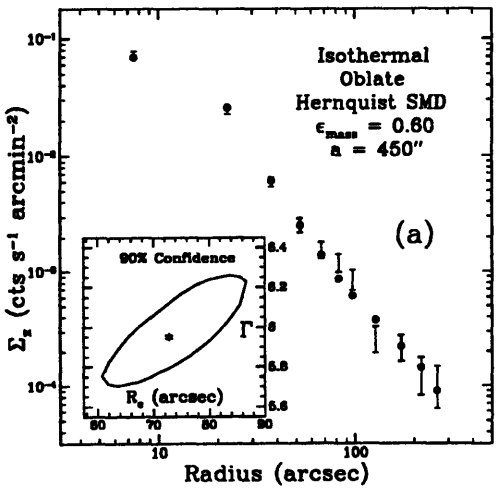

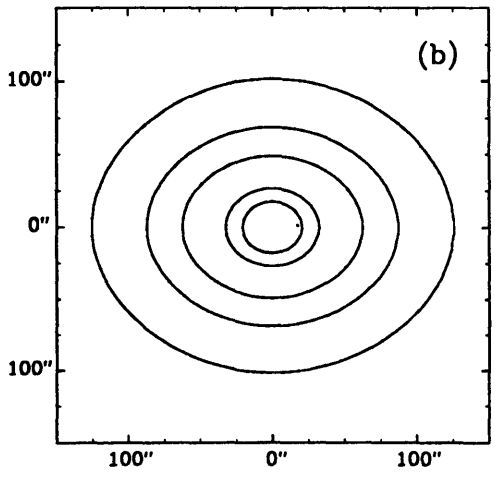

Fig. 9.—
(a) Radial profile of a typical isothermal SP model (filled circles) consistent with the PSPC data (error bars). The model displayed is an oblate Logarithmic SMD with $\epsilon_\Phi = 0.25$ which corresponds to $\epsilon_{mass} = 0.63$ using the aggregate shape determination explained in §3.6.2. The best-fit parameters are $R_c = 6.4''$, $\Gamma = 5.92$, and $\chi^2_{min} = 9.3$. The 90% confidence contour and the best-fit parameter values are displayed in the inset. (b) X-ray isophotes for the best-fit model separated by a factor of 2 in intensity.

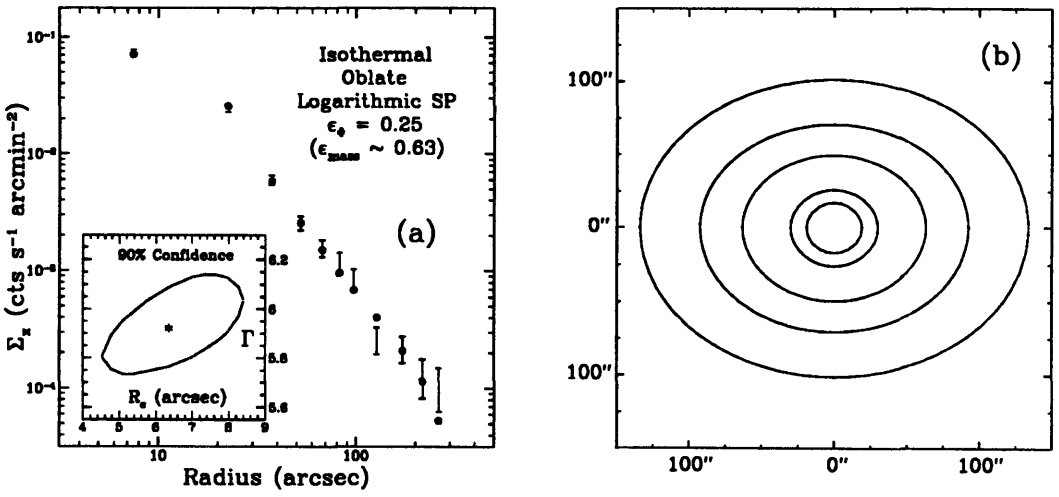

Fig. 10.—
(a) Upper and lower solid (dashed) curves show 90% confidence limits of the integrated mass as a function of elliptical radius (am) for the isothermal SMD Hernquist model having $\epsilon_{mass} = 0.60$ and $a = 450''$. (b) same as (a) except $n = 1$ SMD model. (c) same as (a) except shown are the spherically averaged mass profiles of the isothermal logarithmic SP model with $\epsilon_\Phi = 0.25$ corresponding approximately to $\epsilon_{mass} = 0.63$.

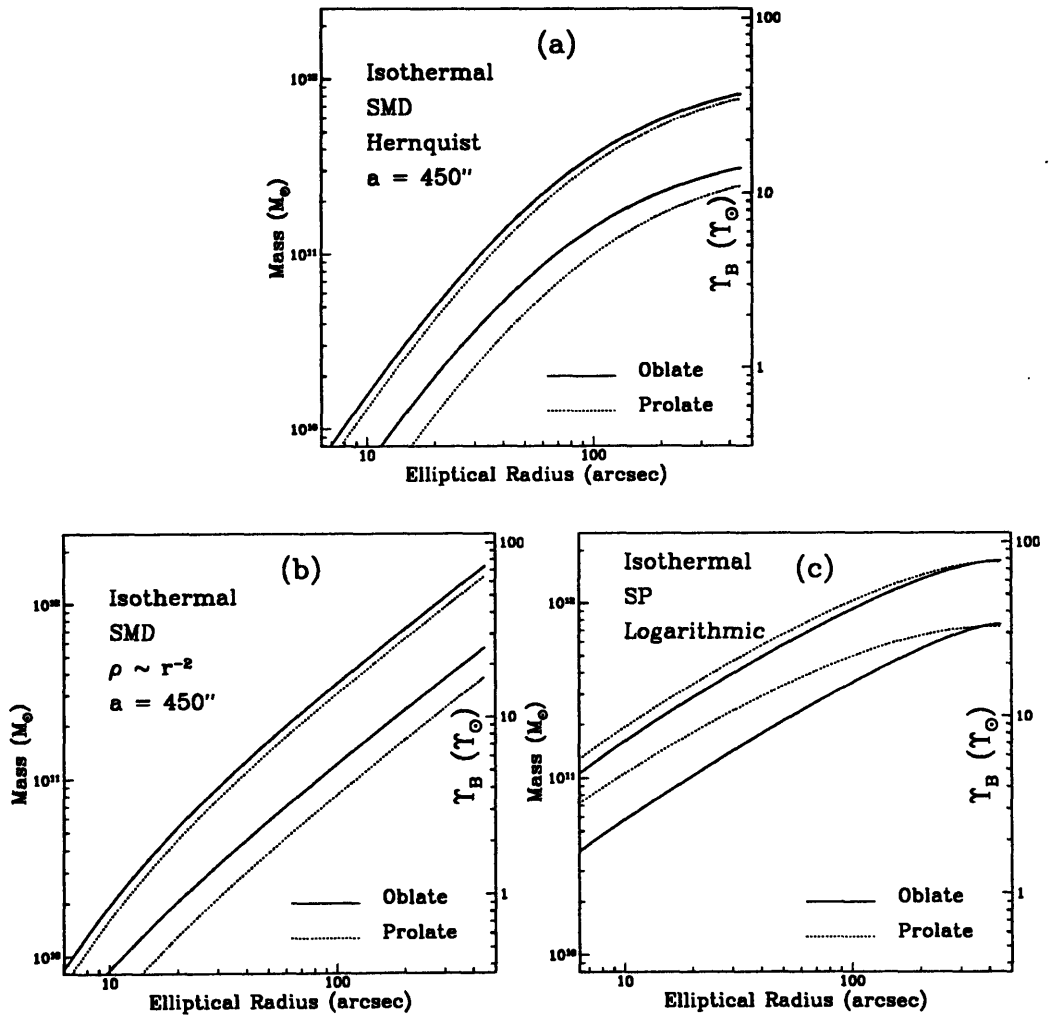

Fig. 11.—
(a) Integrated mass as a function of elliptical radius (am) for the dark matter, stars, and gas. The dark matter is an $n = 1$ SMD, with $a = 450''$, $\epsilon_{mass} = 0.60$, and $M_{DM}/M_{stars} = 10$. Interior to $R_e \sim 50''$ (which is the radius enclosing half the light) M_{DM} is comparable to M_{stars}. At larger radii, however, the dark matter dominates. The self-gravitation of the gas is not important anywhere in the galaxy. (b) Here we show the total mass for this model and the corresponding Υ_B as a function of ellipsoidal radius. Υ_B slowly rises interior to R_e but increases dramatically at larger radii.

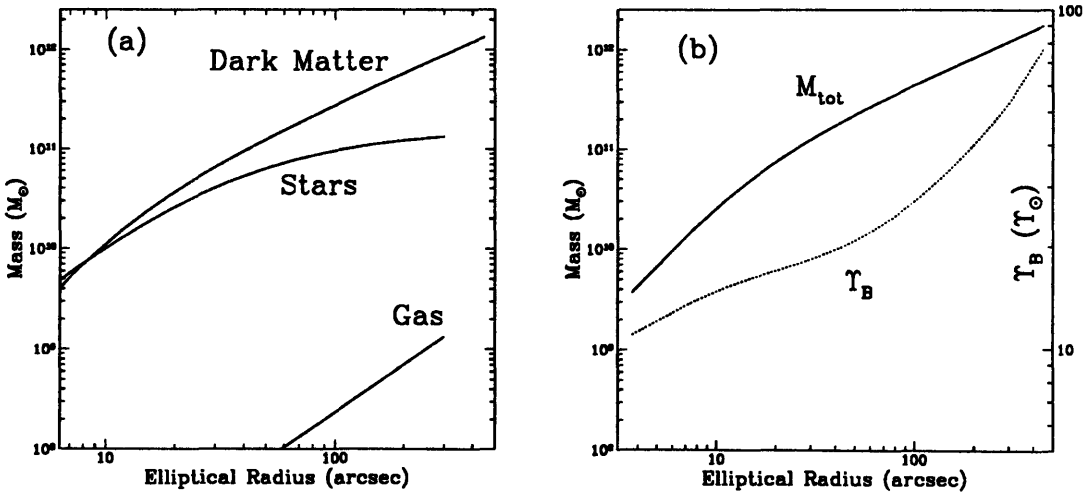

Fig. 12.—
(a) Shown are the 90% confidence limits on ϵ_M computed from the PSPC image (error bars; see Table 4) and the ϵ_M profiles computed from surface brightnesses of typical detailed isothermal models of the composite mass in §3.6.2. The mass models (all oblate) are (solid) $n = 1$ SMD with $\epsilon_{mass} = 0.60$ and $a = 450''$, (short dash - long dash) Hernquist SMD with $\epsilon_{mass} = 0.60$ and $a = 450''$, (dotted) Logarithmic SP with $\epsilon_\Phi = 0.25$ ($\epsilon_{mass} \sim 0.63$), (short dash) Hernquist SMD rotation model with $\epsilon_{mass} = 0.40$ and $a = 450''$, (long dash) $n = 1$ SMD with $\epsilon_{mass} = 0.60$ and $a = 450''$ and discrete compoent with $F_{ds}/F_{hg} = 1/3$, and (dot - short dash) Hernquist rotation model with $\epsilon_{mass} = 0.35$ and $a = 450''$ + discrete compoent with $F_{ds}/F_{hg} = 1/3$. (b) We show the true *isophotal* ellipticities of the X-ray surface brightness produced by the models of (a); by "true" we mean no PSF convolution; by "isophotal" we mean the ellipticity of an individual isophote, not of a large elliptical aperture.

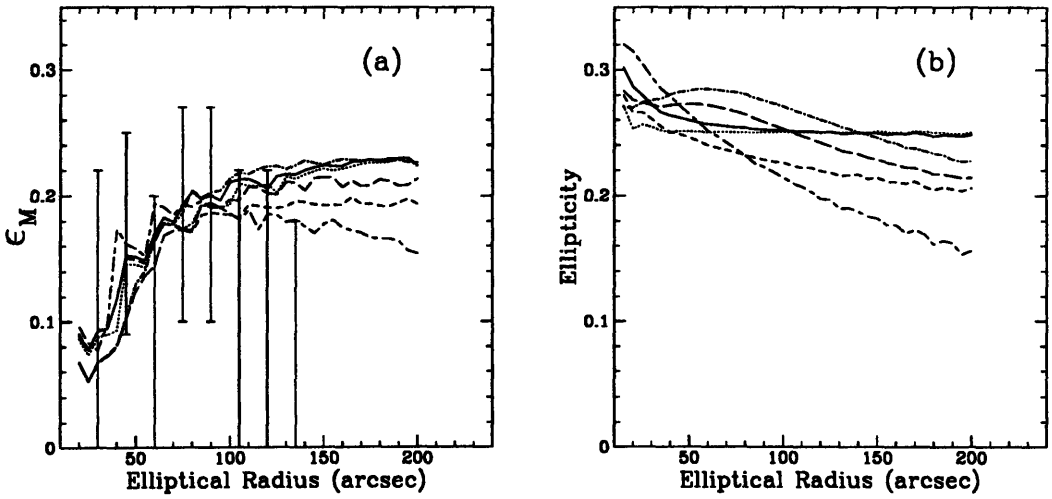

Chapter 4

The Reliability of X-ray Constraints of Intrinsic Cluster Shapes[1]

We now consider X-ray analysis of the intrinsic shapes of galaxy clusters. Unlike elliptical galaxies, there is increasing evidence that many or most clusters have substructure (e.g., West 1995) which suggests that the assumption of hydrostatic equilibrium is not generally valid in these systems. Using the simulation of Katz & White (1993) we have tested the viability of X-ray analysis for constraining the intrinsic shapes of clusters of galaxies considering the effects of both substructure and steep temperature gradients. We restrict our analysis to the aggregate shapes of clusters on scales of $r \sim 1 - 2$ Mpc in order to reduce our sensitivity to subclustering in the core. For low redshifts ($z \lesssim 0.25$) the X-ray method accurately measures the true ellipticity of the three-dimensional cluster dark matter provided the inclination of the cluster is known to within $\sim 30°$; assuming the gas is isothermal adds only small errors to the derived shapes. At higher redshifts the X-ray method yields unreliable results since the gas does not trace the cluster gravitational potential. We proffer some necessary conditions for the reliability of X-ray methods characterized by both

[1]The majority of this Chapter has been published as Buote & Tsai 1995, ApJ, 439, 29.

the amount of substructure in the X-ray surface brightness images and the shapes of the isophotes. We conclude that measurements of the aggregate shapes of clusters on scales $r \sim 1 - 2$ Mpc are insensitive to core substructure representing scales of a few hundred kpc. Therefore our results suggest that the X-ray measurements of aggregate cluster shapes by Fabricant, Rybicki, & Gorenstein (1984) and Buote & Canizares (1992) are valid provided that they do not suffer from serious projection effects. A substantial number of Abell clusters observed with the ROSAT PSPC will be amenable to X-ray shape analysis.

4.1 Introduction

The intrinsic shapes of galaxy clusters provide valuable information regarding the cosmological framework in which they were formed (e.g., Eisenstein & Loeb 1994). For example, "Pancake" theories (e.g., Sunyaev & Zeldovich 1972) for structure formation predict mostly oblate clusters while predominantly prolate structures result from theories invoking early tidal distortions (e.g., Binney & Silk 1979). The distribution of intrinsic cluster shapes also probes the nature of the dark matter itself. If, for example, the dark matter in clusters is generally rounder than the galaxy distribution then the dark matter must be dissipational to some extent (e.g., Strimple & Binney 1979; Aarseth & Binney 1978).

As first described in the pioneering papers by Binney & Strimple (1978; Strimple & Binney 1979) X-ray images of clusters provide a powerful probe of their intrinsic shapes. The shape of the three-dimensional cluster mass may be determined from a cluster X-ray image if the X-ray emitting gas is in hydrostatic equilibrium and an assumption is made regarding the cluster mass distribution along the line of sight. Note that these assumptions are not necessary for mapping the projected cluster mass with gravitational lens techniques that use the distorted images of background galaxies (Tyson, Valdes, & Wenk 1990; Kaiser 1992; Kaiser & Squires 1993; Fahlman et al. 1994; Smail et al. 1994). Because of the required source-lens-observer separations, however, these gravitational lens methods are generally restricted to high-redshift

clusters ($0.15 \lesssim z \lesssim 0.6$). In contrast, X-ray methods in principle can be applied at any redshift.

The increasing evidence for substructure in clusters of galaxies suggests that many clusters are young and thus not dynamically relaxed (see Jones & Forman 1992; Bird 1993; West 1994). As a result, the reliability of methods that infer the intrinsic structure of clusters by assuming hydrostatic equilibrium of their X-ray emitting gas has been called into question (for a review see Fitchett 1989; also see Mohr, Fabricant, & Geller 1993). The particular case of A2256 dramatizes this uncertainty.

Fabricant, Rybicki, & Gorenstein (1984) and Fabricant, Kent, & Kurtz (1989) analyzed optical and *Einstein* X-ray data of A2256. Although they could not find any evidence for substructure in their data, they concluded that the observed elongation of the X-ray isophotes was consistent with the mass of Abell 2256 being either a single flattened spheroid ($\epsilon \sim 0.4$) or the superposition along the line of sight of two spherical masses separated by a few hundred kpc in the plane of the sky. The ROSAT image of A2256 (Briel et al. 1991) confirmed the latter assertion of substructure; Buote (1992) and Davis & Mushotzky (1993) re-analyzed the *Einstein* image and located the same substructure.

Does the subclustering on scales of a few hundred kpc invalidate the characterization of the shape of A2256 by a single flattened spheroid? If one is interested in measuring the aggregate shape of the cluster on scales of $1-2$ Mpc from the cluster center, and the shape is quantified by the quadrupole moment of the mass on those scales (or equivalently the principal moments of inertia), then subclustering on scales of a few hundred kpc represents higher order moments which should be unimportant with respect to the quadrupole term in the cluster potential. Hence, the aggregate cluster shape on scales of $1-2$ Mpc should be insensitive to small-scale subclustering.

Another limitation of using X-ray images to determine cluster shapes has been the lack of spatially resolved temperature profiles (e.g., Fitchett 1989). The predicted radial mass distribution depends strongly on the temperature gradient. However, Strimple & Binney (1979) and others (see §4.4.1) have argued that conclusions about the shapes of clusters are not overly sensitive to temperature gradients.

Buote & Canizares (1992; hereafter BC92) analyzed the *Einstein* images of five low-redshift Abell clusters having no obvious subclustering (with the possible exception of Coma) in order to measure the aggregate shapes of the underlying mass on a scale $r \sim 1$ Mpc. They demonstrated that for all the clusters the shapes of the X-ray isophotes ($\epsilon_x \sim 0.15$) were rounder than the inferred dark matter distributions ($\epsilon_{DM} \sim 0.30$) which were rounder than the galaxy isopleths ($\epsilon_{gal} \sim 0.50$). In their analysis BC92 assumed hydrostatic equilibrium and isothermality for the X-ray emitting gas and that subclustering was dynamically unimportant for measuring the aggregate cluster shapes. It is our purpose to ascertain whether these assumptions are indeed justified.

Katz & White (1993; hereafter KW) modeled the formation and evolution of a Virgo-sized cluster ($M \sim 2 \times 10^{14} M_{\odot}$) in a standard flat, biased Cold Dark Matter universe ($\Omega = 1$, $H_0 = 50$ km s^{-1} Mpc^{-1}, b=2.6, $M_{DM}/M_{bary} = 10$). They modeled the dissipational gas component with smoothed particle hydrodynamics (Hernquist & Katz 1989) allowing for cooling via radiative and compton processes; gravitational effects were modeled using the hierarchical tree method. Hence, KW constructed an X-ray cluster that formed and evolved in the context of large-scale structure and thus serves as a laboratory for testing X-ray methods for determining intrinsic cluster shapes. Using the KW cluster in its final time step Tsai, Katz, & Bertschinger (1994; hereafter TKB) tested the accuracy of spherically-symmetric X-ray analysis of the radial mass distribution. They concluded that the mass inferred from the X-rays matched the true mass of the simulation to within $\sim 25\%$ when the true temperature profile was used.

We will address how reliably the aggregate shape of the KW cluster on scales $r \sim 1 - 2$ Mpc can be determined from X-ray analysis as a function of redshift, and thereby assess the validity of the assumptions made by BC92. In §4.2 we discuss the surface brightness of the cluster; in §4.3 we discuss the intrinsic properties of the cluster obtained directly from the KW simulation; in §4.4 we discuss the X-ray modeling procedure and its results; in §4.5 we discuss the implications and in §4.6 we present our conclusions.

4.2 Analysis of the X-ray Surface Brightness

We created X-ray images by folding two-dimensional projections of the simulated cluster of KW through the instrument parameters of the *Einstein* Imaging Proportional Counter (IPC) (Giacconi et. al. 1979) to facilitate comparison to previous X-ray determinations of the shapes of the mass distributions in clusters of galaxies (Fabricant et al. 1984; Buote 1992; BC92). Specifically, the point spread function (PSF) and the energy response matrices of the IPC were applied to the X-rays from the KW simulation (see TKB). Although the IPC has only $\sim 1/3$ the spatial resolution of the ROSAT Positional Sensitive Proportional Counter (PSPC) and significantly less energy resolution, analysis of IPC-convolved cluster images is of equal importance to future studies of PSPC cluster images because (1) the cluster emission important for analysis extends over $50'$ in diameter which renders the differences in the PSF's of the two instruments insignificant for analysis of the large-scale structure of the image, and (2) the spectrum of the image is not used for analysis of the shapes (although use of the exact temperature profile derived from the KW simulations by TKB will be employed for comparison to the temperature-blind analysis). Note that the IPC is also sensitive to energies (0.2 - 4 keV as opposed to 0.1 - 2.4 keV for the PSPC) that are more characteristic of temperatures of rich clusters.

We do not want the accuracy of our measurements to be limited by the skill of the observer or by noise. As a result, we allowed the image to be uniformly exposed with the on-axis effective area parameters of the IPC which corresponds to a perfect flat-field correction by the observer. Moreover, we allowed the image to be exposed for 2×10^6s which effectively eliminated statistical uncertainties; this exposure time translates to $5 - 10 \times 10^6$ counts for each image. Hence we constructed essentially perfect X-ray surface brightness maps.

Each X-ray image is a 120×120 field of $1'$ square pixels. Following the convention of TKB we place the cluster at a fiducial distance of 100 Mpc; i.e. each pixel represents 29.1 kpc. We ignore the limited spectral information of the IPC-convolved images by adding all counts in PI bins 2-9. This translates to photon energies spanning the

range 0.2-3.1 keV (note: BC92 used 0.2-3.5 keV).

Locating and removing any pockets of emission due to individual galaxies in the cluster is all that remains to prepare the images for analysis. This reduction procedure is essential since our hydrostatic analysis (see §4.4) requires that the X-rays are due to thermal emission powered by the gas falling into the smooth underlying cluster gravitational potential. The artificial enhancement of the emission from regions of high gas density due to shortcomings in the KW simulation (also see TKB) exacerbates the contamination of the surface brightness map from local dips in the potential due to large galaxies. Fortunately these excess peaks are easily located by visual examination of the image enabling us to either avoid those regions or remove the excess. We describe in detail the reduction of the three projections of the $z = 0.13$ cluster and then summarize the results for higher redshifts.

4.2.1 Cluster at z=0.13

KW stopped their simulation at $z = 0.13$ when the evolution of the cluster had slowed substantially; in the core two globs (i.e. "galaxy-like objects") are merging while two other globs orbit about 25′ from the center. This redshift represents the cluster at its most relaxed state in the simulation and thus, of all the redshifts, best matches the criteria for X-ray analysis of cluster shapes outlined in §6 of BC92. This cluster, however, has a size and mass comparable to the Virgo cluster which is approximately an order of magnitude less massive than the rich Abell clusters studied by BC92. Moreover, the KW cluster underwent a major merger at $z \sim 0.6$. The clusters studied by BC92 may be, as a result, more evolved than this simulated cluster (this may not be true for Coma as Fitchett & Webster [1988] have argued for a recent merger).

KW project the three-dimensional cluster emission along three random orthogonal axes x, y, and z. In Figure 1 we show contour plots of X-ray images for each projection "observed" with the IPC as described above. Just outside the unrealistically over-dense core region, the emission from extended cluster gas dominates the surface brightness profile. Farther out, the emission from globs substantially distorts the surface brightness contours away from the contour shapes that would result from

the smooth underlying cluster potential. Since in the outer regions the X-ray gas is significantly contaminated by individual globs and, moreover, is less dynamically relaxed, we restrict our analysis of the surface brightness to $r \lesssim 40' \sim 1.2$ Mpc of the cluster center. Within 40′ two prominent sources in excess of the cluster continuum are seen in all three projections. In addition, the isophotes within $\sim 5'$ exhibit asymmetrical distortions due to the gravitational effects of the merging of two globs described by KW.

Source Removal

Point sources can bias measurement of the ellipticity of the X-ray isophotes. Effects resulting from incomplete removal of sources are especially serious when the continuum is nearly circular because any distortion will generate a preferred direction and a non-zero ellipticity. For example, complete subtraction of a source depends crucially on the accuracy of the modeling of the source and continuum. Smoothing the image biases the shapes of the continuum according to the functional form of the smoothing function.

We removed the embedded sources by instead exploiting the symmetry of the surface brightness distribution imposed by the dark matter models in §4.4; i.e. the dark matter potentials generate X-ray isophotes that are concentric, of constant orientation, and possess two orthogonal axes of reflection symmetry. A given source, thus, may be replaced with the emission in the regions obtained by reflecting the source over the symmetry axes of the image. This type of "symmetric substitution" will not add any geometrical effects into the image that are not already being assumed (Strimple & Binney 1979) and is thus more reliable than direct subtraction of the source or smoothing the image. Unfortunately this method is limited to a continuum having a small number of embedded sources where there exists smooth continuum regions available for symmetric substitution for each source.

Consider first the central 40′ of the x-projection. We determine the axes of symmetry by computing the ellipticity and position angle (see below) of the region uncontaminated by the individual sources. Specifically, this entails looking for (1) bumps

in the radial profile (see below) and (2) sudden large changes in the ellipticity and position angle as a function of radius; we also exclude the inner 5′ where the simulation becomes unphysical (see KW and TKB). The uncontaminated region lies between 5′ and 19′ and the position angle of the coordinate system belonging to the symmetry axes is rotated by 20° counter-clockwise from the image coordinate system; note that we do not attempt to replace the irregularly-shaped isophotes to the right of the center since they are not well localized. In terms of this new coordinate frame, the two obvious sources within 40′ lie in the first and second quadrants. We replace the source in the first quadrant (a circular region of radius 7.5′) with the average emission of the reflection-related regions in the third and fourth quadrants; the corresponding region in the second quadrant is contaminated by the other source. Similarly, the source in the second quadrant (a circular region of radius 12.5′) is replaced by the average emission of the corresponding reflection-related regions in the third and fourth quadrants. We followed precisely the same procedure to remove the sources in the y projection with the exceptions that a smaller region from $5' - 13'$ was identified as the uncontaminated region, the corresponding coordinate system of the symmetry axes is rotated by 10° counter-clockwise with respect to the image coordinates (i.e. the coordinate axes displayed in the figures), and we also removed the source in the lower right of the image (see Figure 1). We show the images of the x and y projections with sources removed by symmetric substitution in Figure 2.

The z projection requires more care than the x and y projections because the isophotes are nearly circular away from the two sources in the first quadrant. We make the conservative assumption that the effects of the two sources are contained within half of the image and thus may be removed by replacing the contaminated half with the other half of the image. Unfortunately, the emission from the two sources bias the choice of reflection axis practically to the region where the unphysical central emission dominates. Thus we examine the effects of several different reflection axes oriented by angles spanning 90° through 180°. We find that the new position angles of the isophotes are always aligned with the reflection axis and the ellipticities vary between $0.00 - 0.12$ (for semi-major axes between 5′ and 20′). As there is no priori

reason to discriminate between any of these symmetry axes we have to accept that only an upper limit on the ellipticity of 0.12 can be reliably set for the z projection. However, for ensuing analysis we use 110° as the rotation angle for the symmetry axis because the isophotes appear the most regular in that case. We display this corrected image for the z projection in Figure 2.

Radial Profile

Following Buote & Canizares (1994, hereafter BC94) we constructed azimuthally-averaged radial profiles for each image in radial bins of 1′ width. The centroid of each profile was determined by the origin of the symmetry axes described above and is consistent to better than 1% with the centroid computed from the symmetrically-substituted image for different values of the outer radii. We plot the radial profiles for the three projections in Figure 3. In order to reduce contamination from gas that is not completely relaxed, we restrict analysis to $r \leq 40'$ for each image. We exclude the central 5′ from analysis because of the unphysical behavior of the simulation; even if the KW simulation produced a realistic cooling flow, we would ignore that region since our modeling procedure does not incorporate multi-phase structure in the gas (see §4.4).

Historically the X-ray surface brightness ($\Sigma_X(r)$) of clusters has been parametrized by the β-model (Cavaliere & Fusco-Femiano 1976; Jones & Forman 1984; Sarazin 1986),

$$\Sigma_X(r) \propto \left[1 + \left(\frac{r}{a_X}\right)^2\right]^{-3\beta+1/2}, \tag{4.1}$$

where a_X and β are free parameters. We determine the β-model parameters for each image in order to provide a convenient benchmark to compare to real clusters. In order to obtain physical constraints on these parameters the β-model must be convolved with the PSF of the IPC. The IPC is well approximated by a Gaussian of 1.5′ FWHM over our energy range (Fabricant, Lecar, & Gorenstein 1980; Trinchieri, Fabbiano, & Canizares 1986). Since the cluster image is much larger than the scale of the PSF, folding the PSF into the β-model actually has a very small effect on the fits;

nevertheless we do include it in the fits for completeness. We plot the best-fit β-model and list the best-fit parameters of the images in Figure 3. The quality of the fits is formally atrocious due to the minuscule statistical uncertainties of the "observation". However, the fits are visually outstanding. Our results differ slightly from TKB due to the different bins included in the fits; i.e. TKB include two bins at smaller r and and we include ten bins at larger r. Note that the quality of the fit of the β-model to this simulated cluster far surpasses the fit to the IPC image of Coma but is of similar quality to that of A2256 (see Davis & Mushotzky 1993). Both Coma and A2256 have significant core substructure evident from their IPC and PSPC images (Briel et al. 1991; Buote 1992; Davis & Mushotzky 1993; Mohr, Fabricant, & Geller 1993). Hence this simulated cluster (at $z = 0.13$) may be related to the class of clusters having core substructure and good fits to the β-model like A2256. Clusters like Coma that are not well fit by the β-model may have significantly different structure from this cluster (at $z = 0.13$).

Ellipticity

As described in BC94, we quantify the shape of the X-ray surface brightness using the iterative moment technique introduced by Carter & Metcalfe (1980) to measure the shapes of the galaxy isopleths in rich clusters. In essence this technique entails computing the two-dimensional principal moments of inertia in an elliptical region arrived at by iterating an initially circular region; the square root of the ratio of principal moments yields the axial ratio and the orientation of the principal moments yields the position angle. The parameters obtained from this method, ϵ_M and θ_M, are good estimates of the ellipticity (ϵ) and the position angle (θ) of an intrinsic elliptical distribution of constant shape and orientation. For a more complex distribution, ϵ_M and θ_M are average values weighted heavily by the outer parts of the region. This property is especially desirable because the primary objective of this paper is to measure the underlying smooth shape of the mass distribution, and visual examination of the images (Figure 2) clearly shows that the isophotes are far from perfect ellipses. Standard elliptical isophote fitting, in contrast, would emphasize the

local irregularities at each radius instead of a gross value for a large annular region.

We compute ϵ_M and θ_M in an elliptical aperture for several values of the semi-major axis a omitting the inner 5′; the derived shape parameters are actually not sensitive to the peculiarities of the inner regions since the moments are heavily weighted by the outermost parts of the aperture. For each image we list ϵ_M and θ_M as a function of aperture semi-major axis in Table 1. Due to the extremely large number of counts the statistical and systematic uncertainties (see BC94; Carter & Metcalfe 1980) are negligible for these parameters. Performing Monte Carlo simulations for simulated clusters having the characteristics of each image (i.e. ϵ_M, β, and a_X) we estimate the 99% confidence limits to be $\Delta\epsilon_M < 0.005$ and $\Delta\theta_M < 1°$ for the regions listed in Table 1.

The ellipticities are not a strong function of aperture size: $\epsilon_M \sim 0.27$ in the x-projection, $\epsilon_M \sim 0.15$ in the y-projection, and $\epsilon_M \sim 0.07$ in the z-projection. For a given projection, the differences in ϵ_M for different semi-major axes, although small ($\lesssim 0.05$), are significant. Similarly the position angle variations are small ($\lesssim 10°$), but significant, in these regions. These deviations reflect either the perturbations of the surface brightness resulting from the gravity of individual globs (i.e. substructure), oscillations of the gas due to incomplete relaxation, or any other intrinsic variations of the smooth underlying potential not accounted for in the above Monte Carlo simulations. We mention that the centroids of these regions are consistent within their uncertainties determined by the above Monte Carlo simulations.

The ellipticities of these images are consistent with those obtained by BC92 with the IPC for A401, Perseus, Coma, A2029, and A2199 (see also McMillan, Kowalski, & Ulmer 1989; Mohr, Fabricant,& Geller 1993; Davis & Mushotzky 1993). The agreement is better for the ellipticities of the y and z projections since the x-projection ellipticity is larger by ~ 0.10. However, BC92 argue that the clusters they analyze are probably viewed in nearly their most flattened projection (i.e. edge-on) suggesting that the x and perhaps y projections should be compared to the BC92 clusters (we discuss the intrinsic orientation of the dark matter in §4.3). The x-projection has an ellipticity more similar to that of A2256 where $\epsilon \sim 0.25$ within 1 Mpc (Fabricant et

al. 1984; McMillan et al. 1989; Buote 1992; Mohr et al. 1993; Davis & Mushotzky 1993). This, when coupled with the good fit of the β-model to A2256 (see above), implies that the shape and radial structure of this cluster is similar to A2256, a cluster likely less relaxed than the clusters studied by BC92 (with the possible exception of Coma).

4.2.2 Cluster at higher redshifts

We analyzed the surface brightness of the cluster at higher redshifts using the same techniques as for the $z = 0.13$ case. For the sake of brevity we restrict our attention to the x-projection since that is where the cluster is nearly in its most flattened state; i.e. we are only interested in assessing the accuracy of the dark matter shape determinations as a function of redshift, not as a result of projection effects. We show in Figure 4 the surface brightness maps at $z = 0.83, 0.67, 0.38$, and 0.25.

The emission of the $z = 0.83, 0.67$, and 0.38 clusters is punctuated by several peaks (due to individual glob emission). As a result it is difficult to obtain a meaningful value for the ellipticity anywhere for $z = 0.83$ and $z = 0.67$, although for $z = 0.38$ the ellipticities should be reliable for $r > 25'$. Excluding the region interior to $25'$ and exterior to $40'$ we obtain $\epsilon \sim 0.5$ for $z = 0.83$ and $\epsilon \sim 0.11$ for $z = 0.38$. For $z = 0.67$ we exclude the region interior to $25'$ (and hold the center fixed) and obtain $\epsilon \sim 0.4$ for outer radius $r \sim 40'$. We can remove the glob emission from the radial profiles of the surface brightness by simply flagging the affected pixels and excluding them from analysis. The $z = 0.67$ and $z = 0.38$ clusters are fit well by the β-model for $r = 0.2 - 1$ Mpc, but the β-model is not a good description of the surface brightness of the $z = 0.83$ cluster.

For the $z = 0.25$ cluster we remove two sources by symmetric substitution as done for the $z = 0.13$ cluster; we show the result in Figure 5. The isophotes of the $z = 0.25$ cluster are quite similar in shape to those of the $z = 0.13$ cluster, but are slightly rounder; we list the ellipticities in Table 1. Like the $z = 0.13$ cluster the β-model fits the surface brightness well, although the profile is somewhat flatter than for $z = 0.13$; we show the radial profile and the associated best-fit β model in Figure 5.

The ellipticities of the $z = 0.83$ and $z = 0.67$ clusters are much larger than those of the clusters studied by BC92. These ellipticities are more typical of clusters having substantial substructure, to a degree not observed in the clusters of BC92; e.g., the double cluster A754 (Fabricant et al. 1986) and other bimodal clusters (see Jones & Forman 1991). Although within $25' < r < 40'$ the $z = 0.38$ cluster has a similar shape to the BC92 clusters, outside the cluster there is an elongated tail in the upper right (see Figure 4) and several obvious clumps ($r \lesssim 20'$) indicating substantially more structure. In contrast, the $z = 0.25$ cluster for $r \lesssim 40'$ is quite similar to the clusters of BC92 and should, along with the $z = 0.13$ cluster, provide a fair comparison of the reliability of shape determinations (§4.4) to the BC92 clusters.

4.3 True Structure of the Dark Matter and Gas

In this section we summarize the three-dimensional structural properties of the cluster taken directly from the KW simulation; we refer the reader to KW for views of the cluster along the three orthogonal directions at different redshifts. Following the format of the previous section, we will discuss the $z = 0.13$ cluster at some length and briefly summarize the results for the other redshifts.

We compute the shape and orientation of the dark matter and gas particles following Katz (1991) who generalizes to three dimensions the two-dimensional iterative moment technique of §4.2.1. This method gives the shape and orientation for the particles within the ellipsoidal radius defined by

$$a^2 = x_1^2 + \frac{x_2^2}{q_{21}^2} + \frac{x_3^2}{q_{31}^2}, \tag{4.2}$$

where the x_i refer to the coordinate system where the three-dimensional moment of inertia tensor is diagonal, x_1 is along the direction of the longest axis (i.e. largest principal moment), and the axial ratios q_{i1} are the square roots of the ratios of principal moments of inertia in the i direction to the 1 direction; the principal directions with respect to the fiducial $x - y - z$ coordinate system of KW give the orientation of

the ellipsoid. Because of the finite number of particles for both the dark matter and gas, the ellipticities, $\epsilon_{i1} = 1 - q_{i1}$, and orientations (given by the Euler angles θ_i and ϕ_i) are uncertain due to realization dependency (Strimple & Binney 1979). Following Strimple & Binney we construct pseudo-clusters having the same number of particles as the KW cluster and estimate the uncertainties of the derived shape parameters.

We wish to compute the aggregate shape of the underlying dark matter and gas, not the shape represented by the globs. The globs do not seriously bias the dark matter shapes, but they do substantially affect the gas shapes. Hence we need to remove the clumps via the symmetric-substitution procedure discussed in the previous section. This is important for the gas at distances $\sim 30'$ from the center.

In Table 2 we list for the dark matter and gas ϵ_{i1} and the relative orientations of the smallest principal moment I_3: θ_{DM} is the relative position of I_3 for the dark matter with respect to its value at $10'$; θ_{gas} is the relative position of I_3 for the gas and dark matter at a given radius; we omit the inner $5'$ for determining the gas shapes because of the unphysical behavior there. The uncertainties due to realization dependency are typically $\Delta\epsilon \sim 0.03$ and $\theta \sim 7°$. In Figure 6 we plot isodensity contours of the dark matter projected along the second-longest principal axis which thus corresponds to the most elongated projection (this principal axis is $\sim 10°$ from the x-projection – see below); note the projected dark matter in Figure 6 is smoothed with a Gaussian filter ($3'$ FWHM) for visual clarity.

The dark matter is nearly oblate for $r \lesssim 750$ kpc ($\sim 25'$) and becomes increasingly triaxial at larger radii. In a similar manner, the dark matter is rounder near the center ($\epsilon \sim 0.35$) and becomes increasingly elongated with distance. At ~ 1.5 Mpc ($\sim 50'$) from the cluster center, the dark matter ellipticity is 0.54 which is the fiducial value we will use to parametrize the aggregate shape of the cluster for comparison to the models in §4.4. The orientation of the short axis, which we will call the "symmetry axis" since the cluster is nearly oblate, is nearly constant to within $\sim 10°$ at all radii. Taking the inclination angle i to be defined with respect to the line of sight and the symmetry axis, we have $i = 80°$ for the x-axis, $i = 60°$ for y, and $i = 40°$ for z. Hence the x-projection is nearly edge-on, the z-projection largely face-on, and the

y-direction intermediate.

The gas, like the dark matter, is nearly oblate within $\sim$ 750 kpc and becomes increasingly triaxial farther out; the small ϵ_{21} values are consistent with those of the dark matter to within the stated uncertainties. In contrast, the values of ϵ_{31} are systematically less than those of the dark matter by $\sim$ 0.10. In addition, the orientation of the symmetry axis of the gas is consistent with that of the dark matter to within $\sim$ 10°. Both of these characteristics are consistent with the gas being in quasi-hydrostatic equilibrium with the smooth underlying potential of the dark matter and gas. Moreover, the isopotential shapes are consistent with those of the gas to within $\epsilon \sim 0.05$ and $\theta \sim 10°$; a complete exploration of the dynamical state of the gas will be done by others (N. Katz and A. Babul 1994, in preparation).

To quantify the radial structure of the dark matter and gas we binned each component into ellipsoidal bins using the above average shape properties. We parametrized the dark matter and gas densities by fitting power-law (see equation [15] of BC94) and Dehnen (1993) functions $(a^{-n}(a + a_c)^{n-4}, n = 1 - 4)$ to these density profiles. The power-law density yields good fits for $r > 50$ kpc but is too shallow in the core: $\rho_{DM} \sim r^{-2.2}$ with $r_c \sim 50$ kpc, $\rho_{gas} \sim r^{-2.2}$ with $r_c \sim 250$ kpc; i.e. the dark matter and gas have similar radial dependences, but the dark matter is more centrally condensed. The Dehnen function actually yields an excellent fit to the dark matter all the way into the core and follows very nearly the Hernquist (1990) form (i.e. $a^{-1}(a + a_c)^{-3}$).

The ellipticity profiles of the dark matter for the higher redshifts $z = 0.83$, 0.67, 0.38, and 0.25 do not differ much from that of $z = 0.13$. The higher redshifts are slightly more elongated reaching a maximum $\epsilon_{DM} = 0.60$ for $z = 0.83$ computed within $\sim$ 1.5 Mpc (50′) of the cluster center. Unfortunately, the number of globs at these higher redshifts (except for $z = 0.25$) substantially exceeds that at $z = 0.13$ and thus the gas ellipticities are severely contaminated by the glob emission. Nevertheless, we estimate for $z = 0.83$ that the gas, like the X-ray isophotes, is highly elongated ($\epsilon_{gas} \sim 0.5$) with nearly the same shape as the dark matter itself. The gas isodensity surfaces of the $z = 0.67$ cluster ($\epsilon_{gas} = 0.4$) are somewhat rounder than the dark

matter but still flatter than the potential ($\epsilon_\Phi \sim 0.30$). For the $z = 0.38$ cluster the shape of the gas, like the X-ray isophotes, varies drastically with radius ranging from $\epsilon = 0.1 - 0.4$. For $z = 0.25$, in contrast, the gas is everywhere rounder than the dark matter and in fact traces the potential quite accurately, just like the $z = 0.13$ case.

The temperature gradients are similar for all of the redshifts considered (see Figure 11 of KW). The temperature outside of 50 kpc follows a steep negative gradient having $\frac{d\ln T_{gas}}{d\ln r} \sim -2.5$ while inside it falls rapidly due to the cooling flow (KW; TKB). In §4.5 we discuss the importance of this steep temperature gradient.

4.4 The Shape of the Three-Dimensional Dark Matter Distribution Deduced from the X-ray Images

4.4.1 Method

The technique we employ to constrain the shape of the cluster potential, and hence its mass, from the X-ray images derives from the pioneering work of Binney & Strimple (1978 Strimple & Binney 1979) and is discussed in detail by BC94 (also BC92). The fundamental assumptions of this method are that the gas is a single-phase ideal gas in a state of quasi-hydrostatic equilibrium with the gravitational potential of the cluster. It would be relatively simple to incorporate effects due to rotation or a multi-phase structure of the gas, but since previous X-ray detectors have not been sensitive enough to place detailed constraints on such properties, the simplest conditions have been assumed. In particular, the inability of previous X-ray satellites to accurately measure the two-dimensional temperature profile of the gas restricts our ability to measure the gravitational potential. If the two-dimensional temperature of the gas is known precisely, then the best model-independent procedure to constrain the shape of the potential is to solve the hydrostatic equation for the potential in terms of the gas density and temperature, both of which may be determined from direct deprojection

of the surface brightness and the spatially-resolved spectra (e.g., Palmer 1994). Since, however, the temperature profile is generally poorly known, a more practical approach to constrain the unknown potential is to exploit the best-determined quantity, the surface brightness, while making "reasonable" assumptions about the temperature profile. As in previous studies (BC92; BC94) we adopt this approach by solving the equation of hydrostatic equilibrium for the gas density while assuming functional forms for the gas temperature and the gravitational potential. From the gas density we construct the X-ray emissivity and then, by projection onto the sky, the X-ray surface brightness. Finally, we convolve the surface brightness with the IPC PSF to compare to the "observed" images.

The first step in our analysis is to model the cluster gravitational potential. For simplicity we restrict the models to oblate and prolate spheroids in order to bracket the behavior of the general triaxial models (Strimple & Binney 1979). We consider the following two families of potentials: (1) potentials generated by mass distributions stratified on concentric, similar spheroids and (2) potentials which are themselves stratified on concentric, similar spheroids. Following the convention of Kassiola & Kovner (1993), who study the properties of two-dimensional elliptical potentials, we refer to three-dimensional potentials of model (1) as SMD (Spheroidal Mass Distributions) and (2) as SP (Spheroidal Potentials). Although the SP models have some properties that are undesirable for a physical mass model (see below), the constant shape of the potential and the ellipticity gradient of the mass distribution contrast nicely with the SMD's. (In addition, the simple analytic forms for the potential significantly increase computational speed.) Hence studying both SMD's and SP's allows for testing a wide range of cluster mass distributions which hopefully bracket the physical behavior of the real cluster.

The SMD potentials are generated by mass densities $\rho(m)$, where $m^2 = R^2/a^2 + z^2/b^2$, R and z are the conventional cylindrical coordinates, a is the semi-major axis and b the semi-minor axis of the spheroid that bounds the mass; full accounts of SMD potentials are given by Chandrasekhar (1969) and Binney & Tremaine (1987). As described in BC94, we consider mass densities having either a Ferrers (i.e. power-

law) or Hernquist (1990) form. The free parameters of the SMD models are the core parameter, R_c, semi-major axis length, a, the ellipticity $\epsilon = 1 - b/a$ of the mass, and the power-law index n. Generally we fix a and n and normalize the potential to its central value. In this manner we construct potentials of varying scale (R_c) and shape (ϵ).

The SP models are given by $\Phi = \Phi(\xi)$, where $\xi^2 = R^2 + z^2/q_\Phi^2$; q_Φ is the constant axial ratio of the SP such that $q_\Phi < 1$ for oblate and $q_\Phi > 1$ for prolate SP's. In particular, we consider the spheroidal logarithmic potential of Binney (1981; Binney & Tremaine 1987; also Kuijken & Dubinski 1994),

$$\Phi(R,z) = \frac{v_c^2}{2} \log\left(\frac{R_c^2 + \xi^2}{R_{ref}^2}\right), \tag{4.3}$$

where v_c is the circular velocity $\sqrt{R d\Phi/dR}$ evaluated at infinity, R_c is a core parameter of the potential, and R_{ref} defines the unit of distance; in order that Φ not be positive we define R_{ref} so that $R_c^2 + \xi^2 \leq R_{ref}^2$ for all (R,z) considered. The mass density that generates this potential is,

$$\rho(R,z) = \left(\frac{v_c^2}{4\pi G q_\Phi^2}\right) \frac{(2q_\Phi^2 + 1)\, R_c^2 + R^2 + 2\,(1 - 1/2q_\Phi^2)\, z^2}{\left(R_c^2 + R^2 + z^2/q_\Phi^2\right)^2}. \tag{4.4}$$

Extending the Binney SP to a general power law we also consider the power-law potentials (Evans 1994; in two dimensions called "Tilted Plummer" models by Kassiola & Kovner 1993),

$$\Phi(R,z) = -\left(\frac{v_c^2(R_c,0) 2^n R_c^{2n}}{n}\right)\left(R_c^2 + \xi^2\right)^{-n}, \tag{4.5}$$

where $n > 0$ and $v_c(R_c,0)$ is the circular velocity evaluated at $(R_c,0)$. The corresponding density is,

$$\rho(R,z) = \left(\frac{v_c^2(R_c,0) 2^{n+1} R_c^{2n}}{4\pi G q_\Phi^2}\right) \times \tag{4.6}$$

$$\frac{(2q_\Phi^2 + 1)\, R_c^2 + (1 - 2nq_\Phi^2)\, R^2 + 2\,(1 - (1+2n)/2q_\Phi^2)\, z^2}{\left(R_c^2 + R^2 + z^2/q_\Phi^2\right)^{n+2}}, \tag{4.7}$$

For particular values of q_Φ and n the mass densities have peculiar properties; namely, the density can become "peanut-shaped" and possibly somewhere take negative values. These undesirable properties result because of the constant shape of the SP's. That is, the shape of the mass must counteract the tendency for the potential to become rounder with distance due to the rapid decay of higher order multipole moments. The density of the Binney potential, for example, has negative values on the z-axis for $q_\Phi < 0.707$ (Binney & Tremaine 1987). The power-law SP's have negative values somewhere on the R-axis when $q > 1/\sqrt{2n}$ $(n > 0)$ and on the z-axis when $q < \sqrt{n+1/2}$ $(n > -1/2)$. The free parameters for these models are R_c, ϵ_Φ (which is $1-q_\Phi$ for the oblate models and $1-1/q_\Phi$ for prolate models), and n for the power-law models; R_{ref} in the logarithmic potential is arbitrarily fixed to the outer boundary of the X-ray gas. As with the SMD's we fix n and normalize the potential to its central value Φ_0; note we relate ρ to Φ by $v_c^2(R_c,0) = -n\Phi_0$. We then compute potentials of varying scale (R_c) and shape (ϵ_Φ).

The gas density is computed by assuming the gas is ideal and in quasi-hydrostatic equilibrium with the cluster potential; by "quasi" we mean that additional gas motions are dynamically unimportant with respect to the cluster gravity. TKB showed that the spherically-averaged $z = 0.13$ cluster is indeed in quasi-hydrostatic equilibrium; for purposes of shape analysis, however, this has not been demonstrated, although the agreement of the three dimensional shapes of the gas and potential in §4.3 is suggestive of hydrostatic equilibrium. In this paper we will assume that quasi-hydrostatic equilibrium holds for all z and remark when the assumption appears to yield erroneous mass shape determinations.

If the gas is isothermal, the equation of hydrostatic equilibrium gives for the gas density,

$$\tilde{\rho}_{gas}(\vec{x}) = \exp\left[1 - \tilde{\Phi}(\vec{x})\right]^\Gamma, \tag{4.8}$$

where $\tilde{\rho}_{gas}$ and $\tilde{\Phi}$ are the gas density and potential normalized to their central values, $\Gamma = \frac{\mu m_p \Phi_0}{k_B T_{gas}}$, μ is the mean atomic weight, m_p is the proton mass, T_{gas} is the constant gas temperature, and k_B is Boltzmann's constant. For a given potential Φ, Γ is

well constrained by the radial profile of the X-ray surface brightness (see BC92 and BC94) and hence does not require knowledge of either the gas temperature (T_{gas}) or the potential depth (Φ_0) (i.e. the total mass of the cluster). This simple solution is of particular interest for study of the cluster shape since detailed two-dimensional temperature maps were beyond the capabilities of past X-ray satellites. As first shown by Strimple & Binney (1979) and then by Fabricant et al. (1984), the shapes of the X-ray isophotes for a given Φ do not radically differ if the gas is assumed to be isothermal or adiabatic. BC94 generalized these findings by demonstrating that for a wide class of potentials and emissivities the shapes of the X-ray isophotes are very similar ($\Delta\epsilon \lesssim 0.04$), independent of the temperature gradient. Thus, the isothermal solution should yield an accurate estimate of the shape of the cluster even if the gas is not isothermal. The constraints on the radial distribution, however, will be in error for large temperature gradients. Since the $z = 0.13$ cluster has a steep temperature gradient, we have a formidable test of this assertion.

Since we know the exact temperature distribution for the cluster (§4.3) we also consider the solution of the hydrostatic equation for an arbitrary temperature profile,

$$\tilde{\rho}_{gas}(\vec{x}) = \frac{1}{\tilde{T}_{gas}(\vec{x})} \exp\left[-\Gamma_0 \int_0^{\vec{x}} \frac{\nabla\tilde{\Phi}(\vec{x}') \cdot d\vec{x}'}{\tilde{T}_{gas}(\vec{x}')}\right], \tag{4.9}$$

where $\tilde{T}$ is the gas temperature expressed in terms of its value at $\vec{x} = 0$; the integral is independent of path. Γ_0 is equal to Γ as given above for the isothermal solution except with T_{gas} replaced by $T_{gas}(0)$.

We construct the X-ray emissivity j_{gas} from ρ_{gas} via the relation,

$$j_{gas} \propto \rho_{gas}^2 \Lambda_{IPC}(T_{gas}), \tag{4.10}$$

where Λ_{IPC} is the plasma emissivity convolved with the IPC spectral response in the appropriate energy band (0.2 - 3.1 keV). Since Λ_{IPC} is a relatively weak function of temperature (e.g., Fabricant et al. 1980; Trinchieri et al. 1986), we use the approximation $j_{gas} \propto \rho_{gas}^2$ for the isothermal models; for completeness we use the

values of Λ_{IPC} from Raymond & Smith (1977, updated to the current version) for the exact temperature models although the results hardly differ if we assume Λ_{IPC} is constant. By integrating j_{gas} along the line of sight we obtain the model X-ray surface brightness Σ_X. The final step to prepare the model image for comparison to observations is to convolve Σ_X with the IPC PSF.

For each model we consider the cases $i = 90°$ (i.e. edge-on) and i set to the true inclination angle of the symmetry axis of the cluster spheroid. We expect the errors in assuming the cluster to be edge-on to be substantial for large tip angles (i.e. $i \ll 90°$) because we can only measure the elongation of the cluster projected onto the plane of the sky; i.e. overestimating the inclination angle is equivalent to underestimating the intrinsic elongation of the cluster. Binney & Strimple (1978) and Fabricant et al. (1984) have shown that for moderate tip angles ($70 \leq i \leq 90$) the inferred shape of the underlying mass distribution is little affected. The y and z projections of the KW cluster at $z = 0.13$ have substantial tip angels and thus provide a test of these assertions.

4.4.2 Results for $z = 0.13$ Cluster

We determine the intrinsic shape of the underlying cluster mass by comparing ϵ_M and the azimuthally averaged radial profiles of the simulated X-ray images (§4.2) to those generated by the models (§4.4.1). Because we are concerned only with the aggregate shape of the cluster on scales $\sim$ 1.5 Mpc from the center, not with small-scale perturbations due to individual globs, we quantify the elongation of the surface brightness by using the values of ϵ_M computed within $5' - 20'$ and $5' - 40'$; we consider the two values to accommodate a possible change in elongation with radius. Employing more values of ϵ_M at different radii for comparison would sample the cluster on scales smaller than those we are attempting to quantify with our aggregate analysis. For the same reason, we use the azimuthally averaged radial profile instead of fitting to individual pixels of the surface brightness. We could use elliptical annuli that better correspond to the shapes of the X-ray isophotes, but the fitted parameters and the quality of the fits is not affected.

For the SMD models we begin by specifying the semi-major axis (a) of the bounding mass spheroid, the power-law index of the particular mass model (i.e. Ferrers or Hernquist), and the inclination angle (i) of the symmetry axis (i.e. either $i = 90°$ or i = true inclination of cluster). Then for a given ellipticity of the dark matter (ϵ_{DM}; really the total mass but since the dark matter dominates the potential we refer to it as the dark matter) we generate model X-ray surface brightness maps for any values of the free parameters R_c and Γ associated with the particular solution of the hydrostatic equation; i.e. isothermal or arbitrary temperature profile. The procedure is the same for the SP models except that (1) the boundary of the mass is not specified, and (2) the power-law index of the potential (logarithmic or $n = 0.1 - 0.5$) and the ellipticity of the potential (ϵ_Φ) are specified. We determine the free parameters by performing a χ^2 fit that compares the radial profiles of the model and image. Since the images from the simulation have essentially no noise (see §4.2), the best-fit parameters are taken to be the only solution. We determine a particular model to be consistent with the image if ϵ_M computed from the model in either the $5' - 20'$ or $5' - 40'$ apertures is consistent with that computed from the image in §4.2.1. Those models that are consistent with neither are rejected. We take the union instead of the intersection because the ellipticity in one of the apertures may be affected by clumping at a particular radius or by incomplete relaxation of the gas. Thus we aim to include all of the models consistent with the aggregate shape of the cluster on scales of ~ 1.5 Mpc.

Recall that we want to compare the aggregate shape of the true dark matter from the simulation with the dark matter from the models on a scale of ~ 1.5 Mpc; i.e. a comparison of their quadrupole moments, or equivalently, their principal moments of inertia. The SMD models have dark matter that is of constant ellipticity and thus the aggregate shape is the same as that computed on smaller scales. For the SP models, however, the dark matter changes shape with radius and thus we employ the iterative moment technique (see §4.2.1) to obtain the desired aggregate ellipticity.

We display in Figure 7 the results for the ellipticity of the dark matter for both the SMD and SP models; the true dark matter ellipticity computed within 1.5 Mpc

($\epsilon_{DM} = 0.54$, see §4.3) is represented by a horizontal dashed line in the Figure 7. For the models where the true inclination of the symmetry axis is used the ellipticities of the dark matter models agree well with the true value from the simulation. The true-temperature models generally agree within $\Delta\epsilon \sim 0.05$ of the true value while the isothermal models underestimate the ellipticity by $\Delta\epsilon \sim 0.10$; these deviations are within the typical estimated errors obtained by BC92 for *Einstein* IPC clusters using the SMD models. Note that due to the projection properties of oblate and prolate spheroids (e.g., Fabricant et al. 1984) the oblate models for the y and z models corrected for the true cluster inclination represent essentially the upper halves of the ellipticity ranges in Figure 7 while the prolate models correspond to the lower halves; i.e. the oblate models give better agreement for these cases. As expected, when the inclination of the symmetry axis is not taken into account the deviations from the true ellipticity increase considerably. For the y-projection the true-temperature models underestimate the true dark matter ellipticity by ~ 0.10 and the isothermal models by ~ 0.20; note that the former deviation is within the typical uncertainty of BC92. For the z-projection the deviations are ~ 0.25 and ~ 0.35 respectively. The difference in ellipticity between the true-temperature and isothermal models, however, is typically ~ 0.10 which is comparable to the uncertainty of BC92.

Similar to the β-models (see §4.2.1), the best-fit models are generally excellent visual fits to the radial profile of the surface brightness for most of the models considered. The fits do not distinguish between oblate and prolate models, consistent with the real triaxiality of the dark matter (see §4.3). As reflected by their χ^2 values, the SMD models having $\rho_{DM} \sim r^{-2}$ (and SP logarithmic models) generally fit the simulation data better than the $\rho_{DM} \sim r^{-3}$ (and SP $n = 0.5$) models, although visually the differences are not flagrant. The Hernquist models fit the data well but with large core parameters indicating that the r^{-4} regime is suppressed. This behavior is consistent with that of the true dark matter (§4.3). The semi-major axis of the SMD models (set to 1.75 Mpc) is not well constrained and the dark matter shapes are not very sensitive to it. However, the quality of the fits diminishes for smaller a and we estimate a lower limit $a > 0.5$ Mpc from visual examination of the fits.

The core parameters R_c of the models behave differently for the isothermal and true-temperature models. For an isothermal gas the equation of hydrostatic equilibrium requires the core radius of the gas density and the total gravitating mass to be nearly the same; our models reproduce this expected similarity. For the true-temperature models we obtain model core radii in excellent agreement with that of the true dark matter core radii (see §4.3).

4.4.3 Results for $z > 0.13$ Clusters

Recall from §4.3 that the gas isodensity surfaces for the $z = 0.83, 0.67$ and $z = 0.38$ clusters do not trace the isopotential surfaces. The X-ray emitting gas in the $z = 0.83$ nearly traces the dark matter itself, not the potential while for the $z = 0.67$ and $z = 0.38$ clusters the X-rays trace neither the dark matter nor the potential. In fact, the distortion of the isophotes of the $z = 0.38$ cluster suggests the gas is "sloshing" as a result of the infall of the clump seen in the upper-right of the earlier redshift plots. These properties suggest that the gas is out of equilibrium and the hydrostatic analysis of the mass distribution of these clusters is not justified. Indeed large errors in the derived dark matter shapes result; e.g., the ellipticity of the dark matter derived for the $z = 0.38$ cluster is less than the true ellipticity by greater than 0.25 for all models considered. The $z = 0.25$ cluster, in contrast, mirrors the $z = 0.13$ case by giving excellent agreement between the X-ray-derived shapes and the true dark matter shapes; i.e. we obtain $\epsilon_{DM} = 0.46 - 0.55$ for the true temperature models and $\epsilon_{DM} = 0.40 - 0.49$ for the isothermal models, comparable to the true dark matter ellipticity of $\epsilon = 0.55$.

4.5 Discussion

Do the peculiar features (i.e. biased CDM, no star formation) of the KW simulation preclude generalizing the results of the previous section to real clusters? The primary virtue of the KW simulation is that it produces a "non-trivial" cluster: the KW cluster (1) is quite flattened having an ellipticity of about 0.55 within 1.5 Mpc, (2) has a steep

temperature gradient that does not appear to be typical of real clusters (Mushotzky 1994), and (3) has substructure at all redshifts. Surely if the KW simulation produced a round, isothermal, and smooth cluster the X-ray methods could not have failed. Therefore, the KW cluster may not be a perfect representation of a real cluster but it provides a formidable test for the X-ray methods of shape determination.

We determined for the KW cluster that the X-ray method for constraining the aggregate shape of the dark matter on a scale of $r \sim 1.5$ Mpc is valid for $z \lesssim 0.25$. If, however, the evolution of a real cluster substantially differs from the KW cluster (e.g., because of a different cosmology or the presence of star formation) then these "safe" redshifts for X-ray analysis may not apply to a real cluster; for a discussion of the effect of cosmology on the epoch of cluster formation see, e.g., White (1994).

The X-ray images of the KW cluster exhibit general properties as a function of redshift that correlate with the reliability of the X-ray methods. Clearly the strong subclustering in the $z = 0.83, 0.67$ and $z = 0.38$ clusters and the distorted X-ray isophotes in the $z = 0.38$ cluster are not seen at the lower redshifts. Moreover, the isophotes of the lower redshift clusters ($z \lesssim 0.25$) are overall more regularly shaped and rounder than those at higher redshifts. If the gas were in hydrostatic equilibrium at the earlier times ($z \gtrsim 0.38$) then the large ellipticities ($\epsilon_x \gtrsim 0.4$) of their isophotes would imply dark matter ellipticities larger than 0.7 (cf. end of §5.1 of BC92); this is unphysical because dynamical considerations forbid such flat, non-rotating, ellipsoidal structures (Merritt & Stiavelli 1990; Merritt & Hernquist 1991). Thus a qualitative statement of necessary conditions for the reliability of the X-ray methods is that (1) there is no obvious subclustering on the same scale used to compute the aggregate shape and (2) the isophotes are regularly shaped and not too elongated ($\epsilon_x \lesssim 0.3$). Of course these conditions are not sufficient since they could both be the results of projection effects.

The clusters studied by BC92 satisfy these necessary conditions with the possible exception of Coma. Fitchett & Webster (1987) have suggested that Coma is bimodal on scales of several hundred kpc, comparable to the scale used by BC92 to compute the aggregate shape. Davis & Mushotzky (1993) have provided further evidence for

such bimodality from analysis of *Einstein* X-ray data. For A2256, in contrast, the substructure appears to reside in the core on a scale of a few hundred kpc (e.g., Briel et al. 1991) which is substantially smaller than the aggregate scales ($\sim$ 1 Mpc) used by Fabricant et al. (1984) and Buote (1992) to measure the intrinsic dark matter shape. Moreover, the core substructure in A2256 appears to be very similar to that present in the $z = 0.13$ cluster of the KW simulation. *We thus conclude that core substructure representing scales of a few hundred kpc does not invalidate X-ray measurements of intrinsic aggregate (i.e. $r \sim 1 - 2$ Mpc) cluster shapes.*

Although we have examined simulated X-ray images having essentially unlimited photon statistics, the additional uncertainties due to noise for the Abell clusters studied by BC92 with *Einstein* are not prohibitive (see Table 7). However, a large sample of such clusters is required for intrinsic shapes of clusters to be employed as a cosmological constraint (see §4.1). In order to obtain shape constraints with the ROSAT PSPC of similar quality to BC92 we need to restrict ourselves to clusters that are sufficiently bright (for S/N) and nearby (for sufficient angular resolution). From examination of the ROSAT master log of pointed observations (in the HEASARC-Legacy data base) for Abell clusters having (1) a measured flux $> 10^{-11}$ erg cm^{-2} s^{-1} as published by Ebeling (1993), (2) exposure times $\geq$ 5000s, and (3) $z < 0.11$, we find 36 eligible clusters. Higher redshift clusters will be available for analysis with AXAF because of its superior spatial resolution (FWHM 1.9″ at 1 keV). As a result, a total of 124 Abell clusters from Ebeling (1993) having flux $> 10^{-11}$ erg cm^{-2} s^{-1} will in principle be eligible for analysis. It is difficult to interpret these numbers of eligible clusters because we do not know how many have substantial substructure that invalidates the X-ray shape analysis. However, our analysis of the KW simulation demonstrates that the presence of core substructure does not invalidate the shape analysis thus indicating that a sizeable fraction of the 36 PSPC and 124 AXAF Abell clusters should enable reliable X-ray constraints of their intrinsic shapes.

4.6 Conclusions

We investigate the reliability of X-ray methods for determining the intrinsic shapes of galaxy clusters by analyzing the cluster simulation of Katz & White (1993); the effects of subclustering and temperature gradients on the shape determinations are examined. Specifically, we test the X-ray technique used by BC92 (BC94; Buote 1992), who built on the original study of Binney & Strimple (1978; Strimple & Binney 1979), to constrain the shapes of the dark matter in five Abell clusters using *Einstein* images. In order to reduce effects of small-scale substructure (few hundred kpc) we measure the aggregate shapes of clusters on scales of $1 - 2$ Mpc from the cluster center.

For low redshifts ($z \lesssim 0.25$) we find that the X-ray method accurately measures the true ellipticity of the cluster dark matter when the true inclination of the cluster is taken into account. The X-ray models employing the true temperature profile deviate from the true cluster ellipticity ($\epsilon \sim 0.55$) by $\epsilon \sim 0.05$ while the isothermal models have slightly larger deviations $\epsilon \sim 0.10$; both of these deviations underestimate the true ellipticity but are less than the typical uncertainties obtained by BC92 for real clusters.

The reason for this underestimate is the following. The hydrostatic equation requires that the gravitating mass has a core radius similar to that of the gas itself when the gas is isothermal, but it has a smaller core radius when the gas has a negative temperature gradient. The core radius of the gas for the KW cluster is about five times larger than the core radius of the dark matter (see §4.3); i.e. the isothermal solution for the KW cluster is less centrally condensed than the true-temperature solution. At a given radius the spherically-symmetric monopole term in the gravitational potential is more important for the centrally-condensed cluster. Thus, in order to generate the same ellipticity (i.e. quadrupole) of the potential at a given distance, the cluster having a negative temperature gradient for the X-ray emitting gas will have to be more elongated than the cluster having an isothermal gas.

When the inclination of the cluster is not taken into account we obtain results for the true temperature models in accordance with Binney & Strimple (1979) and Fabricant et al. (1984); of course, the effects of inclination on cluster shapes may be uncovered by analyzing a well-defined statistical sample of clusters (e.g., Plionis, Barrow, & Frenk 1991). Our results affirm the assertion that conclusions regarding the shape of the dark matter are not overly sensitive to the temperature gradient of the gas (§4.4.1); i.e. the ellipticities of the true-temperature models differ from the isothermal models by less than the typical statistical uncertainties of BC92. We expect that the assumption is even more valid for real clusters since they likely do not have such a steep temperature gradient like that present in the simulation (§4.3).

At higher redshifts ($0.38 \lesssim z \lesssim 0.83$) the X-ray method yields unreliable results. The gas at these early times does not trace the shape of the cluster gravitational potential as it must if it were in hydrostatic equilibrium. At $z \sim 0.83$ the gas traces the dark matter itself and for $z \sim 0.38-0.67$ it follows neither the dark matter nor the potential. Since the peculiarities of the simulation (§4.2) may obfuscate interpretation of the results at these redshifts in terms of real clusters, we offer qualitative necessary conditions for the reliability of X-ray methods characterized by both the amount of substructure in the X-ray surface brightness and the shapes of the X-ray isophotes.

We conclude that measurements of the aggregate shapes of clusters on scales of $1-2$ Mpc from the cluster center are practically unaffected by core substructure representing scales of a few hundred kpc. Therefore our results suggest that the X-ray studies of such aggregate shapes of clusters by Fabricant et al. (1984) and BC92 (Buote 1992) are valid provided that they do not suffer from serious projection effects.

Since our analysis of the KW simulation demonstrates that the presence of core substructure does not necessarily invalidate X-ray shape analysis, we conclude that a sizeable fraction of 36 bright, low-redshift ($z \lesssim 0.1$) Abell clusters from ROSAT PSPC pointed observations should yield reliable X-ray constraints of their intrinsic shapes. With the inclusion of higher redshift ($z \lesssim 0.3$) clusters, AXAF can observe in principle 124 candidate Abell clusters.

We are grateful to Neal Katz for graciously allowing us to use the KW simulation. DAB acknowledges Claude Canizares and Eric Gaidos for useful discussions. We thank Claude Canizares for a critical reading of the manuscript. We extend our appreciation to Timothy Beers for his prompt refereeing of this paper and for his useful suggestions. DAB acknowledges grants NAS8-38249 and NASGW-2681 (through subcontract SVSV2-62002 from the Smithsonian Astrophysical Observatory). JCT was supported by an NRC associateship.

Table 1: X-ray Ellipticities and Position Angles

		$z = 0.13$						$z = 0.25$	
a		x		y		z		x	
(arcmin)	(kpc)	ϵ_M	θ_M	ϵ_M	θ_M	ϵ_M	θ_M	ϵ_M	θ_M
10	291	0.26	20	0.19	10	0.04	27	0.17	49
15	436	0.26	15	0.16	11	0.04	20	0.17	46
20	582	0.27	18	0.16	7	0.07	19	0.17	46
25	728	0.27	20	0.15	5	0.08	20	0.17	46
30	873	0.27	21	0.14	2	0.08	20	0.18	44
35	1018	0.25	22	0.13	0	0.08	20	0.19	44
40	1164	0.25	23	0.13	0	0.09	20	0.20	44

Note. — a is the semi-major axis of the elliptical aperture used to compute the iterative moments (see §4.2.1); the inner 5′ is not included so the aperture is actually the annulus defined from $5' - a$. θ_M is in degrees measured with respect to the horizontal axis in Figure 1.

Table 2: True 3-D Dark Matter and Gas Shapes for $z = 0.13$ Cluster

a		Dark Matter			Gas		
(arcmin)	(kpc)	ϵ_{21}	ϵ_{31}	θ_{DM}	ϵ_{21}	ϵ_{31}	θ_{gas}
10	291	0.15	0.30	0	0.09	0.27	30
15	436	0.11	0.35	5	0.06	0.25	16
20	582	0.04	0.39	11	0.12	0.29	12
25	728	0.10	0.41	9	0.12	0.30	8
30	873	0.08	0.45	9	0.12	0.33	7
35	1018	0.12	0.45	9	0.13	0.34	10
40	1164	0.18	0.49	8	0.12	0.31	9
45	1310	0.21	0.52	8			
50	1455	0.27	0.54	9			

Note. — a is the semi-major axis of the ellipsoidal aperture used to compute the iterative moments (see §4.3); the inner 5′ is not included in the gas so the aperture in that case is actually the annulus defined from $5' - a$. ϵ_{21} is the ellipticity in the plane of the two largest principal moments and ϵ_{31} is the ellipticity in the smallest-largest principal moment frame. The position angles are relative positions of the smallest principal axes (I_3): θ_{DM} is the relative direction of the dark matter at semi-major axis a with respect to $a = 10'$; θ_{gas} is the relative direction of the gas at a and the dark matter at a.

REFERENCES

Aarseth, S. J., & Binney, J. J. 1978, MNRAS, 185, 227

Binney, J. J. 1981, MNRAS, 196, 455

Binney, J. J., & Silk, J. 1979, MNRAS, 188, 273

Binney, J., & Strimple O. 1978, MNRAS, 187, 473

Binney, J., & Tremaine, S. 1987, Galactic Dynamics (Princeton: Princeton Univ. Press)

Bird, C. M. 1993, Ph.D thesis, University of Minnesota

Briel, U. G., et al. 1991, A&A, 246, 10

Buote, D. A. 1992, M.S. Thesis, Massachusetts Institute of Technology

Buote, D. A., & Canizares, C. R. 1992, ApJ, 400, 385 (BC92)

Buote, D. A., & Canizares, C. R. 1994, ApJ, 427, 86 (BC94)

Carter, D., & Metcalfe, N. 1980, MNRAS, 191, 325

Cavaliere, A., & Fusco-Femiano, R. 1976, A&A, 49, 137

Chandrasekhar, S. 1987, Ellipsoidal Figures of Equilibrium (New York: Dover)

Davis, D. S., & Mushotzky, R. F. 1993, AJ, 105, 409

Dehnen, W. 1993, MNRAS, 265, 250

Ebeling, H. 1993, Ph.D thesis, Ludwig-Maximilians-Universität München

Eisenstein, D. J., & Loeb, A. 1994, ApJ, submitted

Evans, N. W. 1994, MNRAS, 267, 333

Fabricant, D., Beers, T. C., Geller, M. J., Gorenstein, P., Huchra, J. P., & Kurtz, M. J. 1986, ApJ, 308, 530

Fabricant, D. G., Kent., S. M., & Kurtz, M. J. 1989, ApJ, 336, 77

Fabricant, D., Lecar, M., & Gorenstein, P. 1980, ApJ, 241, 552

Fabricant, D., Rybicki, F., & Gorenstein, P. 1984, ApJ, 286, 186

Fahlman, G. G., Kaiser, N., Squires, G., & Woods, D. 1994, preprint

Fitchett, M. J., & Webster R. 1987, ApJ, 317, 653

Fitchett, M. J. 1989, in Clusters of Galaxies (STScI Symp. 4), ed. W. R. Oegerle, M. J. Fitchett, & L. Danly (Cambridge: Cambridge University Press), 111

Giacconi, R., et al. 1979, ApJ, 230, 540

Hernquist, L. 1990, ApJ, 356, 359

Hernquist, L., & Katz, H. 1989, ApJS, 70, 419

Jones, C., & Forman W. 1984, ApJ, 276, 38

Jones, C., & Forman W. 1991, in Clusters and Superclusters of Galaxies (NATO ASI Vol. 366), ed. A. C. Fabian, (Dordrecht/Boston/London: Kluwer), 49

Kaiser, N. 1992, ApJ, 388, 272

Kaiser, N., & Squires, G. 1993, ApJ, 404, 441

Kassiola, A., & Kovner, I. 1993, ApJ, 417, 450

Katz, N. 1991, ApJ, 368, 325

Katz, N., & White, S. D. M. 1993, ApJ, 412, 455 (KW)

Kuijken, K., & Dubinski, J. 1994, preprint

McMillan, S. L., Kowalski, M. P., & Ulmer, M. P. 1989, ApJS, 70, 723

Merritt, D., & Stiavelli, M. 1990, ApJ, 358, 399

Merritt, D., & Hernquist, L. 1991, ApJ, 376, 439

Mohr, J. J., Fabricant, D. G., & Geller, M. J. 1993, ApJ, 413, 492

Mushotzky, R. F. 1994, in Clusters of Galaxies (Proceedings of the 29th Rencontres de Moriond), ed. F. Durret, A. Mazure, J. Trân Thanh Vân, & S. D. M. White (Gif sur Yvette: Frontier Editions)

Palmer, P. L. 1994, MNRAS, 266, 697

Plionis, M., Barrow, J. D., & Frenk, C. S. 1991, MNRAS, 249, 662

Raymond, J. C., & Smith, B. W. 1977, ApJS, 35, 419

Sarazin, C. L. 1986, Rev. Mod. Phys., 58, 1

Smail, I., Ellis, R. S., Fitchett, M. J., & Edge, A., 1994, MNRAS, submitted

Strimple, O., & Binney, J. 1978, MNRAS, 188, 883

Sunyaev, R. A., & Zeldovich, Y. A. 1972, A&A, 20, 189

Trinchieri, G., Fabbiano, G., & Canizares, C. 1986, ApJ, 310, 637

Trumpler, R. J., & Weaver, H. F. 1953, Statistical Astronomy, (Berkeley: Univ. California Press)

Tsai, J. C., Katz, N., & Bertschinger, E. 1994, ApJ, 423, 553 (TKB)

Tyson, J. A., Valdes, F., & Wenk, R. 1990, ApJ, 349, 1

West, M. J. 1994, in Clusters of Galaxies (Proceedings of the 29th Rencontres de Moriond), ed. F. Durret, A. Mazure, J. Trân Thanh Vân, & S. D. M. White (Gif sur Yvette: Frontier Editions)

White, S. D. M. 1994, in Clusters of Galaxies (Proceedings of the 29th Rencontres de Moriond), ed. F. Durret, A. Mazure, J. Trân Thanh Vân, & S. D. M. White (Gif sur Yvette: Frontier Editions)

Fig. 1.—
Contour plots of the X-ray surface brightness of the KW cluster (see §4.2.1) at $z = 0.13$ for the three orthogonal projections x ($i = 80°$), y ($i = 60°$), z ($i = 40°$); the contours are separated by a factor of 2 in intensity and the coordinate axes are labeled in arcminutes. The cluster is placed at a distance of 100 Mpc so that $1'$ represents 29.1 kpc.

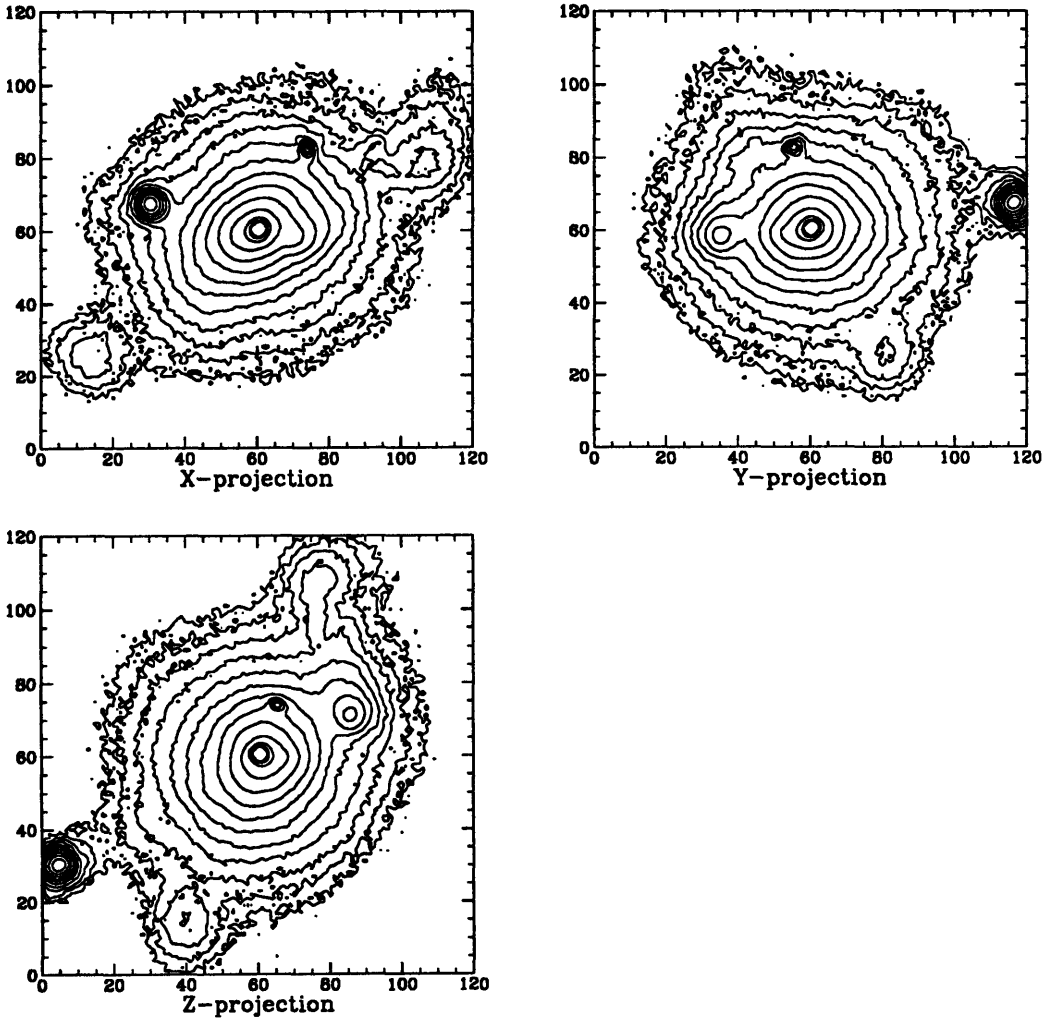

Fig. 2.—
Contour plots of the same images in Figure 1 where now the images have been corrected for contamination from individual globs (see§4.2.1).

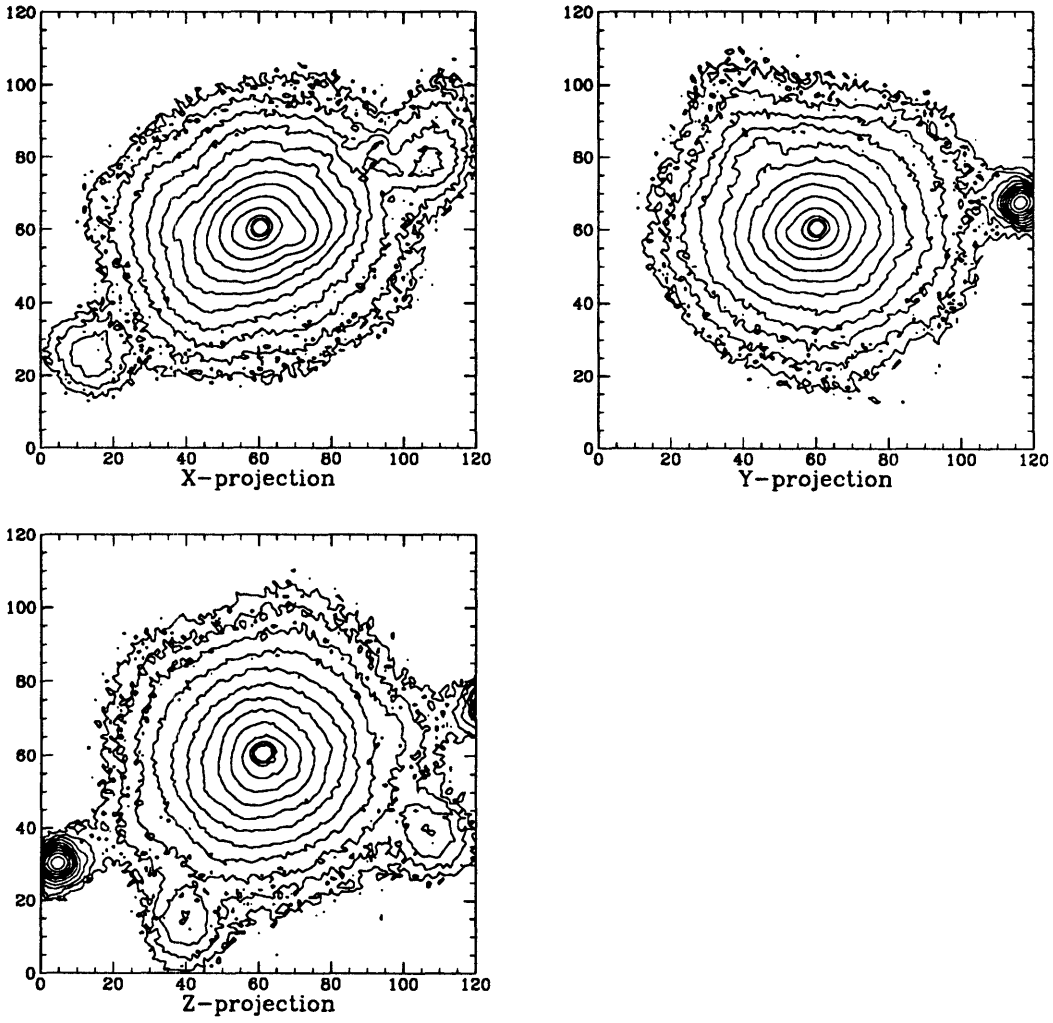

Fig. 3.—
The azimuthally-averaged radial profiles of the reduced $z = 0.13$ images from Figure 2 and their best-fit β models.

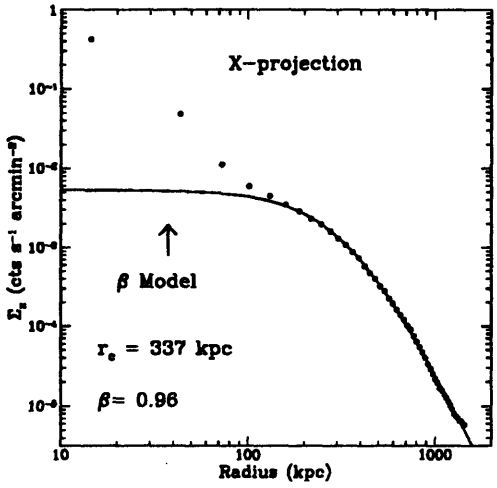

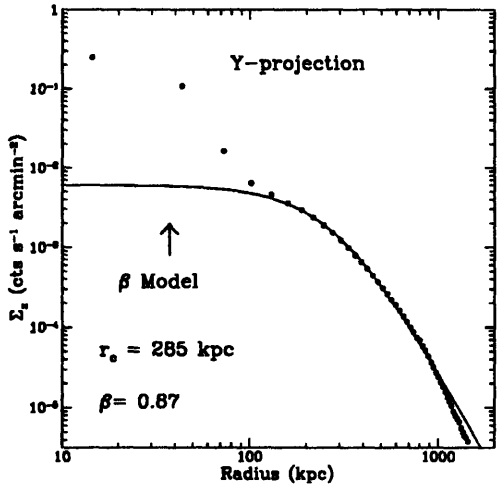

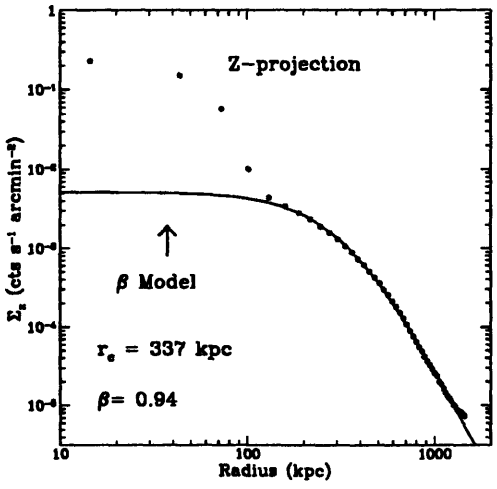

Fig. 4.—
Contour plots of the X-ray surface brightness for the x-projection of the KW cluster at higher redshifts (see§4.2.2); the images are prepared as in Figure 1.

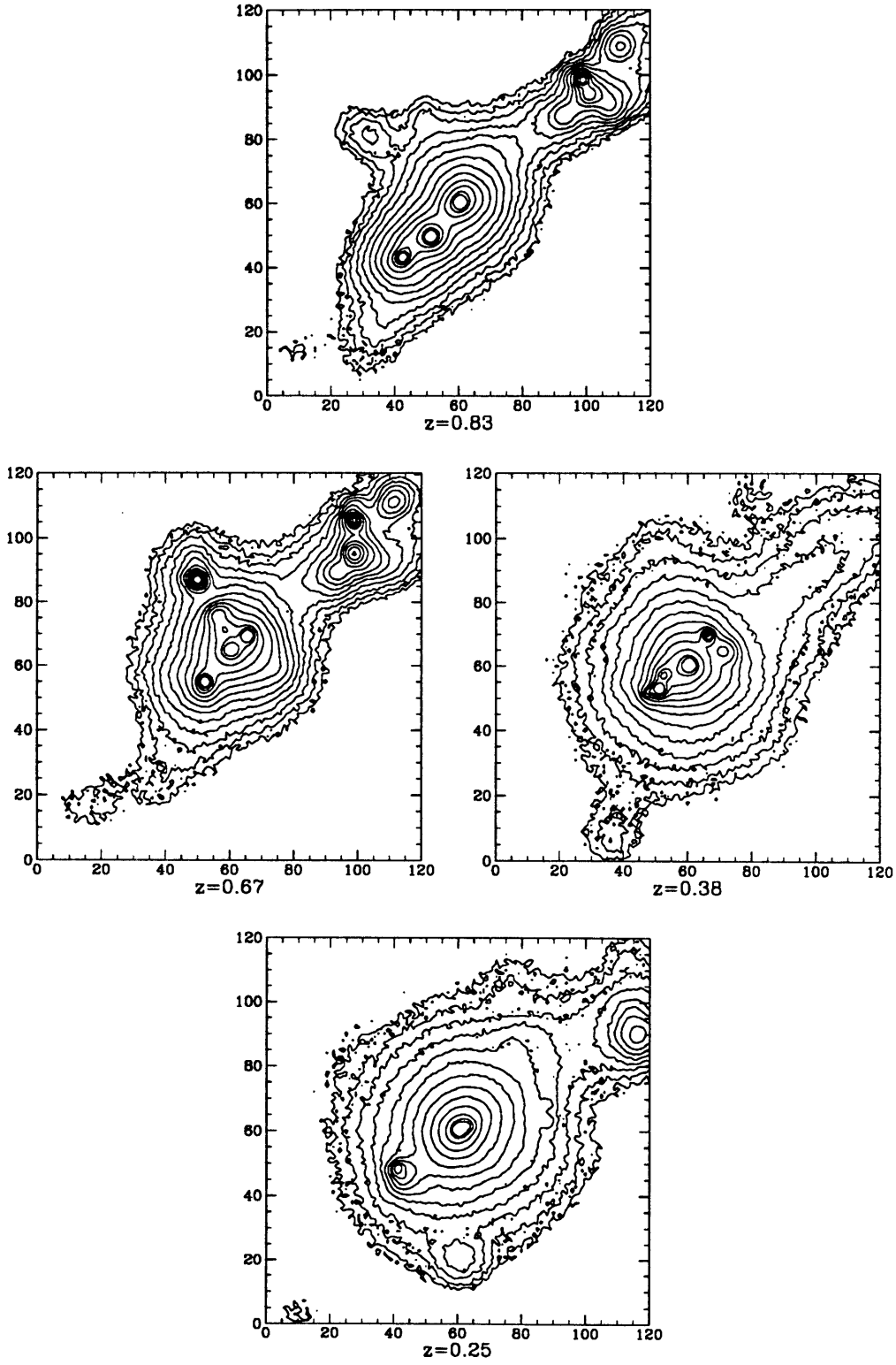

Fig. 5.—
(a) Contour plot of the $z = 0.25$ image in Figure 4 where now the image has been corrected for contamination from individual globs (see §4.2.1 and §4.2.2).

(b) The azimuthally-averaged radial profile of the reduced $z = 0.25$ image and the best-fit β model.

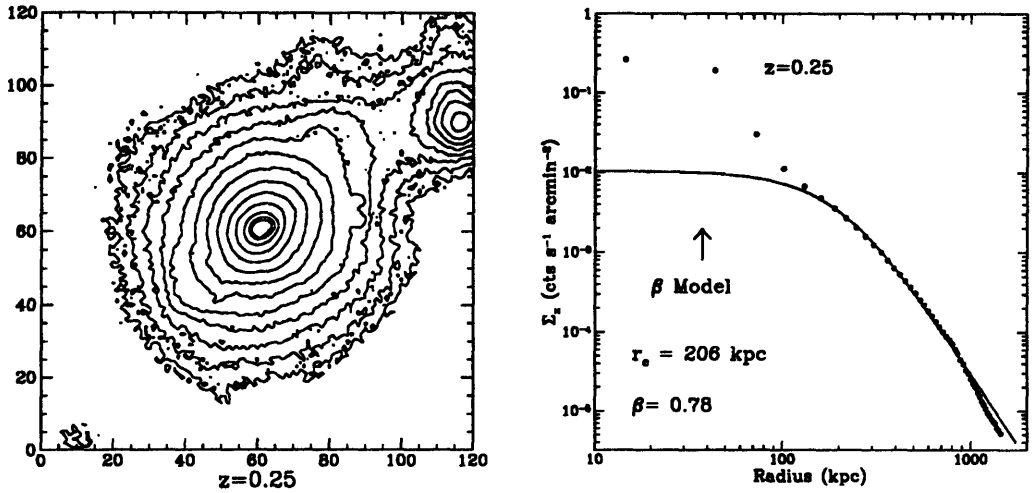

Fig. 6.—
Contour plot of the $z = 0.13$ dark matter projected in the plane of the longest and shortest principal moments of inertia; the plot has been smoothed with a Gaussian filter ($\sigma = 3'$ FWHM) for visual clarity and the contours a separated by a factor of two in mass. See Table 2 for the ellipticity and degree of triaxiality of the dark matter.

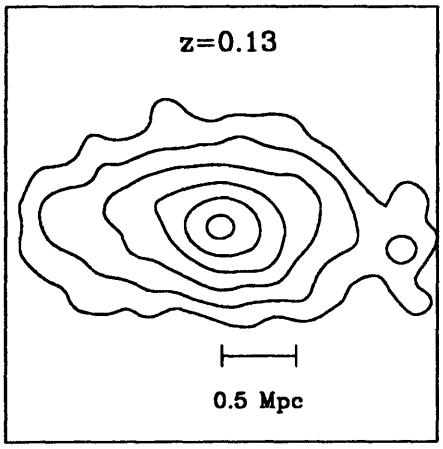

Fig. 7.—
Results for the intrinsic three-dimensional ellipticity of the dark matter of the $z = 0.13$ cluster as estimated from the spheroidal X-ray models in §4.4.1. The ellipticities represent the aggregate shape of the dark matter computed for $r \lesssim 1.5$ Mpc (see §4.3 and §4.4.2). The long dashed line represents the aggregate dark matter ellipticity of 0.54 computed directly from the simulation in §4.3. The solid error bars represent the range of X-ray models where the true temperature profile of the simulation has been used while the dotted error bars indicate the results for the isothermal models. The models enclosed in boxes have been corrected for the true inclination of the cluster. The dumbbell represents the typical uncertainty obtained by BC92 for the dark matter ellipticities of five Abell clusters with the *Einstein* IPC.

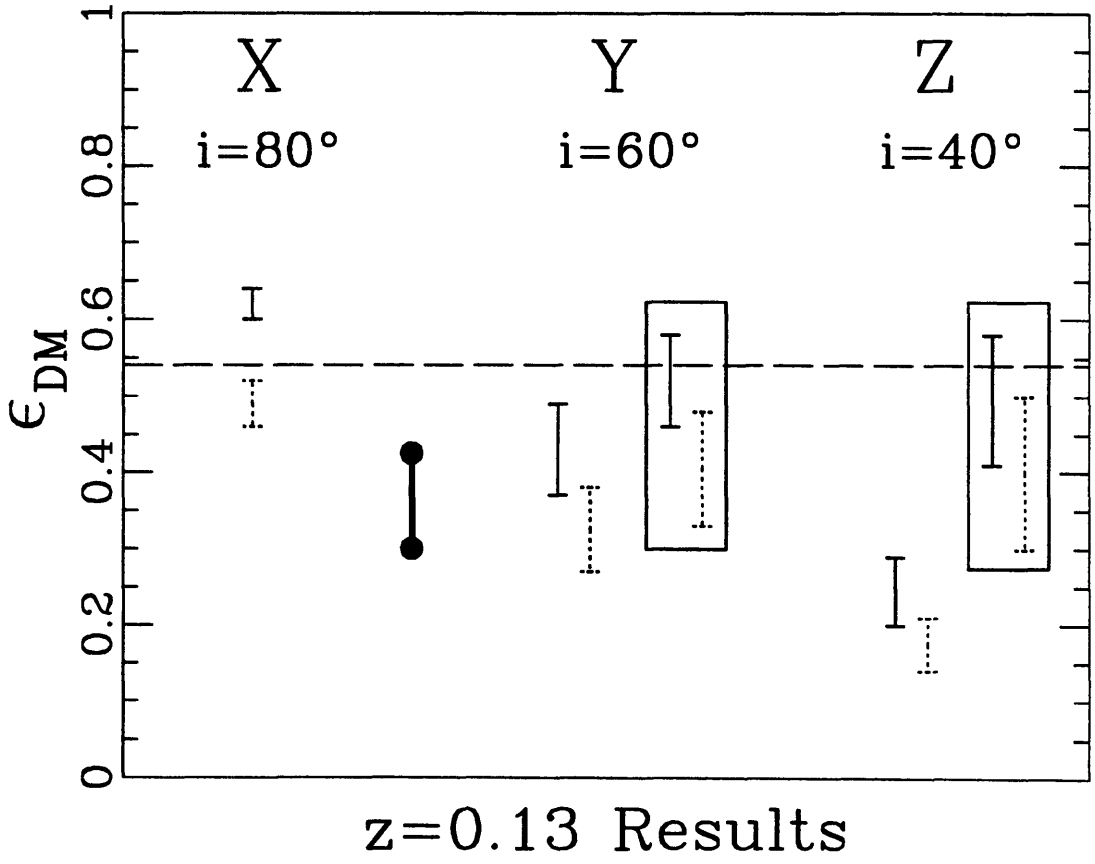

Chapter 5

X-ray Constraints on the Intrinsic Shapes and Baryon Fractions of Five Abell Clusters

Now that we have some confidence in the reliablity of X-ray constraints on intrinsic cluster shapes we now follow up our previous study of five abell clusters using *Einstein* data (Buote & Canizares 1992; Buote 1992). We analyzed ROSAT PSPC images of the bright, nearby ($z < 0.1$) galaxy clusters A401, A1656 (Coma), A2029, A2199, and A2256 to constrain their intrinsic shapes and baryon fractions; the intrinsic shapes of these clusters were analyzed previously by us using *Einstein* data (Buote & Canizares 1992; Buote 1992). Following Buote & Tsai we probed the aggregate structure of the clusters on scales $\sim 1.5h_{80}^{-1}$ Mpc to reduce effects of possible substructure on smaller scales ($\lesssim$ a few hundred kpc). The ellipticities of the X-ray isophotes are typically $\epsilon \approx 0.15 - 0.25$ and display negative radial gradients highly significant at the 95% confidence limit for all the clusters except Coma. By assuming hydrostatic equilibrium and a variety of mass models we obtain ellipticities $\epsilon_{mass} \approx 0.40 - 0.55$ for isothermal models of the total gravitating matter of the clusters; the ϵ_{mass} constraints change by $< 10\%$ upon consideration of the small temperature gradients shown by ASCA to be typical for rich clusters. Estimates of the gas masses are highly insensitive to the ellipticities of the X-ray isophotes as noted by White et al. (1994). The clusters in

our sample have increasing fractions of gas mass to total mass with radius and have $M_{gas}/M_{tot} = (4\% - 11\%)h_{80}^{-3/2}$ within a radius $1.5h_{80}^{-1}$ Mpc, in excellent agreement with the results of White & Fabian and the Baryon Catastrophe proposed by White et al. (1993). Finally, the ellipticities of the dark matter distributions are essentially identical to ϵ_{mass} and are consistent with the shapes of dark halos predicted by N-body simulations and the shapes of the galaxy isopleths in the clusters in contrast to our previous conclusions using *Einstein* data.

5.1 Introduction

The structures of galaxy clusters probe cosmological theories in a variety of ways. The influence of early tidal distortions in the formation of clusters (Binney & Silk 1979), the degree of dissipation of the dark matter (e.g., Strimple & Binney 1979; Aarseth & Binney 1978), and the density of the universe (Eisenstein & Loeb 1995) all affect the intrinsic shapes of clusters. Morphological differences between the X-ray–emitting gas and the underlying mass in clusters may reflect the nature of the dark matter itself (Kaiser 1991). Finally, the large baryon fractions observed for Coma (White et al. 1993) and other clusters (White & Fabian 1995) may have serious repercussions for many cherished notions of the standard cosmology (White et al. 1993).

We (Buote & Canizares 1992 – hereafter BC; Buote 1992) have previously analyzed the shapes of a small sample of bright, low-redshift ($z < 0.1$) Abell clusters having no obvious subclustering (with the possible exception of Coma) using the *Einstein* Image Proportional Counter (IPC; Giacconi et al. 1979) and concluded that the ellipticities of the gravitating mass ($\epsilon \sim 0.3$) were smaller than the ellipticities of the galaxy isopleths ($\epsilon \sim 0.5$). However, the increasing evidence for substructure in clusters (e.g., West 1995) calls into question any analysis of clusters that approximates them as relaxed systems. Buote & Tsai (1995a; hereafter BT) used the N-body / hydrodynamic simulation of Katz & White (1993) to test the reliability of X-ray constraints of intrinsic cluster shapes considering the effects of substructure. For the X-ray method to be reliable they concluded it is necessary that there is no subclus-

tering on the same scale used to compute the shape of the cluster. Specifically, BT demonstrated that X-ray constraints of the aggregate shape of the Katz & White cluster on scales $r \sim 1.5$ Mpc are very insensitive to subclustering on scales $\lesssim$ few hundred kpc. This is simply a statement that in a hierarchical clustering scenario the bulk of a cluster within $r \sim 1 - 2$ Mpc may be essentially relaxed even though a small subcluster (or two) has recently fallen in to the central regions.

Following the suggestion of BT, in this paper we use data from the ROSAT satellite to probe the aggregate shapes of the bright, low-redshift ($z < 0.1$) Abell clusters A401, A1656 (Coma), A2029, A2199, and A2256 corresponding to clusters we analyzed previously with IPC data (BC: Buote 1992); some of these clusters have now been shown to have significant subclustering in their cores (e.g., Mohr, Fabricant, & Geller 1993). The image reduction and spatial analysis is described in §5.2. The hydrostatic modeling of the clusters, the results for intrinsic shapes, and the baryon fractions are discussed in §5.3. We present our conclusions in §5.4

5.2 Spatial Analysis of X-ray Data

The cluster images were obtained from the ROSAT Public Data Archive operated by the HEASARC-Legacy database at Goddard Space Flight Center; see Trümper (1983) for a description of ROSAT and Aschenbach (1988) for a discussion of the X-ray telescope. We selected images observed with the Position Sensitive Proportional Counter (PSPC; Pfeffermann et al. 1987) instead of the High Resolution Imager (HRI) because of the PSPC's superior sensitivity, larger field of view, and, most importantly, all of the clusters were observed with the PSPC. Each cluster has at least one observation pointed near the center of the cluster, while a few of the clusters have multiple pointings, some of which are offset from the centers of the clusters. Only certain pointings, however, are useful for our analysis of the intrinsic shapes and mass distributions in the clusters.

Interior to the 40′ diameter ring of the window support structure of the PSPC the spatial resolution is substantially higher than outside (Hasinger et al. 1994).

Outside the ring the PSPC "spokes" supporting the window fan radially outward from the ring and thus add structure to the PSPC images. Since the poor resolution and "spokes" outside the ring degrade and bias measurement of the ellipticity of the surface brightness (i.e. quadrupole; see §5.2.3) we restrict our analysis to regions interior to the PSPC ring (although see §5.2.2 regarding A2199). Moreover, when considering multiple pointings, we only used those that completely encircled a cluster about its center. In Table 1 we list the ROSAT sequence numbers and exposure times for the relevant observations of the clusters.

5.2.1 Image Reduction

To prepare the images for analysis we (1) removed time intervals of high background, (2) selected PI bins corresponding to photon energies between 0.5 and 2 keV, (3) corrected for exposure variations and telescopic vignetting, (4) merged multiple pointings for relevant clusters into one image, (5) subtracted the background (only for radial profile), and (6) rebinned the image into pixels corresponding to $\sim 50h_{80}^{-1}$ kpc ($H_0 = 80h_{80}$ km s^{-1} Mpc^{-1}). All of these reduction procedures were implemented with the standard IRAF-PROS software.

All of the pointed observations were partitioned into many short exposures in order to maximize the observational efficiency of the ROSAT observing program. We examined the background light curves of the images for short-term enhancements indicative of contamination from scattered X-rays, especially from the sun, the bright earth, and the SAA. Only images for A1656 and A2256 required time-filtering. We list the effective exposure times of these filtered pointings in parentheses in Table 1.

To minimize the effects of the X-ray background and the width of the PSPC point spread function (PSF; see §5.2.2) we selected photons only from energy channels between 0.5 and 2 keV. In addition, we rebinned the images into more manageable 15″ pixels corresponding to 512 × 512 fields. This pixel scale is the same as the exposure maps provided with the standard analysis systems software (SASS); note that the true resolution of the exposure maps actually corresponds to 30″ pixels.

The images were then flattened using the SASS exposure maps. When dividing

the images by these exposure maps, we corrected for both exposure variations and telescopic vignetting. In principle this correction depends on the energy of each individual photon, but for energies above 0.2 keV the energy dependence is small and we neglect it (Snowden et al. 1994).

We merged multiple pointings for A401, A1656, and A2256. Point sources common to the images of each cluster were used to align the fields. A401, which has two images nominally centered on the same position, required a N-S shift of 1.8 ± 0.5 pixels, slightly larger than the ~ 1 pixel uncertainty (i.e. 15″) expected of the pointings of ROSAT. The merged images for A1656 included $\sim 500 h_{80}^{-1}$ kpc within the ring of the PSPC. The five pointings for A2256 easily fit 1.5 h_{80}^{-1} Mpc radius within the PSPC ring.

The next step is to remove point sources embedded in the cluster continuum emission. It is imperative to carefully remove such sources to prevent contamination of measurements of the ellipticity of the surface brightness (see BT). Our preferred method to remove sources is by "symmetric substitution" as outlined in BT. This method exploits the property that since our models used for analysis of the intrinsic shape (see §5.3.1) assume elliptical symmetry we may replace a localized region of the surface brightness with the corresponding regions related by reflection over the major and minor axes of the elliptical isophotes. Unfortunately, this method may only be implemented for an image containing very few sources and having well-defined elliptical symmetry axes. Only A2029 and A2199 meet these requirements for the clusters in our sample. For the other clusters we removed sources by first selecting a source by eye and choosing an annulus around the source to estimate the local background. We then fit a second order polynomial surface to the background and replace the source with the background especially for estimating the quadrupole moments of high S/N cluster images; see Buote & Tsai (1995c) for a thorough discussion.

We estimated the background for each cluster from source-free regions outside the ring of the PSPC fields; these regions were away from the field center at radii $r \sim 40'$ for A401, 30′ for A2029, 45′ for A2199, and $55 - 60'$ of the *cluster* center for A2256. The background rates in the 0.5 - 2 keV band of these regions are listed

in Table 1. For Coma we adopted the value of White, Briel, & Henry (1993) since they explored regions much farther from the cluster center than we do. We mention that our background estimate for A2256 agrees well with the value 2.24×10^{-4} cts s^{-1} $arcmin^{-1}$ of Briel & Henry (1994).

Finally, we rebinned the images of each cluster in order to probe the aggregate cluster structure as outlined in BT. We rebinned the images into pixels corresponding to $\sim 50h_{80}^{-1}$ kpc for computation of the radial profiles of the clusters; this arbitrary choice provides enough resolution to determine the radial structure suitable for analysis of the aggregate radial structure of the cluster. However, because reliable computation of the ellipticity (see §5.2.3) requires a sufficiently large number of pixels in a given aperture, we generally selected a finer pixel scale for computing the ellipticities (see Table 2).

The reduced images for each cluster are plotted in Figure 1 using the pixel scales of the radial profiles listed in Table 2. The images are smoothed with a circular gaussian ($\sigma = 15''$) for display purposes only and the contours are separated by a factor of 2 in intensity; the displayed regions correspond to slightly larger than the region analyzed (i.e. out to radius D_{max} in Table 2). The image for Coma stands out since we are viewing a much smaller region ($r \sim 500h_{80}^{-1}$ kpc) than for the other clusters ($r \sim 1500h_{80}^{-1}$ kpc). Binned into these large pixels Coma appears very smooth whereas on smaller scales there is significant structure (see §5.2.2). This is in keeping with our strategy to measure the aggregate structure of the clusters to reduce possible nonequilibrium effects of small-scale subclustering.

5.2.2 Radial Profile

We constructed the azimuthally averaged radial profile for each cluster using the background-subtracted images. First we computed the centroid of the cluster within a circular aperture containing $\sim 90\%$ of the total flux. This centroid was determined by selecting an origin by eye and then iterating until the centroid changed by < 0.1 pixels. For the clusters with known cooling flows (i.e. A2029 and A2199) we excluded the region interior to the radius where the cooling time $\sim$ cluster age; this radius is

typically $\sim$ 100 kpc (see Sarazin, O'Connell, & McNamara [1992] concerning A2029; see Fabian [1994] for a review of cooling flows in clusters). We exclude the cooling flow region since our models in §5.3.1 do not apply there.

When computing the centroid of A2256 we must carefully consider the well-known substructure in the core (Briel et al. 1991). Our analysis of the mass distribution in §5.3.1 assumes the cluster is in hydrostatic equilibrium. We prefer to exclude the region in A2256 were the gas is unrelaxed. To determine where in the cluster the gas is likely to be relaxed we appeal to the power ratios of A2256 (Buote & Tsai 1995b,c). The power ratios classify clusters according to their dynamical state and depend on the scale of the cluster being probed. Buote & Tsai (1995c) find that on a scale of $0.5h_{80}^{-1}$ Mpc A2256 has power ratios similar to clusters that are manifestly unrelaxed. However, on $1.0h_{80}^{-1}$ Mpc scales A2256 has power ratios similar to clusters with only a small amount of substructure and is morphologically much closer to evolved clusters like A2029 than on the $0.5h_{80}^{-1}$ Mpc scale. To achieve a balance between eliminating as much of the inner $\sim 0.5h_{80}^{-1}$ Mpc because of substructure and sampling enough of the radial profile to usefully constrain the mass models in §5.3.1, we decided to excise the inner $\sim 300h_{80}^{-1}$ kpc from analysis which effectively encompasses the subcluster in question. We thus compute the centroid in an annular aperture from $(300-1500)h_{80}^{-1}$ kpc.

For all of the clusters we computed the radial profiles out to $\sim 1.5h_{80}^{-1}$ Mpc where the specific outer bin being determined by a S/N criterion (see below). Both Coma and A2199, however, fall well short of $1.5h_{80}^{-1}$ Mpc within the PSPC ring. We decided to extend the radial profile of A2199 outside the ring in order to compute its baryon fraction to larger distances (see §5.3.3); the radial profile is not as sensitive as the ellipticity to the larger PSF and spokes outside the ring. Extending the radial profile does not improve our constraints on the intrinsic shape of A2199 since it is the X-ray ellipticity that is the most important determinant which is still confined to within the ring (see Buote & Canizares 1995a). We do not extend the radial profile of Coma since its baryon fraction has been analyzed in detail by others (White et al. 1993).

We rebinned the radial profiles so that all bins had an appropriate minimum

signal-to-noise ratio (S/N): 7 for A2029 and A2199, and 20 for A2256; A401 and Coma required no additional binning. The background-subtracted radial profiles are displayed in Figure 4. The top axes are labeled in h_{80}^{-1} kpc and the error bars are placed at the center of each radial bin and the boxes indicate bins omitted from analysis; the bins that were excluded from analysis as noted above are denoted by diamonds. All of the radial profiles appear to be quite smooth for our chosen bin sizes. In particular, Coma's profile displays no large irregularities when binned into $\sim 50h_{80}^{-1}$ kpc pixels, but is known to be very lumpy when probed on galactic scales of ~ 5 kpc (e.g., White et al. 1993; Davis & Mushotzky 1993). This property that the cluster is sufficiently relaxed for analysis of its aggregate structure while it is clearly not a smooth, equilibrium configuration on smaller scales exemplifies the arguments of BT and is the driving force for our present investigation.

A convenient parametrization of the X-ray radial profiles of galaxy clusters is the β model (Cavaliere & Fusco-Femiano 1976; Jones & Forman 1984; Sarazin 1986),

$$\Sigma_x(R) \propto \left[1 + \left(\frac{R}{a_X}\right)^2\right]^{-3\beta+1/2}, \tag{5.1}$$

where a_x and β are free parameters. The β model is especially useful as (1) a benchmark for comparison of $\Sigma_x(R)$ to other clusters and (2) an analytic parametrization of the radial parameters for computing the gas mass. In order to obtain physical constraints on the parameters a_X and β, we convolved Σ_X with the off-axis PSPC PSF (Hasinger et al. 1994) and performed a χ^2 fit to the radial profile; note for the evaluation of the PSF we set the energy to 1 keV and for A1656 and A2256, which have pointings on different regions of the clusters, we fixed the off-axis angle to 10′. Since our radial bins are larger, in some instances substantially larger, than the width of the PSF, including the PSF in the fits has a negligible ($\lesssim 1\%$) effect on the fitted parameters. Nevertheless, we include the PSF in the fits for completeness.

In Table 3 we list the best-fit parameters and 95% confidence limits on two interesting parameters; the best-fit models are also plotted in Figure 4. The β model is an excellent visual fit to the radial profiles for all of the clusters, although the χ^2 values

are rather large. For the purposes of analyzing the aggregate structure of the clusters on ~ 1 Mpc scales, though, the fits give very acceptable descriptions of the surface brightness distribution. Except for A2256, the fitted parameters are generally insensitive to the aperture size used to evaluate the centroid; i.e. $\Delta a_x \lesssim 5\%, \Delta\beta \lesssim 1\%$. A2256, which is known to have a large centroid shift (Mohr et al. 1993), has substantially different parameters depending on the chosen aperture used for computing the centroid. The values listed in Table 3 for A2256 are for the centroid evaluated in an annular aperture $(300 - 1100)\ h_{80}^{-1}$kpc representing $\sim 90\%$ of the flux in the annulus $(300 - 1500)\ h_{80}^{-1}$kpc. If we instead use a circular aperture of radius $300h_{80}^{-1}$ kpc then we obtain best-fit parameters $a_x = 5'.21$ and $\beta = 0.815$. These values are in excellent agreement with those obtained by Briel & Henry (1994). As stated above, we prefer to exclude from analysis the region $r < 300h_{80}^{-1}$ kpc because of the substructure. Hence, except for A2256, the clusters have a_x and β that agree well with those found in the literature (e.g., Jones & Forman 1984; Briel, Henry, & Bohringer 1991).

5.2.3 Ellipticity

We quantify the elongation of the clusters using the iterative moment technique introduced by Carter & Metcalfe (1980). This method is particularly suited to measure the aggregate ellipticity of the clusters in a large aperture (see BT and Buote & Canizares [1994] for detailed discussions). In essence, this technique entails computing the analogue of the two-dimensional moments of inertia arrived at by iterating an initially circular region; the square root of the ratio of the principal moments is the axial ratio and the orientation of the principal moments yields the position angle. The parameters obtained from this method, ϵ_M and θ_M, are good estimates of the ellipticity (ϵ) and position angle (θ) of an intrinsic elliptical distribution of constant shape and orientation. For a more complex intrinsic shape distribution, ϵ_M and θ_M are average values weighted heavily by the outer parts of the region.

We applied a simple Monte Carlo procedure to characterize the uncertainties on ϵ_M and θ_M due to undetected point sources and Poisson noise. For each cluster we simulated β models having the best-fit a_x and β obtained in §5.2.2 modified to have a

constant ellipticity and orientation; i.e. we replaced $R = \sqrt{x^2 + y^2}$ with the elliptical radius $\sqrt{x^2 + y^2/q^2}$, where q is the constant axial ratio. These models were scaled to have the same number of counts (or count rate) as the background-subtracted PSPC images of the clusters. We then added the uniform background for each cluster (see Table 1). To each image we added point sources having spatial properties consistent with the PSPC PSF and numbers consistent with the $\log N(> S)$ - $\log S$ distribution given by Hasinger (1992); see Buote & Tsai (1995b) for a detailed discussion. Finally, we added Poisson noise to the composite images. Since ϵ_M is unaffected by a uniform background (see Carter & Metcalfe) we did not then subtract the background. We performed 1000 simulations each for a suite of input ellipticities ($\epsilon_x = 1 - q$) for each cluster.

To determine the 95% confidence intervals on the measured ϵ_M we proceeded as follows; for now we focus our attention on a particular aperture size. We arrange the results of the 1000 simulations for a given input ϵ_x into ascending order of measured ellipticity ϵ_M; i.e. $\epsilon_M^1 < \epsilon_M^2 < \cdots < \epsilon_M^{1000}$. The 95% upper limit for this model is defined to be the value of ϵ_M corresponding to the $0.95 \times 1000 = 950$th value of ϵ_M in the ordered array; i.e. ϵ_M^{950}. The 95% confidence lower limit of the real data is given by the model with input ϵ_x whose ϵ_M^{950} just equals the measured value of ϵ_M from the real image (see below). Similarly, the 95% confidence upper limit of the real data is given by the model with input ϵ_x whose ϵ_M^{50} just equals the measured value of ϵ_M from the real image.

We estimated the confidence limits for the position angles θ_M from the model having $\epsilon_x = \epsilon_M$ of the data for the specific aperture size. We define the 95% confidence limits to be $(\theta_M^{25}, \theta_M^{975})$. This procedure is not the most rigorous means to determine the uncertainties on θ_M because the value of ϵ_M in each simulation is not equal to ϵ_x. Since, however, we do not use θ_M in our modeling (see §5.3.1) the estimates are sufficient for our purposes.

In Table 3 we list the values of ϵ_M and θ_M and their associated 95% confidence limits for different apertures (in 5 pixel increments) for each of the clusters. Similar to our analysis of the radial profiles, we excluded the cooling-flow regions of A2029

and A2199 from the ϵ_M computation. Similarly, we excluded the region $a \lesssim 300h_{80}^{-1}$ kpc for A2256 to lessen the influence of the core substructure. Generally the values of ϵ_M are larger than the ellipticities obtained by BC (Buote 1992; also Fabricant et al. 1984 for A2256) from *Einstein* IPC images of these clusters reflecting the superior spatial resolution of the PSPC; note BC used a slightly modified version of the iterative moment technique. All of the clusters except A1656 have ϵ_M that are consistent within their uncertainties with being monotonically decreasing with increasing aperture size; in fact, the ellipticities of Coma appear to be increasing with radius but over a much smaller range. The position angles vary $\lesssim 10°$ over the regions probed except for Coma and A2029 which have $\sim 15°$ variations. The θ_M are generally in good agreement with the previous IPC studies and with the orientations of the galaxy isopleths (Carter & Metcalf).

Following BT we designated two apertures within the $\sim 1.5h_{80}^{-1}$ Mpc regions for use in constraining the mass models in §5.3.1; for Coma we only used the largest aperture available. Using two large, well-separated apertures is in keeping with our scheme to analyze the aggregate structure of clusters while still allowing us to obtain information on any ellipticity gradients. We denote these special apertures with an asterisk in Table 3.

5.3 Intrinsic Shapes and Mass Profiles from the X-rays

5.3.1 Method

The technique we use to constrain the intrinsic shape and mass profile of the total gravitating mass for a cluster of galaxies is discussed in detail by BT. Buote & Canizares (1994,1995a) describe how we use the the observed light distributions to infer the shape and profile of the dark matter from X-ray images. We refer the reader to these papers for exposition of the modeling procedures we employ in this paper. Here we summarize only a few small additions to the method introduced for this

particular study.

Because of the increasing evidence from gravitational-lens observations of giant arcs (e.g., Miralda-Escude & Babul 1995) and N-body simulations (e.g., White 1995) that galaxy clusters have small or perhaps no core radii, in this paper we will explore density profiles that are simple generalizations of the Hernquist (1990) model,

$$\rho_H \propto (am)^{-1} (R_c + am)^{-n}, \tag{5.2}$$

where R_c is a core parameter, a is the semi-major axis of the bounding spheroid of the SMD (Spheroidal Mass Distribution – see BT), and m is the dimensionless spheroidal radius. For $am \ll R_c$, $\rho_H \sim r^{-1}$, and thus these densities have no core. At large radii, $am \gg R_c$, $\rho_H \sim r^{-(n+1)}$ and falls as r^{-4} for the Hernquist (1990) density ($n = 3$) we used in previous studies. We consider models having n ranging from $1 - 3$ which covers plausible ranges of density profiles of clusters. These models complement the "cored" power-law SMD models ($\rho \propto [R_c^2 + (am)^2]^{-\eta}$) that we also use to model the masses of clusters.

To describe the mass distribution of the X-ray-emitting gas We use simple models having isodensity surfaces that change shape with radius. We are lead to this choice since the X-ray ellipticity profiles of the clusters measured from the PSPC data (Table 3) display significant gradients. An accurate model for the gas distribution is desirable not only for obtaining a precise measure of the total gas mass, but also for constraining the shape and profile of the dark matter. That is, in galaxy clusters the dominant mass component is the dark matter which typically contains $80\% - 90\%$ of the mass. The gas mass is $10\% - 20\%$ of the total while the mass of the stellar material, which is not nearly as well constrained as the gas, is generally much smaller than the gas mass (e.g., the case of A2256 – Briel & Henry 1994). Since the total mass of the galaxies is not well constrained, and in any case probably insignificant with respect to the gas, we neglect it (i.e. $M_{tot} = M_{gas} + M_{DM}$); note that for elliptical galaxies the opposite is true – the gas may be neglected in favor of the stellar mass (e.g., Buote & Canizares 1994,1995a).

The models we use to describe the gas mass are the oblate (and prolate, see below) spheroids of varying ellipticity introduced by Ryden (1990). Ryden computes the monopole and quadrupole terms of the gravitational potential generated by a mass distribution of concentric, oblate, spheroidal shells whose eccentricity ($e^2 = 1 - q^2$) varies as a function of the semi-major axis of the shell. Like Ryden, we consider spheroids that have eccentricity,

$$e(a) = \frac{e_0}{1 + (a/a_0)^\alpha}, \tag{5.3}$$

where we have inserted the extra parameter e_0 to allow for an arbitrary central eccentricity. This simple function yields surprisingly good descriptions of the ellipticity profiles of the X-ray isophotes (see Table §3). Since we also desire to explore prolate models we extend Ryden's formalism to the prolate case in the Appendix.

For each cluster we construct Ryden models for the gas mass. Since β models describe the radial profiles of the clusters in our sample so well (§5.2.2) we model the three-dimensional density profiles as $\rho_{gas} = (a_x^2 + a^2)^{-3\beta/2}$. Here a_x and β are the best-fit parameters obtained from fitting the β model convolved with the PSPC PSF to all of the radial bins for each cluster. To completely specify the gas model we assign $e(a)$ (eqn. [5.3]) to ρ_{gas} appropriate to the ellipticity of the X-rays. That is, we generate a model X-ray surface brightness from projecting ρ_{gas}^2 onto the sky plane and convolving it with the PSPC PSF. By comparing the ellipticities of this model with those of the real image (see Table 3) we determine the parameters of $e(a)$.

5.3.2 Shapes of the Composite Mass Distributions

Our procedure to constrain the hydrostatic models using the radial profiles (§5.2.2) and ellipticities (asterisked values in Table 3) is described in detail in BT §4.2. For all of the spheroidal models we set the symmetry axis to lie in the plane of the sky; i.e. we are not attempting to uncover projection effects in this analysis, although we believe them to be small for these clusters (see BC). We set the semi-major axis of the SMD models to $1.5h_{80}^{-1}$ Mpc for all the clusters.

Isothermal Models

Recent ASCA observations show that that gas is nearly isothermal within the central $\sim$ 1 Mpc of rich clusters (Mushotzky 1995). Since the shape of a cluster inferred from X-ray analysis is mostly insensitive to small temperature gradients (BT; also Strimple & Binney 1979 and Buote & Canizares 1994), we focus our attention on isothermal models. The effects of temperature gradients consistent with PSPC data are discussed in §5.3.2.

We list in Table 5 the 95% confidence limits on the ellipticities of the composite mass (ϵ_{mass}) for the isothermal models that best characterize the X-ray data. Similar to our experience from fitting the β models (§5.2.2), the isothermal models give excellent visual fits to the data but with rather large values of χ^2. The two cooling-flow clusters, A2029 and A2199, require steep mass density profiles ($\rho_{mass} \sim r^{-4}$) to reproduce the observed ellipticity gradients of the X-rays; even with this steep density the models for A2029 only marginally reproduce the X-ray ellipticity gradient within the estimated 95% confidence uncertainties. The ellipticities in Table 5 for A2029 and A2199 are for the Hernquist (1990) models (i.e. $n = 3$ in eq.[5.2]), although the cored power-law models with $\eta = 2$ give essentially identical values.

The clusters A401 and A2256, which have no observed cooling flows (Fabian 1994), also have steep X-ray ellipticity gradients that imply steep mass density profiles ($\rho_{mass} \sim r^{-4}$). For these clusters, though, we list the results in Table 5 for the cored power-law models with $\eta = 2$ since their radial profiles have large core radii (§5.2.2); as was the case for A2029 and A2199, the ellipticities for A401 and A2256 are not substantially sensitive to the density model and we obtain similar results for the Hernquist models. Coma, for which we only use a single aperture to constrain the ellipticity (and thus have no information on the large-scale ellipticity gradient), is fitted equally well by all of the models considered. We show in Table 5 the results for both the $\eta = 1, 2$ cored power-law models ($\rho_{mass} \sim r^{-2}$ and $\rho_{mass} \sim r^{-4}$).

The ellipticities required by the isothermal models are quite large for all of the clusters, much larger than those we obtained from analysis of *Einstein* IPC data in

BC. However, the ellipticities for A2256 are in good agreement with IPC analyses of Fabricant, Rybicki, & Gorenstein (1984) and Buote (1992). We attribute the discrepancy to BC not accounting for the steep ellipticity gradients of the X-ray isophotes obtained for these clusters (see Table 3). In BC we selected only one aperture size to constrain the X-ray ellipticity and the size of the aperture was only a few times the width of the IPC PSF for all the clusters but Coma (and Perseus). Since in BC we did not incorporate the IPC PSF into the hydrostatic modeling procedure we did not accurately estimate the uncertainty due to possible ellipticity gradients being smeared out by the IPC PSF. In the case of Coma the discrepancy is due primarily to the larger aperture we use in this paper to compute the X-ray ellipticity; when we use the same aperture size as in BC we obtain ϵ_{mass} in good agreement. The agreement of the shape of A2256 with previous analyses appears to have been due to a fortuitous conspiracy of the different region analyzed in this paper and the larger X-ray ellipticities due to the better spatial resolution of the PSPC.

Models with Temperature Gradients

We now consider temperature gradients allowed by the PSPC data. Unfortunately, since the PSPC energy band corresponds to much lower energies than the temperatures of the rich clusters in our sample we are unable to obtain precise constraints on the temperature gradients. In general we find that the uncertainty in the gradients allowed by the PSPC data dwarf those obtained by PV-phase ASCA observations of rich clusters (Mushotzky 1995). Instead of giving serious consideration to models that do not appear to be realistic, we will simply illustrate this uncertainty with the case of A2029. We defer serious consideration of the effects of real temperature gradients in these clusters on the shapes to analysis of ASCA data (Buote & Canizares 1995b).

In order to obtain the narrowest constraints on the temperature gradient we placed plausible restrictions on the spectrum and the temperature profile. Our intention is to demonstrate that even when such restrictions are applied there is still an implausibly large range of temperature gradients allowed. We first divide the surface brightness of A2029 into two annular regions having equal S/N: (140-336,336-1400) h_{80}^{-1} kpc; we

exclude the region $r < 140h_{80}^{-1}$ kpc because of the cooling flow. The temperature of each region was determined by fitting (with XSPEC) a Raymond-Smith (1977) model with Galactic absorption and 50% solar metallicities. We obtain $T_{in} = 7.7(6.7 - 9.3)$ keV and $T_{out} = 6.1(4.8 - 8.1)$ keV at 68% confidence.

We take the three-dimensional temperature profile to follow a broken power law,

$$T(r) = T_0 \qquad r \leq r_0 \tag{5.4}$$

$$T(r) = T_0 \left(\frac{r}{r_0}\right)^p \qquad r > r_0 \tag{5.5}$$

where $r_0 \equiv 140h_{80}^{-1}$ kpc, and T_0 and p are free parameters. For the purposes of the determination of the temperature gradients implied by the spectral constraints, we suppress the information supplied by the elongation of the X-ray isophotes which only has a small effect on the parameters T_0 and p. However, for the hydrostatic models (see below) we force the isotemperature surfaces given by equation [5.5] to be stratified on the isopotential surfaces.

We construct the emission-weighted temperature ($\langle T \rangle$) projected along the line of sight (dl) into an area dA,

$$\langle T \rangle = \frac{\int dA \int_{-\infty}^{\infty} j_{gas} T \, dl}{\int \Sigma_x \, dA}, \tag{5.6}$$

where j_{gas} is the gas volume emissivity and $\Sigma_x = \int_{-\infty}^{\infty} j_{gas} \, dl$ is the surface brightness.

To determine T_0 and p we evaluate equation[5.6] over A corresponding to the two annular regions (140-336,336-1400) h_{80}^{-1} kpc and then perform a χ^2 fit to the 68% confidence limits on the temperatures; note we defined the temperatures in the bins to be the middle of the 68% confidence temperature results and the 1σ weights are half the widths of the confidence intervals.

The best-fit parameters are $T_0 = 8.8$ keV and $p = -0.27$; the 68% lower limit is $T_0 = 11.1$ keV and $p = -0.68$ and the upper limit is $T_0 = 6.7$ keV and $p = 0.07$. The slopes of the best-fit ($p = -0.27$) and 68% lower limit ($p = -0.65$) temperatures imply substantially larger gradients than observed in real clusters (Mushotzky 1995),

although the 68% upper limit slope is modest ($p = +0.07$). We list in Table 6 the derived mass ellipticities for the temperature gradients determined above using the same mass density models for A2029 given in Table 5. As expected, the ellipticities for the small gradient given by the 68% upper limit are shifted down only by ~ 0.03 with respect to the isothermal results; even ϵ_{mass} for the best-fit temperature parameters are shifted upwards by only ~ 0.05. However, the very large gradient given by the 68% lower limit temperature gradient implies implausibly flat mass distributions for a non-rotating, self-gravitating mass (Merritt & Stiavelli 1990; Merritt & Hernquist 1991).

5.3.3 The Gas Mass and Composite Mass

In order to determine the shapes of the dark matter we must first know the ratio of the gas mass to total gravitating mass (see §5.3.1) for the clusters. To compute the gas mass we simply integrated the models for ρ_{gas} in §5.3.1. We normalized ρ_{gas} for each cluster by first constructing the X-ray emissivities, j_{gas}, (see eq.[9] of Buote & Canizares 1994) from ρ_{gas} and then projected j_{gas} onto the sky plane to obtain Σ_x. We then normalized Σ_x to the total flux between 0.5 - 2.0 keV determined by fitting the spectrum (with PROS) to a Raymond-Smith (1977, updated to 1992 version) model with Galactic absorption (David et al. 1993 who use the results of Stark et al. 1992) and temperatures from Edge et al. (1990); see Table 2. By normalizing to the flux we have completely specified ρ_{gas} and hence the gas mass. Our estimates for the gas mass take into account the following uncertainties: (1) 95% confidence statistical errors on the β-model parameters (see Table §3) used to define the radial profile of ρ_{gas}, (2) oblate and prolate geometry, and (3) variation in flux and plasma emissivity due to the 90% uncertainties in the gas temperatures from Edge et al.. There is an additional source of uncertainty due to the restriction of the adopted models for ρ_{gas} to having radial profiles of the β models. Since, however, the β models describe the clusters so well over the regions considered the uncertainty in the gas mass should be quite small, certainly $\lesssim 10\%$. We list in Table 9 the gas masses computed in spheres of radii $(0.5, 1.0, 1.5)h_{80}^{-1}$ Mpc considering (1) - (3) for all of the clusters; note for

Coma we only compute the gas mass out to $0.5h_{80}^{-1}$ Mpc.

The gas masses are extremely well constrained for the clusters, generally to better than a few percent. Our values for M_{gas} appear to be slightly larger than estimates found in the literature. White & Fabian (1995) used *Einstein* IPC data to compute gas masses and total masses of clusters assuming spherical symmetry for a sample of Abell clusters, including A401 and A2029. They obtain $M_{gas} = 1.32 \pm 0.07 \times 10^{14} M_{\odot}$ for A401 ($r \leq 1.265$ Mpc) and $M_{gas} = 1.26 \pm 0.11 \times 10^{14} M_{\odot}$ for A2029 ($r \leq 1.291$ Mpc), all quantities evaluated for $H_0 = 50$ km s^{-1} Mpc^{-1}; note that $M_{gas} \propto h^{-5/2}$. Using the same apertures and Hubble constant as White & Fabian we obtain $M_{gas} = (1.99 - 2.02) \times 10^{14} M_{\odot}$ for A401 and $M_{gas} = (1.90 - 1.97) \times 10^{14} M_{\odot}$ for A2029. Although our values are only $\sim 50\%$ larger, the discrepancy appears to be significant within the estimated uncertainties. White & Fabian, however, acknowledge that their estimates of the gas masses are likely to be somewhat conservative because of the procedure they employ to obtain core radii for the gas profiles. If we neglect the ellipticity of the surface brightness the masses are hardly affected; e.g., $M_{gas} = (1.85 - 1.92) \times 10^{14} M_{\odot}$ for A2029. This confirms earlier statements that ellipticity has negligible impact on estimates of gas masses in clusters (e.g., White et al. 1994). By extrapolating our model for ρ_{gas} to a 3 Mpc ($H_0 = 50$ km s^{-1} Mpc^{-1}) radius for A2029 we obtain $M_{gas} = (5.6 - 5.9) \times 10^{14} M_{\odot}$, in good agreement with Jones & Forman's (1984) value of $M_{gas} = 5.3 \times 10^{14} M_{\odot}$ obtained from IPC data considering their expected (unstated) uncertainties.

The gas mass for A2256 has been computed by Briel & Henry (1994) using the ROSAT PSPC data. They obtain $M_{gas} = 6.33 \pm 1.17 \times 10^{14} M_{\odot}$ within a 1.4 Mpc radius ($H_0 = 100$ km s^{-1} Mpc^{-1}). At this distance we obtain (neglecting the ellipticity of the gas) $M_{gas} = (7.46 - 7.84) \times 10^{14} M_{\odot}$, only $\sim 15\%$ larger than the result of Briel & Henry (1994). This small discrepancy can likely be attributed to that fact that Briel & Henry exclude a large section of the data from analysis (as explained in Henry, Briel, & Nulsen 1993) in order to avoid the subclump in the interior.

Using the isothermal spheroidal models of Table 5 we present in Table 9 the total gravitating masses of the clusters computed in spheres of radii $(0.5, 1.0, 1.5)h_{80}^{-1}$ Mpc.

The uncertainties in the masses reflect 95% confidence statistical errors on R_c and n (or η) from the mass models and the 90% errors on the temperatures from Edge et al. which is the dominant source of uncertainty. When scaled to 1.4 Mpc ($H_0 = 100$ km s^{-1} Mpc^{-1}), we obtain $M_{tot} = (1.2-2.1) \times 10^{15} M_\odot$ for A2256, in excellent agreement with the result of Briel & Henry (1994), $\sim 9.5 \times 10^{14} M_\odot$, which only considers statistical uncertainties on the β-model parameters (not temperature variations). As expected, we find that the masses derived assuming spherical symmetry agree very well with those incorporating the ellipticity of the X-ray isophotes; the viability of X-ray mass estimates assuming spherical symmetry has already been addressed in the literature (Tsai, Katz, & Bertschinger 1994; Navarro, Frenk, & White 1995). All of the clusters in our sample that are measured to large radii have M_{gas}/M_{tot} increasing with radius. Scaling to $H_0 = 50$ km s^{-1} Mpc^{-1} the mass ratios are $(8-22)\%$ consistent with the results of White & Fabian (1995) for their sample of 19 Abell clusters; $M_{gas}/M_{tot} \propto h^{-3/2}$.

5.3.4 Shapes of the Dark Matter Distributions

Using the ratios M_{gas}/M_{tot} in Table 9 we determine the ellipticity of the dark matter distributions, ϵ_{DM}, for the clusters. In order to consider the maximum possible effects of the self-gravitation of the gas we also consider the upper limits of M_{gas}/M_{tot} scaled to $H_0 = 50$ km s^{-1} Mpc^{-1}; i.e. this scaling amounts to doubling the values of M_{gas}/M_{tot} in Table 9. The results for ϵ_{DM} corresponding to the mass models in §5.3.2 (see Table 5) are listed in Table 14. The ellipticities of the dark matter are hardly affected upon consideration of the self-gravitation of the gas; i.e. for all the clusters $\epsilon_{DM} \approx \epsilon_{tot} + 0.02$.

Also listed in Table 14 are the 1σ ellipticities of the galaxy isopleths, ϵ_{gal}, computed by Carter & Metcalfe (1980) using the same iterative moment technique of §5.2.3. All of clusters have ϵ_{DM} consistent with ϵ_{gal} within the $(1-2)\sigma$ uncertainties of ϵ_{gal}, although ϵ_{DM} for A2256 is only marginally consistent with the 2σ lower limit for ϵ_{gal}. The case for A2256 is actually uncertain since Fabricant, Kent, & Kurtz (1989) obtained a much smaller lower limit for $\epsilon_{gal} = 0.23$ (90% confidence) using a different

sample with more redshifts and a different technique to compute the ellipticity from Carter & Metcalf. Hence, the shapes of the dark matter distributions and galaxy isopleths are consistent for each of the clusters in our sample contrary to our previous conclusions in BC.

Finally, the ellipticities of the dark matter distributions for the clusters are consistent with the predictions from dissipationless formation of halos in a universe filled with Cold Dark Matter (Frenk et al. 1988; Efstathiou et al. 1988). The dark matter halos produced by these N-body simulations are triaxial and generally have $\epsilon_{DM} \leq 0.5$ but several have ϵ_{DM} approaching 0.67. Our mass models fit the observed X-ray radial profiles and ellipticities equally well for both oblate and prolate models which is consistent with the halos being typically triaxial. These results are also consistent with the cluster formed in the simulation of Katz & White (1993) which has $\epsilon_{DM} = 0.54$ within $1.5h_{50}^{-1}$ Mpc (see BT).

5.4 Conclusions

We have analyzed ROSAT PSPC X-ray images of five bright, low-redshift ($z < 0.1$) Abell clusters for the purpose of constraining their intrinsic shapes and mass profiles. The intrinsic shapes of the clusters in our sample (A401,A1656,A2029,A2199,A2256) were analyzed previously by us (Buote & Canizares 1992; Buote 1992) using *Einstein* IPC X-ray images. In this paper we specifically follow Buote & Tsai's (1995a) procedure to constrain the aggregate shapes of clusters on large scales ($\sim$ 1.5 Mpc) to reduce the effects of possible substructure in the cluster cores ($\lesssim$ few hundred kpc).

For all the clusters we computed the azimuthally averaged radial profiles and ellipticities (i.e. quadrupole moments) of the X-ray surface brightness distributions within $\sim 1.5h_{80}^{-1}$ Mpc for the all clusters except Coma where we were restricted to $\sim 0.5h_{80}^{-1}$ Mpc. Fitting β models to the radial profiles yields very precise constraints on the core radii and β parameters in good agreement with previous results from *Einstein* (e.g., Jones & Forman 1984). The ellipticities of the X-ray images are also tightly constrained in their 95% confidence intervals and are systematically larger

($\epsilon \approx 0.15 - 0.25$) than those ($\epsilon \approx 0.10 - 0.20$) obtained by Buote & Canizares (1992; Buote 1992) using *Einstein* data. This discrepancy is a direct result of the superior spatial resolution of the PSPC. All of the clusters (except Coma) display substantial ellipticity gradients within $r \sim 1.5 h_{80}^{-1}$ Mpc not seen in the *Einstein* data.

Using the X-ray radial profiles and ellipticities and assuming hydrostatic equilibrium we constrained the ellipticity of the total gravitating matter following Buote & Tsai (1995a). Isothermal mass models for the clusters yield ellipticities, $\epsilon_{mass} \approx 0.40 - 0.55$ (95% confidence), which are systematically larger (i.e. $\Delta\epsilon_{mass} \sim 0.15$) than obtained by Buote & Canizares (1992; Buote 1992) using *Einstein* data; we understand this discrepancy to be a combination of effects due to different cluster regions being probed, modeling differences between the two investigations, and most importantly the X-ray ellipticity gradients obtained from the PSPC data. We mention that the measured X-ray ellipticity gradients require steep mass profiles ($\rho \sim r^{-4}$) for our SMD models; i.e. models where the mass is stratified on concentric spheroids of constant ellipticity. Of course, this does not exclude the possibility of a flatter profile where the mass changes shape with radius. Models with small temperature gradients typical for rich clusters (Mushotzky 1995) affect the isothermal ϵ_{mass} estimates by $< 10\%$.

We computed the masses of the X-ray–emitting gas and the total gravitating matter in spheres of radii $(0.5, 1.0, 1.5) h_{80}^{-1}$ Mpc using the 95% statistical uncertainties of our gas and total mass models and the 90% uncertainties on the gas temperatures from Edge et al. (1990). The effects of the X-ray ellipticity on the gas masses is generally less than a few percent in agreement with the result of White et al. (1994). The ratio of gas mass to total gravitating mass of the clusters increases with radius and has values $M_{gas}/M_{tot} = (4\% - 11\%) h_{80}^{-3/2}$ within a $1.5 h_{80}^{-1}$ Mpc radius, in excellent agreement with the results of White & Fabian (1995) and thus consistent with the "Baryon Catastrophe" proposed by White et al. (1993).

The shapes derived for the dark matter distributions using the isothermal models are essentially identical to those obtained for the total gravitating matter: $\epsilon_{DM} \approx \epsilon_{tot} + 0.02$. The observed ellipticities of the galaxy isopleths (Carter & Metcalf 1980)

are consistent with the ellipticities of the dark matter. Moreover, the ellipticities of dark halos predicted by N-body simulations of a universe dominated by cold dark matter (Frenk et al. 1988; Efstathiou et al. 1988; Katz & White 1993) agree with the results for the clusters in our sample.

Our modeling procedure has generated tight constraints on the intrinsic ellipticities and density profiles of the dark matter from the X-ray data. To obtain the most general constraints a non-parametric estimation of the dark matter is warranted and should be feasible given the high S/N and spatial resolution of the observations along with the highly relaxed appearance of A401, A2029, and A2199 (see Buote & Tsai 1995b for discussion of judging degree of relaxation). For these clusters a non-parametric treatment simply involves solving the hydrostatic equation for the potential in terms of the gas density and temperature which may be obtained from general spheroidal deprojection following Palmer (1994).

It is a pleasure to thank E. Bertschinger and J. Tonry for insightful discussions. We extend our gratitude to R. Mushotzky for communicating unpublished ASCA results on the temperature profiles in clusters, M. Corcoran for assistance with the ROSAT archive, D. Harris for his advice regarding merging PSPC images, and to U. Hwang for providing software to compute plasma emissivities. We acknowledge use of the following astrophysical databases: ADS, HEASARC-Legacy, NED, and SIMBAD. This research was supported by grants NAG5-1656, NAS8-38249 and NASGW-2681 (through subcontract SVSV2-62002 from the Smithsonian Astrophysical Observatory).

A. Prolate Ryden Potentials

Ryden (1990) computes the gravitational potentials (up to quadrupole order) of oblate spheroids having ellipticity that varies with radius. Generalization of Ryden's result to prolate spheroids is a straightforward (albeit tedious) application of the multipole expansion of the three-dimensional gravitational potential (e.g., Binney & Tremaine

1987). Ryden considers the three-dimensional density distribution to be completely specified by the density, $\rho(a)$, along the semi-major axis, a, and the eccentricity, $e(a)$, of the isodensity surfaces. The isodensity surface for the prolate case is,

$$\frac{r^2\cos^2\theta}{a^2} + \frac{r^2\sin^2\theta}{a^2(1-e^2)} = 1, \tag{A1}$$

where r is the distance from the center, θ is the conventional polar angle, and we have suppressed the dependence on a in e for notational convenience. Expressing the gradient in eccentricity as,

$$\Sigma = \frac{a}{1-e^2}\frac{d(1-e^2)}{da}, \tag{A2}$$

the mass of a thin shell of matter of width δa and uniform density ρ is,

$$\delta M = 4\pi(1-e^2)\rho a^2 \delta a\,[1+\Sigma/3]\,. \tag{A3}$$

The oblate potential is completely specified by the coefficients for the interior and exterior potential given by Ryden's equations (7) and (12). For the prolate case we obtain the following values,

$$B_{00} = 8\pi\sqrt{\pi}G\rho a(1-e^2)(1+\Sigma/3) \tag{A4}$$

$$B_{20} = \frac{8\pi\sqrt{\pi}}{3\sqrt{5}}G\rho a e^2(1-e^2)\left[1+\frac{3-2e^2}{5e^2}\Sigma\right] \tag{A5}$$

$$C_{00} = 4\pi\sqrt{\pi}G\rho a(1-e^2)\left[I+\left(\frac{1+e^2}{2}I-1\right)\frac{\Sigma}{2e^2}\right] \tag{A6}$$

$$C_{20} = \frac{\pi\sqrt{\pi}}{\sqrt{5}}G\rho a\frac{(1-e^2)}{e}\frac{dA}{de}\Sigma, \tag{A7}$$

where,

$$I(e) = \frac{1}{e}\ln\left(\frac{1+e}{1-e}\right) \tag{A8}$$

$$A(e) = 2\frac{1-e^2}{e^2}\left[\frac{1}{2}I-1\right]. \tag{A9}$$

Substituting the coefficients into equations (16) and (17) of Ryden gives the prolate gravitational potential up to quadrupole order.

Table 1: Cluster Observations

Cluster	Sequence #	Exposure (s)	Background (10^{-4} cts s^{-1} $arcmin^{-2}$)
A401	rp800235	7465	2.07
	wp800182	6797	
A1656	rp800005	22183(20032)	4.08
	rp800006	21893(20136)	
	rp800009	20691(19604)	
	rp800013	22427(20954)	
A2029	rp800249	12550	5.50
A2199	wp150083	10563	3.14
A2256	wp100110	17865(14572)	2.50
	wp800162	9108(5380)	
	wp800163	10803(6690)	
	wp800339	4978(2437)	
	wp800340	9430(7119)	
	wp800341	10480(7469)	

Note. — Time-filtered exposure times are given in parentheses.

Table 2: Pixel Scales

		Radial Profile		D_{max}	Ellipticity		
Cluster	z	(arcsec)	(h_{80}^{-1} kpc)	(h_{80}^{-1} kpc)	(arcsec)	(h_{80}^{-1} kpc)	Flux
A401	0.0748	40	54.4	1251	20	27.2	29.6-29.7
A1656	0.0232	105	44.3	487	45	19.0	153
A2029	0.0768	40	55.7	1448	20	27.9	40.6-41.0
A2199	0.0299	90	48.9	1321	30	16.3	63.8-64.0
A2256	0.0581	60	63.4	1458	30	31.7	34.0-34.4

Note. — D_{max} is the edge of the outermost bin of the radial profiles. The fluxes are between energies 0.5-2.0 keV (10^{-12} erg cm^{-2} s^{-1}) and are computed in a circle of radius D_{max}.

Table 3: β Models

	a_X (h_{80}^{-1} kpc)		β			
Cluster	bf	95%	bf	95%	χ^2	dof
A401	178	173-185	0.606	0.597-0.617	27	20
A1656	267	262-273	0.785	0.771-0.799	136	8
A2029	157	141-174	0.682	0.664-0.700	27	16
A2199	85	77-92	0.653	0.643-0.663	56	17
A2256	397	367-427	0.908	0.870-0.947	53	9

Note. — The 95% confidence limits reflect only statistical uncertainties on two interesting parameters.

Table 4: X-ray Ellipticities and Position Angles (N through E)

Cluster	a_{out} (h_{80}^{-1} kpc)	ϵ_M	95%	θ_M (deg)	95%
A401:	($a_{in} = 0$)				
	272	0.290	0.280-0.340	29.2	18.1-40.9
	408	0.214	0.190-0.240	33.4	29.1-37.8
	544*	0.238	0.225-0.265	38.3	35.0-41.7
	680	0.193	0.180-0.215	39.0	35.2-42.7
	816	0.174	0.155-0.190	37.6	33.3-41.0
	952*	0.175	0.155-0.190	33.1	28.4-37.9
	1088	0.148	0.125-0.165	29.2	24.3-34.2
A1656:	($a_{in} = 0$)				
	285	0.146	0.150-0.155	82.7	81.4-84.0
	380	0.160	0.160-0.165	93.2	92.7-93.6
	475*	0.199	0.200-0.205	97.7	97.2-98.2
A2029:	($a_{in} = 139$)				
	278	0.254	0.255-0.290	23.3	21.2-25.4
	418	0.257	0.255-0.285	22.1	19.7-24.4
	557*	0.207	0.190-0.225	19.6	16.4-22.3
	696	0.181	0.160-0.205	13.8	9.99-17.7
	836	0.155	0.140-0.180	12.5	7.88-17.2
	975*	0.131	0.110-0.160	10.9	4.23-17.2
	1114	0.116	0.090-0.160	10.5	2.78-18.5
	1253	0.100	0.060-0.125	2.19	-8.01-12.2
A2199:	($a_{in} = 114$)				
	245	0.195	0.180-0.210	42.9	39.6-46.1
	326	0.178	0.175-0.200	40.8	37.7-44.0
	408*	0.164	0.150-0.180	36.4	33.2-39.5
	489	0.149	0.135-0.165	36.8	33.1-40.7
	571	0.146	0.125-0.160	34.3	30.2-38.1
	652*	0.142	0.115-0.155	34.3	29.4-38.8
A2256:	($a_{in} = 317$)				
	634	0.286	0.280-0.290	122.6	122.1-123.1
	792	0.243	0.235-0.250	123.6	122.8-124.3
	951*	0.211	0.205-0.215	123.2	121.9-124.4
	1109	0.197	0.190-0.205	122.1	120.9-123.3
	1268	0.185	0.170-0.185	120.7	118.9-122.4
	1426*	0.164	0.130-0.155	119.3	116.6-121.4

Note. — a_{in} and a_{out} are respectively the inner and outer semi-major axes of the aperture.

Table 5: Shapes of The Total Gravitating Matter

Cluster	Model	Oblate ϵ_{mass}	Prolate ϵ_{mass}
A401	C ($\eta = 2$)	0.52-0.61	0.48-0.55
A1656	C ($\eta = 1$)	0.40-0.41	0.37-0.38
A1656	C ($\eta = 2$)	0.42-0.43	0.39-0.40
A2029	H ($n = 3$)	0.46-0.49	0.42-0.44
A2199	H ($n = 3$)	0.56-0.64	0.49-0.55
A2256	C ($\eta = 2$)	0.36-0.38	0.34-0.36

Note. — These are the 95% confidence uncertainties on ϵ_{mass} for the isothermal mass models of §5.3.2. The models are C = "cored" power law and H = Hernquist (see §5.3.1).

Table 6: Effects of Temperature Gradients on Mass Shapes

T Model	Oblate ϵ_{mass}	Prolate ϵ_{mass}
$p = -0.27$	0.51-0.56	0.47-0.50
$p = -0.65$	$\gtrsim 0.6$	$\gtrsim 0.6$
$p = +0.07$	0.43-0.46	0.40-0.42
$p = 0$	0.46-0.49	0.42-0.44

Note. — These are the 95% confidence uncertainties on ϵ_{mass} for A2029 for different temperature gradients (§5.3.2) where p corresponds to the temperature index in equation [5.5]. All of the models have Hernquist ($n = 3$) densities (see §5.3.1) and the $p = 0$ temperature index model is simply the isothermal case given in Table 5.

Table 7: Gas Mass and Composite Mass ($10^{14} M_{\odot}$)

	$0.5 h_{80}^{-1}$ Mpc			$1.0 h_{80}^{-1}$ Mpc			$1.5 h_{80}^{-1}$ Mpc		
Cluster	M_{gas}	M_{tot}	%	M_{gas}	M_{tot}	%	M_{gas}	M_{tot}	%
A401	0.276-0.288	9.2-10.6	3	0.863-0.884	14.1-25.0	3-6	1.54-1.64	16.0-35.8	4-10
A1656	0.258-0.259	4.4-7.5	3-6	...	...	...	...	...	...
A2029	0.287-0.308	6.0-13.0	2-5	0.799-0.843	11.4-22.5	4-7	1.38-1.53	14.5-26.8	5-11
A2199	0.144-0.147	9.4-12.7	1	0.387-0.408	12.2-17.0	2-3	0.657-0.711	13.2-18.3	4-5
A2256	0.232-0.256	3.4-5.9	4-8	0.725-0.753	9.4-16.8	4-8	1.16-1.28	12.9-22.3	5-10

Note. — These masses are each computed in a sphere of radii $(0.5, 1, 1.5) h_{80}^{-1}$ Mpc. The "%" column denotes the percent ratio M_{gas}/M_{tot}. The gas mass uncertainties represent the 95% errors of the β-model parameters and the 90% errors in the temperatures from Edge et al. (1990) as they affect determination of the X-ray flux and plasma emissivity. The composite mass uncertainties represent the 95% statistical uncertainties from the mass models and the 90% errors in the temperatures from Edge et al. (1990).

Table 8: Shapes of The Dark Matter

Cluster	Model	% M_{gas}/M_{tot}	Oblate ϵ_{DM}	Prolate ϵ_{DM}	r_{gal}	ϵ_{gal}
A401	C ($\eta = 2$)	10	0.53-0.62	0.48-0.56	0.625	0.46-0.66
		20	0.54-0.63	0.49-0.56		
A1656	C ($\eta = 2$)	5	0.43-0.44	0.40-0.41	0.313	0.51-0.71
		10	0.43-0.44	0.41-0.42	0.625	0.40-0.54
A2029	H ($n = 3$)	10	0.47-0.50	0.42-0.44	0.625	0.41-0.61
		20	0.48-0.51	0.43-0.45		
A2199	H ($n = 3$)	5	0.57-0.65	0.50-0.56	0.625	0.47-0.67
		10	0.58-0.66	0.51-0.58	1.25	0.45-0.63
A2256	C ($\eta = 2$)	10	0.37-0.39	0.34-0.36	0.469	0.50-0.70
		20	0.39-0.41	0.34-0.36		

Note. — These are the 95% confidence uncertainties on ϵ_{DM} for the isothermal mass models of Table 5 where now the models correspond to the dark matter for different ratios of gas mass to total mass. $r_{gal} \equiv \sqrt{ab}$ is the geometric mean radius (in h_{80}^{-1} Mpc) of the aperture used to compute the galaxy isopleth ellipticities, ϵ_{gal}, by Carter & Metcalfe (1980).

REFERENCES

Aarseth, S. J., & Binney, J. J. 1978, MNRAS, 185, 227

Aschenbach, B. 1988, Appl.Optics, 27, No. 8, 1404

Binney, J. J., & Silk, J. 1979, MNRAS, 188, 273

Binney, J., & Tremaine, S. 1987, Galactic Dynamics (Princeton: Princeton Univ. Press)

Briel, U. G., et al. 1991, A&A, 246, L10

Briel, U. G., & Henry, J. P. 1994, Nature, 372, 439

Briel, U. G., Henry, J. P., & Böhringer, H 1992, A&A, L31

Buote, D. A. 1992, S.M. Thesis, Massachusetts Institute of Technology

Buote, D. A., & Canizares, C. R. 1992, ApJ, 400, 385 (BC)

Buote, D. A., & Canizares, C. R. 1994, ApJ, 427, 86

Buote, D. A., & Canizares, C. R. 1995a, ApJ, in press

Buote, D. A., & Canizares, C. R. 1995b, ApJ, in preparation

Buote, D. A., & Tsai, J. C. 1995a, ApJ, 439, 29 (BT)

Buote, D. A., & Tsai, J. C. 1995b, ApJ, in press

Buote, D. A., & Tsai, J. C. 1995c, ApJ, submitted

Carter, D., & Metcalfe, N. 1980, MNRAS, 191, 325

Cavaliere, A., & Fusco-Femiano, R. 1976, A&A, 49, 137

David, L. P., Slyz, A., Jones, C., Forman, W., & Vrtlek, S. D. 1993, ApJ, 412, 479

Davis, D. S., & Mushotzky, R. F. 1993, AJ, 105, 409

Edge, A. C., Stewart, G. C., Fabian, A. C., & Arnaud, K. A. 1990, MNRAS, 245, 559

Efstathiou, G., Frenk, C. S., White, S. D. M., & Davis, M. 1988, MNRAS, 235, 715

Eisenstein, D. J., & Loeb, A. 1995, ApJ, in press

Fabian, A. C. 1994, ARA&A, 32, 277

Fabricant, D., Kent, S. M., & Kurtz, M. J. 1989, ApJ, 336, 77

Fabricant, D., Rybicki, F., & Gorenstein, P. 1984, ApJ, 286, 186

Frenk, C. S., White, S. D. M., Efstathiou, G., & Davis, M. 1988, ApJ, 327, 507

Giacconi, R. , et al. 1979, ApJ, 230, 540

Hasinger, G. 1992, in The X-ray Background (Cambridge: Cambridge University Press), ed. X. Barcons & A. C. Fabian, 229

Hasinger, G., Turner, T. J., George, I. M., & Boese, G., 1993, MPE/OGIP Calibration Memo CAL/ROS/93-015

Henry, J. P., Briel, U. G., & Nulsen, P. E. J. 199, A&A, 271, 413

Hernquist, L. 1990, ApJ, 356, 359

Jones, C., & Forman W. 1984, ApJ, 276, 38

Kaiser, N. 1991, ApJ, 383, 104

Kaiser, N., & Squiers, G. 1993, ApJ, 404, 441

Katz, N., & White, S. D. M. 1993, ApJ, 412, 455

Merritt, D., & Stiavelli, M. 1990, ApJ, 358, 399

Merritt, D., & Hernquist, L. 1991, ApJ, 376, 439

Miralda-Escudé, J. & Babul, A. 1995, ApJ, in press

Mohr, J. J., Fabricant, D. G., & Geller, M. J. 1993, ApJ, 413, 492

Mushotzky, R. F. 1995, in Dark Matter (AIP Conference Proceedings), ed. C. Bennett, (New York: AIP Press), in press

Navarro, J. F., Frenk, C. S., & White, S. D. M. 1995, MNRAS, in press

Palmer, P. L. 1994, MNRAS, 266, 697

Pfeffermann, E. et al., 1987, Proc. SPIE, 733, 519

Raymond, J. C., & Smith, B. W. 1977, ApJS, 35, 419

Ryden, B. S. 1990, MNRAS, 244, 341

Sarazin, C. L. 1986, Rev. Mod. Phys., 58, 1

Sarazin, C. L., O'Connell, W. O., & McNamara, B. R. 1992, ApJ, L59

Smail, I., Ellis, R. S., Fitchett, M. J., & Edge, A. C. 1995, MNRAS, 273, 277

Snowden, S. L., Plucinsky, P. P., Briel, U., Hasinger, G., & Pfeffermann, E. 1992, ApJ, 393, 819

Stark, A. A., et al. 1992, ApJS, 79, 77

Strimple, O., & Binney, J. 1978, MNRAS, 188, 883

Trümper, J. 1983, Adv. Space Res., 2, 241

Tsai, J. C., Katz, N., & Bertschinger, E. 1994, ApJ, 423, 553

West, M. J. 1995, in Clusters of Galaxies (Proceedings of the 29th Rencontres de Moriond), ed. F. Durret, A. Mazure, J. Trân Thanh Vân, & S. D. M. White (Gif sur Yvette: Frontier Editions), in press

White, D. A., & Fabian, A. C. 1995, MNRAS, 273, 72

White, D. A., Fabian, A. C., Allen, S. W., Edge, A. C., Crawford, C. S., Johnstone, R. M., Stewart., G. C., & Voges, W. 1994, MNRAS, 269, 589

White, S. D. M. 1995, in Dark Matter (AIP Conference Proceedings), ed. C. Bennett, (New York: AIP Press), in press

White, S. D. M., Briel, U. G., & Henry, J. P. 1993, MNRAS, 261, L8

White, S. D. M., Navarro, J. F., Evrard, A. E., & Frenk, C. S. 1993, Nature , 366, 429

Fig. 1.—

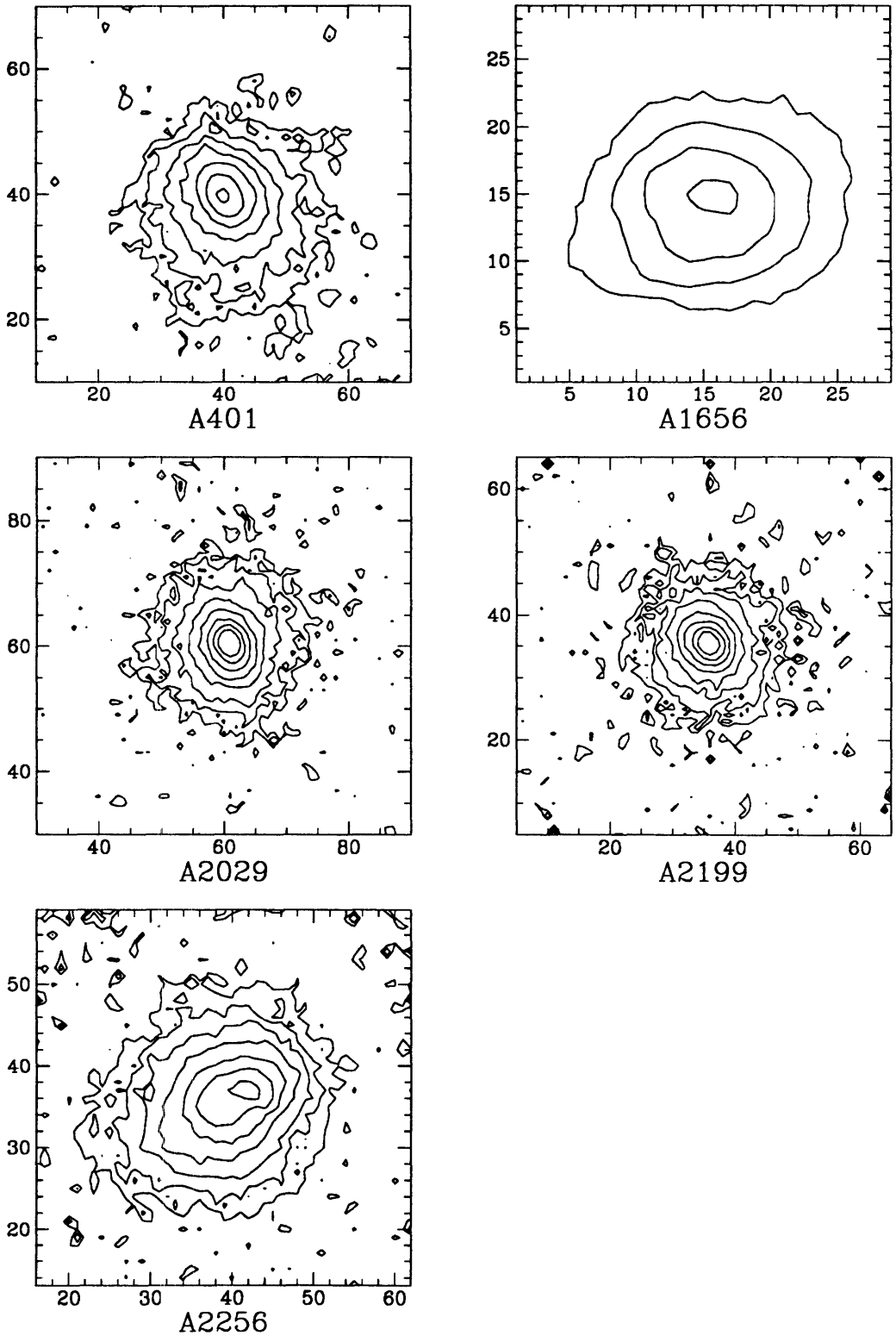

Fig. 2.—

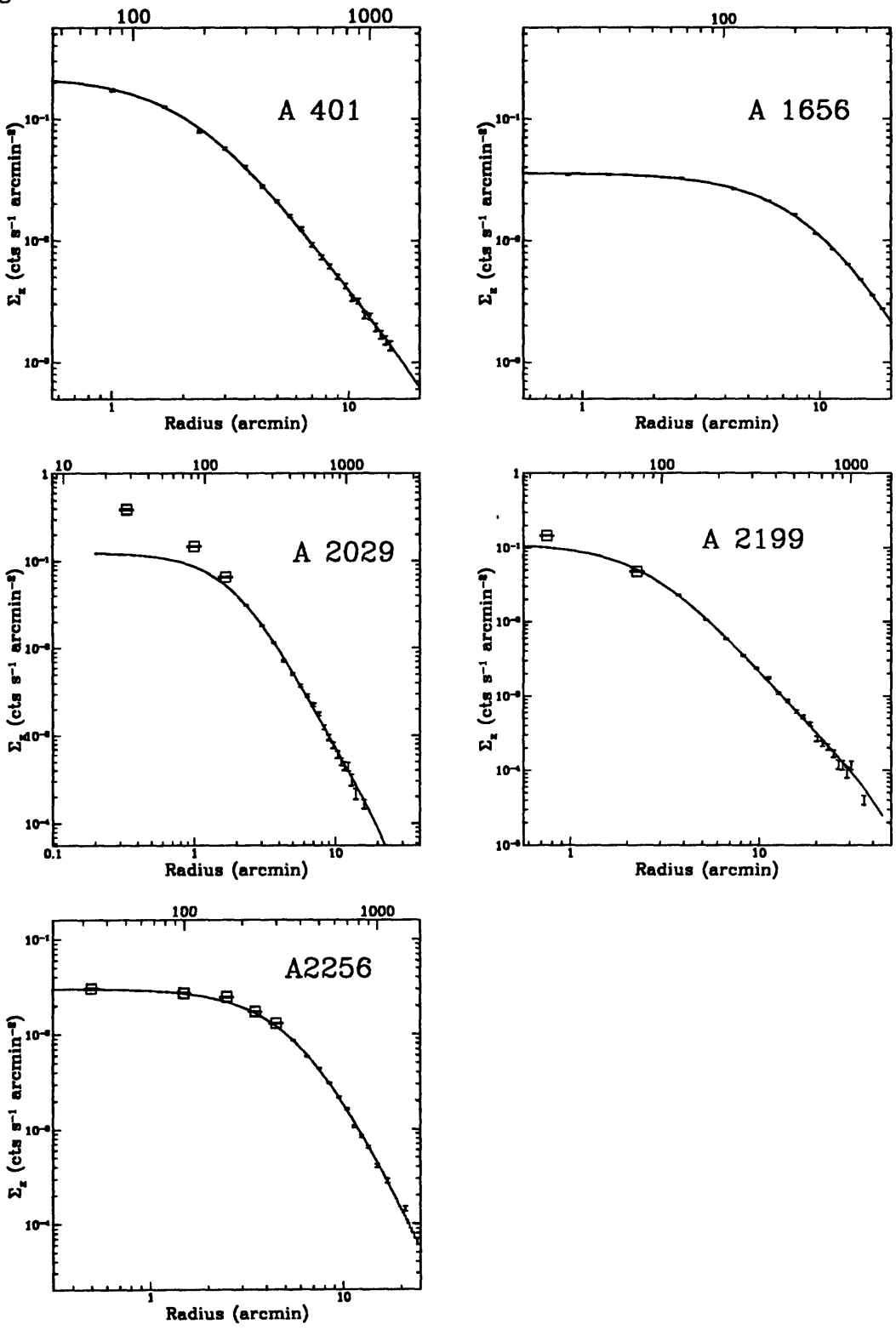
A 401
A 1656
A 2029
A 2199
A2256
Radius (arcmin)
Σx (cts s⁻¹ arcmin⁻²)

Chapter 6

Quantifying the Morphologies and Dynamical Evolution of Galaxy Clusters. I. The Method

Whereas in the previous two chapters we have analyzed the structure of clusters assuming that they are approximately equilibrium configurations, now we focus our attention on the nonequilibrium aspects of clusters. Specifically, we consider how the morphologies of clusters describe their evolutionary states. In this chapter we describe and test a method to quantitatively classify clusters of galaxies according to their projected morphologies. This method will be subsequently used to place constraints on cosmological parameters (Ω and the power spectrum of primordial fluctuations on scales at or slightly smaller than that of clusters) and to test theories of cluster formation. We specifically address structure that is easily discernible in projection and dynamically important to the cluster. The method is derived from the two-dimensional multipole expansion of the projected gravitational potential and yields dimensionless *power ratios* as morphological statistics. If the projected mass profile is used to characterize the cluster morphology, the power ratios are directly related to the cluster potential. However, since detailed mass profiles currently exist for only a few clusters, we use the X-ray–emitting gas as an alternative tracer of cluster morphology. In this case, the relation of the power ratios to the potential is qualitatively preserved.

We demonstrate the feasibility of the method by analyzing simulated observations of simple models of X-ray clusters using the instrument parameters of the ROSAT PSPC. For illustrative purposes, we apply the method to ROSAT PSPC images of A85, A514, A1750, and A2029. These clusters, which differ substantially in their X-ray morphologies, are easily distinguished by their respective power ratios. We discuss the suitability of this method to address the connection between cluster morphology and cosmology and to assess whether an individual cluster is sufficiently relaxed for analysis of its intrinsic shape using hydrostatic methods. Approximately 50 X-ray observations of Abell clusters with the PSPC will be amenable to morphological analysis using the method of this paper.

6.1 Introduction

Clusters of galaxies, the largest bound objects in the universe, are especially useful laboratories for probing the underlying cosmology (for reviews see Oegerle, Fitchett, & Danly 1990; Durret et al. 1995). The dynamical state of clusters in particular has received much recent attention because of its implications for estimations of the detailed mass distributions (e.g., Fitchett 1990) and intrinsic shapes (Buote & Tsai 1995a) of clusters, and it may provide a powerful constraint on the cosmological density parameter Ω (Richstone, Loeb, & Turner 1992, hereafter RLT; Evrard et al. 1993). These studies emphasize that the dynamical state of a cluster is qualitatively related to the degree of substructure present. Hence there is a need for a scheme that quantifies the morphology of clusters in relation to how much "dynamically relevant" substructure they possess.

What constitutes "dynamically relevant" substructure is at present poorly defined. For cosmological purposes RLT make the provisional suggestion that the relevant substructure must have a density contrast compared to the mean cluster density in the range 2-10, contain at least 20% of the cluster mass, and lie within a projected radius of 1.5 Mpc. Denser structures would also be important for studies of the underlying mass distribution and intrinsic shape.

Present techniques to measure substructure in clusters generally provide estimates of the statistical significance of the existence of substructure. The KMM algorithm (Ashman, Bird, & Zepf 1994), for example, detects and quantifies the significance that a given cluster is bimodal. Mohr, Fabricant, & Geller (1993) introduced the centroid shift to quantify substructure in X-ray images of clusters. Although useful for establishing the existence of substructure, these methods do not specifically address the relation of the structure to the dynamical state of the cluster.

We propose a method to quantitatively classify clusters of different morphologies in direct relation to the dynamical state of the cluster as indicated by the gravitational potential. We focus on structure that is obvious in projection; e.g., the morphological classes described by Jones & Forman (1992) for X-ray clusters. That is, the significance of the substructure is a given, what the structure implies for the cluster dynamics is the focus of this paper. The method yields dimensionless quantities that are especially suited to statistical analysis of a large cluster sample. Future papers will apply this technique to a large sample of X-ray clusters (Buote & Tsai 1995b) and to clusters generated by N-body / hydrodynamic simulations. In §6.2 we describe the method. We demonstrate the performance of the method on simple models of X-ray clusters in §6.3 and on simulated observations of these models with the ROSAT PSPC in §6.4. We apply the method to real ROSAT PSPC images of four Abell clusters in §6.5. In §6.6 we discuss the implications of our method. In §6.7 we present our conclusions.

6.2 Method

The objective of this paper is not to introduce another technique to detect subtle manifestations of substructure in galaxy clusters (e.g., Ashman et al. 1994; Bird & Beers 1993; for a comprehensive review see Bird 1993), but instead is to propose a simple quantitative scheme to categorize clusters (in projection) of different morphological types; e.g., a smooth single-component cluster or a widely separated bimodal in the plane of the sky. We focus on subclustering that is easily discernible in projection and dynamically important to the whole cluster; i.e. hidden substructure along the line of sight is not our concern nor are individual galaxies and small groups that do not significantly contribute to the potential energy of the cluster. More precisely, we will consider a cluster having two or more components that constitute a sizeable fraction ($\gtrsim$ 10%) of the total cluster gravitational potential within $\sim$ 1 Mpc of the cluster center (in projection) to possess the type of substructure relevant to this paper; these criteria should include much of the substructure suggested by RLT as relevant for cosmological studies. We define a cluster possessing this type of substructure to be a *multicluster*.

The natural basis for classifying multiclusters is the two-dimensional multipole expansion of the projected gravitational potential. Let $\Sigma(R,\phi)$ be the two-dimensional projection of the multicluster mass density, where (R,ϕ) are the conventional polar coordinates. This $\Sigma(R,\phi)$ generates the two-dimensional potential $\Psi(R,\phi)$,

$$\nabla^2\Psi(R,\phi) = 4\pi G\Sigma(R,\phi), \tag{6.1}$$

where ∇^2 is the two-dimensional Laplacian and G is the gravitational constant. The standard analysis using Green's functions (e.g., Jackson 1975) shows that the potential due to material interior to R is,

$$\Psi(R,\phi) = -2Ga_0 \ln\left(\frac{1}{R}\right) - 2G\sum_{m=1}^{\infty}\frac{1}{mR^m}\left(a_m\cos m\phi + b_m \sin m\phi\right), \tag{6.2}$$

where the moments a_m and b_m are given by,

$$a_m(R) = \int_{R' \leq R} \Sigma(\vec{x}')\,(R')^m \cos m\phi' d^2x',$$
$$b_m(R) = \int_{R' \leq R} \Sigma(\vec{x}')\,(R')^m \sin m\phi' d^2x',$$

and $\vec{x}' = (R', \phi')$. This expansion, similar to its cousin in three-dimensions (e.g., Binney & Tremaine 1987), has the general properties that (1) the circularly symmetric monopole term (i.e. the logarithmic term in eq. 6.2) is always at least as important as higher-order terms, and (2) the dipole ($m = 1$) vanishes when the origin of the coordinate system is set to the center of projected mass. Ψ does not represent the total gravitational potential due to Σ since eq. (6.2) neglects the mass exterior to R. However, as indicated below, we will only be concerned with the gravitational effects due to the interior mass.

A single elliptical cluster only contributes to even terms in the multipole expansion for Ψ (eq. [6.2]) when the origin is defined to be the center of projected cluster mass [1]. Hence, a significant contribution to odd multipole terms unambiguously reflects substructure (asymmetry) in the projected cluster, although a multicluster need not have odd multipoles (e.g., a bimodal cluster composed of equal-sized subclusters). The even multipoles are also important since multiclusters of different morphologies differ in their relative contributions to the even (and odd) multipole terms. In keeping with the above definition of a multicluster, we will only consider the first few multipole moments ($m = 0, 1, 2, 3, 4$) since higher-order terms reflect smaller-scale, dynamically less significant structures (see §6.3).

Each term of the multipole expansion (eq. [6.2]) is a function of position (R, ϕ). Since we want to characterize the dynamical state of a large region of a multicluster, a simple procedure is to evaluate the multipole moments in a circular aperture; a circular aperture does not introduce biases and systematic effects inherent when the aperture shape is modified (through iteration) to conform to the shape of an individual multicluster. By computing the moments in a circular aperture of radius R_{ap},

[1] We will, however, make some use of the dipole term (see the following sections).

the multipole expansion is sensitive to structures having a scale $\lesssim R_{ap}$ and is most sensitive to scales $\sim R_{ap}$; e.g., if R_{ap} is much greater than any scale associated with the cluster then the only significant term in the multipole expansion will be that corresponding to $m = 0$. Since we are uninterested in structure on scales greater than the aperture size, it is sensible to neglect the contribution to the potential of mass exterior to R_{ap} as we have done in the multipole expansion of eq. (6.2).

Because the $m \geq 1$ terms of eq. (6.2) vanish when integrated over ϕ, we instead consider the magnitude of the terms of each order integrated over ϕ. Let Ψ_m equal the mth term in the multipole expansion of Ψ. Define the quantity

$$P_{m,m'}(R_{ap}) = \frac{1}{2\pi}\int_0^{2\pi} \Psi_{m'}(R_{ap},\phi)\,\Psi_m(R_{ap},\phi)\,d\phi. \tag{6.3}$$

Only terms for which $m = m'$ are non-vanishing. Therefore $P_m \equiv P_{m,m}$ measures the "power" within R_{ap} of the terms of order m. Ignoring factors of $2G$, these are given by,

$$P_0 = [a_0 \ln(R_{ap})]^2, \tag{6.4}$$

for $m = 0$ and

$$P_m = \frac{1}{2m^2 R_{ap}^{2m}}\left(a_m^2 + b_m^2\right) \tag{6.5}$$

for $m > 0$. The total power of all multipole moments is simply given by

$$P = \sum_{m=0}^{\infty} P_m. \tag{6.6}$$

The ratio P_m/P reflects the contribution of the mth multipole moment to the power of the total gravitational potential within R_{ap}. Since the gravitational potential is directly related to the dynamical state of a cluster, the P_m are precisely the measures for substructure we seek. Each P_m has units $(mass)^2$ and the scale is set by R_{ap}. Since we are primarily interested in the dimensionless ratios of P_m (see §6.3) the only dimension that needs to be specified is the scale R_{ap}.

Because we ignore structures outside of the aperture of radius R_{ap} we naturally may obtain different indications for the dynamical state of a cluster depending on the

aperture size. For example, a widely separated bimodal of equal-sized components may appear essentially relaxed if the aperture is small enough so that it encloses only one of the subclusters. If the aperture is large enough to include both components, then the P_m will show that the cluster is unrelaxed (actually P_m/P_0 – see §§6.3 and 6.5). The ability to quantify the dynamical state of the cluster on varying scales is a great asset of the method. If a cluster is virialized then its dynamical state is trivially well defined; i.e. the cluster is relaxed on scales larger than the constituent galaxies. However, for clusters with significant substructure (e.g., the above bimodal with individually virialized subclusters) the dynamical state is a meaningful concept only when referred to a particular scale; the relevant scale for the above bimodal is determined by the relative separation of the subclusters. The cluster on scales smaller than this, or significantly greater than this, may well be virialized.

If we know the projected cluster mass density Σ, then the physical interpretation of the P_m is manifest. One may non-parametrically construct an accurate map of Σ by analyzing the weak distortions of background galaxies (e.g., Kaiser & Squires 1993). Unfortunately, since this technique is in its infancy and the measurement is difficult (requires sub-arcsecond seeing), such maps of the projected cluster mass density exist for only a few clusters (e.g., Fahlman et al 1994; Smail et al. 1995). In any event, the required source-lens-observer distances ($0.15 \lesssim z \lesssim 0.6$, where z is the redshift) fundamentally limits the number of clusters for which weak-lensing maps of Σ may be obtained.

In order to analyze the structures of a large sample of clusters we must appeal to either X-ray images or galaxy positions as a practical substitute for Σ. X-ray maps of clusters have several advantages over galaxy positions. First, the statistical uncertainties associated with galaxy positions are intrinsically fixed by the finite number of cluster galaxies whereas the noise of X-ray images is limited only by the sensitivity of the detector and the exposure time of the observation. Second, the projection along the line of sight of small groups of galaxies not associated with the cluster are less important for X-ray images because the ratio of X-ray luminosity of a cluster to a group is much greater than the corresponding ratio of projected galaxy number densities.

Third, in a similar manner, the projection of small groups within the cluster itself is less significant in the X-rays than in the galaxy counts; i.e. the large clumps that are dynamically important to the cluster as a whole are proportionally more important in the X-rays. Although X-ray images are more suitable for our categorization of multiclusters than galaxy positions, neither exactly represents the projected mass density of the multicluster. As a result, we must revise our interpretation of the multipole expansion (eq. [6.2]) when analyzing X-ray images.

The X-ray surface brightness, Σ_x, physically differs from Σ of clusters in several respects. Since the X-ray gas emissivity is proportional to ρ_{gas}^2, small increases in the gas density enhance the X-ray emission correspondingly more than in the underlying mass density. Moreover, the relationship of the gas distribution to the underlying mass is unclear because the gas may trace the underlying matter, the underlying potential, or neither (e.g., Buote & Tsai 1995a). In any event, the gas is unlikely to dominate the cluster gravitational potential.

To achieve successful quantitative classification of multiclusters we require that multiclusters of different morphological types as determined from analysis of the projected mass density (Σ) be categorized into corresponding morphological types when using X-ray images. However, the actual values of the P_m derived from the X-ray images need not be the same as those derived from Σ. In order to investigate this issue let us consider the projected gas emissivity, Σ_x, as the source term of a hypothetical two-dimensional X-ray emissivity potential Ψ_x. Consider a single elliptical cluster and a widely separated bimodal multicluster with different sized components. The qualitative features of the multipole expansion for Ψ_x and Ψ are the same: the odd multipole terms will vanish for the single cluster but not for the bimodal multicluster and the relative proportions of the P_m will differ for both clusters. Therefore, if the X-ray emission for a given multicluster exhibits the same qualitative structure present in the projected mass density Σ, then the multipole analysis of X-ray images should enable quantitative classification of multiclusters in the same manner as multipole analysis of Σ. We explore the feasibility of this scheme in the following sections.

6.3 Models

We investigate the capacity of multipole decomposition of X-ray images of galaxy clusters to differentiate multiclusters from single-component clusters; by "single-component" we mean one cluster component dominates the gravitational potential in projection. To this end we examine simple models that capture the features of real X-ray clusters essential for evaluating the utility of multipole analysis. Here we shall only consider the fundamental ability of multipole analysis to distinguish the different models. In the next section we address the expected real performance of the technique by analyzing simulated observations of these models using the instrument parameters of the ROSAT PSPC.

X-ray images of clusters exhibit a variety of morphologies (see Forman & Jones 1990; Jones & Forman 1992) ranging from smooth, single-component clusters with regular, nearly elliptical isophotes to multi-component clusters possessing several independent emission peaks. We will focus our attention on the simplest multicluster, the bimodal. A multicluster with more than two components typically has more power in higher order moments and thus is easier to distinguish from a single-component cluster; we will, however, investigate real clusters spanning the observed range of X-ray morphologies in §6.5. Therefore, by examining bimodal multiclusters we will obtain a conservative estimate of the viability of multipole analysis.

We employ simple models of the aggregate structure of X-ray clusters. For our purposes the radial surface brightness profiles of X-ray clusters are sufficiently well parametrized by the β-model (e.g., Cavaliere & Fusco-Femiano 1976; Jones & Forman 1984; Sarazin 1986),

$$\Sigma_x(r) \propto \left[1 + \left(\frac{r}{a_x}\right)^2\right]^{-3\beta+1/2}, \tag{6.7}$$

where a_x is the core radius and β the slope parameter. From analysis of a sample of bright *Einstein* clusters, Jones & Forman found $\beta \sim 0.5 - 1$ and $a_x \sim 50 - 750$ kpc. Jones & Forman noticed that the smooth, single-component clusters with a dominant central galaxy had the smallest core radii in their sample, $a_x \lesssim 300$. The clusters with large core radii probably possess significant core substructure like Abell 2256

(see Jones & Forman 1991; Briel et al. 1991). As a result, we assign parameters consistent with the smooth single-component clusters having a centrally dominant galaxy to each subclump of a bimodal multicluster. In order to incorporate models having a constant ellipticity (ϵ) and orientation, we substitute for r the elliptical radius a, where $a^2 = x^2 + y^2/q^2$, where q is the constant axial ratio.

We compute P_m on a large sample of cluster models. The single-component clusters are represented by single β-models with $\epsilon = 0.1 - 0.6$, $a_x = 100 - 700$ kpc, and $\beta = 0.5 - 1$. The ellipticity range spans plausible values for a single-component, ellipsoidal, non-rotating, self-gravitating mass (Merritt & Stiavelli 1990; Merritt & Hernquist 1991) appropriate to the case where the gas traces the underlying mass. If the X-ray gas is in hydrostatic equilibrium, then it will trace the potential and thus be rounder $\epsilon = 0 \sim 0.3$; for a discussion of the evolution of X-ray gas shapes see Buote & Tsai (1995a). Although large a_x and ϵ probably characterize a multicluster, we include these values for single-component clusters so as to make the distinction between multiclusters and single-component clusters more difficult to observe; in this manner we may obtain a conservative evaluation of the method. For the bimodals we consider for each component $a_x = 100 - 300$ kpc and for convenience set each β to 0.75. The relative separation of the components ranges from 250 kpc to 1.5 Mpc and their relative normalization ranges from 1:1 to 1:100. We also allowed the primary component in the bimodal to have $\epsilon = 0 - 0.4$ while the secondary component is always kept circular and placed on the major axis of the primary component; note all models were normalized to have the same value of a_0 within an aperture of radius 2 Mpc. The range of models we have selected should bracket most bimodals that would be considered multiclusters.

For each model we compute the powers, P_m (eq. [6.4] and [6.5]), for $m = 0 - 6$ within a circular aperture of radius $R_{ap} = 1$ Mpc; we also examine $R_{ap} = 2$ Mpc. The projected gravitational potential given by equation (6.2) is defined up to a constant which we specify by choosing units for R_{ap}; note the choice of units for R_{ap} is irrelevant for the $m \geq 1$ terms. In order to ensure that the P_m have the same values for a cluster independent of its distance we express R_{ap} in units of kpc. In Figure 1 we display

contours of four models placed at $z = 0.10$ (see §6.4).

Each choice for the location of the aperture center gives rise to a different multipole expansion (eq. [6.2]). First, we place the origin of the aperture at the centroid; i.e. where P_1 vanishes. By doing so, any information possibly found in the first moment is transferred to the higher order terms. The quadrupole power, P_2, in this case, is related to the ellipticity of the cluster. The next moment, P_3, is sensitive to bimodal structure where the components are of unequal size. P_4 is similar to P_2 but is more sensitive to smaller-scale structure. Hence P_2, P_3, and P_4 yield complementary information on the structure of the cluster.

We investigate a second case where we place the center of the aperture at the peak of the surface brightness. To avoid confusion with the previous case, moments generated with the origin at the emission peak are denoted $P_m^{(pk)}$. Here, the first non–symmetric moment $P_1^{(pk)}$ only vanishes if the cluster exhibits reflection symmetry about two orthogonal axes centered on the origin (such as for a pure elliptical cluster). This moment is then particularly sensitive to bimodal multiclusters having nearly equal-sized components. $P_1^{(pk)}$ essentially characterizes a circularly-averaged, centroid-shifting power of the cluster within R_{ap}. Although there exists some combination of the P_m (centroided) that contains the information given by $P_1^{(pk)}$, we employ $P_1^{(pk)}$ because of its higher sensitivity to nearly equal-sized bimodal multiclusters relative to P_2, P_3, and P_4.

We list in Table 1 the powers P_2, P_3, and P_4 computed for a selection of the above models expressed as a ratio of P_0. These values are indicated by "True" in the table. In Table 2 we list the power $P_1^{(pk)}$ in terms of $P_0^{(pk)}$, where $P_0^{(pk)}$ is the $m = 0$ power computed in the circle of radius R_{ap} centered at the emission peak. We prefer to consider power ratios, P_m/P_0, instead of the individual P_m because (1) dividing by P_0 normalizes to the flux within R_{ap} which enables consistent comparison between clusters of different X-ray brightnesses, and (2) the ratio more easily distinguishes between an image that is centrally concentrated (i.e. lower P_m/P_0) to one that is more spread out (i.e. higher P_m/P_0); e.g., even if a single and bimodal cluster (of the same luminosity) have the same P_2 within R_{ap}, the bimodal will necessarily have a

smaller P_0. Moreover, clusters that are more relaxed should be more dominated by their monopole terms. We do not list results for the higher order moments ($m \geq 5$) since they are, as expected, particularly sensitive to the bimodal multiclusters having relative normalizations greater than 10 : 1. These models are inconsistent with our definition of a multicluster or the substructure described by RLT and are also more susceptible to the hazards of real data (e.g., noise, unresolved sources – see next section).

As expected the odd terms yield the largest differences between single and bimodal clusters since they vanish identically for the single-component clusters. The results also demonstrate the complementary behavior of $P_1^{(pk)}/P_0^{(pk)}$ and P_3/P_0; i.e. the former is larger for equal-sized bimodals while the latter vanishes; the former is much less sensitive for unequal-sized bimodals while the latter is most sensitive to them. The even ratios, P_2/P_0 and P_4/P_0, also perform well at distinguishing bimodals from low-ellipticity ($\epsilon \lesssim 0.3$) single-component clusters. However, there is considerable overlap of the flatter single-component clusters ($\epsilon \gtrsim 0.3$) and moderately separated bimodals (0.5 Mpc separation of each subclump). For 1 Mpc separation the degeneracy is lifted and the even ratios separate well the single-component and bimodal models.

From the results listed in Tables 1 and 2, it is clear that the power ratios ($m \leq 4$) easily discriminate bimodal multiclusters from single-component clusters; here we considered multiclusters to have relative separations $500 < r < 1500$ kpc and relative normalizations $< 10 : 1$. Moreover, they do not significantly distinguish bimodals with relative separations < 500 kpc or relative normalizations $> 10 : 1$ from single-component clusters implying that these power ratios are essentially only sensitive to structure relevant to multiclusters; although we mention that P_3/P_0 and P_4/P_0 are sensitive to some models with larger relative normalizations when the components are sufficiently well separated.

The ability of the power ratios to distinguish models is dependent on the aperture size. In Table 3 we list the power ratios as a function of aperture size (radii 0.5,1.0,1.5, and 2.0 Mpc) for two models of very different morphologies: a single-component cluster with $\epsilon = 0.3$, core radius 300 kpc, and $\beta = 0.75$; and a bimodal where both

components have $\epsilon = 0$, core radius 300 kpc, $\beta = 0.75$, are separated by 1 Mpc, and have relative normalization 2 : 1. The power ratios of the single-component model (which naturally has vanishing odd P_m) are largest for the smallest apertures and decrease monotonically with increasing aperture size. This behavior simply reflects the decay of higher-order multipole terms with distance just as if the X-rays represented a true mass distribution (see §6.2); i.e. the qualitative picture of the multipole expansion is preserved for our simple models. In the 0.5 Mpc aperture, the bimodal cluster has smaller values of P_2/P_0 and P_4/P_0 than the single-component cluster because the aperture only encloses the dominant subcluster; i.e. these power ratios are similar to low-ellipticity single-component models (see Tables 1 and 2). However, the small non-zero values of the odd power ratios, $P_1^{(pk)}/P_0^{(pk)}$ and P_3/P_0, demonstrate that some indication of a large-scale asymmetry is detected within the 0.5 Mpc aperture. At 1 Mpc the centroided power ratios peak and then decay for larger apertures illustrating the power-ratios' sensitivity to the scale of the substructure (i.e. 1 Mpc separation of the two components). As expected, the higher-order moments decay most rapidly. In contrast, $P_1^{(pk)}/P_0^{(pk)}$ peaks at $\sim$ 1.5 Mpc but otherwise behaves similarly to the centroided moments.

6.4 Simulated Observations

Although we have demonstrated the ability in principle of the power-ratio method to quantitatively differentiate single-component clusters from multiclusters, we have not shown if these statistics can by usefully constrained by present observations. We now assess the practical feasibility of the power-ratio method by simulating real X-ray observations of the cluster models with the ROSAT Position Sensitive Proportional Counter (PSPC); for a description of ROSAT see Trümper (1983), of the ROSAT X-ray telescope see Aschenbach (1988), and of the PSPC see Pfeffermann et al. (1987). The PSPC is more suited to this kind of study than the *Einstein* Imaging Proportional Counter because of its superior resolution ($\sim 30''$ FWHM, on axis) and sensitivity. The sensitivity of the PSPC even outweighs the better spatial resolution

($\sim 4''$ FWHM) of the ROSAT High Resolution Imager (HRI). Moreover, many more clusters have been observed with the PSPC (see §6.6) than the HRI. The PSPC is also well suited for our study because the energy band pass and spectral response implies that the observed Σ_x depends almost exclusively on ρ^2 and is independent of temperature. Hence variations in Σ_x will not be due to temperature fluctuations in the gas.

Since our primary motive for introducing the power-ratio method is to facilitate consistent comparison of the morphologies of statistical samples of clusters (see §6.1 and §6.6), we simulated observations of a well-defined cluster sample. We also chose our observational parameters to take advantage of the large number of cluster observations that are becoming available in the ROSAT archive. In keeping with the spirit of the power-ratio method (see beginning of §6.2), we concentrated on bright (for S/N) and nearby ($z \lesssim 0.2$; for resolution) clusters. We considered clusters having characteristic X-ray luminosity $L_x^\star$ obtained from fitting the Schechter luminosity function to Abell and ACO clusters in the ROSAT All-Sky Survey (RASS; Ebeling 1993). Ebeling obtains $L_x^\star = 1.69 \pm 0.37 \times 10^{44}$ erg s^{-1} for his sample which translates to a flux $F_x^\star = 1.6 z^{-2} \times 10^{-13}$ erg cm^{-2} s^{-1}, where z is the cluster redshift and we have assumed a linear distance-redshift relation; this assumption amounts to assuming a static Euclidean universe which is suitable for our purposes to explore the effects of angular scale and S/N on the power ratios of low-redshift clusters. We placed $L_x^\star$ clusters at a series of redshifts ($z = 0.05, 0.10$, and 0.20) appropriate for most of the bright clusters that will be available in the ROSAT archive; a Hubble constant $H_0 = 80$ km s^{-1} Mpc^{-1} is assumed so these redshifts correspond to 187.5, 375 and 750 Mpc respectively. To agree with typical observations, we simulated observations having exposure times (t_{exp}) of 5ks, 10ks, and 20ks.

We constructed a simulated observation for a given model by first choosing the redshift of the cluster and then the exposure time. The flux was converted to PSPC counts in the hard band (0.4 - 2.4 keV) using the energy-conversion factors (ECFs) given in NRA 91-OSSA-3, Appendix F, ROSAT mission description. For each cluster we assumed a thermal line spectrum for temperatures $T = 4 - 8$ keV and column

densities $N_H = 10^{19.5} - 10^{21}$ cm^{-2} which translates to a typical $ECF = 0.575 \times 10^{11}$ counts cm^2 erg^{-1}; the total counts were then $(F_x^*)(ECF)(t_{exp})$. The counts within 1 Mpc of the centroid were normalized to the above total counts. We added a uniform background with a count rate of 3×10^{-4} counts s^{-1} arcmin^{-2} which is the average of the background rates of two PSPC images previously studied (Buote & Canizares 1994,1995). The models were then convolved with the off-axis point spread function of the PSPC evaluated at 1 keV (MPE/OGIP Calibration Memo CAL/ROS/93-015); note we did not include the support structure of the PSPC and thus we confined our study to within the inner 40′ diameter ring of the PSPC. Moreover, we did not add any exposure variations or vignetting since we assumed the observer can adequately correct for these effects. We set the pixel scale to 15″ for all the models.

We included the effects of noise from point sources and Poisson statistics in the simulations. First, to each image we added point sources having spatial properties consistent with the PSF of the PSPC and numbers consistent with the $\log N(> S) - \log S$ distribution given by Hasinger (1991) from analysis of the RASS; see Soltan & Fabricant (1990) and Mohr, Fabricant, & Geller (1993) for the inclusion of point sources in simulated *Einstein* images. The flux of each source was determined randomly from the probability distribution $dN(> S)/dS$ and then positioned randomly in the field. As before, we converted fluxes to PSPC counts using the ECFs in NRA 91-OSSA-3. We modeled the point sources with power-law spectra having indices $1.1 - 1.9$ and $N_H = 10^{19.5} - 10^{21}$ cm^{-2} which gave ECFs ranging from $(0.40 - 0.55) \times 10^{11}$ counts cm^2 erg^{-1}. For each point source we randomly selected an ECF from these values. Any point source that would be detected by an observer we excluded from the image, although we did count such a source toward the total number of sources dictated by $N(> S)$. We evaluated the significance of each source by comparing the source counts to the total counts in a circle of radius 30″ centered on the source. We conservatively excluded any source $\geq 5\sigma$ above the total noise.

For each model corresponding to a particular redshift and exposure time we generated 1000 simulated observations, and for each simulated observation we computed the power ratios $P_1^{(pk)}/P_0^{(pk)}$, P_2/P_0, P_3/P_0, and P_4/P_0 as described in §6.3; here we

set $R_{ap} = 1$ Mpc. Although a uniform background will not contribute to P_m for $m \geq 1$, it does contribute to P_0. Hence, we subtracted the mean background to ensure proper normalization of the power ratios. To evaluate P_2/P_0, P_3/P_0, and P_4/P_0 we computed the centroid within R_{ap} and iterated until the centroid shifted by less than 10^{-5} pixels (or 25 iterations had been performed).

We were compelled to adopt a more sophisticated procedure for $P_1^{(pk)}/P_0^{(pk)}$ because the position of the emission peak is much more sensitive to noise then the centroid. For determination of the peak position we first convolved the simulated image with a Gaussian filter having σ corresponding to a physical dimension of 40 kpc. (For example, this corresponds to 3 pixels for $z = 0.05$.) Then we took the highest 25% of the pixels within a circle of radius 0.15 R_{ap} centered at the peak of the smoothed image and computed the centroid of the highest points. We defined this centroid to be the emission peak. Using this position for the peak, we computed $P_1^{(pk)}/P_0^{(pk)}$ on the original unsmoothed simulated image.

We computed simulated observations of a subset of models from §6.3 possessing the essential distinguishing characteristics of the single-component and multicluster models. The single-component models have $\epsilon = 0, 0.3$, and 0.6 while the core radius was set to 300 kpc and β to 0.75. The multiclusters have for both cluster components $\epsilon = 0$, core radii set to 300 kpc, β set to 0.75, relative separations 0.5 and 1 Mpc, and relative normalizations 1:1, 2:1, and 5:1. In Figure 2 we display contour plots of simulated observations for four of these cluster models.

The mean value and the 90% confidence limits of the power ratios computed for the 1000 simulated observations of each model are listed in Tables 1 and 2; for lack of space we only include the $t_{exp} = 10$ks exposures. The 90% confidence limits are specified so that 10% of the simulated observations give power ratios above the upper limit and 10% give power ratios that are below. It is clear that for our chosen sample of bright, nearby clusters the power ratios perform nearly as well on the simulated observations as on the exact models (§6.3) for distinguishing multiclusters from single-component clusters. In fact, the mean value of P_2/P_0 is generally within $\sim 10\%$ of the true values and the 90% confidence limits bracketed the true value in all but a few cases.

$P_1^{(pk)}/P_0^{(pk)}$, P_3/P_0, and P_4/P_0 behave similarly, although they are usually only within $\sim$ 25% of the true values. In addition, for $P_1^{(pk)}/P_0^{(pk)}$ and P_3/P_0 the observations give noticeable non-zero values (as high as a few times 10^{-7} for P_3/P_0 and a few times 10^{-6} for $P_1^{(pk)}/P_0^{(pk)}$) for some models where the true value is identically zero. The point sources and Poisson noise do indeed contribute noticeable uncertainty, but the uncertainties are generally less than the systematic differences in power ratios between the two classes of models. We mention that the contribution to noise in the power ratios is roughly equal between the point sources and Poisson noise. We also find that the effects of using pixelized images to determine power ratios are very small for the chosen redshifts. We do this by essentially determining the difference between a locally smoothed version of the image to the observed pixelized image.

The results for $P_1^{(pk)}/P_0^{(pk)}$ listed in Table 2 demonstrate that the systematic effects due to locating the emission peak are insignificant with respect to noise, pixelization, etc.. This systematic effect is due to noise and pixelization of the image only in the sense that the emission peak is difficult to determine accurately from a realistic observation. That is, our procedure for determining the center by smoothing and then centroiding on the highest surface brightness pixels tends to move the center closer to high surface brightness structures which are near the absolute peak. For example, if there are two high emission structures which are not extremely widely separated, say in a bimodal cluster, then the center will be moved in the direction of the centroid of the image. This leads to a smaller amount of power in the given ratio. This effect does not influence cases such as the single elliptical cluster where the center is well separated from other emission peaks. We emphasize that given realistic observations, the ratio $P_1^{(pk)}/P_0^{(pk)}$ is a good discriminator between single clusters and bimodals, especially those bimodals with nearly equal sized components, and brackets the results of the true models within the $\sim$ 90% confidence level.

We examine whether the sample of multiclusters may be distinguished from the sample of single-component clusters by applying a Kolmogorov-Smirnov test to the individual distributions of power ratios. That is, we have 1000 simulated observations of 27 single-component cluster models and 54 bimodal multicluster models which form

two well-defined cluster samples that differ only in their morphology, not in their luminosity or distribution or distances; the bimodal models with relative normalizations 2:1 were omitted for $P_1^{(pk)}/P_0^{(pk)}$ leaving 36 total bimodals for that case. We obtained, for example, the distribution of P_3/P_0 values for each sample by selecting P_3/P_0 randomly from one of the 1000 simulations of each model. We list in Figure 3 the cumulative distributions of $P_1^{(pk)}/P_0^{(pk)}$, P_2/P_0, P_3/P_0, and P_4/P_0 obtained in this manner The K-S tests yield probabilities of $< 0.001\%$ for $P_1^{(pk)}/P_0^{(pk)}$, 3% for P_2/P_0, 0.03% for P_3/P_0, and 0.1% for P_4/P_0 that the singles and bimodals originate from the same population. Thus the K-S test for each power ratio convincingly demonstrate that the two data sets could not have come from the same parent population. Although the K-S test is useful for hypothesis testing, in §6.6 we discuss the correlations of the power ratios as a means to provide detailed classification of clusters into different morphological types.

6.5 Application to Four Real Clusters

As a final illustration of the performance of the power-ratio technique, we analyzed ROSAT PSPC X-ray images of the four Abell clusters A85, A514, A1750, and A2029. A2029 is a classic single-component cluster having regular, moderately flattened ($\epsilon_x \sim 0.15$) elliptical isophotes; it is nearby ($z = 0.0768$) and very X-ray bright ($\sim \frac{5}{2}L_x^*$; the fluxes of the clusters are listed in Table 5). The other three clusters represent the quintessential examples from the qualitative morphological classification scheme of Jones & Forman (1992). A85 ($z = 0.0556$) has a dominant primary component with a small secondary and is one of the brightest clusters ($\sim \frac{3}{2}L_x^*$). A1750 has two components of roughly equal size with a respectable X-ray luminosity ($\sim \frac{2}{3}L_x^*$). Finally, A514 is a complex X-ray cluster as classified by Jones & Forman because it has at least three distinct emission peaks and highly irregular isophotes; it is at similar redshift as the others ($z = 0.0731$) but is somewhat fainter in X-rays ($\sim \frac{1}{6}L_x^*$). Therefore, the four clusters span the range of observed X-ray morphologies of clusters and hence serve as convenient benchmarks for demonstrating the ability of the power-

ratios to quantitatively classify real clusters.

We prepared the images for analysis using the standard IRAF-PROS software. First we searched for spikes in the light curves of the images that signal contamination from solar radiation; no statistically significant spikes were found for the images. Next we rebinned the images into 15″ pixels corresponding to 512×512 fields; i.e the same scale used for the simulated observations in §6.4. Only data from the hard band ($0.5 - 2$ keV) were used in order to minimize the blurring due to the point spread function (PSF) of the PSPC and the contamination from the X-ray background. We corrected for exposure variations and telescopic vignetting by dividing the images by the exposure maps provided with the observations. To subtract the background we selected an area $\sim 35'$ from the field centers apparently uncontaminated by emission from nearby sources or the cluster itself. Typically we identified the background region from examination of the radial profile centered on the cluster; we designated the background region where the radial profile flattened. This procedure undoubtedly suffers to some extent from contamination by emission from the cluster, but the errors are insignificant in relation to the total cluster flux which is all that we require (see §6.4). In Table 4 we list the observational data for the four clusters; in Figure 4 we show contour plots of the images.

The final step in the image reduction is to remove embedded sources from the cluster continuum. In keeping with the simulated observations of the previous section, we identified and removed "obvious" contaminating point sources from visual examination of the images; note we arrived at this subjective procedure because automated techniques like the *detect* package in PROS had difficulty identifying sources located in the continuum of the clusters. Although some of these sources that we remove are either noise or intrinsic features of the clusters, removing them only serves to smooth out the cluster emission thereby decreasing the power from higher-order moments; i.e. these small effects only make a multicluster appear more similar to a single-component cluster. Hence, the quantitative significance of a multicluster as separate from a single-component cluster is made more robust. The uncertainties and biases regarding source removal are investigated in detail in our companion pa-

per (Buote & Tsai 1995b). In Figure 5 we show contour plots of the four clusters with the embedded sources removed.

In Table 5 we list the power ratios computed on these four images for R_{ap} of 0.5, 1, and 1.5 Mpc, where we have used $H_0 = 80$ km s^{-1} Mpc^{-1} as in the previous section. From examination of the simulations in §6.4 we estimate that $\sim 50\%$ uncertainties should reflect the 90% confidence limits for the clusters. The clusters are clearly differentiated by their power ratios. For example, A514 and A2029 have $P_1^{(pk)}/P_0^{(pk)}$ and P_3/P_0 values that generally differ by over two orders of magnitude and the P_2/P_0 values differ by one order of magnitude, a discrepancy that is highly significant considering the $\sim 50\%$ uncertainties. In fact, $P_1^{(pk)}/P_0^{(pk)}$, P_2/P_0, and P_3/P_0 easily distinguish A2029 from the each of the other clusters in each aperture. In the 1 Mpc aperture P_4/P_0 for A514 is one hundred times larger than the value for A2029, although the difference in P_4/P_0 is negligible in the other apertures.

A85 is a prime example of the type of cluster described by RLT as being relevant for cosmological tests (§6.1). Moreover, next to A2029, it is the cluster with the least obvious structure in our sample. In the 0.5 Mpc aperture the P_2/P_0 and P_4/P_0 values for A85 are completely consistent with those of the smooth A2029. The other two ratios, however, demonstrate substantial discrepancy with A2029. All of the power ratios easily distinguish A85 from A2029 in the 1 Mpc aperture with the ratio P_4/P_0 being in marginal agreement. Hence the power ratios clearly distinguish A85 from single-component clusters like A2029.

The example of A85 demonstrates that the power ratios are indeed sensitive to the aperture size and classify the clusters according to the scale of the substructure they possess as we demonstrated for the toy models in §6.3 and Table 3. A more extreme case is A1750 where the 0.5 Mpc aperture only encloses one of the subclusters. The power ratios for A1750 on this scale are completely consistent with those of A2029 except for P_3/P_0. It is because a bridge of emission connects the two subclusters that P_3/P_0 is able to measure an asymmetry signaling the presence of the subcluster outside the aperture. Unlike A1750, A514 registers very large power ratios in all apertures except for P_4/P_0 which is only larger in the 1 Mpc aperture. The sensitivity

to the aperture size in this case is a result of the edge of the 1 Mpc aperture falling right on the two subclusters to the West.

The value of $P_1^{(pk)}/P_0^{(pk)}$ for $R_{ap} = 0.5$ Mpc for A2029 in Table 5 appears to significantly differ from the simulations of single-component clusters in the previous section. For several reasons, we do not take this is as an indication of subtle substructure in the central regions of A2029, although such structure is in any case not our primary interest. First, A2029 is known to contain a massive cooling flow (Sarazin, O'Connell, & McNamara 1992) which implies that the surface brightness of the central few hundred kpc does not follow that of the β model used in our simulations. Moreover, Sarazin et al. find complicated structure in the X–ray emission that may be due to any of a number of possibilities (e.g., lumpy absorption or magnetic fields) not intimately related to the total cluster gravitational potential. Since our simulations were restricted to β models, they may not have adequately accounted for the variety of surface brightness laws to be found in actual clusters, especially in the central regions. Hence the range of values quoted in Table 2 for the single clusters may not extend to higher values because of the restricted set of models considered and thus the presence of subtle substructure should not be concluded. Despite this slight discrepancy with the simulations, the relatively small values of $P_1^{(pk)}/P_0^{(pk)}$ clearly distinguish A2029 from the other real clusters.

6.6 Discussion

The power-ratio method differs from conventional techniques for analyzing substructure in galaxy clusters because it is designed to quantitatively label clusters of different aggregate morphologies, not simply to quantify the significance of substructure. Moreover, the power-ratio method is motivated by cluster dynamics. If the cluster surface mass density is known (e.g., from weak-lensing maps), the power-ratio method classifies structure in direct proportion to its contribution to the cluster gravitational potential. For X-ray images of clusters this relationship to the gravitational potential is not so clear (§6.2), but if the X-rays trace the structure in the surface density then

the dynamical interpretation is qualitatively preserved; this was demonstrated by the success of the power ratios at discriminating between the X-ray cluster models and simulations in §6.3 and §6.4.

We envisage the power-ratio method to quantitatively distinguish clusters where the substructure is obvious to the eye. For this purpose the significance of the substructure is a given, what this structure implies for the aggregate cluster dynamics is our primary concern. For example, a definitive measurement of a non-zero value of P_3 unequivocally demonstrates that substructure is significant for the cluster, but only in relation to the other P_m can it be determined whether the substructure is meaningful to the cluster on a particular scale (R_{ap}); the same argument applies to $P_1^{(pk)}$ and therefore to centroid shifts (Mohr et al. 1993). Thus, methods that are particularly suited to locate subtle manifestations of substructure and quantifying its significance (e.g., the KMM algorithm described by Ashman et al. 1994; also see Bird 1993) are not as well suited as the power-ratio method for quantitatively classifying clusters of different morphologies.

To fully realize the capacity of this technique to distinguish clusters by their dynamics, the correlations of the power ratios, rather than each ratio alone, should be analyzed; cf. the K-S tests in §6.4. We illustrate these correlations from analysis of the projections of the vector $(P_2/P_0, P_3/P_0, P_4/P_0,)$ onto the two-dimensional coordinate planes for a sample of single-component cluster and multicluster models computed in §6.3; we exclude $P_1^{(pk)}/P_0^{(pk)}$ because it necessarily has a trivial correlation with the P_m/P_0. The sample of cluster models we now consider is slightly more extensive then shown in Tables 1 and 2 to better illustrate the complete range of cluster behavior. We consider single cluster models with $\epsilon = 0.1, 0.2, 0.3$, $a_x = 100, 300$ kpc, and $\beta = 0.75$; we include only single-component models with $\epsilon < 0.3$ since flatter X-ray clusters probably are not relaxed (e.g., Buote & Tsai 1995a). The bimodals have $a_x = 300$ kpc, $\beta = 0.75$, relative separations 0.5, 1 Mpc, relative normalizations $1:1, 2:1, 5:1$, and $10:1$, and $\epsilon = 0, 0.2$ for the primary component. For the bimodal models with an elliptical primary ($\epsilon = 0.2$) we consider the cases where the secondary is either aligned along the major axis or the minor axis of the primary. In Table 7 we list the

true power ratios for these models computed in apertures of radii $R_{ap} = 1, 2$ Mpc; again we defined R_{ap} in units of kpc.

We plot the correlations of the power ratios in Figure 6 for $R_{ap} = 1$ Mpc; since the singles (represented by filled ovals) vanish for P_3/P_0 they have been placed on the P_2/P_0 or P_4/P_0 axes to show their range in these ratios. In each case the power ratios display positive correlations in the sense that clusters with small relative separations and normalizations inhabit the lower left of the plots while the top right is populated by the nearly equal-sized, widely separated bimodals; i.e. generally the dynamically "mature" clusters are located near the bottom left of the plots while "young" clusters populate the upper right. The tightest correlation is in the $P_2/P_0 - P_4/P_0$ plane for the single-component models where essentially $P_2/P_0 \propto P_4/P_0$. The bimodal multiclusters, although following the same general trend, have much larger scatter especially when the relative normalization $> 5 : 1$. The correlations clearly show that the multiclusters primarily inhabit a localized region of the three-dimensional space of power ratios; this space is typically $P_2/P_0 = 10^{-6} - 10^{-4}$, $P_3/P_0 = 10^{-8} - 10^{-5}$, and $P_4/P_0 = 10^{-9} - 10^{-6}$. Clusters with smaller relative separations ($\lesssim 0.5$ Mpc) and larger relative normalizations ($\gtrsim 10 : 1$) generally lie outside this volume in the direction of small values of the power ratios.

In Figure 6 we draw a dashed box to represent the region inhabited by single-component clusters considering the effects of noise, pixelization etc. from simulated observations of these clusters with the PSPC (see §6.4). Although some of the multiclusters lie in this region in one of the planes, they are usually removed from correlation with the remaining power ratios. For example, the bimodal with relative separation 1 Mpc, relative normalization $1 : 1$, and primary $\epsilon = 0.2$ with secondary on the major axis is the model with the lowest P_3/P_0 and P_4/P_0 shown in Figure 6 and within the error box for single-component clusters in the $P_2/P_0 - P_4/P_0$ plane. However, this model lies outside the error boxes in the other planes and is thus distinguished as a multicluster. In general, where the clusters lie in the volume classifies them by the type of structure they possess; i.e. clusters falling in the multicluster region possess substructure that is dynamically relevant to the aggregate cluster

dynamics on a scale $\sim R_{ap}$ (see §6.2).

The correlations of the power ratios for $R_{ap} = 2$ Mpc are displayed in Figure 7. Although the power ratios still exhibit positive correlations (with values about 10 times less than before), the distinction between the single-component models and the bimodals is not as pronounced as for the $R_{ap} = 1$ Mpc case – especially upon considering the effects of real observational uncertainty (i.e. as above the dotted lines show the allowed region for single-component clusters considering simulated observations in §6.4). This is again a manifestation of the multipole description at work. That is, since the bimodal models we have constructed have separations either 0.5 or 1 Mpc, the higher-order multipoles are largest on those scales. For aperture sizes larger than these scales the monopole term quickly dominates as the higher-order moments rapidly decay. It is thus important to examine different aperture sizes to determine on which scale substructure is particularly important for real clusters. (We mention that the bimodal model with $\epsilon = 0.2$, $R_s = 0.5$ Mpc, and $REL = 2:1$ and secondary aligned along the major axis of the primary has a P_3/P_0 value larger at $R_{ap} = 2$ Mpc than $R_{ap} = 1$ Mpc – although both values are very small. This appears to be an interesting case where the ellipticity of the primary acts to reduce the value of P_3/P_0 which does not happen for the models where the secondary is aligned along the minor axis of the primary. In a similar case, the bimodal model with $\epsilon = 0.2$, $R_s = 1.0$ Mpc, $REL = 10:1$ and secondary aligned along the minor axis of the primary has P_2/P_0 value larger at $R_{ap} = 2$ Mpc than $R_{ap} = 1$ Mpc. More interesting, though, is that this model has a smaller value of P_2/P_0 than P_4/P_0 for $R_{ap} = 1$ Mpc. We find that these interesting cases are not well-represented by real clusters [see Buote & Tsai 1995b] which may simply be the result of the cluster initially collapsing along its shortest axis – e.g., Lin, Mestel, & Shu 1965.)

A potential application of the power-ratio method is for determining quantitatively whether a quasi-hydrostatic equilibrium description for the X-ray emitting gas of an individual cluster is justified for the purpose of constraining its intrinsic shape and its total mass distribution. Buote & Tsai (1995a) tested the viability of X-ray analysis for constraining the intrinsic shapes of clusters of galaxies using the simulation of

Katz & White (1993). They concluded that at low redshifts ($z \lesssim 0.25$) the X-ray method accurately measured the true ellipticity of the three-dimensional cluster dark matter up to projection effects. At higher redshifts ($z \gtrsim 0.25$), however, the X-ray method yielded unreliable results since the gas does not trace the cluster gravitational potential. Buote & Tsai proffer some necessary conditions for the reliability of X-ray methods: (1) that there is no obvious substructure on the same scale used to compute the aggregate shape and (2) the isophotes are regularly shaped and not too elongated ($\epsilon_x \lesssim 0.3$). The power-ratio method is particularly suited to quantify these necessary conditions. Results on our study will be presented elsewhere, but see Buote & Tsai (1995b) for an outline of a prescription for this program.

The power-ratio method is ideally suited to constrain Ω via the Morphology - Cosmology connection (see §6.1; RLT; Evrard et al. 1993). The method provides a simple, consistent comparison of the structure of clusters since the power ratios are (1) computed in a well-defined aperture, (2) normalized to the flux within that aperture, and (3) do not require any fitting. Because it is particularly sensitive to structure relevant to the dynamical state of the cluster, the power-ratio method specifically quantifies the type of substructure described by RLT as relevant for cosmology. The ratio P_3/P_0 (and P_4/P_0), being sensitive to unequal-sized bimodal multiclusters, is most relevant to the structure envisioned by RLT, while $P_1^{(pk)}/P_0^{(pk)}$ and P_2/P_0 are more sensitive to roughly equal-sized subclumps.

A large number of clusters similar to those of our sample in §6.4 will be available in the ROSAT archive. From examination of the ROSAT master log of pointed observations (in the HEASARC-Legacy database) for Abell clusters having (1) measured flux $\gtrsim 10^{-11}$ erg cm^{-2} s^{-1} as published by Ebeling (1993), (2) exposure times $>$ 5ks, and (3) $z \lesssim 0.2$ we find ~ 50 eligible clusters. Higher redshift clusters will be available for analysis with AXAF because of its superior resolution. As a result, at least 124 Abell clusters from Ebeling (1993) having flux $> 10^{-11}$ erg cm^{-2} s^{-1} will in principle be eligible for analysis. Thus application of the power-ratio method to these samples should enable a thorough statistical investigation of the viability of using the observed structure of clusters to place interesting constraints on Ω. In Buote & Tsai

(1995b) we apply the power-ratio method to 55 ROSAT PSPC clusters to furnish a catalog of power ratios suitable for statistical analysis.

An effort to analyze the Morphology - Cosmology connection was undertaken by Evrard et al. (1993). These authors proposed to quantify the structure of *Einstein* clusters using a mean centroid shift (Mohr et al. 1993), a mean axial ratio, and a mean slope of the surface brightness of the entire X-ray image; the mean centroid shift and mean axial ratio are related to our $a_1^{(pk)}$, $b_1^{(pk)}$ and a_2, b_2. By computing the power ratios in apertures defined by the cluster distances, we consistently sample the same intrinsic scales of clusters. In addition, by using a series of aperture sizes we also obtain information regarding the scale of the substructure in the cluster sample. Evrard et al., in contrast, sample different cluster scales for each cluster because they compute mean quantities for the entire X-ray images; the size of a cluster X-ray image is dependent on the flux, intrinsic size, and distance of the cluster. Evrard et al. also do not employ a third (or forth) moment which is in fact more sensitive to the unequal-sized bimodal multiclusters envisioned by RLT than the lower-order moments.

The manner in which Evrard et al. compute the centroid-shift and axial ratio (as explained in Mohr et al. 1993) also makes a direct comparison to intrinsic properties of the cluster uncertain. Specifically, the surface brightness in a circular annulus of a given width is first Fourier expanded to low order given a trial center for the annulus. The expansion is then fitted to the image taking the Fourier coefficients as parameters of the fit. The location of the center of the image is then iterated so as to minimize the coefficient of the $m = 1$ term (C_1). This center is then used to compute the centroid shift and the axial ratio. This procedure gives correct values for these latter quantities only if the cluster being considered is very nearly elliptical and higher order terms in the Fourier expansion of the surface brightness are small. This is because the values of the coefficients determined by *fitting* a highly truncated version of the expansion to the image are not necessarily the true values of the Fourier coefficients when higher order terms are important. Given a center, the true Fourier coefficients are given by moments of the surface brightness distribution; fitted values will depend

on the highest order considered and will not have their usual meanings.

Mohr et al. (1993) only considered clusters for which the condition that higher order terms in the expansion of the surface brightness be small is satisfied. Their values of the centroid shift and the axial ratio are probably accurate. However, consideration of substructure in these clusters are of limited use in cosmological considerations since the substructure required by RLT will indeed give rise to significant higher order terms, as seen in §3.

6.7 Conclusions

We have described a technique to quantitatively classify clusters of galaxies according to their projected morphology. In particular, we addressed structure that is easily discernible in projection and dynamically important to the whole cluster. A cluster possessing substructure of this type (§6.2) we defined to be a *multicluster*. We specifically designed our method to quantitatively distinguish multiclusters from single-component clusters in projection. The method is derived from the two-dimensional multipole expansion of the projected cluster gravitational potential; i.e. the square of each multipole term averaged over a circular aperture is called the *power*, P_m, and when divided by another P_m (particularly P_0) we call it a *power ratio*. For the case where the surface mass density of the cluster is known, e.g., from analyzing the weak distortions of background galaxies (e.g., Kaiser & Squires 1993), the power-ratio method classifies structure in relation to its contribution to the cluster gravitational potential.

For X-ray images of clusters this relationship to the gravitational potential is not so transparent (§6.2), but if the X-rays approximately trace the structure in the surface mass density then qualitatively the dynamical interpretation is preserved. We demonstrated this assertion by analyzing the performance of the power-ratio method applied to simple models capturing the essential features of real X-ray clusters. In particular we focused on models of single-component clusters and bimodal multiclusters. By construction the structure of these models of X-ray clusters reflected structure

in the projected mass; clumps in the X-rays corresponded to the same clumps in the mass, although not in exactly the same proportions. We determined that the ratios $P_1^{(pk)}/P_0^{(pk)}$, P_2/P_0, P_3/P_0, and P_4/P_0 performed best for distinguishing between single-component clusters and multiclusters; the powers were computed in a circle located at the cluster centroid except for $P_1^{(pk)}/P_0^{(pk)}$ which was centered at the emission peak. The ability of the power ratios to differentiate clusters was optimized when the aperture size was of order the separation of the clumps of the bimodals.

We simulated observations of these models using the instrument parameters of the ROSAT PSPC for a sample of nearby ($z \leq 0.2$) and bright (flux $= F_x^\star = 1.6z^{-2} \times 10^{-13}$ erg cm^{-2} s^{-1}) clusters. The effects of point sources, X-ray background, Poisson noise, and realistic exposure times were also incorporated into the simulations. The power ratios perform nearly as well on the simulated observations as on the exact models (§6.3) for distinguishing multiclusters from single-component clusters. The point sources and Poisson noise do contribute noticeable uncertainty, but generally less than the systematic differences in power ratios between the two classes of models; the contribution to noise in the power ratios is roughly equal between the point sources and Poisson noise. Applying a Kolmogorov-Smirnov test to the power-ratios obtained from the simulations clearly demonstrates the sample of multiclusters may be distinguished from the sample of single-component clusters.

We applied the power-ratio method to ROSAT PSPC images of A85, A514, A1750, and A2029. These clusters each have very different X-ray morphologies with A2029 being a smooth, single-component cluster; A85 being a dominant smooth component with a small secondary; A1750 being two components of nearly equal size; and A514 being the quintessential complex cluster in the qualitative classification scheme of Forman & Jones (1990; Jones & Forman 1992); A85 and A1750 are also listed by Forman & Jones as the definitive members of their own classes. We find that the power ratios easily differentiate the clusters, especially when the aperture size is 1 Mpc ($H_0 = 80$ km s^{-1} Mpc^{-1}). In a companion paper (Buote & Tsai 1995b) we apply the power ratios to a large sample of clusters observed with the PSPC.

We have discussed the suitability of the power-ratio method to constrain Ω via the

Morphology - Cosmology connection (see §6.1; RLT; Evrard et al. 1993). The method provides a simple, consistent comparison of the structure of clusters since the power ratios are (1) computed in a well-defined aperture, (2) normalized to the flux within that aperture, and (3) do not require any fitting. Moreover, the power-ratio method is specifically sensitive to the type of substructure described by RLT as relevant for cosmology. We also discussed the ability of the power ratio method to assess the viability of a particular cluster being described by hydrostatic equilibrium for the purposes of X-ray analysis of its intrinsic shape and of its total mass distribution.

It is a pleasure to thank Claude Canizares, Eric Gaidos, Lam Hui, and John Tonry for insightful discussions. We gratefully acknowledge Claude Canizares for a critical reading of the manuscript and Isamu Hatsukade for providing the A1750 data prior to public release. Finally, we thank Janet De Ponte at hotseat@cfa.harvard.edu for assistance in converting the German A1750 data to US/PROS format. DAB acknowledges grants NAS8-38249 and NASGW-2681 (through subcontract SVSV2-62002 from the Smithsonian Astrophysical Observatory). JCT was supported by an NRC associateship.

Table 1. Power Ratios

Model	True	$z = 0.05$		$z = 0.10$		$z = 0.20$	
P_2/P_0 (10^{-7})							
Single (ϵ):							
0	0.000	0.160	0.068 - 0.182	0.482	0.181 - 0.548	1.61	0.609 - 1.86
0.3	39.6	41.9	38.4 - 45.4	42.5	35.6 - 49.4	43.2	29.9 - 56.8
0.6	162	167	160 - 175	169	155 - 183	168	141 - 196
Bimodal (R_s, REL):							
(0.5, 1 : 1)	59.9	62.7	58.0 - 67.2	63.0	53.2 - 72.8	63.7	45.0 - 84.0
(0.5, 2 : 1)	46.3	48.0	43.7 - 52.1	49.1	40.5 - 57.7	48.7	32.7 - 66.1
(0.5, 5 : 1)	16.8	18.3	15.7 - 21.0	18.8	13.7 - 24.0	19.2	9.32 - 30.2
(1.0, 1 : 1)	882	865	845 - 887	876	834 - 918	860	707 - 945
(1.0, 2 : 1)	550	525	507 - 544	554	516 - 596	534	461 - 614
(1.0, 5 : 1)	85.9	82.2	75.1 - 89.1	90.9	77.1 - 107	90.5	58.9 - 122
P_3/P_0 (10^{-7})							
Single (ϵ):							
0	0.000	0.030	0.003 - 0.067	0.116	0.012 - 0.275	0.456	0.049 - 1.06
0.3	0.000	0.025	0.003 - 0.058	0.103	0.009 - 0.244	0.413	0.039 - 0.945
0.6	0.000	0.021	0.003 - 0.048	0.081	0.009 - 0.180	0.337	0.031 - 0.767
Bimodal (R_s, REL):							
(0.5, 1 : 1)	0.000	0.032	0.004 - 0.075	0.133	0.013 - 0.320	0.501	0.054 - 1.14
(0.5, 2 : 1)	0.471	0.505	0.291 - 0.727	0.626	0.179 - 1.16	0.985	0.134 - 2.17
(0.5, 5 : 1)	0.664	0.693	0.441 - 0.960	0.805	0.299 - 1.38	1.18	0.196 - 2.47
(1.0, 1 : 1)	0.000	0.061	0.007 - 0.146	0.275	0.026 - 0.657	1.045	0.112 - 2.44
(1.0, 2 : 1)	29.6	28.4	26.2 - 30.6	28.7	24.2 - 33.2	28.6	20.4 - 37.3
(1.0, 5 : 1)	14.1	12.6	11.4 - 14.0	14.2	11.4 - 17.1	14.3	8.54 - 20.2

Table 1—Continued

Model	True	$z = 0.05$		$z = 0.10$		$z = 0.20$	
P_4/P_0 (10^{-7})							
Single (ϵ):							
0	0.000	0.014	0.001 - 0.033	0.054	0.006 - 0.121	0.209	0.022 - 0.474
0.3	0.099	0.135	0.068 - 0.205	0.170	0.042 - 0.324	0.320	0.046 - 0.703
0.6	2.18	2.24	1.97 - 2.51	2.34	1.76 - 2.95	2.53	1.43 - 3.76
Bimodal (R_s, REL):							
$(0.5, 1:1)$	0.036	0.068	0.021 - 0.120	0.107	0.014 - 0.233	0.303	0.037 - 0.700
$(0.5, 2:1)$	0.051	0.080	0.029 - 0.139	0.125	0.015 - 0.271	0.279	0.031 - 0.628
$(0.5, 5:1)$	0.056	0.087	0.031 - 0.150	0.131	0.020 - 0.281	0.273	0.032 - 0.610
$(1.0, 1:1)$	7.90	7.75	6.78 - 8.75	8.12	6.57 - 9.67	8.27	5.37 - 11.3
$(1.0, 2:1)$	10.1	9.65	8.84 - 10.4	10.1	8.36 - 11.7	9.94	6.67 - 13.3
$(1.0, 5:1)$	3.98	3.68	3.23 - 4.14	4.15	3.19 - 5.16	4.37	2.23 - 6.63

Note. — The power ratios are computed in a 1 Mpc circular aperture about the centroid. "True" corresponds to the intrinsic power ratio from §6.3 and the values for the different redshifts are the mean and 90% confidence limits for the 1000 simulated observations of the models (see §6.4) having exposure time 10ks. The core radii and β parameters of the models are fixed as described in §6.4. The single-component models only differ in their ellipticity ϵ. The bimodal multiclusters models are listed for different values of their relative separation, R_s (Mpc), and their relative normalization, REL.

Table 2. Power Ratios

Model	True	$z = 0.05$		$z = 0.10$		$z = 0.20$	
$P_1^{(pk)}/P_0^{(pk)}$ (10^{-7})							
Single (ϵ):							
0	0.000	2.36	0.078 - 3.31	5.21	0.370 - 8.43	14.8	1.64 - 29.6
0.3	0.000	0.798	0.065 - 1.49	2.87	0.239 - 6.68	11.6	1.10 - 25.9
0.6	0.000	0.588	0.051 - 1.27	2.47	0.207 - 3.77	8.17	0.758 - 19.3
Bimodal (R_s, REL):							
(0.5, 1 : 1)	4437	4378	3762 - 4851	3705	2887 - 4706	2896	1336 - 4192
(0.5, 5 : 1)	472	444	294 - 621	350	214 - 614	254	39.9 - 666
(1.0, 1 : 1)	5148	7092	6825 - 7318	5991	5574 - 6408	6149	5289 - 6955
(1.0, 5 : 1)	372	399	294 - 512	322	202 - 509	257	69.4 - 575

Note. — The power ratio is computed assuming an aperture of radius 1 Mpc centered on the emission peak. Quantities are listed as in Table 1

Table 3. Power Ratios vs. Aperture Size

R_{ap} (Mpc)	$P_1^{(pk)}/P_0^{(pk)}$	P_2/P_0	P_3/P_0	P_4/P_0
		Single: $\epsilon = 0.3$:		
0.5	0.	93.6	0.	0.235
1.0	0.	39.6	0.	0.099
1.5	0.	17.8	0.	0.038
2.0	0.	9.26	0.	0.017
		Bimodal ($R_s = 1.0, REL = 2:1$):		
0.5	16.5	0.822	0.062	0.007
1.0	1824.	550.	29.6	10.1
1.5	3288.	166.	3.38	0.720
2.0	2078.	55.	0.643	0.083

Note. — The power ratios are expressed in units of 10^{-7}.

Table 4: Observational Parameters

Cluster	z	Exposure (ks)	0.1-2.4 keV Flux (10^{-12} erg cm^{-2} s^{-1})	Background (10^{-4} cts s^{-1} arcmin^{-2})
A85	0.0556	10.240	80.61	3.22
A514	0.0731	18.111	5.00	2.24
A1750	0.0855	13.148	14.62	2.79
A2029	0.0768	12.550	66.67	5.50

Note. — Only the 0.5 and 1 Mpc values are listed for A85 because 1.5 Mpc lies outside the central ring of the PSPC. The fluxes are from Ebeling (1993) except A514 which we computed in this paper (see §6.5). The background rate is computed in regions $\sim 30 - 40'$ from the field centers.

Table 5: Power Ratios of Abell Clusters

	P_1^{pk}/P_0^{pk}			P_2/P_0			P_3/P_0			P_4/P_0		
Cluster	0.5	1.0	1.5	0.5	1.0	1.5	0.5	1.0	1.5	0.5	1.0	1.5
A85	311	333	...	15.4	13.8	...	1.10	0.811	...	0.032	0.166	...
A514	9369	4833	2557	273	300	179	22.7	5.83	7.40	0.679	13.6	0.155
A1750	7	3670	3996	8.9	818	311	8.60	6.08	0.679	0.058	12.6	7.33
A2029	37	9	5	14.0	1.7	2.0	0.031	0.004	0.020	0.050	0.073	0.060

Note. — Power ratios in units of 10^{-7} for real PSPC images of Abell clusters computed for aperture radii 0.5, 1, and 1.5 Mpc.

Table 6. Correlations of the Power Ratios

Models	$P_1^{(pk)}/P_0^{(pk)}$ 1.0	2.0	P_2/P_0 1.0	2.0	P_3/P_0 1.0	2.0	P_4/P_0 1.0	2.0
Single (ϵ, a_x):								
(0.1, 0.1)	0.	0.	0.527	0.081	0.	0.	7.8e-5	9e-6
(0.1, 0.3)	0.	0.	4.15	1.05	0.	0.	9.6e-4	1.9e-4
(0.2, 0.1)	0.	0.	2.07	0.314	0.	0.	1.3e-3	1.5e-4
(0.2, 0.3)	0.	0.	17.1	4.16	0.	0.	0.017	3.2e-3
(0.3, 0.1)	0.	0.	4.55	0.680	0.	0.	7.1e-3	8.0e-4
(0.3, 0.3)	0.	0.	39.6	9.26	0.	0.	0.099	0.017
Bimodal (ϵ, R_s, REL):								
(0.0, 0.5, 1 : 1)	4437	1223	59.9	4.44	0.	0.	0.036	2.3e-4
(0.0, 0.5, 2 : 1)	1929	543	46.3	3.50	0.471	0.010	0.051	3.3e-4
(0.0, 0.5, 5 : 1)	472	135	16.8	1.36	0.664	0.016	0.056	3.9e-4
(0.0, 0.5, 10 : 1)	139	40.3	5.68	0.480	0.330	8.3e-3	0.030	2.3e-4
(0.0, 1.0, 1 : 1)	5148	4716	882	70.6	0.	0.	7.90	0.059
(0.0, 1.0, 2 : 1)	1824	2078	550	55.3	29.6	0.643	10.1	0.089
(0.0, 1.0, 5 : 1)	372	515	85.9	21.1	14.1	0.968	3.98	0.096
(0.0, 1.0, 10 : 1)	101	153	17.5	7.31	3.47	0.502	0.993	0.055
Major Axis:								
(0.2, 0.5, 1 : 1)	4367	1217	95.2	9.74	0.480	0.041	0.203	5.7e-3
(0.2, 0.5, 2 : 1)	1889	539	90.6	10.4	3.7e-3	6.4e-3	0.184	5.6e-3
(0.2, 0.5, 5 : 1)	460	134	56.7	8.19	0.179	1.5e-4	0.144	5.3e-3
(0.2, 0.5, 10 : 1)	135	39.9	37.6	6.48	0.117	5.6e-4	0.092	4.7e-3
(0.2, 1.0, 1 : 1)	5042	4690	993	88.2	1.15	0.152	12.5	0.155
(0.2, 1.0, 2 : 1)	1779	2062	677	76.9	19.1	0.202	13.0	0.159
(0.2, 1.0, 5 : 1)	362	510	163	39.3	10.3	0.577	4.55	0.144
(0.2, 1.0, 10 : 1)	98.6	151	64.6	20.7	2.57	0.330	1.25	0.086
Minor Axis:								
(0.2, 0.5, 1 : 1)	4367	1217	36.4	1.25	0.629	0.046	1.9e-3	7.6e-5
(0.2, 0.5, 2 : 1)	1889	539	17.4	0.276	1.97	0.086	0.039	1.3e-3
(0.2, 0.5, 5 : 1)	460	134	0.401	0.285	1.53	0.059	0.099	3.7e-3
(0.2, 0.5, 10 : 1)	135	39.9	2.01	1.35	0.660	0.026	0.080	4.2e-3
(0.2, 1.0, 1 : 1)	5042	4690	850	56.6	3.19	0.186	5.49	0.020
(0.2, 1.0, 2 : 1)	1779	2062	423	37.7	47.1	1.43	9.12	0.062
(0.2, 1.0, 5 : 1)	362	510	28.6	8.35	17.6	1.49	4.09	0.112
(0.2, 1.0, 10 : 1)	98.6	151	0.026	0.708	4.29	0.716	1.19	0.078

Note. — The power ratios (in units of 10^{-7}) computed in apertures of radii 1 Mpc and 2 Mpc; units of a_x and R_s are also Mpc and ϵ in the bimodal models refers to the ellipticity of the primary component. Bimodal models where the secondary component lies along the major axis of the primary are listed under Major Axis.

REFERENCES

Aschenbach, B. 1988, Appl.Optics, 27, No. 8, 1404

Ashman, K. M., Bird, C. M., & Zepf, S. E. 1994, AJ, 106, 1637

Binney, J., & Tremaine, S. 1987, Galactic Dynamics (Princeton: Princeton Univ. Press)

Bird, C. M. 1993, Ph.D thesis, University of Minnesota

Bird, C. M., & Beers, T. C. 1993, AJ, 105, 1596

Briel, U. G., et al. 1991, A&A, 246, 10

Buote, D. A., & Canizares, C. R. 1994, ApJ, 427, 86

Buote, D. A., & Canizares, C. R. 1995, ApJ, in press

Buote, D. A., & Tsai, J. C. 1995a, ApJ, 439, 29

Buote, D. A., & Tsai, J. C. 1995b, ApJ, submitted

Cavaliere, A., & Fusco-Femiano, R. 1976, A&A, 49, 137

Durret, F., Mazure, A, Trân Thanh Vân, J. & White, S. D. M. ed. 1995, in Clusters of Galaxies (Proceedings of the 29th Rencontres de Moriond), (Gif sur Yvette: Frontier Editions)

Ebeling, H. 1993, Ph.D thesis, Ludwig-Maximilians-Universität München

Evrard, A. E., Mohr, J. J., Fabricant, D. G., & Geller, M. J. 1993, ApJ, 419, 9

Fahlman, G., Kaiser, N., Squires, G., & Woods, D. 1994, ApJ, 437, 56

Fitchett, M. J. 1989, in Clusters of Galaxies (STScI Symp. 4), ed. W. R. Oegerle, M. J. Fitchett, & L. Danly (Cambridge: Cambridge University Press), 111

Forman, W., & Jones, C. 1990, in Clusters of Galaxies (STScI Symp. 4), ed. W. R. Oegerle, M. J. Fitchett, and L. Danly, (Cambridge: Cambridge University Press), 257

Hasinger, G. 1992, in The X-ray Background (Cambridge: Cambridge University Press), ed. X. Barcons & A. C. Fabian, 229

Jackson, J. D. 1975, Classical Electrodynamics (New York: Wiley)

Jones, C., & Forman W. 1984, ApJ, 276, 38

Jones, C., & Forman W. 1992, in Clusters and Superclusters of Galaxies (NATO ASI Vol. 366), ed. A. C. Fabian, (Dordrecht/Boston/London: Kluwer), 49

Kaiser, N., & Squires, G. 1993, ApJ, 404, 441

Katz, N., & White, S. D. M. 1993, ApJ, 412, 455

Lin, C. C., Mestel, L., & Shu, F. H. 1965, ApJ, 142, 1431

Merritt, D., & Stiavelli, M. 1990, ApJ, 358, 399

Merritt, D., & Hernquist, L. 1991, ApJ, 376, 439

Mohr, J. J., Fabricant, D. G., & Geller, M. J. 1993, ApJ, 413, 492

Oegerle, W. R., Fitchett, M. J.,& Danly, L. ed. 1990, Clusters of Galaxies (STScI Symp. 4), (Cambridge: Cambridge University Press)

Pfeffermann, E. et al., 1987, Proc. SPIE, 733, 519

Richstone, D. O., Loeb, A., & Turner, E. L. 1992, ApJ, 393, 477

Sarazin, C. L. 1986, Rev. Mod. Phys., 58, 1

Smail, I., Ellis, R. S., Fitchett, M. J., & Edge, A., 1995, MNRAS, 273, 277

Soltan, A., & Fabricant, D. G. 1990, ApJ, 364, 433

Trümper, J. 1983, Adv. Space Res., 2, 241

Fig. 1.—
Contour plots of four simple models for X-ray clusters placed at $z = 0.10$: (a) is a single-component model with core radius 300 kpc and $\epsilon = 0.30$; (b) - (d) are bimodals each separated by 1 Mpc and have core radii 300 kpc but the clumps are in proportion 1 : 1 for (b), 2 : 1 for (c), and 5 : 1 for (d). The contours are separated by factors of two in surface brightness (arbitrary units). The units are in 15″ pixels which translates to 36.7 pixels/Mpc and 2.7 Mpc/side for $H_0 = 80$ km/s/Mpc.

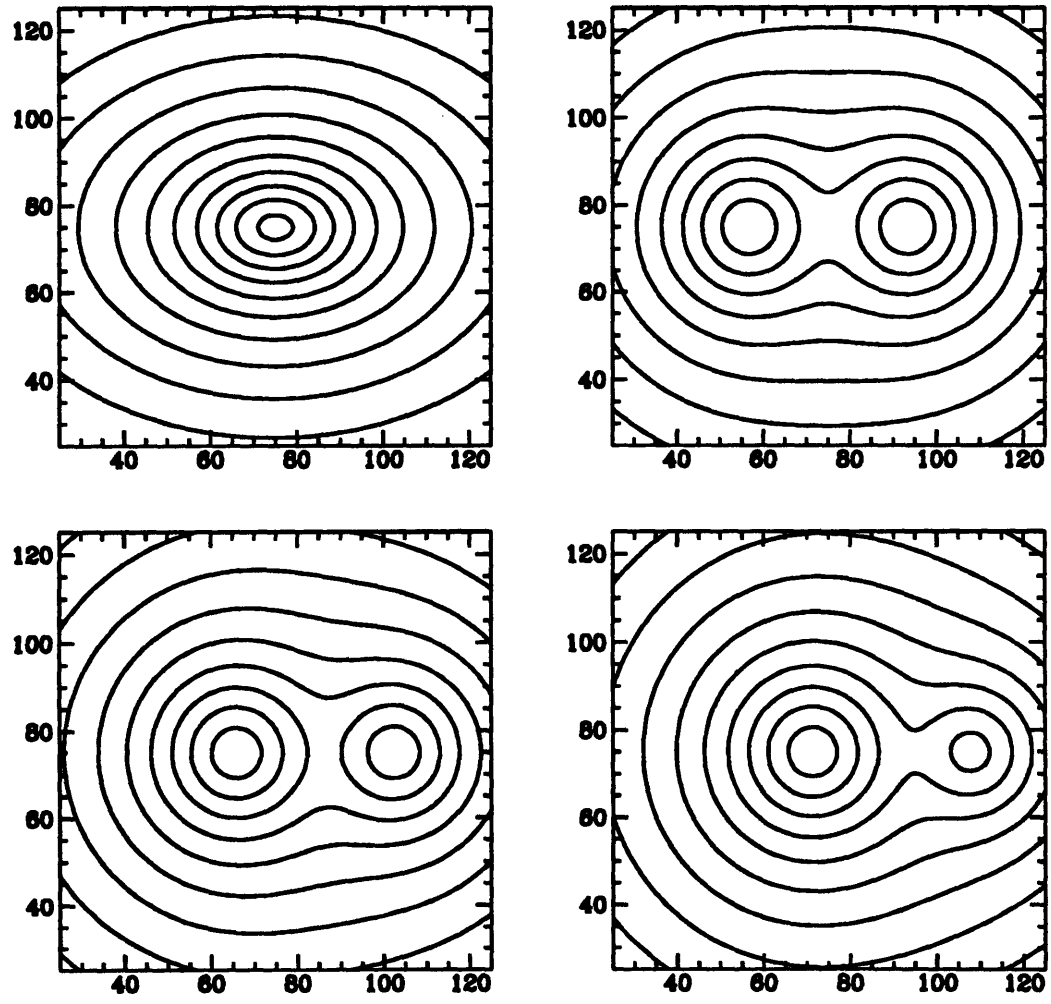

Fig. 2.—
Contour plots of 10ks simulated observations of the cluster models in Figure 1 as described in §6.4. The images have been smoothed with the PSPC PSF for viewing purposes only.

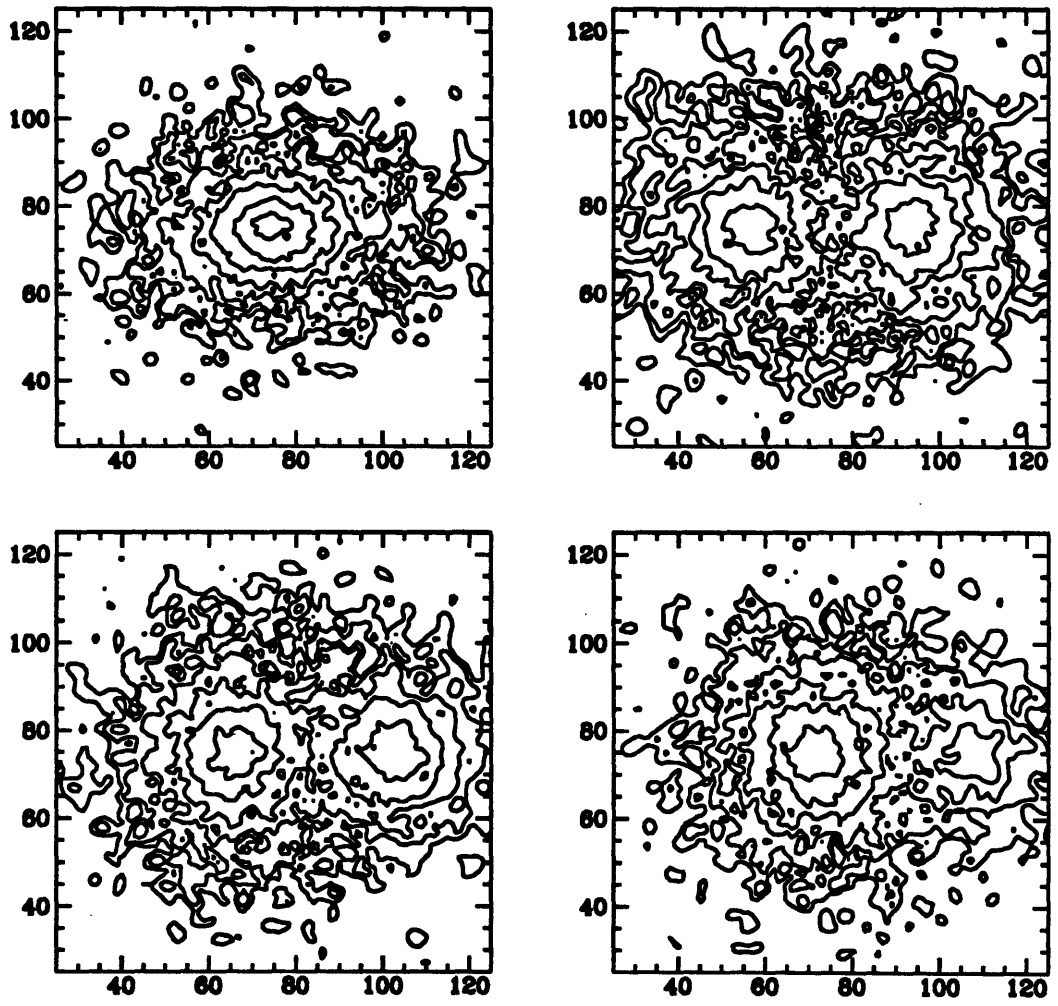

Fig. 3.—
Cumulative distributions of $P_1^{(pk)}/P_0^{(pk)}$, P_2/P_0, P_3/P_0, and P_4/P_0 for the simulated cluster samples of single-component clusters (solid) and bimodal clusters (dotted).

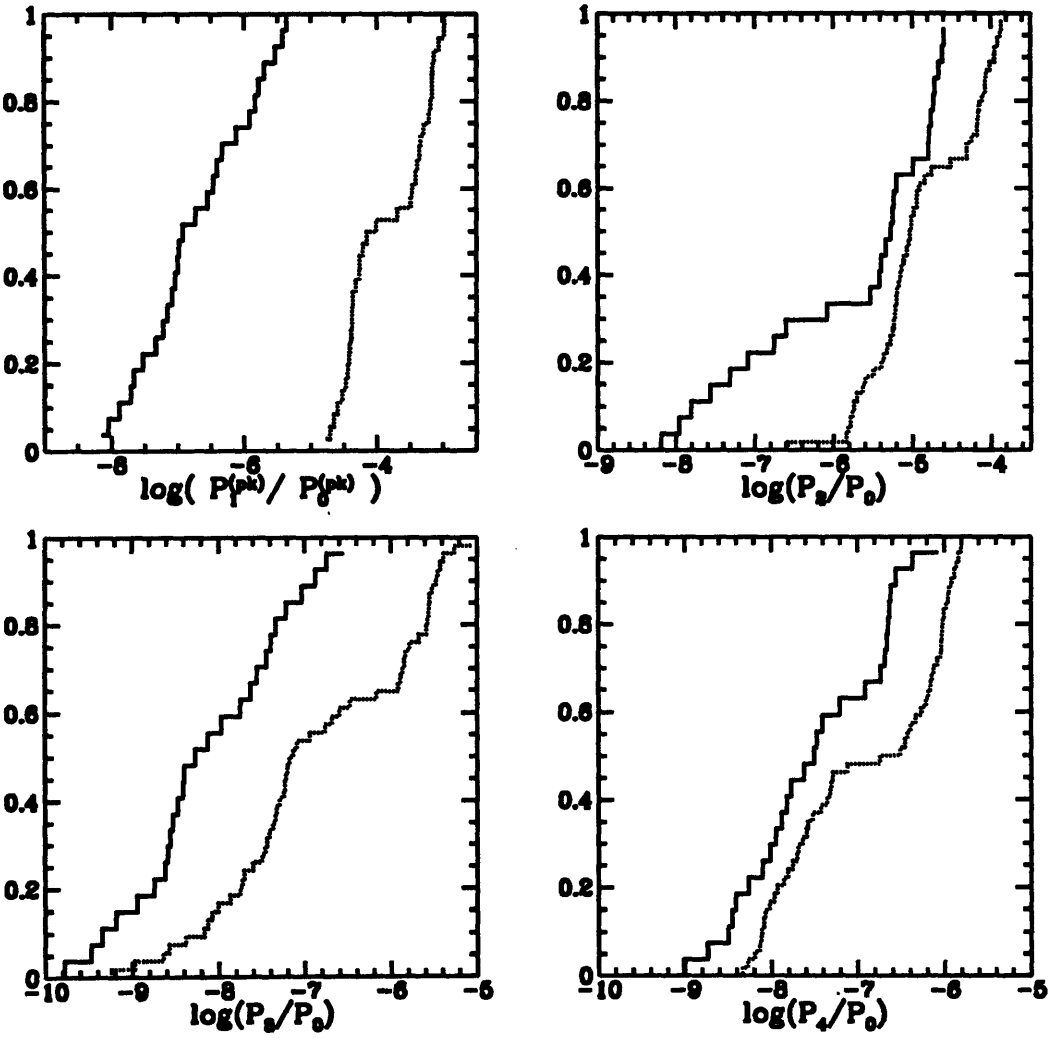

Fig. 4.—
Contour plots of the PSPC images of Abell clusters A85, A514, A1750, and A2029 corrected for exposure, vignetting, and background; the angular sizes of the fields are the same as Figure 1. The contours are separated by factors of 2 in intensity and the images have been smoothed with the PSPC PSF for viewing purposes only.

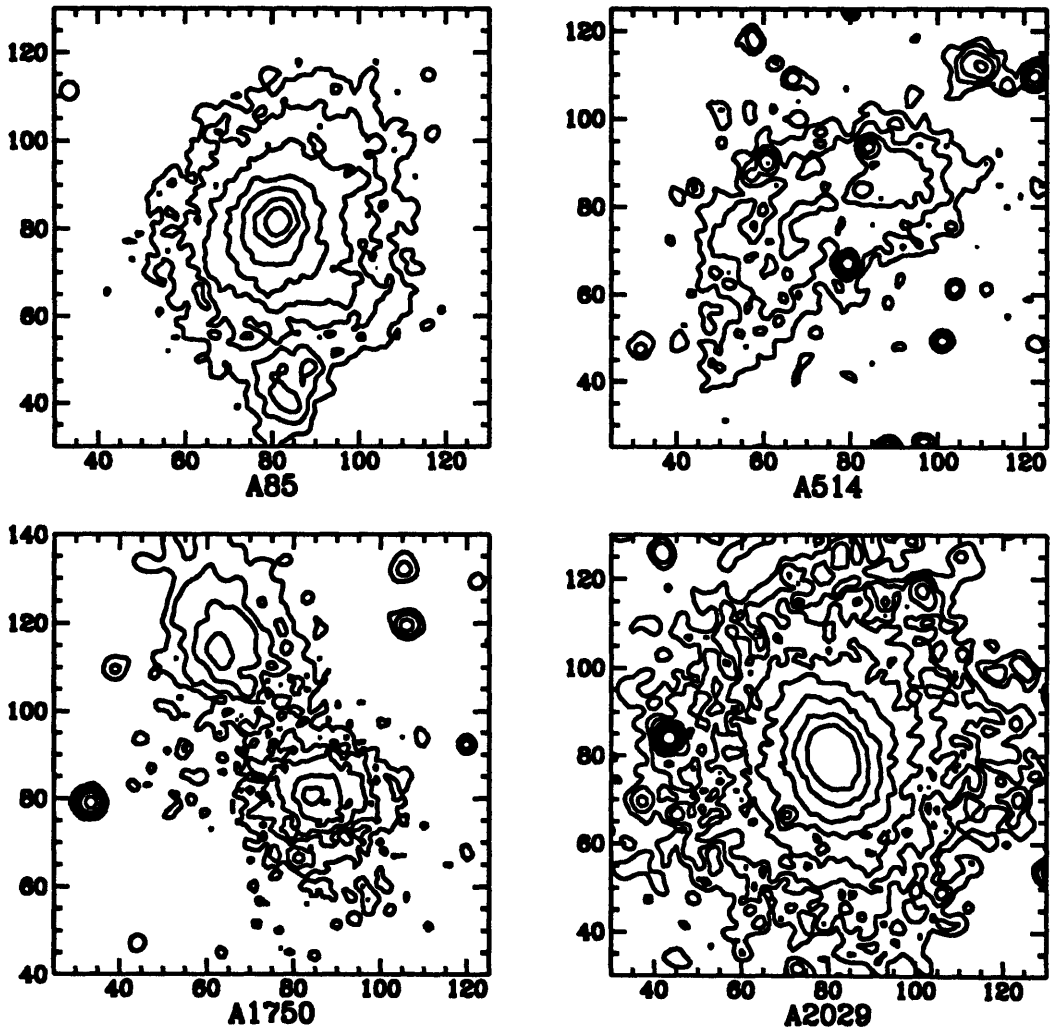

Fig. 5.—
Contour plots of the PSPC images of Abell clusters A85, A514, A1750, and A2029 prepared as in Figure 4 but with sources removed as described in §6.5. The images have been smoothed with the PSPC PSF for viewing purposes only.

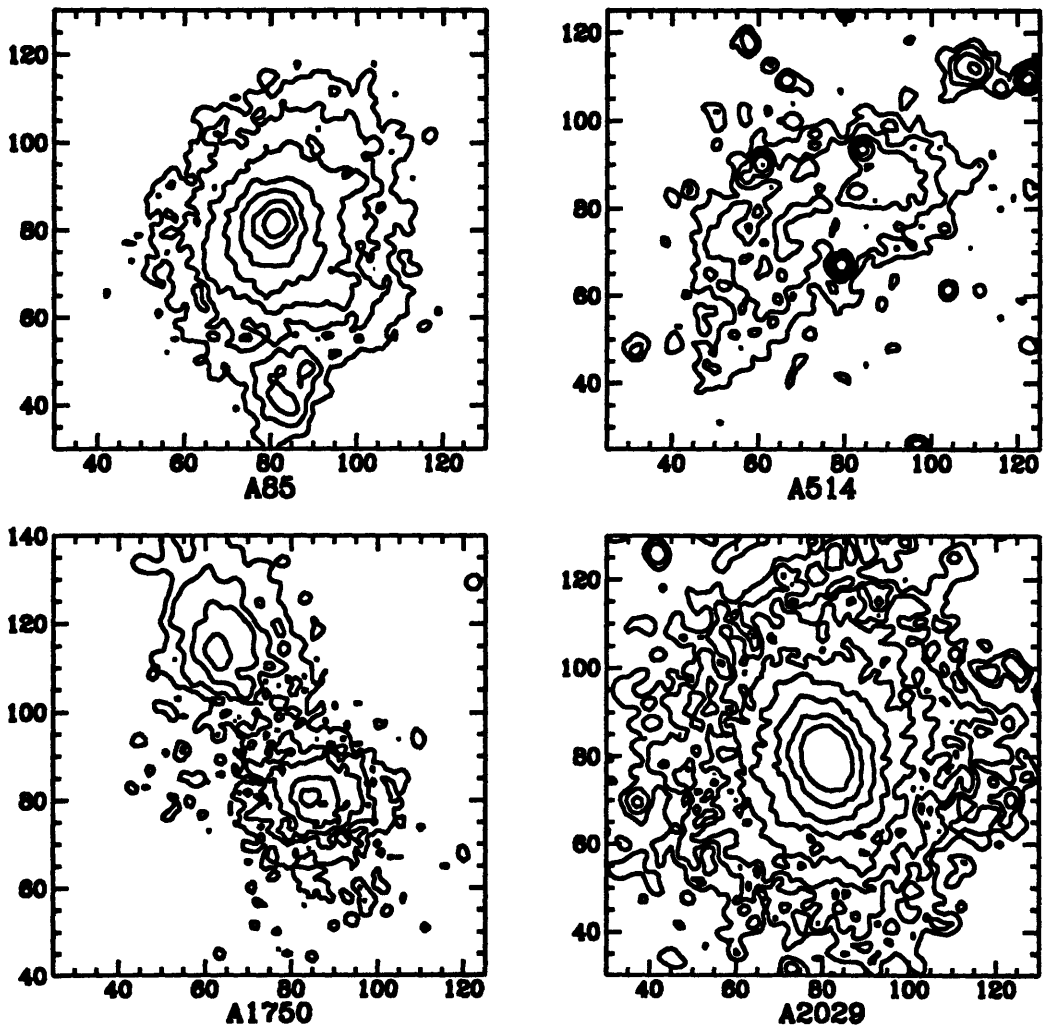

Fig. 6.—
Correlations of the power ratios for a sample of models of single-component clusters (filled ovals) and bimodal multiclusters (crosses); see Table 3 for a description of the sample. The dashed lines represent the region where single-component clusters are allowed due to observational uncertainty as determined by the simulated PSPC observations in §6.4.

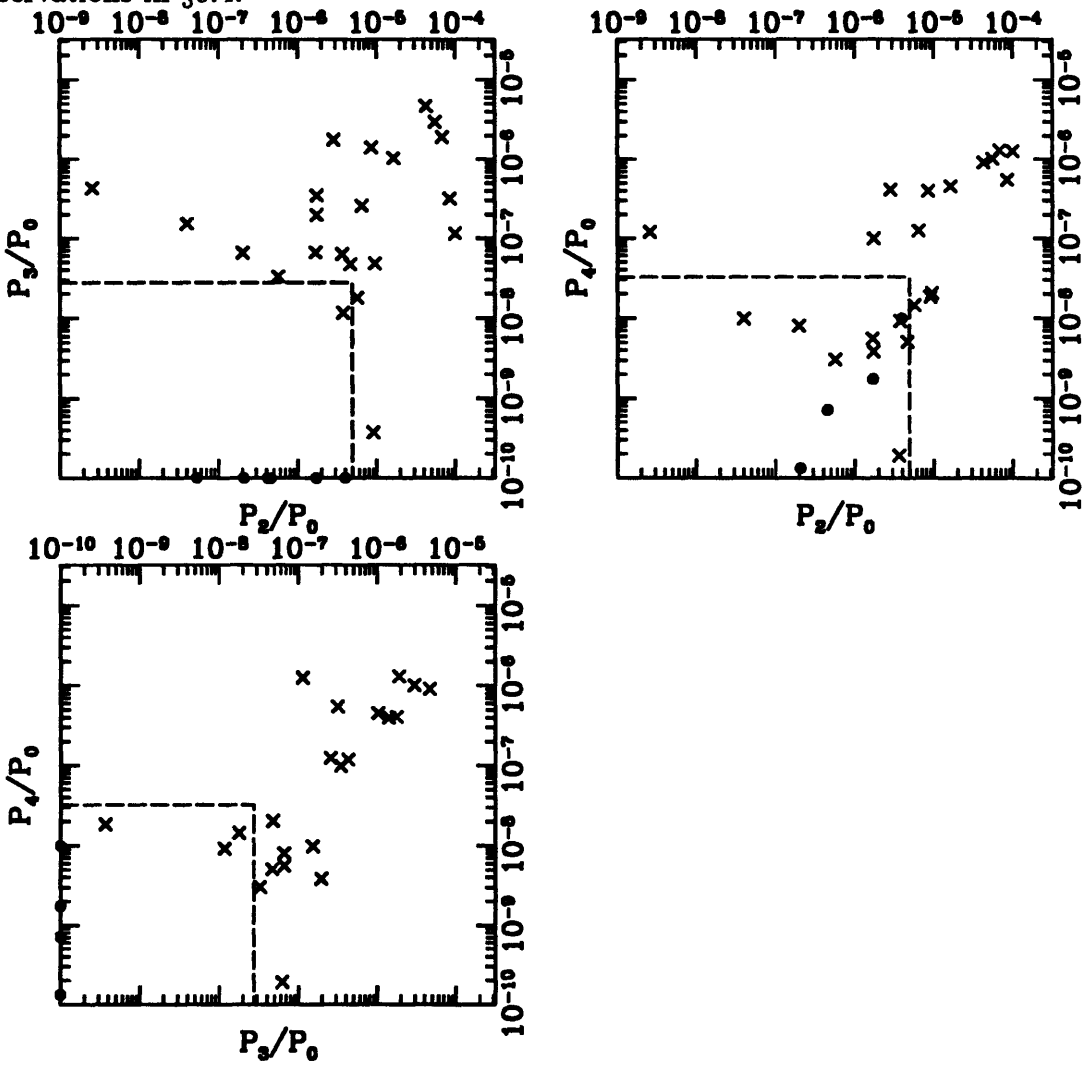

Fig. 7.—
Same as Figure 6 for the power ratios computed in the 2 Mpc aperture.

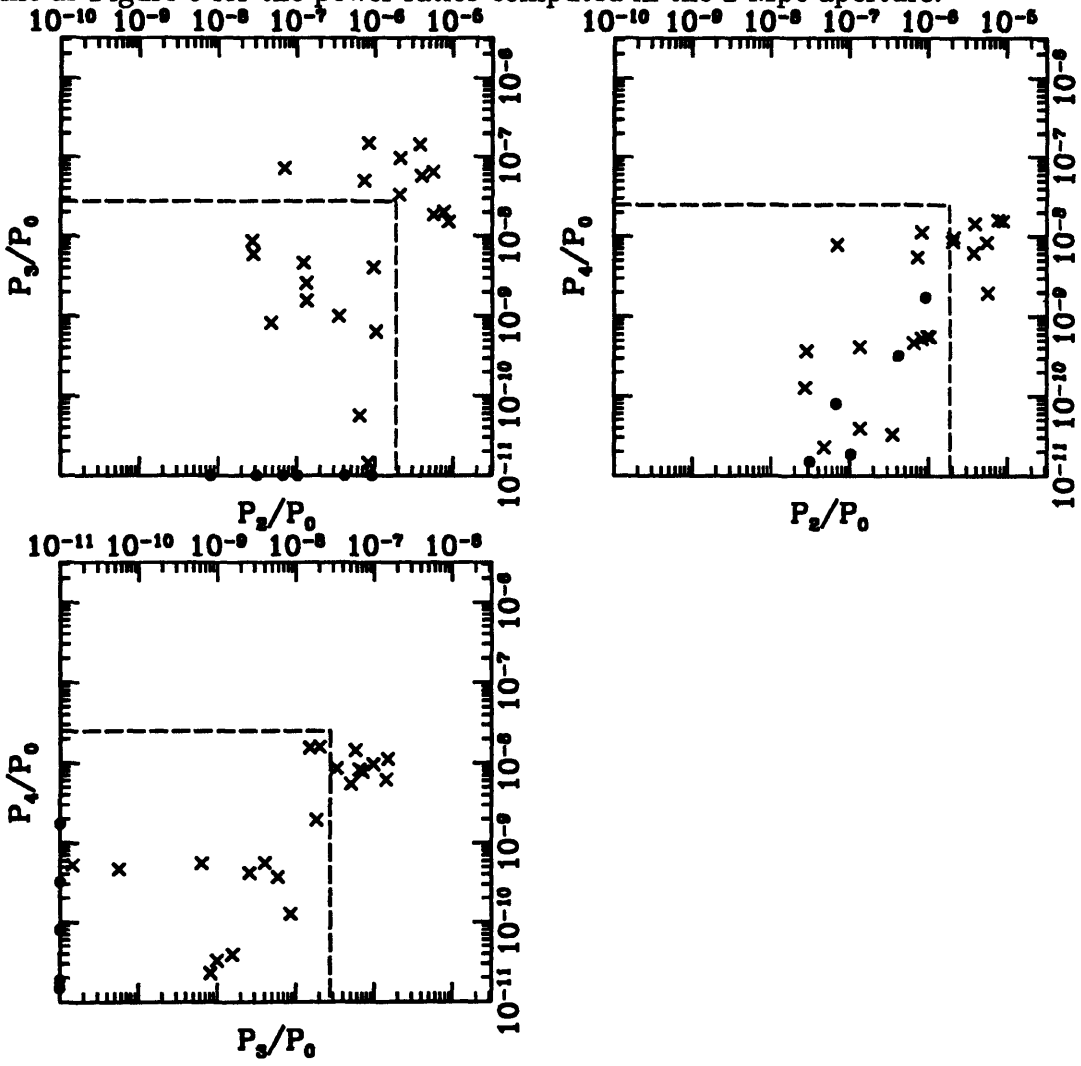

Chapter 7

Quantifying the Morphologies and Dynamical Evolution of Galaxy Clusters. II. Application to a Sample of ROSAT Clusters

We now apply the power-ratio method introduced in the previous chapter to ROSAT PSPC X-ray images of 55 galaxy clusters. The clusters exhibit a particularly strong $P_2/P_0 - P_4/P_0$ correlation in the $1h_{80}^{-1}$ Mpc aperture which may be interpreted as an evolutionary track; the location of a cluster on the correlation line indicates the dynamical state of the cluster and the distribution of clusters along this track measures the rate of formation and evolution of clusters in our sample. The power ratios anti-correlate with the cooling-flow rate indicating a reasonable quantitative dependence of the flow rate on cluster morphology. The relationship of the power ratios to the optical Bautz-Morgan (BM) Type is more complex. This is because the power ratios are sensitive to unrelaxed regions of clusters within a specified scale, whereas BM types are sensitive to unrelaxed regions over many scales. We discuss further astrophysical applications exploiting the relationship between the power ratios and the evolutionary states of clusters.

7.1 Introduction

The important connection between the morphologies of galaxy clusters and the cosmological density parameter Ω has received much recent attention (Richstone, Loeb, & Turner 1992; Evrard et al. 1993; Mohr et al. 1995). This connection has generally been formulated in terms of the frequency of "substructure" in clusters, where "substructure" is an ambiguous statement of the dynamical youth of a cluster (see West [1990] for a discussion of this issue). For example, Jones & Forman (1992) attempted to devise a more consistent description of "substructure" by visually separating clusters into six morphological classes. Using a sample of $\sim$ 200 clusters observed with *Einstein*, Jones & Forman computed the frequency of these morphological classes and concluded that about 40% of clusters displayed some type of "substructure". Recent studies suggest a substantial increase in this percentage (e.g., West 1995).

From these qualitative measures of "frequency of substructure" in clusters, investigators have attempted to determine Ω (e.g., Richstone et al. 1992) and the power spectrum of primordial density fluctuations (e.g., David et al. 1993) by comparison to Press-Schechter (1974) type predictions of the distribution of collapsed (i.e. virialized) objects. However, these comparisons are inherently uncertain because of the unknown relation between a particular investigator's definition of "substructure" and the dynamical state of a cluster. Even well defined and quantitative measures of morphology which employ centroid-shifts and axial ratios, (Evrard et al. 1993, Mohr et al. 1995) fail to provide any physical connection of these parameters to the dynamical states of clusters.

We previously presented a method to quantify the morphologies of galaxy clusters in direct relation to their dynamical states as given by their gravitational potentials (Buote & Tsai 1995b; hereafter BT). The statistics of this method, i.e. "power ratios", in essence measure the square of the ratio of higher-order multipole moments of the two-dimensional potential to the monopole moment. The power-ratio description of the morphologies of X-ray clusters is intended to classify structure that is obvious to the eye, not subtle substructure that requires more robust techniques (e.g., Bird &

Beers 1993); i.e. the significance of the substructure is a given, what the structure implies for the aggregate cluster dynamics is our concern.

Because of their intimate link to cluster dynamics, power ratios are not only ideal for cosmological studies, but also for studies of clusters themselves. It is our purpose in this paper to create a database of power ratios for testing the predictions of various cosmogonies and to present initial results on the implications of the measured power ratios. We discuss the cluster sample in §7.2 and the data reduction and analysis in §7.3. We consider correlations of the various power ratios among themselves and how these relate to Jones – Forman classes in §7.4. We present the evolutionary track of clusters and the correlations of the power ratios to other X–ray cluster properties and optical measures of substructure in §7.5. Further important astrophysical applications of the power ratios are discussed in §7.6, and we present our conclusions in §7.7.

7.2 The Sample

In principle one desires a large (> 100), complete, volume-limited sample of high signal-to-noise (S/N) X-ray images of clusters for use in cosmological analysis. Although not ideal, X-ray images of clusters taken with the ROSAT Position Sensitive Proportional Counter (PSPC; see Pfeffermann et al. 1987) are the best data currently available for a relatively large number of clusters (see BT §4 for a discussion). Ebeling (1993) has compiled a flux-limited sample ($\sim$ 200 members) of nearby ($z < 0.2$) Abell and ACO clusters from PSPC data taken during the ROSAT All-Sky Survey (RASS); this sample, however, is estimated to be at most only 72% complete. Unfortunately, the RASS is not available to the public and, in any event, the images of the RASS are not suitable for our needs because of the short exposures ($\sim$ 500s). Long exposures of $\sim$ 50 of the clusters in Ebeling's sample were taken as part of the Guest Observers (GO) program and are currently available in the ROSAT Public Data Archive operated by the HEASARC-Legacy database. However, only $\sim$ 30 of the brightest clusters of Ebeling's sample are well represented by GO observations.

Since we have good coverage for only $\sim$ 30 of the $\sim$ 200 clusters in Ebeling's

sample, we also consider the X-ray flux-limited sample of Edge et al. (1990). This sample of the brightest 55 clusters from EXOSAT and *Einstein* data is estimated to be $\sim$ 90% complete and most are included in Ebeling's catalogue. We analyze all of the clusters in the ROSAT archive common to both the Ebeling and Edge et al. samples. Given that our composite sample is not complete we will, in addition to presenting results for the whole sample, emphasize results for those clusters that overlap that Edge et al. sample.

Not all of the GO cluster images are useful for our analysis of the power ratios. Most importantly we require that a circle of at least a $500h_{80}^{-1}$ kpc ($H_0 = 80h_{80}$ km s^{-1} Mpc^{-1}) radius be entirely enclosed within the central 40′ diameter ring supporting the PSPC window. We only analyze regions interior to the PSPC ring because the support structure would contribute to the power ratios.

In Table 1 we list our sample of ROSAT PSPC clusters along with relevant data for each cluster. The fluxes listed in the table correspond to the $0.1 - 2.4$ keV band (10^{-12} erg cm^{-2} s^{-1}) and have been taken from Ebeling where possible. For those clusters not in Ebeling's catalogue we compute a flux using the standard IRAF-PROS software; i.e. we extract the background-subtracted spectrum interior to the PSPC ring and fit an absorbed, single-temperature Raymond-Smith plasma having 1/2 solar metallicity. In addition to the flux, we give the redshift, the exposure time for the observation, temperature from the literature, background count-rate used in this paper (10^{-4} counts s^{-1} arcmin^{-2}) , and the Bautz-Morgan Type (see §7.5.3). For those clusters with multiple exposures of the pointing we give the total exposure time of the merged observations. For COMA (A1656) and A2256 we refer the reader to the discussion of individual clusters in Appendix A..

7.3 Image Reduction and Analysis

To prepare the images for analysis we (1) eliminated time intervals of high background count rate, (2) selected energy channels corresponding to photon energies 0.5 - 2 keV and rebinned the image into 512 × 512 fields of 15″ pixels, (3) corrected for

exposure variations and telescopic vignetting, (4) merged multiple pointings into one image when available, (5) removed point sources (see §7.3.1), and (6) subtracted the background. All the data reduction was implemented with the standard IRAF-PROS software. In Appendix A. we note the reduction peculiarities for each cluster.

The GO observations were partitioned into many short exposures to maximize the observing efficiency of ROSAT. We eliminated time intervals corresponding to large, short-term enhancements in the background light curves indicative of contamination from scattered X-rays, especially from the Sun, the bright Earth, and the SAA. Only a few clusters required time-filtering (Appendix A.).

To minimize the effects of the X-ray background and the width of the PSPC PSF (see Hasinger et al. 1994) we selected photons only from energy channels between 0.5 and 2 keV. In addition, we rebinned the images into more manageable 15″ pixels corresponding to 512×512 fields in accordance with BT. This pixel scale is the same as the exposure maps provided with the standard analysis systems software (SASS); note that the true resolution of the exposure maps actually corresponds to 30″ pixels.

The images were then flattened using the SASS exposure maps. When dividing the images by these exposure maps we corrected for both exposure variations and telescopic vignetting. In principle this correction depends on the energy of each individual photon, but for energies above 0.2 keV the energy dependence is small and we neglect it (Snowden et. al. 1994).

For the few clusters having multiple pointings we merged them into one image for each cluster. Point sources common to each of the images for a particular cluster were used to align the fields. After removing point sources (see §7.3.1) we then subtracted the background. For most of the clusters we computed the background in a source-free region $\sim 45' - 50'$ from the field center.

7.3.1 Source Removal

Excising bright point sources from the cluster images is perhaps the most critical aspect of the image reduction. Because of the width of the PSPC PSF ($FWHM \sim 30''$) point sources are endowed with finite spatial extent and may contribute substantially

to the power ratios (see §7.3.2) For the low-order power ratios that we consider the point sources do not appreciably affect the power ratios when the aperture radius $\gg$ width of the PSPC PSF. However, when this is not the case, precise source removal becomes vital.

As discussed in BT, removing only the brightest ($\gtrsim 5\sigma$) sources is generally sufficient for obtaining reliable measurements of the power ratios. We easily and effectively locate these brightest sources from visual examination of the cluster images. Nevertheless, in an effort to eliminate any non-cluster contamination, we also excise any dubious fluctuations not obviously associated with the host cluster. When done properly this only serves to smooth out the cluster image on small scales without altering the large-scale structure of the image (important to the power ratios under consideration – see §7.3.2) which would occur by smoothing with, for example, a Gaussian filter.

From visual examination of the X-ray images it is impossible to unequivocally distinguish foreground/background sources from structures that are gravitationally associated with the clusters. However, the vast majority of the clusters in our sample have a single dominant component or two components that are sufficiently extended and bright which dominate the power ratios irrespective of our decision to include or exclude a few faint sources. Only for a few clusters (e.g., A500, A2382, and A514 – see Appendix A.) having complex spatial structures is identification of real structures important. Even for these cases, though, the decision to include/exclude a source does not alter the power ratios to such a degree so as to give a complex cluster like A514 power ratios appropriate to a smooth cluster like A2029 (see §7.4). In any event, to achieve the most stringent constraints on the power ratios it is necessary to verify whether features in the complex clusters are indeed associated with the cluster; i.e. from detailed X-ray spectral analysis of the features and/or obtaining the appropriate redshifts.

We removed sources from the cluster images using the following simple procedure. For each source we constructed a circular annulus about the center of the source; typical annuli widths were 1-2 pixels. Then we fit a second-order polynomial surface

to the background in the annulus. Finally, we replaced the source region with this background surface. In Figure 1 we show the image for A1795 before and after the sources have been removed. Of all the clusters in our sample A1795 has the largest number of detected sources within an aperture (i.e. $1h_{80}^{-1}$ Mpc) used to compute power ratios. The possibilities of biases due to excising sources from the images is discussed in §7.3.3.

7.3.2 Computation of Power Ratios

The power ratios are derived from the multipole expansion of the two-dimensional gravitational potential, $\Psi(R,\phi)$, due to matter interior to R,

$$\Psi(R,\phi) = -2Ga_0 \ln\left(\frac{1}{R}\right) - 2G\sum_{m=1}^{\infty}\frac{1}{mR^m}\left(a_m\cos m\phi + b_m \sin m\phi\right), \qquad (7.1)$$

where the moments a_m and b_m are given by,

$$\begin{aligned} a_m(R) &= \int_{R'\leq R}\Sigma(\vec{x}')\,(R')^m \cos m\phi' d^2x', \\ b_m(R) &= \int_{R'\leq R}\Sigma(\vec{x}')\,(R')^m \sin m\phi' d^2x', \end{aligned}$$

and $\vec{x}' = (R',\phi')$. For analysis of X-ray cluster images we associate the surface density, Σ, with the X-ray surface brightness; we refer the reader to BT for a more detailed discussion. By integrating the magnitude of each term of Ψ over a circular aperture of radius R_{ap} we arrive at the following definition,

$$P_m\left(R_{ap}\right) = \frac{1}{2\pi}\int_0^{2\pi}\Psi_m\left(R_{ap},\phi\right)\Psi_m\left(R_{ap},\phi\right)d\phi, \qquad (7.2)$$

where Ψ_m is the $m-$th term in the expansion of eq. (7.1). The quantity P_m is the "power" within R_{ap} of the multipole terms of order m. Ignoring factors of $2G$, the powers are given by,

$$P_0 = \left[a_0 \ln\left(R_{ap}\right)\right]^2, \qquad (7.3)$$

for $m = 0$ and

$$P_m = \frac{1}{2m^2 R_{ap}^{2m}} \left(a_m^2 + b_m^2\right) \tag{7.4}$$

for $m > 0$. The total power of all multipole moments is simply,

$$P = \sum_{m=0}^{\infty} P_m. \tag{7.5}$$

The values for the individual P_m depend on the coordinate system chosen. We utilize coordinate systems where the aperture is located at (1) the centroid of the cluster emission (i.e. where P_1 vanishes), and (2) at the peak of the cluster emission. To distinguish between these two cases we denote the moments of case (2) by $P_m^{(pk)}$. We consider case (2) in order to extract information from the dipole moment; i.e. $P_1^{(pk)}$ is akin to a centroid-shifting power, a quantity already known to be significant for many clusters (Mohr et al. 1993; Mohr et al. 1995).

We consider $P_m (m = 0, 1, 2, 3, 4)$ and $P_m^{(pk)} (m = 0, 1)$ for quantifying the morphologies of galaxy clusters. BT demonstrated that these powers are sensitive to the type of substructure most relevant to the dynamics of clusters and hence to cosmology (see Richstone et al. 1992). Rather than the powers individually, the power ratios, P_m/P_0 and $P_1^{(pk)}/P_0^{(pk)}$, classify clusters according to the dynamical importance of substructure (see BT). For example, consider a widely separated bimodal cluster of equal-sized components and a single-component ellipsoidal cluster having the same luminosity. Assume these clusters also happen to have identical values of P_2 within an aperture, R_{ap}. The bimodal cluster in this case necessarily has a smaller monopole moment within R_{ap}, and hence a smaller P_0, than the ellipsoidal cluster. Hence, P_2/P_0 differs for these clusters as a result of the different dynamical importance of substructure present in the clusters. Considering the power ratios P_m/P_0 and $P_1^{(pk)}/P_0^{(pk)}$ also has the advantage of normalizing to the cluster fluxes within R_{ap}, thus allowing consistent comparison between images of clusters having different fluxes and/or exposures.

We compute the power ratios in apertures of radii 0.5, 1, and 1.5 h_{80}^{-1}Mpc under the condition that all points on the aperture boundary be separated by at least 1

pixel from the inside of the PSPC ring; for clusters just falling short of this criteria we decreased the appropriate aperture sizes up to 10% to allow computation of the power ratios. This criterion yields measurements of power ratios in the $0.5h_{80}^{-1}$ Mpc aperture for all 55 clusters, 41 clusters have $1h_{80}^{-1}$ Mpc aperture measurements, and only 27 have power ratios measured in a $1.5h_{80}^{-1}$ Mpc aperture. By using apertures of different sizes we obtain information regarding the scale where the substructure is dynamically important; this is particularly useful for assessing where the gas is relaxed (see §7.6).

7.3.3 Estimation of Uncertainty

We investigated the possibility of a bias introduced into the power ratios resulting from excising point sources from the cluster images. Returning to the case of A1795, we computed the power ratios in the 1 h_{80}^{-1}Mpc aperture as a function of the the number of sources removed in decreasing order of brightness. The results are displayed in Figure 2. After the brightest few sources are removed the power ratios approach a stable solution, with the residual variations being substantially less than the uncertainties due to noise (see below and Table 2). Since A1795 encloses the most detected sources in our sample, any biases resulting from our source removal should be most pronounced. Hence, we conclude that the power ratios are not significantly biased as a result of our method for subtracting sources from the cluster images.

We applied a simple Monte Carlo procedure to estimate the uncertainties on the power ratios due to point sources and Poisson noise. Our starting point for a particular cluster was the reduced image except that the background was not yet subtracted. Following BT we added to the images point sources having spatial properties consistent with the PSPC PSF and numbers consistent with the $\log N(> S)$ - $\log S$ distribution given by Hasinger (1991). We excised the brightest simulated sources corresponding to (on average) the same number of point sources removed from the real image. Poisson noise was then added to the images. Since pixels having "0" counts represent poor estimates of the Poisson mean, we instead used the average counts in a 1′ radius circle about the "0"-counts pixels. (We prefer to use the real

image instead of an elliptical β model [Mohr et al. 1995] since many of the clusters are not well described by the β model.) After the sources and noise have been added we then subtract the mean background and compute the power ratios.

For each cluster we performed 100 realizations. We defined the 90% confidence limits on a given P_m/P_0 to be the 5th smallest and the 5th largest values obtained from the 100 simulations. Although this definition is arbitrary it serves our purpose for providing a simple, realistic measure of the significance of a given power ratio; i.e. we do not require formal error estimates for any fitting. In a few cases the derived confidence limits do not enclose the actual value of the power ratio. This is expected since on average 10% of the power ratios should not be enclosed by the 90% confidence limits. Moreover, our arbitrary definition of the confidence intervals may be inadequate in a few cases where the power ratios in the 100 simulations deviate substantially from a distribution symmetric about its mean.

7.4 Correlations of Power Ratios and The Jones – Forman Morphological Classes

We list the power ratios and their 90% confidence estimates in Table 2. The clusters in our sample generally span two decades in the various power ratios; i.e. $P_1^{(pk)}/P_0^{(pk)} \sim 10-1000$, $P_2/P_0 \sim 1-100$, $P_3/P_0 \sim 0.05-5$, and $P_4/P_0 \sim 0.01-1$ (all power ratios given in units of 10^{-7}). Typically $P_1^{(pk)}/P_0^{(pk)}$, P_3/P_0, and P_4/P_0 have half-decade uncertainties, although P_4/P_0 appears to be slightly better constrained than P_3/P_0 on average. The best determined power ratio is P_2/P_0 which is generally constrained to better than a tenth of a decade; i.e. the even power ratios are more precisely measured than the odd ones.

The values listed in Table 2 can be used to construct individual distribution functions for the four power ratios considered here. Specifically, for each P_m/P_0 where $m = 1,...,4$, the distribution of the number of clusters which have power ratios of given values can be determined. These distribution functions can then be used to con-

strain differing aspects of the morphology of clusters produced by cosmogonic models, much as the observed luminosity function of galaxies is currently used to constrain theories of galaxy formation. This manner of comparison to theory will be investigated in a subsequent paper. Significant insights into cluster evolution and structure, however, can be more readily gained by considering correlations of the various power ratios.

Consider the three dimensional space defined by the centroided power ratios $(P_2/P_0, P_3/P_0, P_4/P_0)$. For the moment we exclude $P_1^{(pk)}/P_0^{(pk)}$ because it is necessarily trivially correlated to some combination of the P_m/P_0. Projections of the power ratios of the "best measured" clusters in Table 2 onto the three coordinate planes of power ratio space are shown in Figures 3 and 4, where assumed aperture sizes are $0.5h_{80}^{-1}$ Mpc and $1h_{80}^{-1}$ Mpc, respectively. We do not consider the $1.5h_{80}^{-1}$ Mpc aperture because there are unsatisfactorily few clusters that meet our precision criteria. Our criterion for selecting the "best measured" values is that P_3/P_0 and P_4/P_0 do not have error estimates that span larger than a decade unless their upper limit is $\leq 0.25 \times 10^{-7}$. This arbitrary upper limit is used because clusters with small values of P_3/P_0 and P_4/P_0 often have large fractional uncertainties but still occupy a region of power ratio space well separated from that occupied by the other clusters. Since P_2/P_0 is the most precisely determined power ratio, the plots do not discriminate whether a cluster is "best measured" based on the values of this ratio. Next to each correlation plot we give an equivalent plot for the subset of clusters also included in the Edge et al. (1990) sample.

Despite the small number of clusters having well measured P_3/P_0 or P_4/P_0 (i.e., ~ 20 and ~ 15 clusters in the 0.5 and $1h_{80}^{-1}$ Mpc apertures, respectively), the power ratios are obviously correlated with each other. The most pronounced of these is the P_2/P_0 - P_4/P_0 correlation, especially for the $1h_{80}^{-1}$ Mpc aperture. In fact, the $1h_{80}^{-1}$ Mpc correlation is consistent with $P_2/P_0 \propto P_4/P_0$ to within the estimated uncertainties (except A665, see below). Although only the clusters having the most precise measurements are displayed, all of the clusters are consistent with the trends shown in Figures 3 and 4.

Since clusters of all observed morphologies are included in our sample (see below), a first result is that the above correlations provide structural constraints on individual clusters. For example, consider the P_2/P_0 - P_4/P_0 correlation. All observed clusters regardless of morphology (again except for A665) have roughly the same amount of quadrupole structure (P_2/P_0) as octupole structure (P_4/P_0), modulo some constant factor; note this correlation is not evident when computing the power ratios on simulated blank images with Poisson noise. Although it would be reasonable for complex clusters having significant quadrupole structure to also have a large amount of octupole structure, the observed correlation implies that these differently scaled structures must increase or decrease in direct proportion to each other. An imaginary cluster assembled and evolving by arbitrary means certainly need not satisfy these constraints as shown in Figures 6 and 7 of BT. In fact, the toy clusters in BT which lie far to the right of the correlation track represent bimodal models where the small component lies along the short axis of the dominant component which would not be expected if the cluster initially collapsed along its shortest axis (e.g., Lin, Mestel, & Shu 1965). Our correlations readily show that since only one cluster lies off the correlation line, any theory of cluster formation must produce a large majority of clusters which obey the correlation. The strong correlation of P_2/P_0 and P_4/P_0 also implies that there is little additional information in the distribution function for P_4/P_0 alone that is not contained in the distribution function for P_2/P_0.

We can further understand these correlations by considering the location of specific clusters in Figures 3 and 4 and how the power ratios relate to the qualitative classification system of Jones & Forman (1992; hereafter JF). We selected six clusters from our sample that span the complete range of power ratios and the six morphological classes of JF: A2029 – SINGLE, A1750 – DOUBLE, A85 – PRIMARY WITH SMALL SECONDARY, A2142 – OFFSET CENTER, A545 – ELLIPTICAL, A514 – COMPLEX. The dynamical states of these clusters is obvious: A2029 is a smooth, relaxed cluster; A1750 is a double cluster in the midst of a merger event; A85 has a dominant, mostly relaxed component and a small component about $\sim 600h_{80}^{-1}$ kpc away that contains only a few percent of the total flux; A2142 possesses a center offset

($\sim 2'$) obvious from visual examination yet it only has a modest value of $P_1^{(pk)}/P_0^{(pk)}$; it is, however, quite elongated ($\epsilon \sim 0.35$ at a semi-major axis of $\sim 700h_{80}^{-1}$ kpc) which clearly signals an unrelaxed state over large scales of the cluster (see, e.g., Buote & Tsai 1995a); A545 is the only cluster in our sample that is highly elongated but does not display any obvious center offset; A514 is highly irregular with several resolved mass components and is clearly in the very earliest stages of formation. We include A514, which is not in our original sample (see §7.2), because the JF COMPLEX class, of which A514 is the archetype, is not well represented in our sample. A2382, which appears to be the most COMPLEX cluster in our sample, is substantially more centrally condensed and smoother than A514. It will be useful to also consider the cluster A2319 (OFFSET CENTER) as a contrast to A2142 since the center displacement for A2319 translates to a substantial value of $P_1^{(pk)}/P_0^{(pk)}$ but the scale of the offset is confined to the core (i.e $\lesssim 300h_{80}^{-1}$ kpc); i.e. the scale of unrelaxation differs for A2142 and A2319. We refer to the six clusters (A2029,A1750,A85,A2142,A545,A514) as the "reference" clusters and (A2319,A2382) as the "intermediate" clusters.

The JF classifications separate clusters based specifically on morphology and not on the scale over which that morphology exists. Obviously, the given morphological characteristics must exist within the aperture of the given observation by *Einstein* so there is some scale dependence present, but it is not evident what this scale is since observations of various clusters had different useful apertures. The power ratios specifically address the length scales over which the morphology is quantified by setting a consistent aperture size. We find that the power ratios evaluated on apertures of $0.5h_{80}^{-1}$ Mpc separate our sample of clusters along the lines of the JF classification scheme, hence the JF scheme qualitatively describes cluster morphology on $\sim 0.5h_{80}^{-1}$ Mpc scale. This is shown in Figure 5 where we plot the correlations of the P_m/P_0 computed in the $0.5h_{80}^{-1}$ Mpc aperture for the subset of clusters selected in the preceding paragraph.

The reference clusters are separated into two groups in the $P_2/P_0 - P_4/P_0$ plane. The group (A2029,A1750,A85) essentially appears smooth on this scale, since within the $0.5h_{80}^{-1}$ Mpc aperture only one of the subclusters is enclosed for A1750 and only

the primary is enclosed for A85. However, by appealing to P_3/P_0 (see $P_3/P_0 - P_2/P_0$) these cluster are distinguished easily according to their dynamics; i.e. A1750 has the largest P_3/P_0, A85 an intermediate value, and A2029 the smallest P_3/P_0 as expected. The other group (A514,A545,A2142) appears unrelaxed in the $P_2/P_0 - P_4/P_0$ plane on this scale (i.e. guilt by association with A514). Again appealing to P_3/P_0, we see that A514 is well separated from the other two (A545,A2142) which themselves appear to have similar structure on the $0.5h_{80}^{-1}$ Mpc scale; this similarity is consistent with A545 ($z = 0.1540$) being similar in structure to A2142 ($z = 0.0899$) but less resolved. Note that the intermediate clusters A2382 and A2319 lie between these two groups but nearer the unrelaxed group as expected. For the reference and intermediate clusters $P_4/P_0 \propto P_2/P_0$ within the relatively large uncertainties for P_4/P_0 and thus do not appear to add significant information to that provided by P_2/P_0 alone. This is in contrast to P_3/P_0 which, when correlated with P_2/P_0, easily distinguishes the clusters according to their different stages of evolution within the $0.5h_{80}^{-1}$ Mpc aperture.

The power ratios computed in a $1h_{80}^{-1}$ Mpc aperture for the above subset of clusters do not in general classify clusters in accordance with the JF classifications, consistent with the above result that JF classes characterize cluster morphologies on a scale of $\sim 0.5h_{80}^{-1}$ Mpc. In Figure 6 we display the $P_2/P_0 - P_4/P_0$ correlation in the $1h_{80}^{-1}$ Mpc aperture for the reference clusters. The locations of some clusters have changed based on the structures that are most significant on the new length scale. For example, A1750 is now moved to the upper right hand corner because both subclumps of the cluster are now within the aperture. The breakdown of the JF classification system on this scale is easily seen by considering A2142 and A2319. These are both classified as OFFSET CENTER clusters by the JF scheme, however, they are well separated on the $P_2/P_0 - P_4/P_0$ correlation line indicating significantly different morphologies. In addition, the two clusters between A2142 and A2319 on the correlation line, A545 (ELLIPTICAL) and A85 (PRIMARY WITH SMALL SECONDARY), are of different JF classes.

7.5 Cluster Evolution and Correlations

7.5.1 The Evolutionary Track

The tight $P_2/P_0 - P_4/P_0$ correlation in Figure 6 as well as the placement of clusters of various morphologies on the correlation line allows a very simple interpretation for the plot. In the bottom–up cluster formation scenario, clusters in their infancy, born either via a merger event or the virialization of a single clump of material, have significant substructure and appear in the upper right hand part of the $P_2/P_0 - P_4/P_0$ plot. In the case of a merger, the cluster could be born as a double cluster like A1750. The non–axisymmetric structure gradually is erased as the cluster virializes, becoming a cluster like A2142, and then like A545. Finally the cluster becomes a single, well relaxed cluster such as A2029. The correlation line of Figure 6 (and Figure 4) is then interpreted as the track followed by clusters as they evolve from infancy to virialized states. Starting from the upper right, clusters move along the track down towards the lower left as they virialize. Alternatively, a cluster born as a single virializing object may first appear like A514 as a series of small substructures. These structures gradually agglomerate into a state represented by A2382. Possible continued accretion of small groups may lead to a mostly regular primary with a final renegade subgroup such as in A85. Finally, the subgroup merges and forms a completely relaxed cluster inhabiting the lower left part of the $P_2/P_0 - P_4/P_0$ correlation line.

Of course, evolution along the $P_2/P_0 - P_4/P_0$ sequence may proceed towards the upper right as well. A relaxed cluster like A2029 could subsequently accrete a small neighboring subcluster at which point it will be bumped back up to a position near A85 on the correlation line. Or, if a merger with a major secondary occurs, the merging cluster will occupy a position near that of A1750 (e.g., this may happen to A399 and A401 in $\sim 10^9$ yr).

In principle, it should be possible to distinguish the evolutionary tracks of the merging clusters (the double sequence) from that of the virializing single clumps (the complex sequence). Because the members of the complex sequence have more small scale power, we expect that for a given P_2/P_0, members of the complex sequence

should have larger P_4/P_0 than members of the double sequence. The determinations of the power ratios, however, are not sufficiently accurate with currently available data to allow this distinction. Finally, note that the $P_2/P_0 - P_3/P_0$ correlation (Figure 6) could operate in the same manner as the $P_2/P_0 - P_4/P_0$ sequence if measured more accurately. The correlations for the power ratios in the $1.5h_{80}^{-1}$ Mpc aperture for the "reference" clusters sufficiently distant to fit inside the PSPC central ring are entirely consistent with the evolutionary picture described for the $1h_{80}^{-1}$ Mpc aperture, but with much larger uncertainties.

We comment on the one cluster in our sample that significantly deviates from the evolutionary picture described above. The outlier A665 (given by the point which lies farthest from the $P_2/P_0 - P_4/P_0$ correlation line of Figure 4), has large values of $P_1^{(pk)}/P_0^{(pk)}$ and P_3/P_0, and modest (but uncertain) values of P_4/P_0 typical of a cluster in our sample being dynamically unrelaxed on both $0.5h_{80}^{-1}$ Mpc and $1h_{80}^{-1}$ Mpc scales. However, the P_2/P_0 values are anomalously low and indicative of a very relaxed cluster on these scales. These characteristics are consistent with a state in which the X–ray emitting gas neither traces the total mass nor the the potential of the cluster. For example, it was shown (Buote & Tsai 1995a) that during the late time (i.e. $z = 0.83 - 0.13$) evolution of the Katz & White (1993) simulation, the simulated cluster experienced a brief period during a merger (i.e. $z \sim 0.5 - 0.3$) where the X-rays did not follow the dark matter distribution or the potential. During this time the X-ray isophotes were very distorted yet the ellipticity (i.e. quadrupole moment) was very small ($\epsilon \sim 0.15$), much less than at earlier ($\epsilon \sim 0.5$) and later ($\epsilon \sim 0.3$) times.

If this description for A665 is indeed correct, this cluster has been captured during a very interesting phase of cluster formation. The gas is undergoing the greatest dissipation in going from a distribution like that of the dissipationless component of the cluster (or being distributed in virial equilibrium with individual subclumps, such as for A1750) to that of following the total cluster potential. Clusters which lie higher than A665 on the evolutionary track must then have gas that is not following the total cluster potential and clusters lying below A665 must have gas virialized with

the total potential. Since only 1 cluster in our sample of 55 clusters deviates from the evolutionary track, this epoch of cluster formation must be very short, as already hinted at by simulations (Buote & Tsai 1995a). The consideration of A665 also slightly modifies the picture of cluster evolution described above. That is, as clusters virialize and move toward the lower left on the correlation line, they experience a brief episode where they evolve off the track, and then fall back to it after the cluster gas has dissipated sufficiently to follow the overall potential.

7.5.2 Correlations with other X-ray Properties

We investigated correlations of the power ratios with X-ray temperature, X-ray luminosity ($0.1 - 2.4$ keV), and cooling-flow rate using data from the literature (see Table 1; Edge et al. 1990,1992; David et al. 1993; Fabian 1994). Although correlations with X-ray temperature and X-ray luminosity cannot be ruled out because of the generally small number of data points (i.e. $\lesssim 20$ for each quantity), there is no obvious correlations of these quantities with the power ratios. This is expected since the power ratios measure evolution without regard for the mass of the cluster to which these other quantities are sensitive (Edge & Stewart 1991). In accordance with this argument we find no evidence for a correlation of the power ratios with the optical velocity dispersions from Struble & Rood (1991).

Using the mass-flow rates from Fabian (1994) for the Edge et al. (1990;1992) clusters we find that the power ratios computed in both the $0.5h_{80}^{-1}$ Mpc and $1h_{80}^{-1}$ Mpc apertures are clearly anti-correlated with mass-flow rate; the weakest trend is observed for $P_1^{(pk)}/P_0^{(pk)}$. In Figure 7 we show the mass-flow rate vs P_2/P_0 computed in the $1h_{80}^{-1}$ Mpc aperture; clusters with no detected mass-flow rates were placed on the bottom of the plot to show the range in P_2/P_0 for these clusters. A negative correlation of mass-flow rate with evolution (as given by P_2/P_0) is clearly reasonable if the rate of central cooling of gas can be reduced by recent mergers or by only recently virializing structure. Much of the scatter in Figure 7 may be due either to the large uncertainty in the mass-flow rates, which are accurate perhaps only to a factor of a few, or to a definite (albeit weak) correlation with X-ray luminosity (Edge

et al. 1992). Nevertheless, the power ratios and central cooling rates give consistent pictures of the evolutionary states of galaxy clusters.

7.5.3 Comparison to Bautz-Morgan Type

We investigate whether the power ratios yield a description of the evolutionary state of the clusters consistent with the optical Bautz-Morgan (1970; BM) classification scheme. The BM type of a cluster measures, "the degree to which the brightest member stands out against the general cluster background"(BM). Although assigning BM types to clusters is inherently subjective and prone to systematic errors (see, e.g., Leir & van den Bergh 1977) the BM scheme generally provides some measure of the evolutionary state (e.g., Sandage & Hardy 1973; Leir & van den Bergh 1977). In Table 1 we give the BM types for clusters available from the literature. The BM types are uncertain to at least a half-type and those with a ":" are even less certain.

Since the BM scheme measures the cluster evolutionary state (Type I being the most relaxed, Type III most unrelaxed), we expect a positive correlation of the power ratios with BM type if both X–ray and galaxy distributions do indeed trace the evolution of the cluster. The BM scheme, however, does not specifically address different scales for a given cluster and only specifies the "dominance of the brightest members" globally. Furthermore, the BM scheme is unlike the JF classifications because this latter method does sort clusters by their morphology on scales $\sim 0.5h_{80}^{-1}$ Mpc (see §7.4), although this may not necessarily have been originally intended. To illustrate this difference we again consider A2319. Recall that the power ratios computed in the $0.5h_{80}^{-1}$ Mpc aperture classify A2319 as an unrelaxed cluster due to the substructure in the core, but in the $1h_{80}^{-1}$ Mpc aperture the gravitational effects of the core subclustering are unimportant and A2319 appears relaxed. The BM scheme in this case identifies the unrelaxed nature of the core of A2319 and classifies it as Type II-III. In contrast, A1750, which is classified by power ratios as relatively relaxed on small scales ($0.5h_{80}^{-1}$ Mpc) but unrelaxed at a scale of $1h_{80}^{-1}$ Mpc also has a BM type of II – III. We therefore expect the power ratio – BM correlations to be the superposition of a positive correlation for those clusters which have substructure on

the scale currently specified by the power ratios and a negative correlation for those clusters which do not have substructure on the current scale, but do have substructure on a different scale.

We first consider the BM Types for the reference clusters examined in §7.4. The power ratios P_m/P_0 computed in the $0.5h_{80}^{-1}$ Mpc aperture (Figure 5) clearly separate BM Type in the positive sense – larger power ratios imply larger BM Type. Although A545 (III) and A2142 (II), which are classified into essentially the same region of power-ratio space, differ in BM Type by 1, the disagreement is not highly significant considering the BM uncertainties. In the $1h_{80}^{-1}$ Mpc aperture (Figure 6), BM Type and the power ratios correlate extremely well with the exception of A545; i.e. A1750 and A514 (both II-III) are at the top of correlation line, A2142 (II) is in the middle, A85 and A2029 (both I) are at the bottom. However, since A545 is a good candidate for core substructure the different BM classification may be result of the scale-dependence effect we discussed above for A2319 and A1750. Overall the power ratios for our reference clusters and the BM Types correlate well.

The BM Type – power ratio correlation for the whole sample does not present such a clean picture. We focus on the BM – P_2/P_0 correlation since P_2/P_0 is the most precisely measured power ratio and it has the most straightforward evolutionary interpretation (for the $1h_{80}^{-1}$ Mpc aperture). In Figure 8 we plot the results for all the clusters and for those included in the Edge et al. (1990) sample. Both plots, particularly for the Edge et al. subset, show the expected superposition of the positive and negative correlation discussed previously. That is, the most relaxed clusters inhabit the bottom left of the plots and for slightly larger values of P_2/P_0 the BM Type also increases slowly from I to II. For clusters with large-scale substructure (A514,A1750) this positive correlation continues to the largest values of P_2/P_0 and BM (almost). A noticeable outlier in this positive correlation is A3558 classified as BM Type I. There is obvious substructure in the PSPC image (see Appendix A.) which, if indeed gravitationally associated with the cluster, implies A3558 should be considered dynamically young.

Along with this positive correlation, however, there is a negative correlation that is

particularly evident in the top left of the plot of the Edge et al. clusters. These clusters appear relatively relaxed on the current scale but have departures from equilibrium on smaller scales. Appealing to the other power ratios (which are not as well constrained as P_2/P_0) does not add any additional clarification when combined with the already uncertain BM description. Thus, to within the uncertainties present, both galaxies and X–rays consistently trace the dynamical state of clusters. Although the BM classifications are qualitative, the results of this section suggest that much can be learned from future joint considerations of structure in the gas and galaxies.

7.6 Discussion

If galaxy clusters form hierarchically then a simple intepretation of the strong $P_2/P_0 - P_4/P_0$ correlation in Figure 6 is a track followed by clusters as they evolve from infancy to virialized states (§7.5.1); i.e. the power ratios distill from the morphologies of galaxy clusters a clear, quantitative measure of their evolutionary states. Other methods that attempt to use morphologies to probe cluster evolution suffer because they neglect to weigh the intrinsic scales of the morphological features in proportion to the cluster gravitational potential (i.e. the JF visual classification scheme discussed in §7.4 and the statistics of Evrard et al. 1993 and Mohr et al. 1995; see BT §6). We now discuss some potential astrophysical applications of the power-ratio connection to cluster evolution.

Perhaps the most important use for the power ratios is for comparison with cosmological N-body / hydrodynamic simulations. As we discussed in BT (§6) the power ratios are ideally suited to test the Morphology – Cosmology Connection (MCC; Evrard et al. 1993; Mohr et al. 1995). This MCC simply states that the observed structure of X-ray clusters is sensitive to the cosmological density parameter Ω, an idea suggested by Richstone et al. (1992). However, it is actually the current merger rate (or formation rate), *which describes the current dynamical states of clusters*, that is highly sensitive to Ω (see Figure 1 of Richstone et al.). As we stressed above (and in BT) morphology alone does not clearly indicate the dynamical state of a cluster unless

the intrinsic scales of the morphological features are weighed appropriately. The distribution of power ratios (particularly P_2/P_0 in the $1h_{80}^{-1}$ Mpc aperture), which are by construction directly related to the dynamical state, provide a direct measure of the formation rate of clusters in our sample and should thus allow for substantially more precise constraints on Ω to be obtained than methods which quantify morphologies without regard to dynamics.

Whereas the distribution of clusters along the tight $P_2/P_0 - P_4/P_0$ correlation in the $1h_{80}^{-1}$ Mpc aperture should suffice for testing the MCC, the joint use of individual distributions of the power ratios, P_m/P_0, can provide a further test of the MCC and can also give constraints on the primordial power spectrum on scales at or somewhat below that of clusters. The discovery of the evolutionary track also provides vital constraints on cluster formation in general; our interpretations of both placement and movement along the track can be tested in detail by hydrodynamical simulations of cluster formation. The unique position in cluster evolution occupied by A665 can be tested also by comparing the distribution of projected mass, as can be determined by weak lensing (Kaiser & Squires 1993), to the gas distribution as quantified by the present work.

Since the power ratios delineate the evolutionary states of clusters, they may be used to search for and summarily remove the effects of evolution in particular investigations of clusters. For example, if the relative proportions of galaxy morphological types within clusters is correlated with evolution (i.e. the Dressler [1980] Morphology - Density relation; also see Whitmore [1990]) they should correlate with the power ratios. Distance indicators like brightest cluster galaxies (BCGs) and the universality of the luminosity function (Schechter & Press 1976) may also be affected by the evolutionary states of clusters. For example, Sandage & Hardy (1973) use the observed correlation between BCG magnitude and BM Type to reduce the scatter in their Hubble Diagram. The power ratios, which give a similar but much more precise measure of the state of a cluster (see §7.5.3), should be useful in further reducing the scatter in the Hubble Diagram and remove systematic evolutionary effects associated with BCGs (e.g., Weir, Djorgovski, & Bruzal 1990); i.e. in addition to correlating

with P_2/P_0 in the $1h_{80}^{-1}$ Mpc aperture, it may be useful to simultaneously correlate with the $0.5h_{80}^{-1}$ Mpc aperture results if BCG magnitude is especially sensitive to departures from equilibrium in the core of the cluster. Unfortunately there are too few published BCG magnitudes for the clusters in our sample to allow us to meaningfully investigate this issue at present.

The power ratios provide a natural means to "correct" X-ray mass estimates of clusters due to departures from hydrostatic equilibrium. Along with weak gravitational lensing (Kaiser & Squiers 1993), X-ray images of clusters are the most powerful means to measure cluster masses (see Mushotzky 1995 for a recent constraints from ASCA). It would be straightforward to compute the errors in cluster masses assuming hydrostatic equilibrium using N-body / hydrodynamic simulations (e.g., Tsai, Katz, & Bertschinger 1994) of clusters spanning the narrow range of power ratios in Figure 4. This "template" may then be used to correct hydrostatic mass estimates of real clusters. Moreover, the power ratios computed in different apertures indicate where in a given cluster hydrostatic equilibrium is a good approximation; e.g., the power ratios for A2319 (§7.4) show that it is substantially more relaxed in the $1h_{80}^{-1}$ Mpc aperture than in the $0.5h_{80}^{-1}$ Mpc aperture and thus hydrostatic analysis is better suited for that larger scale to reduce the nonequilibrium effects of subclustering in the core – this is precisely the argument previously made by us (Buote & Tsai 1995a). Hence, the power ratios can both indicate where it is best to apply hydrostatic analysis in clusters and, if the errors are indeed correlated with evolution, correct for nonequilibrium effects.

Power ratios may be more suitable for probing the dynamics of clusters than traditional X-ray methods that assume the gas is in hydrostatic equilibrium. For example, Kaiser (1991) predicts morphological differences between the X-rays and mass in high-redshift clusters ($z \sim 0.5$) that may provide important constraints on the nature of the dark matter. The power ratios allow a natural comparison of the dynamical state of a cluster as indicated by the X-ray gas with that indicated by the mass distribution obtained from weak lensing (e.g., Kaiser & Squiers 1993; Smail et al. 1995).

7.7 Conclusion

We have used the power-ratio technique (BT) to quantify the X-ray morphologies of a sample of 55 galaxy clusters. The power ratios quantify substructure in a cluster in direct relation to its influence on the gravitational potential, or, equivalently, the dynamical state of the cluster. Hence, we have in effect a measure of the evolutionary states of the clusters.

Our sample consists of clusters belonging to the X-ray flux-limited samples of Edge et al. (1990) and Ebeling (1993) that have sufficiently high S/N observations with the ROSAT PSPC. Only for the brightest ~ 30 clusters is our sample approximately complete ($\sim 60\%$).

We computed the power ratios in a circular aperture of radius $0.5h_{80}^{-1}$ Mpc for all of the clusters in the sample. For sufficiently distant clusters we also computed power ratios in $1h_{80}^{-1}$ Mpc and $1.5h_{80}^{-1}$ Mpc apertures when the entire aperture fit within the $40'$ diameter ring of the PSPC. We estimated 90% confidence uncertainties on the power ratios using a Monte Carlo procedure.

The power ratios exhibit striking correlations, particularly $P_2/P_0 - P_4/P_0$ in the $1h_{80}^{-1}$ Mpc aperture. From consideration of "reference" clusters spanning the full range of power ratios and belonging to the six morphological classes of JF, we interpreted this $P_2/P_0 - P_4/P_0$ correlation as an evolutionary track for clusters where the young clusters are born at the top of the track (i.e. large values of P_2/P_0 and P_4/P_0) and evolve downwards to small values of P_2/P_0 and P_4/P_0. The relative distribution of clusters along this track provides a quantitative measure of the current formation rate of clusters in our sample – a quantity that has been shown to be very sensitive to Ω (Richstone et al. 1992). We also find that the JF classes qualitatively distinguish clusters on scales of $\sim 0.5h_{80}^{-1}$ Mpc, as indicated by the reference clusters being similarly classified by power ratios on this scale.

We find no evidence for correlations of the power ratios with X-ray temperature, X-ray luminosity, or velocity dispersion as expected; i.e. since the power ratios are not directly sensitive to the masses of clusters the small evolutionary dependences

on these quantities are dwarfed by the differences associated with the individual cluster masses. A negative correlation of the power ratios with mass-flow rate is observed and is consistent with a reasonable expectation that the rate of gas cooling in the cores of clusters is related to the dynamical state of the cluster. We also find that the optical BM classifications for clusters are related to the power ratios in an understandable manner. That is, whereas power ratios are sensitive to some given scale, the BM classes do not differentiate between clusters that are unrelaxed over large scales ($\sim 1h_{80}^{-1}$ Mpc) and those that are substantially unrelaxed only in the core ($< 0.5h_{80}^{-1}$ Mpc). The relation of BM types to power-ratio values suggests that both the gas distribution and the galaxy distribution reflect similar evolutionary states for a cluster.

We describe several astrophysical applications that exploit the connection between the power ratios and evolutionary states of clusters. In particular, we discuss the suitability of the power ratios for (1) constraining Ω via the Morphology – Cosmology Connection, (2) correcting distance indicators like BCGs for the effects of cluster evolution, and (3) correcting mass estimates of clusters for departures from hydrostatic equilibrium. In principle, given adequate observations, power ratios can be used to address any problem where cluster evolution is an issue.

The insights into cluster evolution gleaned from our relatively small sample of clusters, as well as the potential for precise cosmological constraints provided by power ratios, highlight the need for a much larger sample of high-quality X-ray data of clusters of galaxies. With the prospects of the XMT for studying low-redshift clusters and AXAF for high-redshift clusters it will in principle become possible to realize the full potential of the power ratios to be a potent astrophysical tool.

We benefited from discussions with E. Bertschinger, J. Blakeslee, C. Canizares, E. Gaidos, and J. Tonry. We express our gratitude to M. Corcoran for assistance with the ROSAT archive and to D. Harris for his advice regarding merging PSPC images. We acknowledge use of the following astrophysical databases: ADS, HEASARC-Legacy, NED, and SIMBAD. DAB was supported by grants NAG5-1656, NAS8-38249 and

NASGW-2681 (through subcontract SVSV2-62002 from the Smithsonian Astrophysical Observatory).

A. Notes on Individual Clusters

Here we list details of the image reduction for individual clusters with particular emphasis on point sources.

A21: This is a bimodal cluster whose two components are separated by $\sim 3'$ and are easily resolved by the ROSAT PSPC image. Short-term enhancements of the light curve were removed from the original image (exposure: 9068s) to yield an effective 8680s exposure time. One faint source straddling the 0.5 Mpc aperture was removed. An additional bright source was removed from the 1.5 Mpc aperture.

A85: It is the quintessential PRIMARY WITH SMALL SECONDARY cluster in the JF classification scheme. The small secondary structure lies $\sim 10'$ to the S. Five faint sources were removed within the ring. They lie within the 1 Mpc aperture but not the 0.5 Mpc aperture. The large sub-clump to the South is not removed.

A119: This cluster has an interesting tail of emission to the North that suggests significant departures from equilibrium. Two sources were removed from the 0.5 Mpc aperture. The 1 Mpc aperture did not fit inside the ring so we reduced the size to 940 kpc which then did fit inside. Six more sources had to be removed from this larger aperture.

A400: This irregular cluster has a dominant peak and a few secondary peaks. The nearest peak is $2'$ to the East of the dominant peak is a good candidate for a subcluster. We had to decrease the aperture size to 460 kpc in order to meet the criteria of §7.3. Five bright and four faint sources were removed from the 460 kpc aperture.

A401: A very smooth single-component cluster. A399 may be seen outside the PSPC ring to the SW. In order to avoid contamination from A399 we estimated the background in a circle of $5'$ radius $40'$ to the NW. Two pointings (exposures: 7465s and 6797s) on the cluster center were merged into one image. Two faint sources and the

cluster center were used to register the images to a reference coordinate frame. The required shift was consistent with no shift in the E-W direction but 1.8 ± 0.5 pixels N-S which is slightly larger than the expected pointing errors of the PSPC. No sources needed to be excised from the 0.5 and 1 Mpc apertures, but the two aforementioned faint sources were removed from the 1.5 Mpc aperture. Note that the emission from A399 which lies off-axis $\sim 30'$ to the SW begins to become significant within the ring for the 1.5 Mpc aperture.

A478: Two sources were removed from this smooth-looking cluster in the 0.5 Mpc aperture, four more from 1 Mpc, and five more from the 1.5 Mpc aperture.

A496: From this symmetrical single-component cluster we removed four faint sources within the ring.

A500: This very irregular cluster has at least three distinct emission peaks within 0.5 Mpc in addition to the dominant central peak. This emission is roughly centered on galaxies associated with the cluster. Of the peaks near the center we removed only the largest source $\sim 4'$ to the NW because it did not have any clear association with the diffuse emission; follow-up observations need to be performed to determined the nature of these sources. Four bright sources were removed from the 0.5 Mpc aperture. Four bright and 12 faint sources were removed from the 1 Mpc aperture.

A514: This is the archetype COMPLEX cluster in the JF system. There are at least three distinct peaks in the central $\sim 5'$ cluster continuum and then two other peaks $10'$ to the W. All of the peaks appear to be extended and/or are part of the cluster emission; however this needs to be verified. No sources were removed from the 0.5 Mpc, one faint source from the 1 Mpc, and three bright sources from the 1.5 Mpc apertures.

A545: This cluster is highly elongated within the 0.5 Mpc aperture which may reflect dynamical youth of the interior. One bright source was removed from the 1 Mpc aperture and an additional bright and one faint source were removed from the 1.5 Mpc aperture.

A586: Although the cluster appears to be mostly smooth this may be the result of the relatively low S/N of the observation. Two faint sources were removed from the 1.5 Mpc aperture.

A644: This looks like a smooth single component cluster. Two faint sources were removed from the 0.5 Mpc aperture. One bright and four faint sources were removed from the 1 Mpc aperture. In order to fit inside the ring (see §7.3) the last aperture was taken to be 1.45 Mpc. Two faint sources as well as some extended emission near the ring to the East were removed from this 1.45 Mpc aperture.

A665: This irregular cluster has its emission peak clearly displaced from the centroids of the outer isophotes. Starting from the emission peak the isophotes fan out to the North. Because of the long exposure time there are many point sources easily detected in the field. No sources needed to be removed from the 0.5 Mpc aperture; one bright source was removed from the 1 Mpc aperture; five faint sources straddling the 1.5 Mpc aperture were removed. It is interesting that $P_1^{(pk)}/P_0^{(pk)}$, P_3/P_0, and P_4/P_0 classify A665 as unrelaxed but P_2/P_0 is typical of smooth, relaxed clusters (see §7.4).

A754: The center is clearly offset from the outer cluster emission. No sources were removed within the 0.5 Mpc aperture. Because the center of the cluster emission is displaced from the field center, only the 0.5 Mpc fits within the PSPC ring according to our criteria from §7.3.

A1068: No sources needed to be removed from the 0.5 Mpc aperture of this regular-looking cluster. Two faint sources were excised from the 1 Mpc aperture, and one additional faint source was removed from the 1.5 Mpc aperture.

A1361: This cluster appears reasonably smooth but the S/N is relatively low for our sample. While no sources were removed from the 0.5 Mpc aperture, one bright and one faint source were removed from the 1 Mpc aperture. One more bright and three faint sources were removed from the 1.5 Mpc aperture.

A1413: No sources were removed from the 0.5 Mpc aperture of this mostly regular cluster, but two bright and one faint source were removed from the 1 Mpc aperture.

Three more faint sources were removed from the 1.5 Mpc aperture.

A1651: The cluster appears to be mostly smooth and regular. One bright source on the 0.5 Mpc aperture, two bright and one faint sources within the 1 Mpc aperture, and another faint source in the 1.5 Mpc aperture, were removed.

A1656: There were four pointings (exposures: 22183s, 21893s, 20691s, and 22427s) on the Coma field each at a different position. Unfortunately these pointings were not placed symmetrically around the cluster center to accommodate the circular apertures required for the power ratios. Nonetheless, we needed to merge these observations to obtain sufficient pixels to even get the 0.5 Mpc aperture covered. Each of these observations showed evidence of short-term enhancements in their light curves which we removed resulting in exposure times of 20032s, 21893s, 20691s, and 22427s respectively. Four bright point sources were used to register the images to the coordinate frame of the 20032s image and then they were added together. As usual we included only the regions interior to the PSPC ring for each observation. Because of the dominant emission from the cluster we only removed one source within the 0.5 Mpc aperture. There are other sources in the Coma image found by White, Briel, & Henry (1993), but they are faint compared to the cluster continuum. In any event their extent is much smaller than the aperture size and should only contribute appreciable to multipole components higher than we are considering. We had to decrease the aperture size to 0.45 Mpc to meet our criterion of §7.3.1.

A1689: The X-rays appear smooth and symmetrical in this cluster that also is known to have giant arcs due to gravitational lensing of distant galaxies. No sources needed to be removed from the 0.5 and 1 Mpc apertures. One bright source and four faint sources straddling the 1.5 Mpc aperture were removed.

A1750: This is a double cluster with its components separated by $\sim 10'$ (i.e. ~ 1 Mpc). Because the centroid of the two nearly equal-sized subclumps moves with increasing aperture size the 1.5 Mpc aperture just touches the ring. We decrease the aperture to 1.4 Mpc to fit inside the ring within the specifications stated in §7.3; the power ratios are essentially unaffected by this reduction in aperture size. One source was removed

from the 0.5 Mpc aperture, two more from the 1 Mpc aperture, and an additional 7 from the 1.5 Mpc aperture.

A1795: A perfect example of a smooth, single-component, regular-looking cluster. The image of this cluster within the ring is literally peppered with point sources. In all 20 sources were removed within the 1 Mpc aperture. Only two of the sources lie within the 0.5 Mpc aperture. The power ratios are not affected (within the Monte Carlo error estimates) when only the brightest few sources are removed.

A1837: The emission is highly elongated in the inner 5′ of this cluster, but only a single peak is evident to the eye. Two bright and three faint sources were removed from the 0.5 Mpc aperture.

A1914: This cluster looks mostly regular and smooth. No sources needed to be excised from the 0.5 Mpc aperture, but three faint sources and an additional faint source were removed from the 1 and 1.5 Mpc apertures respectively.

A1991: Three faint sources were removed from the 0.5 Mpc aperture of this regular-looking cluster and three bright and five additional faint sources were removed from the 1 Mpc aperture.

A2029: This is a smooth, regular cluster. One source was removed from the 0.5 aperture, four more from the 1 Mpc aperture, and three additional sources from the 1.5 Mpc aperture.

A2034: The centroids of the X-ray isophotes appear to shift to the S at large radii of this somewhat irregular cluster. No sources were removed from the 0.5 Mpc aperture. One faint source was removed from the 1 Mpc aperture and 1 bright and an additional faint source were removed from the 1.5 Mpc aperture.

A2052: Two observations (exposure times: 6215s and 3032s) pointed on the cluster center were merged. One point source and the cluster center (which is very centrally peaked) were used to register the images to the coordinate frame of the 6215s image; the required shift was 1 pixel which is consistent with the pointing accuracy of ROSAT. Only the one source needed to be removed.

A2063: Two bright and four faint sources were removed from the 0.5 Mpc aperture of this mostly symmetrical and smooth cluster.

A2107: Mostly regular in appearance, we removed six faint sources from the 0.5 Mpc aperture.

A2199: This is another regular, single-component cluster. Seven faint sources were removed from the 0.5 Mpc aperture.

A2142: This cluster is highly elongated and has an obvious center displacement from the outer emission; i.e. a classic OFFSET CENTER in the language of JF. We merged three observations (exposure times: 7740s, 6192s, and 4941s) that were pointed on the same coordinates. Each image was flattened first and then three point sources (one bright, two faint) were used to register the images to the coordinate frame of the 7740s image. The required shifts were less than one pixel. Once the images had been merged several more point sources become easily apparent. In particular, the bright source used for registration is 15 pixels NE of the cluster center and must be carefully excised from the cluster continuum. It is the only source removed from the 0.5 Mpc aperture. Five more were removed from the 1 Mpc aperture and another 8 from the 1.5 Mpc aperture.

A2204: No sources needed to be removed from this apparently smooth cluster.

A2218: This cluster is quite elongated but smooth in appearance. Because of the long exposure of the observation there are many resolved point sources in the field. However, because A2218 is at relatively large redshift, the 1.5 Mpc aperture only encloses a small portion of these sources. No sources needed to be removed from the 0.5 Mpc aperture; two faint sources were excised from the 1 Mpc aperture and an additional three faint sources from the 1.5 Mpc aperture.

A2244: The cluster looks regular but this may be a result of the low S/N of the observation. No sources needed to be removed from the 0.5 Mpc aperture; one bright and one faint source were removed from the 1 Mpc aperture and another faint source from the 1.5 Mpc aperture.

A2255: This cluster does not have a large central emission peak and instead appears to have a large core. No sources needed to be removed from the 0.5 Mpc aperture. Four faint sources were removed from the 1 Mpc aperture. Four additional faint sources were removed from the 1.5 Mpc aperture

A2256: There are six observations of A2256 carefully placed at various positions to maximize coverage of the cluster within the ring of the PSPC; the ROSAT sequence numbers (exposure times) of these pointings are wp100110 (17865s), wp800162 (9108s), wp800163 (10803s), wp800339 (4978s), wp800340 (9430s), and wp800341 (10480s). wp100110 is roughly pointed on the cluster center, but it is displaced about 5′ South of the field center. wp800162 and wp800339 are identical pointings where the center is pointed on the PSPC ring and the region NW of the cluster is centered on the field. The remaining pointings are symmetrically placed in a similar manner so that the cluster center is on the ring. The careful placement of the observations allows the 1.5 Mpc aperture to be enclosed by exposures entirely within the PSPC ring.

There are indeed many sources in this merged field as has been reported by Henry, Briel, & Nulsen (1993), most of which appear to lie at large distances from the cluster center. Within the 0.5 Mpc aperture ($\sim 8'$ radius) there are no obvious sources above the cluster continuum. 5 bright sources and seven faint sources were removed from the 1 Mpc aperture and three more bright and 11 faint sources were removed from the 1.5 Mpc aperture.

Note that the power ratios are generally quite large and indicative of an unrelaxed cluster for the 0.5 aperture, but at 1 and 1.5 Mpc the ratios suggest a near equilibrium state. Also, the 0.5 aperture power ratios are nearly the largest of our sample and suggest that A2256 is not so *typical* a cluster as has been suggested.

A2319: Two observations (exposure times: 3171s and 1505s) pointed on the same coordinates were merged into one observation. Apart from the cluster itself, there is only one faint source within the ring and hence we resorted to using the cluster center and the faint source to register the images to a common coordinate frame; the

required shifts between the image were about one-half of a pixel and consistent with no shift. The aforementioned faint source was removed from the 1 Mpc aperture.

A2382: This cluster is quite irregular with several distinct emission peaks. Two observations (exposure times: 17444s and 8231s) pointed on the same coordinates were merged into one observation; several bright sources in the field were used for registration of the images to a reference coordinate frame. Two sources were removed from within the 0.5 Mpc and three faint sources straddling the aperture. Eight faint sources were removed from the 1 Mpc aperture. Since the cluster center is displaced to the South of the field center, the 1.5 Mpc aperture does not fit within the PSPC ring.

A2589: Two bright sources were removed from the 0.5 Mpc aperture of this mostly smooth-looking cluster.

A2597: This is a very symmetrical and smooth cluster. No obvious sources needed to be removed from the 0.5 Mpc aperture. Two bright and two faint sources straddling the 1 Mpc aperture were removed. One additional faint source was removed from the 1.5 Mpc aperture.

A2634: We did not include this cluster in the sample because the emission is contaminated by a background galaxy cluster that extends over several arcminutes.

A2657: Although for the most part smooth in appearance, there is some indication of bimodality in the inner arcminute. Two bright and seven faint sources were removed from the 0.5 Mpc aperture.

A2670: Two emission peaks separated by $1.5'$ are resolved by the PSPC suggesting that A2670 is indeed undergoing a major merger. Although no sources needed to be removed from the 0.5 Mpc aperture, two bright and six faint sources were excised from the 1 Mpc aperture. Another three bright and two faint sources were removed from the 1.5 Mpc aperture. Part of an extended source on the edge of the ring to the East also was also removed. The nature of this extended source is unknown to us but if it is shown to be a subcluster associated with A2670 then its emission should be included in the aperture.

A3158: The low S/N of this observation does not allow any strong conclusions about its structure to be drawn. We used a low-exposure (3022s) observation during the PV phase that is not well centered on the cluster; only the 0.5 Mpc aperture fits within the ring. No sources were removed.

A3532: This is a PV-phase observation roughly centered on A3532 and includes A3530 (which is included in Ebeling's catalogue) which is located on the ring to the West. We do not attempt to remove A3530 and thus assume that it is gravitationally associated with A3532 and not a chance coincidence; the contribution to the X-ray emission only affects the power ratios in the 1 Mpc aperture. No sources were removed from the 0.5 Mpc aperture, but two were removed from the 1 Mpc aperture.

A3558: The dominant component of the cluster is mostly regular but with a small center displacement. There is substantial structure in this image to the East of the center of A3558. An obvious bridge of emission connects A3558 to two clumps just outside the ring. Using NED we identified one of these objects as the galaxy cluster AM 1328-313 which is at redshift 0.04380, essentially the same as A3558 – they are both members of the Shapely Supercluster. Two sources needed to be removed within the 0.5 Mpc aperture and an additional seven were removed from the 1 Mpc aperture.

A3562: The isophotes appear quite distorted and certainly not elliptical. The cluster AM 1328-313 lies to the SW just outside the ring in this image and A3558 is visible at the far W edge of the field. Two sources were removed from the 0.5 Mpc aperture and an additional 16 were removed for the 1 Mpc aperture.

A3667: This cluster has highly elongated and distorted isophotes. Four bright sources were removed within the ring including one near the center of the cluster.

A3921: This irregular cluster appears to be undergoing a merger of a subclump located about 1 Mpc to the West. No sources were removed from the 0.5 Mpc aperture. Two bright and four faint sources were removed from the 1 Mpc aperture. An additional four bright and five faint sources were removed from the 1.5 Mpc aperture.

A4059: This is a very smooth, single-component cluster. There is only one fairly bright point source within the central ring that was removed and was located in the 1 Mpc

aperture only.

HYDRA-A: This cluster is centrally condensed and quite regular in appearance. We removed 1 bright and three faint sources within the 0.5 Mpc aperture and an additional four bright and six faint sources from the 1 Mpc aperture.

MKW3s: This poor cluster looks mostly smooth but quite elongated within the 0.5 Mpc aperture. No sources needed to be removed.

OPHIUCHUS: One bright source within the 0.5 Mpc aperture was removed. The isophotes of this cluster are somewhat asymmetrical. Also, the background rate is high because of the low Galactic latitude.

TRIANGULUM AUSTRALIS: The bright central emission peak appears to be slightly offset from the outer isophotes. Two faint sources were removed from the 1 Mpc aperture (none within 0.5 Mpc).

Table 1: The Sample

NAME	Flux	z	exp(s)	Bkg	BM Type
OPH.	345.00	0.0280	3932	7.36	...
A1656	340.37	0.0232	...	4.08	II
TRI-AUST	104.00	0.0510	7338	4.30	...
A2319	101.00	0.0564	4676	7.56	II-III
A2199	100.30	0.0299	10563	3.38	I
A496	83.17	0.0327	8972	4.61	I:
A3667	82.89	0.0530	12560	5.10	I-II
A85	80.61	0.0556	10240	3.22	I
A1795	72.42	0.0622	36829	3.03	I
A754	67.84	0.0534	6359	3.21	I-II:
A3558	66.85	0.0478	30213	4.89	I
A2029	66.67	0.0768	12550	5.50	I
A2142	65.22	0.0899	18873	2.65	II
A2256	54.38	0.0581	...	2.50	II-III:
A3266	53.44	0.0594	13560	3.09	I-II
A2052	53.01	0.0348	9247	6.25	I-II
HYDRA-A	45.30	0.0522	18403	2.43	I
A401	45.00	0.0748	14262	2.07	I
A478	42.81	0.0881	22139	1.71	...
A2063	42.68	0.0355	10198	7.24	II:
A119	42.12	0.0440	15203	3.33	II-III
A644	39.20	0.0704	10285	2.29	III:
A3158	39.19	0.0590	3022	2.95	I-II
A4059	34.88	0.0478	5514	2.79	I
MKW3S	34.70	0.0430	9996	6.24	II-III
A3562	34.47	0.0499	20202	3.99	I
A2589	28.61	0.0415	7293	2.37	I
A1651	29.05	0.0845	7435	3.55	I-II
A2597	27.38	0.0852	7243	2.25	III
A2657	25.23	0.0414	18911	2.25	III
A2204	24.77	0.1523	5359	8.47	II
A2244	24.71	0.0968	2965	2.39	I-II:
A3532	24.60	0.0585	8620	3.36	II-III
A400	19.31	0.0238	23615	2.23	II-III
A2255	19.02	0.0808	14555	2.29	II-III:
A2107	18.05	0.0421	8274	3.81	I
A3921	16.82	0.0960	12007	3.09	II
A1914	16.37	0.1712	9040	2.72	II:
A1689	16.26	0.1832	13957	3.14	II-III:
A1413	16.22	0.1427	7798	2.52	I
A1991	14.69	0.0579	21281	4.48	I:
A1750	14.62	0.0855	13148	2.79	II-III:
A2034	13.93	0.1510	8958	2.90	II-III:
A665	13.71	0.1819	38641	3.17	III:
A2670	12.31	0.0761	17701	2.95	I-II
A21	10.86	0.0946	8680	3.67	I:
A545	10.63	0.1540	14285	2.05	III
A1068	10.52	0.1386	10648	2.59	I
A586	9.93	0.1710	4082	2.04	I
A1837	9.17	0.0376	15727	3.38	I-II
A2218	8.74	0.1710	44530	3.49	II:
A500	8.45	0.0666	18400	2.13	III
A1361	7.12	0.1167	5675	2.08	I-II
A2382	6.37	0.0648	25675	3.32	II-III
A514	5.00	0.0731	18111	2.24	II-III:

Note. — Fluxes are from Ebeling (1993) otherwise from this paper (see §7.3). Redshifts compiled from Struble & Rood (1991), Edge et al. (1990), and NED. BM Types are primarily from Leir & van den Bergh (1977), otherwise Sandage & Hardy (1973), Bahcall (1980), and ACO.

Table 2. Power Ratios

NAME	R_{ap}	P_2/P_0		P_3/P_0		P_4/P_0	
OPH.	0.50	9.4	6.7 - 11.8	1.971	1.381 - 2.679	0.023	0.002 - 0.086
A1656	0.45	42.5	41.4 - 46.2	0.270	0.164 - 0.395	0.172	0.122 - 0.218
TRI-AUST	0.50	41.5	24.3 - 39.3	0.234	0.082 - 0.854	0.222	0.032 - 0.310
TRI-AUST	1.00	9.8	6.1 - 11.3	0.217	0.090 - 0.587	0.057	0.007 - 0.145
A2319	0.50	28.5	21.3 - 37.8	1.423	0.539 - 2.823	0.951	0.468 - 1.464
A2319	1.00	3.2	1.3 - 4.8	0.820	0.348 - 1.355	0.023	0.004 - 0.178
A2199	0.50	5.9	4.2 - 6.8	0.051	0.005 - 0.152	0.043	0.013 - 0.090
A496	0.50	4.9	2.6 - 6.3	0.081	0.008 - 0.258	0.023	0.005 - 0.113
A3667	0.50	84.2	67.4 - 91.3	1.965	1.109 - 2.847	0.289	0.033 - 0.453
A3667	1.00	84.8	62.0 - 75.8	1.818	0.764 - 1.781	1.280	0.684 - 1.243
A85	0.50	15.4	10.7 - 17.3	1.100	0.576 - 1.340	0.032	0.001 - 0.089
A85	1.00	13.8	9.8 - 14.8	0.811	0.505 - 1.209	0.166	0.104 - 0.304
A1795	0.50	12.8	11.5 - 14.2	0.003	0.001 - 0.045	0.004	0.001 - 0.016
A1795	1.00	2.0	1.3 - 2.1	0.037	0.007 - 0.061	0.001	0.000 - 0.010
A754	0.50	270.8	191.3 - 251.0	2.062	0.767 - 3.028	3.196	1.694 - 4.008
A3558	0.50	46.7	42.0 - 50.7	0.184	0.072 - 0.391	0.164	0.070 - 0.296
A3558	0.97	52.0	38.4 - 45.3	3.210	2.118 - 3.088	0.451	0.219 - 0.439
A2029	0.50	14.0	10.2 - 15.6	0.031	0.003 - 0.115	0.050	0.007 - 0.115
A2029	1.00	1.7	0.9 - 2.2	0.004	0.001 - 0.059	0.073	0.045 - 0.185
A2029	1.50	2.0	1.4 - 3.3	0.020	0.006 - 0.104	0.060	0.031 - 0.152
A2142	0.50	87.9	76.8 - 92.8	0.393	0.150 - 0.565	1.073	0.731 - 1.310
A2142	1.00	30.0	27.5 - 32.5	0.549	0.399 - 0.758	0.344	0.240 - 0.451
A2142	1.50	5.2	4.1 - 6.5	0.090	0.031 - 0.202	0.047	0.008 - 0.099
A2256	0.50	102.6	97.1 - 112.0	1.582	1.158 - 2.148	0.395	0.252 - 0.555
A2256	1.00	20.8	18.7 - 23.5	0.065	0.022 - 0.160	0.151	0.084 - 0.217
A2256	1.50	4.8	3.7 - 7.6	0.144	0.064 - 0.405	0.143	0.062 - 0.295
A3266	0.50	39.0	30.9 - 45.5	0.266	0.039 - 0.635	0.319	0.092 - 0.534
A3266	0.95	24.7	15.8 - 23.9	0.177	0.008 - 0.322	0.086	0.022 - 0.132
A2052	0.50	13.0	9.3 - 16.5	0.033	0.005 - 0.270	0.031	0.005 - 0.172
HYDRA-A	0.50	4.9	2.9 - 5.4	0.044	0.006 - 0.154	0.029	0.003 - 0.069
HYDRA-A	1.00	5.1	4.5 - 7.4	0.133	0.068 - 0.310	0.055	0.016 - 0.105
A401	0.50	38.6	31.4 - 46.5	0.460	0.181 - 1.099	0.157	0.033 - 0.392
A401	1.00	8.7	5.9 - 11.6	0.098	0.015 - 0.324	0.045	0.005 - 0.138
A401	1.50	7.1	3.8 - 8.8	0.273	0.079 - 0.582	0.002	0.001 - 0.072
A478	0.50	13.5	10.9 - 16.5	0.099	0.029 - 0.300	0.025	0.003 - 0.080
A478	1.00	2.2	1.6 - 3.2	0.045	0.012 - 0.121	0.001	0.000 - 0.021
A478	1.50	0.6	0.3 - 1.2	0.003	0.001 - 0.056	0.002	0.000 - 0.041
A2063	0.50	10.0	5.3 - 12.7	0.196	0.020 - 0.865	0.076	0.004 - 0.228
A119	0.50	21.4	11.6 - 25.1	9.847	5.128 - 9.723	1.218	0.475 - 1.555
A119	0.94	5.3	1.3 - 4.8	2.084	0.901 - 2.319	0.155	0.040 - 0.399
A644	0.50	36.1	26.1 - 39.6	0.521	0.195 - 1.205	0.030	0.005 - 0.189
A644	1.00	7.0	4.8 - 10.4	0.097	0.015 - 0.364	0.030	0.008 - 0.158
A644	1.45	2.2	1.6 - 5.3	0.042	0.004 - 0.279	0.205	0.118 - 0.516

Table 2—Continued

NAME	R_{ap}	P_2/P_0				P_3/P_0		P_4/P_0	
A3158	0.50	43.8	24.2	–	55.8	0.396	0.093 - 2.226	0.294	0.027 - 1.110
A4059	0.50	22.9	15.1	–	32.2	0.198	0.045 - 1.235	0.263	0.096 - 0.907
A4059	1.00	9.8	7.8	–	15.9	0.195	0.022 - 0.803	0.163	0.031 - 0.610
MKW3s	0.50	16.0	9.1	–	18.2	0.053	0.007 - 0.362	0.074	0.005 - 0.245
A3562	0.50	4.7	1.6	–	6.8	5.645	2.514 - 6.032	0.367	0.090 - 0.606
A3562	1.00	32.6	18.6	–	31.3	1.052	0.370 - 1.468	0.247	0.102 - 0.545
A2589	0.50	26.5	18.4	–	34.3	0.107	0.007 - 0.549	0.026	0.003 - 0.276
A1651	0.50	9.9	4.5	–	14.8	0.019	0.013 - 0.507	0.205	0.022 - 0.543
A1651	1.00	10.5	7.7	–	19.2	0.145	0.026 - 0.757	0.059	0.005 - 0.261
A1651	1.50	4.4	2.7	–	8.5	0.272	0.124 - 1.149	0.111	0.029 - 0.358
A2597	0.50	10.5	6.1	–	15.4	0.016	0.006 - 0.414	0.074	0.008 - 0.237
A2597	1.00	3.2	1.9	–	7.8	0.437	0.118 - 1.196	0.010	0.005 - 0.216
A2597	1.50	1.6	0.9	–	4.5	0.332	0.073 - 1.067	0.129	0.031 - 0.411
A2657	0.50	29.7	18.0	–	31.2	0.495	0.198 - 1.176	0.295	0.056 - 0.479
A2204	0.50	2.7	0.6	–	5.2	0.075	0.017 - 0.728	0.157	0.025 - 0.429
A2204	1.00	1.0	0.1	–	2.5	0.453	0.129 - 1.275	0.040	0.005 - 0.290
A2204	1.50	0.0	0.0	–	1.6	0.050	0.013 - 0.669	0.148	0.027 - 0.532
A2244	0.50	3.1	0.2	–	15.3	0.261	0.067 - 2.744	0.109	0.011 - 0.962
A2244	1.00	7.1	4.0	–	21.1	0.532	0.082 - 2.342	0.026	0.007 - 0.405
A2244	1.50	0.7	0.2	–	6.4	0.877	0.322 - 2.972	0.616	0.161 - 1.724
A3532	0.50	20.3	7.9	–	31.5	0.344	0.054 - 3.280	0.110	0.025 - 1.678
A3532	1.00	25.1	9.0	–	31.5	2.323	0.658 - 4.158	0.728	0.130 - 1.298
A400	0.46	49.7	34.5	–	55.5	4.616	2.003 - 6.259	0.366	0.096 - 1.053
A2255	0.50	25.8	14.1	–	38.7	0.054	0.015 - 0.827	0.223	0.017 - 0.909
A2255	1.00	18.4	10.2	–	23.7	0.455	0.041 - 1.143	0.034	0.008 - 0.290
A2255	1.50	2.5	0.2	–	3.5	0.394	0.066 - 1.096	0.619	0.281 - 1.210
A2107	0.50	6.8	2.8	–	13.2	0.583	0.097 - 2.115	0.102	0.005 - 0.449
A3921	0.50	63.4	34.4	–	62.5	0.705	0.114 - 2.156	0.360	0.009 - 0.953
A3921	1.00	135.7	87.5	–	123.3	12.72	7.770 - 14.37	2.309	0.783 - 2.401
A3921	1.50	56.5	35.0	–	59.4	0.524	0.094 - 1.587	0.082	0.008 - 0.354
A1914	0.50	17.6	7.1	–	21.6	1.981	0.958 - 3.520	0.072	0.009 - 0.324
A1914	1.00	1.3	0.3	–	3.7	0.469	0.101 - 1.155	0.139	0.007 - 0.303
A1914	1.50	2.0	1.3	–	5.2	0.232	0.086 - 0.845	0.022	0.004 - 0.230
A1689	0.50	10.4	6.9	–	17.0	0.213	0.038 - 0.811	0.054	0.009 - 0.313
A1689	1.00	6.5	3.4	–	8.7	0.016	0.011 - 0.258	0.033	0.002 - 0.145
A1689	1.50	2.5	1.2	–	4.4	0.037	0.003 - 0.307	0.018	0.003 - 0.103
A1413	0.50	52.2	34.3	–	72.3	0.022	0.032 - 1.490	0.112	0.056 - 0.927
A1413	1.00	25.4	17.1	–	35.9	0.010	0.006 - 0.471	0.120	0.011 - 0.505
A1413	1.50	7.3	2.0	–	10.5	0.026	0.011 - 0.655	0.019	0.008 - 0.260
A1991	0.50	9.9	4.5	–	13.0	0.140	0.012 - 0.532	0.001	0.002 - 0.172
A1991	1.00	1.2	0.1	–	2.8	0.642	0.061 - 1.536	0.036	0.005 - 0.389
A1750	0.50	8.9	0.6	–	15.0	8.599	1.732 - 11.23	0.058	0.030 - 0.819
A1750	1.00	818.5	500.4	–	610.4	6.075	2.145 - 8.838	12.63	5.543 - 9.860

Table 2—Continued

NAME	R_{ap}	P_2/P_0				P_3/P_0		P_4/P_0	
A1750	1.40	311.0	167.6	–	228.0	0.679	0.066 - 2.262	7.333	3.608 - 7.553
A2034	0.50	30.6	10.1	–	53.0	0.442	0.055 - 3.052	0.449	0.031 - 1.599
A2034	1.00	25.8	11.0	–	28.3	0.944	0.173 - 2.159	0.556	0.042 - 0.926
A2034	1.50	16.4	6.7	–	20.7	0.306	0.023 - 1.098	0.019	0.002 - 0.290
A665	0.50	13.8	8.1	–	20.9	2.992	1.417 - 4.303	0.264	0.091 - 0.848
A665	1.00	1.2	0.4	–	3.2	1.254	0.683 - 2.113	0.475	0.220 - 0.734
A665	1.50	0.3	0.1	–	2.2	0.501	0.190 - 1.019	0.017	0.003 - 0.167
A2670	0.50	0.6	0.1	–	3.3	1.758	0.720 - 3.211	0.021	0.006 - 0.265
A2670	1.00	1.2	0.1	–	4.1	1.105	0.275 - 2.060	0.116	0.026 - 0.490
A2670	1.50	1.8	0.3	–	5.4	0.800	0.027 - 1.513	0.104	0.009 - 0.289
A21	0.50	73.4	38.4	–	102.9	4.443	0.862 - 7.947	0.293	0.023 - 1.288
A21	1.00	53.1	24.6	–	64.9	0.893	0.036 - 3.099	0.267	0.023 - 1.101
A21	1.50	11.6	3.8	–	17.9	1.030	0.116 - 4.250	0.622	0.099 - 1.932
A545	0.50	94.0	71.1	–	117.6	0.473	0.067 - 1.867	0.586	0.040 - 0.979
A545	1.00	7.7	2.8	–	11.0	0.454	0.018 - 1.129	0.087	0.015 - 0.395
A545	1.50	0.3	0.0	–	1.8	0.025	0.014 - 0.726	0.206	0.061 - 0.758
A1068	0.50	17.4	9.3	–	23.1	0.137	0.014 - 0.792	0.144	0.015 - 0.591
A1068	1.00	8.5	5.5	–	15.5	0.301	0.062 - 1.070	0.023	0.003 - 0.198
A1068	1.50	2.9	1.5	–	7.6	0.027	0.005 - 0.599	0.046	0.020 - 0.421
A586	0.50	0.4	0.4	–	15.7	1.505	0.195 - 8.263	0.275	0.017 - 1.532
A586	1.00	5.3	1.4	–	20.3	0.147	0.044 - 2.227	0.281	0.036 - 1.510
A586	1.50	1.2	0.2	–	8.0	0.096	0.088 - 1.875	0.163	0.026 - 1.409
A1837	0.50	10.7	1.7	–	15.9	0.413	0.088 - 2.468	0.258	0.093 - 1.504
A2218	0.50	30.6	21.9	–	40.2	0.103	0.012 - 0.709	0.009	0.002 - 0.224
A2218	1.00	25.1	17.1	–	27.9	0.192	0.020 - 0.487	0.045	0.007 - 0.238
A2218	1.50	13.3	8.0	–	18.2	0.159	0.047 - 0.635	0.002	0.002 - 0.166
A500	0.50	17.9	7.9	–	31.8	0.095	0.023 - 1.282	1.197	0.236 - 2.628
A500	1.00	10.3	3.6	–	29.5	0.515	0.053 - 2.272	0.396	0.037 - 1.442
A1361	0.50	8.2	1.9	–	27.0	0.620	0.083 - 4.027	0.177	0.038 - 0.965
A1361	1.00	8.7	3.9	–	24.4	0.641	0.167 - 2.948	0.050	0.014 - 0.729
A1361	1.50	2.1	0.5	–	14.7	0.609	0.147 - 4.484	0.186	0.037 - 1.273
A2382	0.50	33.6	17.5	–	49.7	1.769	0.513 - 5.161	0.299	0.011 - 1.119
A2382	1.00	47.2	21.3	–	52.7	0.668	0.029 - 3.637	0.945	0.260 - 2.732
A514	0.50	273.2	147.9	–	274.0	22.71	11.74 - 30.07	0.679	0.058 - 1.961
A514	1.00	299.6	190.8	–	268.0	5.825	2.275 - 8.315	13.62	7.548 - 13.97
A514	1.45	179.2	96.7	–	158.1	7.396	1.593 - 6.640	0.155	0.018 - 0.653

Note. — The power ratios and their 90% confidence estimates are expressed in units of 10^{-7}. R_{ap} is the aperture radius in h_{80}^{-1}Mpc.

Table 3. Power Ratios

NAME	R_{ap}	$P_1^{(pk)}/P_0^{(pk)}$			
OPH.	0.50	53.	35.	–	159.
A1656	0.45	237.	167.	–	270.
TRI-AUST	0.50	483.	350.	–	735.
TRI-AUST	1.00	93.	55.	–	134.
A2319	0.50	1404.	1269.	–	1784.
A2319	1.00	721.	645.	–	912.
A2199	0.50	14.	6.	–	17.
A496	0.50	55.	28.	–	58.
A3667	0.50	322.	63.	–	633.
A3667	1.00	1042.	473.	–	1030.
A85	0.50	311.	92.	–	324.
A85	1.00	333.	171.	–	328.
A1795	0.50	259.	212.	–	269.
A1795	1.00	77.	64.	–	80.
A754	0.50	5704.	4197.	–	6408.
A3558	0.50	936.	874.	–	982.
A3558	0.97	325.	258.	–	303.
A2029	0.50	37.	26.	–	46.
A2029	1.00	9.	4.	–	13.
A2029	1.50	5.	2.	–	9.
A2142	0.50	10.	4.	–	19.
A2142	1.00	70.	56.	–	84.
A2142	1.50	27.	21.	–	33.
A2256	0.50	3844.	2913.	–	3927.
A2256	1.00	2572.	2118.	–	2632.
A2256	1.50	1213.	1014.	–	1294.
A3266	0.50	3726.	2829.	–	3784.
A3266	0.95	1907.	1209.	–	1683.
A2052	0.50	7.	2.	–	16.
HYDRA-A	0.50	21.	12.	–	27.
HYDRA-A	1.00	38.	34.	–	53.
A401	0.50	115.	9.	–	174.
A401	1.00	193.	132.	–	353.
A401	1.50	239.	205.	–	362.
A478	0.50	25.	15.	–	36.
A478	1.00	5.	2.	–	9.
A478	1.50	1.	0.	–	3.
A2063	0.50	66.	26.	–	133.
A119	0.50	128.	26.	–	267.
A119	0.94	234.	132.	–	321.
A644	0.50	893.	709.	–	918.
A644	1.00	419.	326.	–	450.
A644	1.45	200.	143.	–	218.

Table 3—Continued

NAME	R_{ap}	$P_1^{(pk)}/P_0^{(pk)}$			
A3158	0.50	15.	3.	–	178.
A4059	0.50	38.	6.	–	63.
A4059	1.00	20.	7.	–	41.
MKW3s	0.50	100.	60.	–	112.
A3562	0.50	21.	6.	–	33.
A3562	1.00	123.	73.	–	132.
A2589	0.50	47.	16.	–	77.
A1651	0.50	87.	28.	–	129.
A1651	1.00	52.	25.	–	81.
A1651	1.50	22.	9.	–	40.
A2597	0.50	6.	1.	–	19.
A2597	1.00	1.	0.	–	8.
A2597	1.50	7.	2.	–	32.
A2657	0.50	28.	9.	–	48.
A2204	0.50	14.	7.	–	43.
A2204	1.00	9.	3.	–	28.
A2204	1.50	1.	0.	–	10.
A2244	0.50	94.	13.	–	227.
A2244	1.00	14.	1.	–	71.
A2244	1.50	13.	1.	–	51.
A3532	0.50	36.	11.	–	245.
A3532	1.00	91.	42.	–	228.
A400	0.46	465.	167.	–	398.
A2255	0.50	786.	234.	–	2095.
A2255	1.00	587.	189.	–	1377.
A2255	1.50	135.	16.	–	379.
A2107	0.50	15.	1.	–	44.
A3921	0.50	97.	23.	–	303.
A3921	1.00	508.	171.	–	498.
A3921	1.50	461.	189.	–	425.
A1914	0.50	631.	492.	–	2763.
A1914	1.00	89.	52.	–	531.
A1914	1.50	35.	14.	–	199.
A1689	0.50	521.	261.	–	648.
A1689	1.00	193.	36.	–	222.
A1689	1.50	108.	15.	–	121.
A1413	0.50	19.	6.	–	353.
A1413	1.00	40.	11.	–	79.
A1413	1.50	27.	3.	–	61.
A1991	0.50	2.	0.	–	12.
A1991	1.00	16.	5.	–	28.
A1750	0.50	7.	2.	–	229.
A1750	1.00	3670.	1906.	–	2592.

Table 3—Continued

NAME	R_{ap}	$P_1^{(pk)}/P_0^{(pk)}$			
A1750	1.40	3996.	2079.	–	2849.
A2034	0.50	1055.	262.	–	2143.
A2034	1.00	373.	52.	–	557.
A2034	1.50	377.	118.	–	579.
A665	0.50	3134.	2809.	–	3390.
A665	1.00	2399.	2149.	–	2480.
A665	1.50	1467.	1187.	–	1410.
A2670	0.50	461.	11.	–	949.
A2670	1.00	119.	4.	–	197.
A2670	1.50	81.	5.	–	135.
A21	0.50	294.	63.	–	7876.
A21	1.00	6.	1.	–	3898.
A21	1.50	33.	17.	–	1530.
A545	0.50	452.	264.	–	616.
A545	1.00	405.	230.	–	427.
A545	1.50	269.	166.	–	303.
A1068	0.50	383.	217.	–	433.
A1068	1.00	104.	46.	–	129.
A1068	1.50	49.	17.	–	68.
A586	0.50	53.	11.	–	797.
A586	1.00	62.	26.	–	217.
A586	1.50	37.	8.	–	158.
A1837	0.50	284.	80.	–	279.
A2218	0.50	738.	125.	–	900.
A2218	1.00	444.	85.	–	490.
A2218	1.50	280.	58.	–	277.
A500	0.50	389.	123.	–	551.
A500	1.00	637.	366.	–	937.
A1361	0.50	49.	5.	–	161.
A1361	1.00	12.	2.	–	61.
A1361	1.50	2.	1.	–	51.
A2382	0.50	1042.	835.	–	1501.
A2382	1.00	496.	409.	–	844.
A514	0.50	9369.	6470.	–	8498.
A514	1.00	4833.	2746.	–	3760.
A514	1.45	2557.	1104.	–	2520.

Note. — The power ratios and their 90% confidence estimates are expressed in units of 10^{-7}. R_{ap} is the aperture radius in h_{80}^{-1}Mpc.

REFERENCES

Abell, G. O., Corwin, H. G. J.,& Olowen, R. P. 1989, ApJS, 70, 1

Bahcall, N. 1980, ApJ, L117

Bautz, L. P., & Morgan, W. W. 1970, ApJ, L149 (BM)

Bird, C. M., & Beers, T. C. 1993, AJ, 105, 1596

Briel, U. G., & Henry, J. P. 1994, Nature, 372, 439

Buote, D. A., & Tsai, J. C. 1995a, ApJ, 439, 29

Buote, D. A., & Tsai, J. C. 1995b, ApJ, submitted (BT)

David, L. P., Slyz, A., Jones, C., Forman, W., & Vrtlek, S. D. 1993, ApJ, 412, 479

Dressler, A. 1980, ApJ, 236, 351

Ebeling, H. 1993, Ph.D thesis, Ludwig-Maximilians-Universität München

Edge, A. C., Stewart, G. C., Fabian, A. C., & Arnaud, K. A. 1990, MNRAS, 245, 559

Edge, A. C., & Stewart, G. C. 1991, MNRAS, 252, 428

Edge, A. C., Stewart, G. C., & Fabian, A. C. 1992, MNRAS, 258, 177

Evrard, A. E., Mohr, J. J., Fabricant, D. G., & Geller, M. J. 1993, ApJ, 419, 9

Fabian, A. C. 1994, ARA&A, 32, 277

Hasinger, G. 1992, in The X-ray Background (Cambridge: Cambridge University Press), ed. X. Barcons & A. C. Fabian, 229

Hasinger, G, Turner, T. J., George, I. M., & Boese, G. 1993, MPE/OGIP Calibration Memo CAL/ROS/93-015

Henry, J. P., Briel, U. G., & Nulsen, P. E. J. 199, A&A, 271, 413

Jones, C., & Forman W. 1992, in Clusters and Superclusters of Galaxies (NATO ASI Vol. 366), ed. A. C. Fabian, (Dordrecht/Boston/London: Kluwer), 49 (JF)

Kaiser, N., & Squires, G. 1993, ApJ, 404, 441

Katz, N., & White, S. D. M. 1993, ApJ, 412, 455

Leir, A. A., & van den Bergh, S. 1977, ApJS, 34, 381

Mohr, J. J., Fabricant, D. G., & Geller, M. J. 1993, ApJ, 413, 492

Mohr, J. J., Evrard, A. E., Fabricant, D. G., & Geller, M. J. 1995, ApJ, inpress

Mushotzky, R. F. 1995, in Dark Matter (AIP Conference Proceedings), ed. C. Bennett, (New York: AIP Press), in press

Pfeffermann, E. et al., 1987, Proc. SPIE, 733, 519

Press, W. H., & Schechter, P. 1974, ApJ, 187, 425

Sandage, A., & Hardy, E. 1973, ApJ, 183, 743

Schechter, P., & Press, W. H. 1976, ApJ, 203, 557

Snowden, S. L., Plucinsky, P. P., Briel, U., Hasinger, G., & Pfeffermann, E. 1992, ApJ, 393, 819

Struble, M. F., & Rood, H. J. 1991, ApJ, 77, 363

Richstone, D. O., Loeb, A., & Turner, E. L. 1992, ApJ, 393, 477

Tsai, J. C., Katz, N., & Bertschinger, E. 1994, ApJ, 423, 553

Weir, W. N, Djorgovski, S., Bruzual A., G. 1990, in Evolution of the Universe of Galaxies (ASP vol. 10), ed. R. G. Kron (San Francisco: ASP), 356

West, M. J. 1990, in Clusters of Galaxies (STScI Symp. 4), ed. W. R. Oegerle, M. J. Fitchett, & L. Danly (Cambridge: Cambridge University Press), 65

West, M. J. 1995, in Clusters of Galaxies (Proceedings of the 29th Rencontres de Moriond), ed. F. Durret, A. Mazure, J. Trân Thanh Vân, & S. D. M. White (Gif sur Yvette: Frontier Editions), in press

White, S. D. M., Briel, U. G., & Henry, J. P. 1993, MNRAS, 261, L8

Whitemore, B. C. 1990, in Clusters of Galaxies (STScI Symp. 4), ed. W. R. Oegerle, M. J. Fitchett, & L. Danly (Cambridge: Cambridge University Press), 139

Fig. 1.—
ROSAT PSPC image for A1795 before (left) and after (right) excising point sources. For viewing purposes only we smoothed these images with a Gaussian ($\sigma = 15''$).

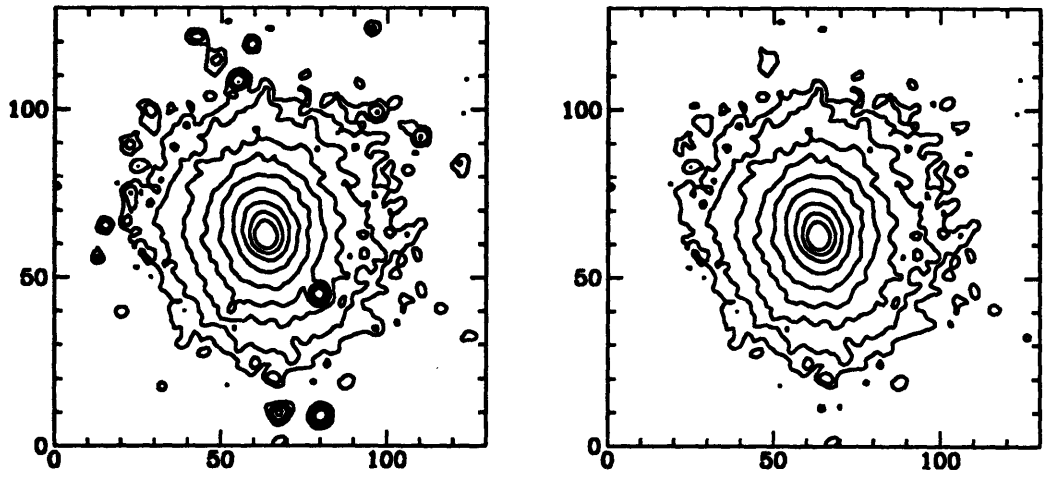

Fig. 2.—
Power ratios as a function of excised sources for A1795. $P_1^{(pk)}/P_0^{(pk)}$ is denoted by crosses, P_2/P_0 by circles, P_3/P_0 by boxes, and P_4/P_0 by stars.

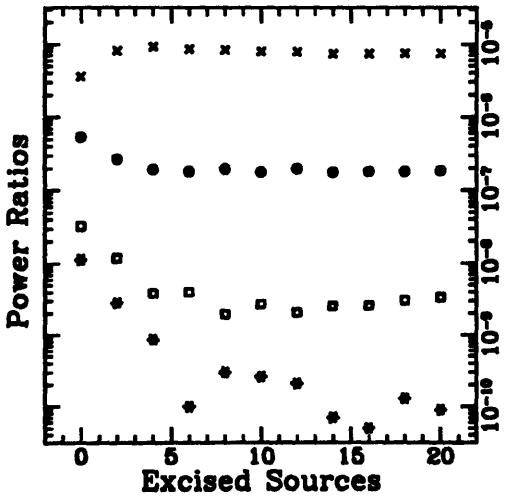

Fig. 3.—
(Left) Power-ratio correlations computed in the $0.5h_{80}^{-1}$ Mpc aperture for the "best measured" clusters (§7.4) and (Right) those also in the Edge et al. (1990) sample.

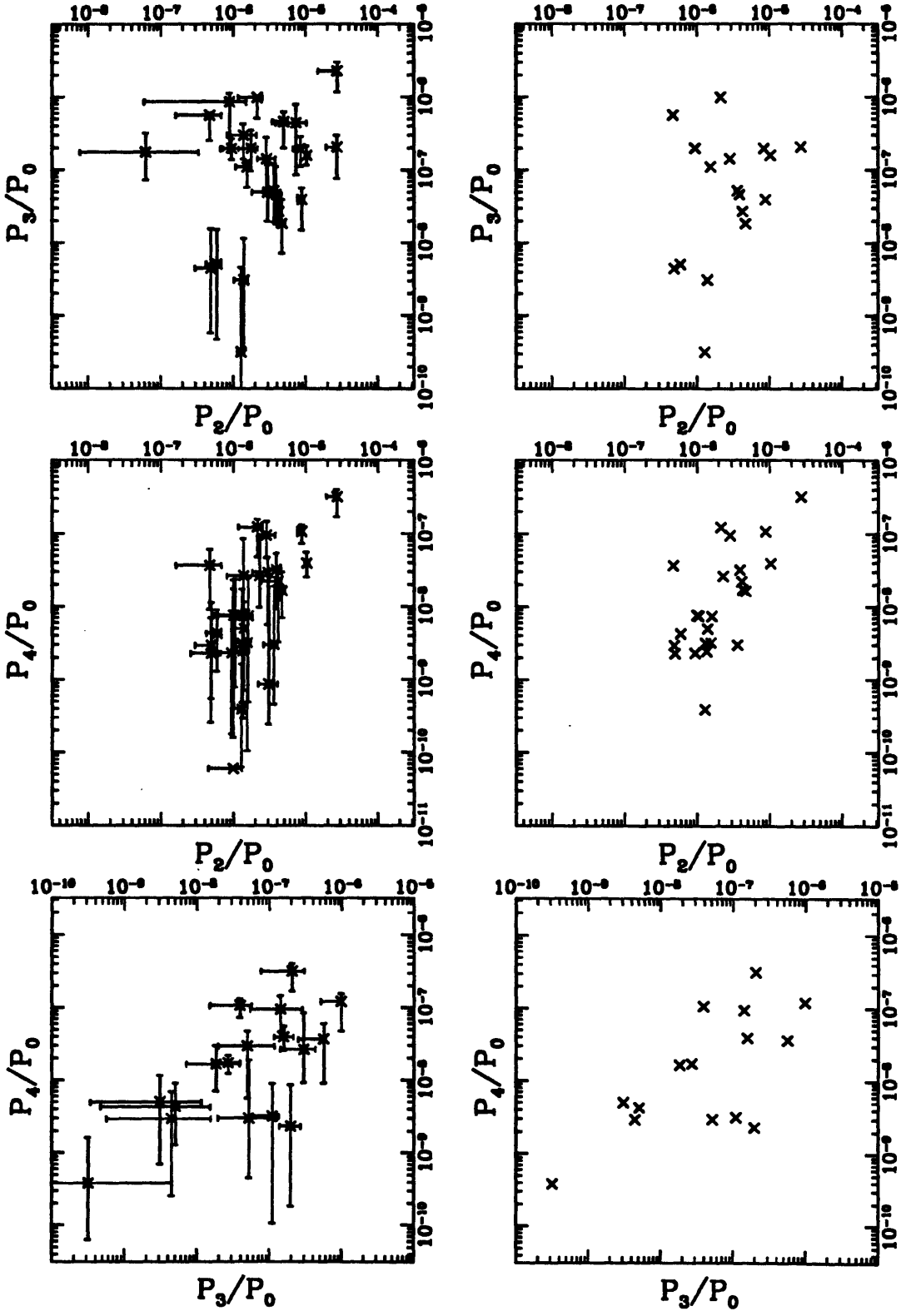

Fig. 4.—
Same as Figure 3 for the power ratios computed in the $1h_{80}^{-1}$ Mpc aperture.

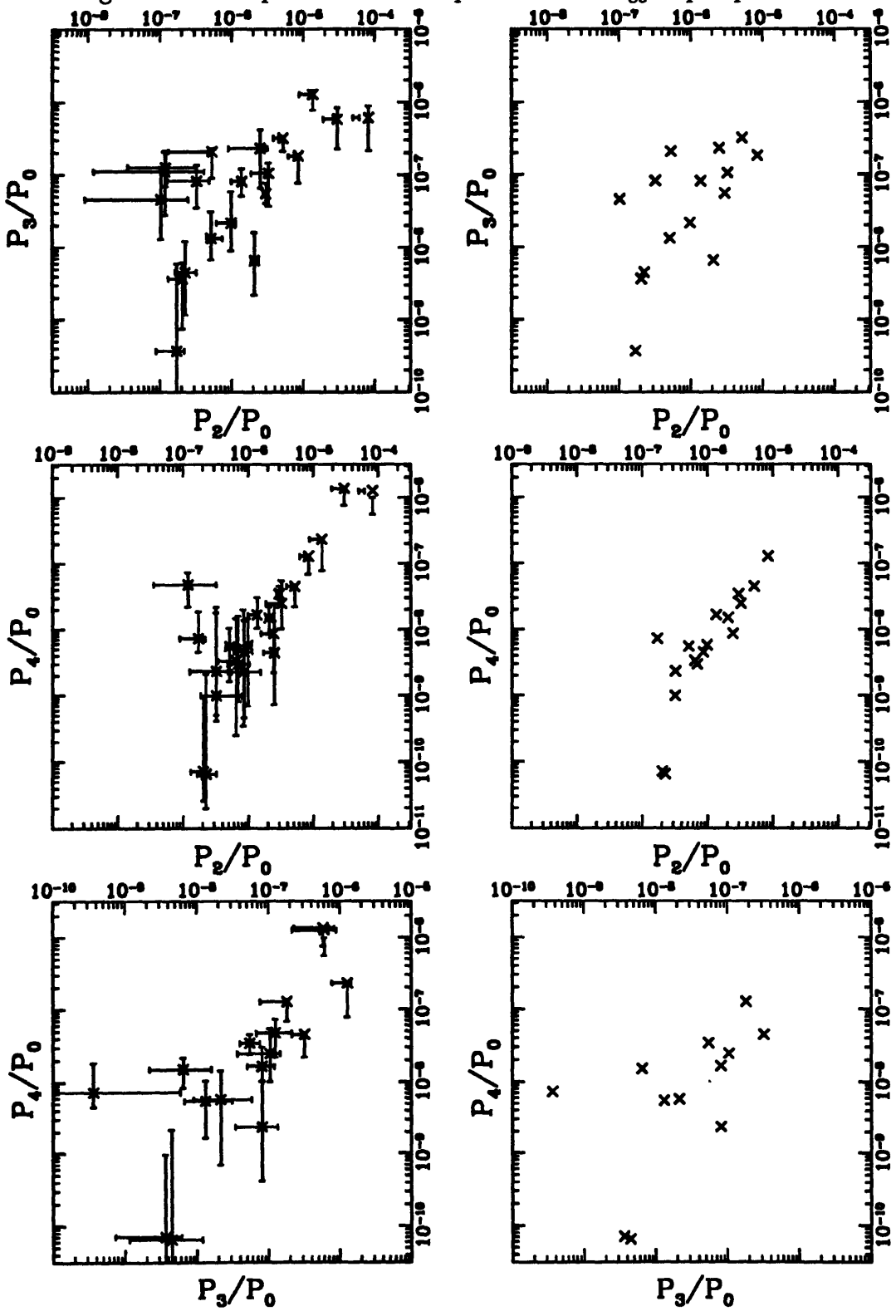

Fig. 5.—
Power ratios for the "reference" clusters computed in the $0.5h_{80}^{-1}$ Mpc aperture (see §7.4).

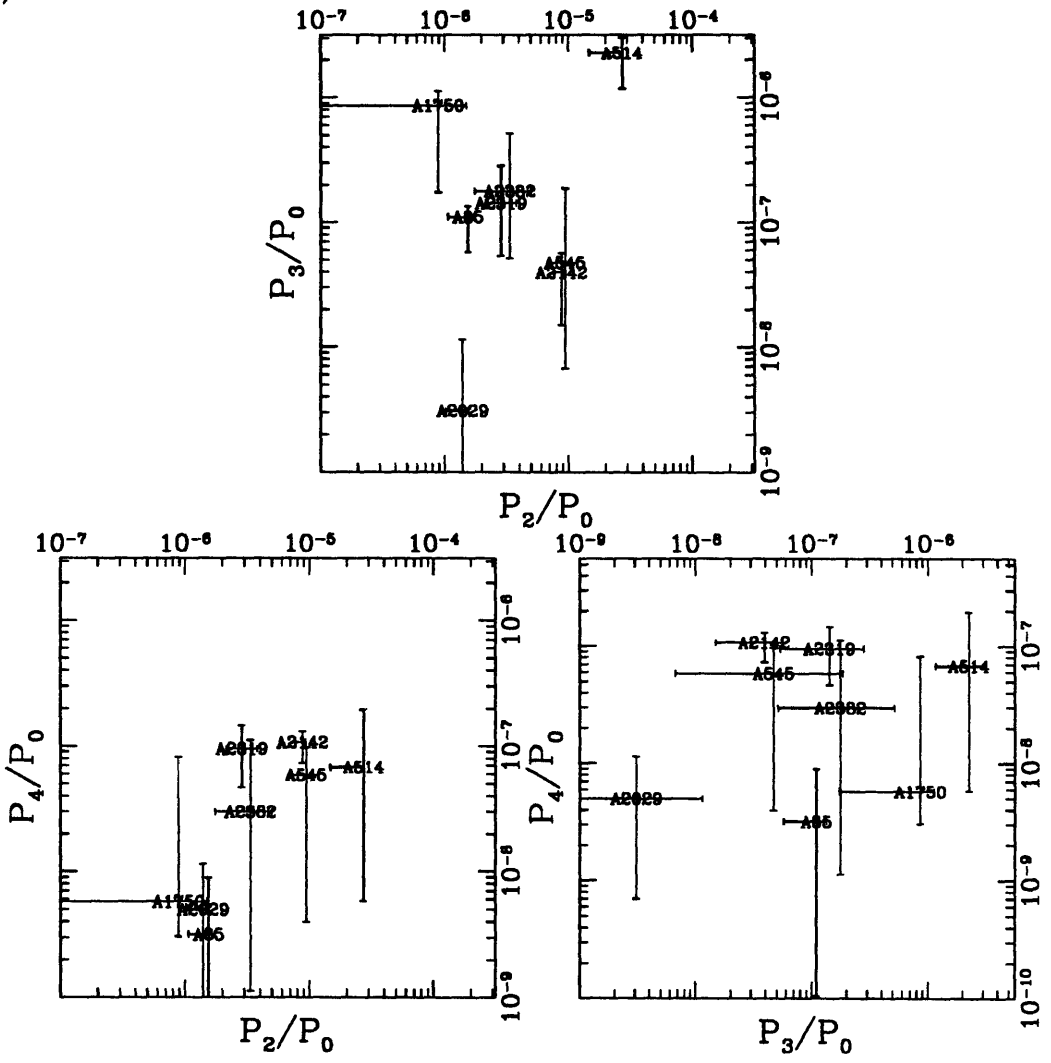

Fig. 6.—
Power ratios for the "reference" clusters computed in the $1h_{80}^{-1}$ Mpc aperture (see §7.4).

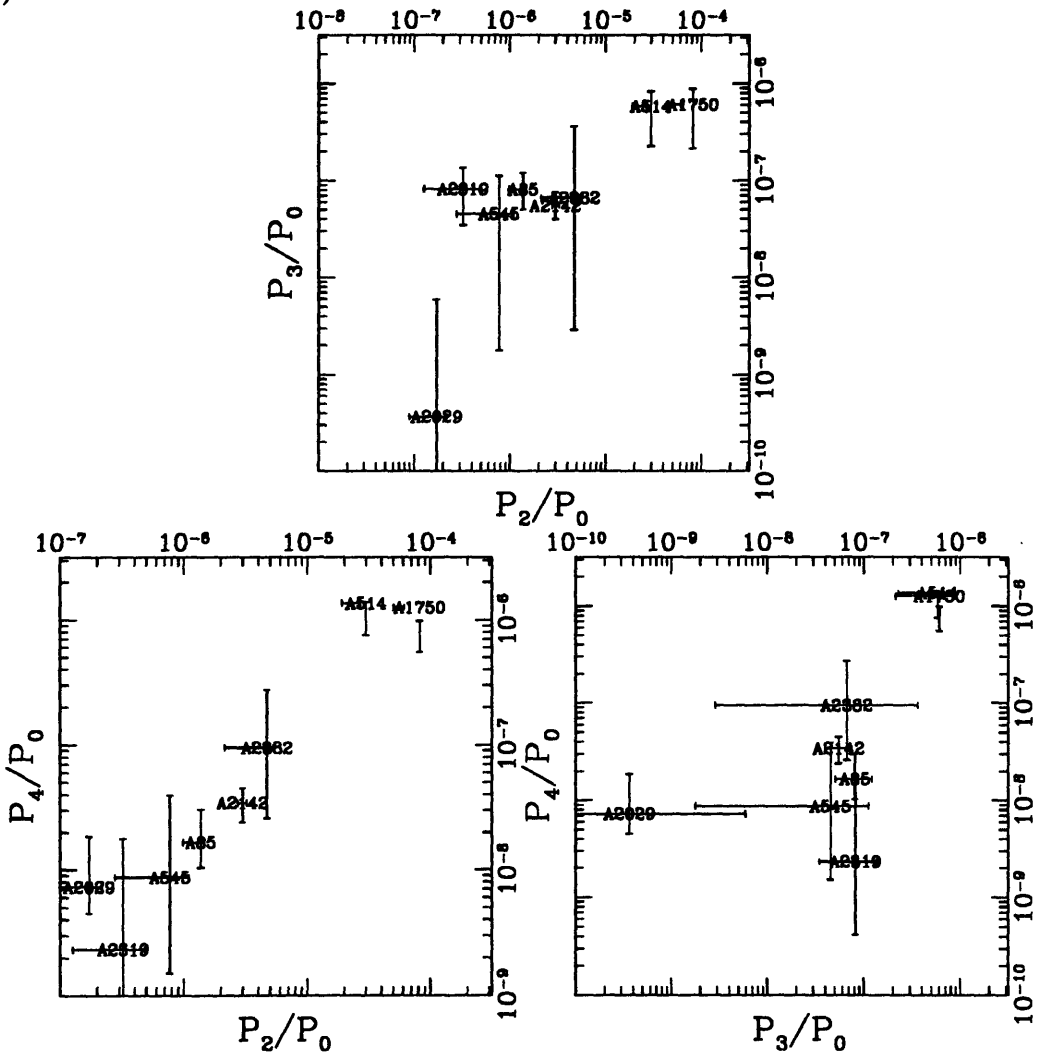

Fig. 7.—
Mass-flow rate from Fabian (1994) vs P_2/P_0 computed in the $1h_{80}^{-1}$ Mpc aperture for the clusters in our sample corresponding to that of Edge et al. (1990). The clusters on the bottom axis have no detected cooling.

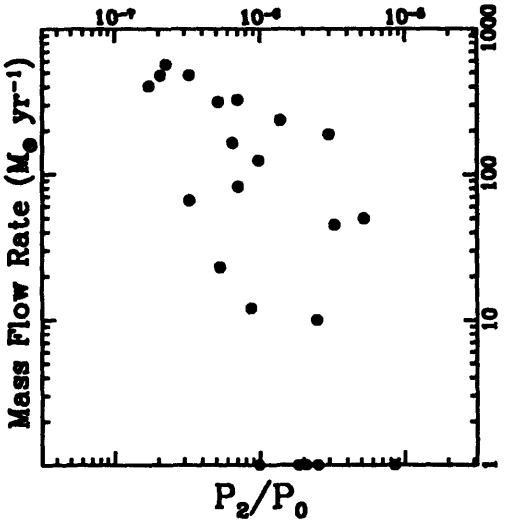

Fig. 8.—
Bautz-Morgan Type (see Table 1) vs P_2/P_0 computed in the $1h_{80}^{-1}$ Mpc aperture for all clusters in our sample (left) and those corresponding to the Edge et al. (1990) sample (right).

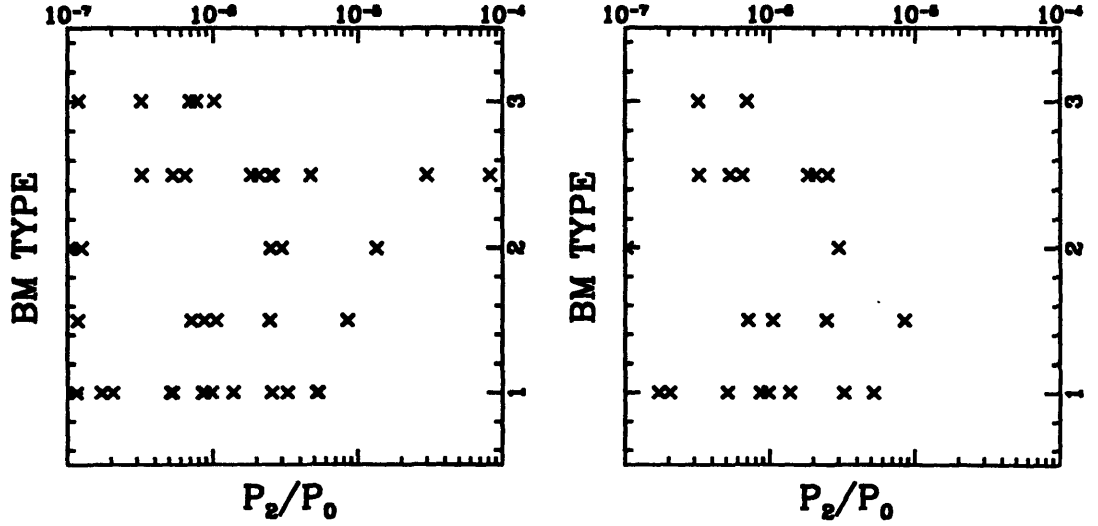

Chapter 8

Conclusions

8.1 Summary

I have had the distinct pleasure to investigate both observational and theoretical issues regarding the structure and dynamics of elliptical galaxies and galaxy clusters. My observational studies were mostly restricted to X-ray analysis of ROSAT PSPC data, both from Claude's guest observations and also from the ROSAT Public Data Archive. The theoretical studies were fortuitous and resulted from questions raised during my observational investigations of the intrinsic shapes of ellipticals and clusters.

I developed a new test for dark matter in ellipticals that specifically addresses the elongation of the X-ray isophotes, yet is completely independent of the temperature gradient of the gas. This test assumes only that the gas is adequately described by a single-phase fluid in hydrostatic equilibrium (i.e. the gas iso-emissivity surfaces trace the isopotential surfaces) and in principle does not require any model fitting. Applying this "geometric" test for dark matter to ROSAT PSPC data of the E4 galaxy NGC 720, as well as extending the traditional hydrostatic modeling techniques, I find that NGC 720 has an extended halo of dark matter that is highly elongated with ellipticity, $\epsilon \approx 0.5 - 0.7$, and at least four times as massive as the visible stars in the galaxy; similar, but weaker, constraints are obtained for the E7/S0 galaxy NGC 1332. These galaxies (especially NGC 720) provide the first strong evidence for flattened dark halos in normal (i.e. no polar ring) galaxies mostly free from uncertainties in

possible temperature gradients. The ellipticities of the dark halos are consistent with those predicted by N-body / hydrodynamic simulations (Dubinski 1994), although they allow for larger ellipticities then produced by the simulations in which case would suggest that the dark matter is significantly dissipational (e.g., Ashman 1992; Sackett et al. 1995).

Using the N-body / hydrodynamic simulation of Katz & White (1993) I tested the viability of X-ray constraints of the intrinsic shapes of clusters of galaxies especially considering the effects of substructure. I concluded that for substructure confined to small scales ($\lesssim 300$ kpc) the X-ray constraints of the aggregate shape of the clusters on scales $r \sim 1-2$ Mpc are indeed valid; i.e. equilibrium analysis of the aggregate shape on large scales is insensitive to subclustering on small scales. Bolstered by this finding, I analyzed the aggregate intrinsic shapes of five Abell clusters with ROSAT PSPC data as a follow-up to my previous study of these clusters with the *Einstein* IPC (Buote & Canizares 1992; Buote 1992). I find that the clusters are very elongated ($\epsilon \approx 0.40-0.55$) on scales $r \sim (1-1.5)h_{80}^{-1}$ Mpc and have large baryon fractions, $(4\%-11\%)h_{80}^{-3/2}$, consistent with the "Baryon Catastrophe" proposed by White et al. (1993). These ellipticities are substantially larger than I obtained in the previous analysis of IPC data which I understand to be the result of me (in Buote & Canizares) not accounting for the steep ellipticity gradients of the X-ray isophotes obtained for these clusters from PSPC data. The dark matter ellipticities I derived from the PSPC data are consistent with N-body simulations (Frenk et al. 1988; Efstathiou et al. 1988) and the shapes of the galaxy isopleths in the clusters. These represent the first robust constraints on the aggregate intrinsic shapes of the dark halos of clusters.

Finally, I devised a method to quantify the morphologies of galaxy clusters in direct relation to their dynamical state; i.e. I have taken the perspective that the existence of "substructure" in clusters is given and have now examined what "substructure" implies for the evolutionary state of a cluster. The statistics of this method, i.e. *power ratios* (P_m/P_0), essentially measure the square of the ratio of the mth multipole moment to the monopole term in the gravitational potential. Applying the power ratios to ROSAT PSPC images of a sample of 55 Abell clusters I find that

they exhibit a particularly strong $P_2/P_0 - P_4/P_0$ correlation in the $1h_{80}^{-1}$ Mpc aperture which may be interpreted as an evolutionary track; the location of a cluster on the correlation line indicates the dynamical state of the cluster and the distribution of clusters along this track measures the rate of formation and evolution of clusters in our sample. Since power ratios provide a measure of the evolutionary states of clusters, in principle they can be used to address any problem where cluster evolution is an issue. They are ideally suited to test the Morphology – Cosmology Connection (MCC; Richstone, Loeb, & Turner 1992; Evrard et al. 1993; Mohr et al. 1995) which states that the observed structure of X-ray clusters is sensitive to the cosmological density parameter Ω. The power ratios provide a natural means to "correct" X-ray mass estimates of clusters due to departures from hydrostatic equilibrium. They may also be used to search for and summarily remove the effects of evolution in distance indicators like Brightest Cluster Galaxies (BCGs).

8.2 Future Prospects

The work I have presented in this thesis represents initial thrusts into areas previously either sparsely explored or completely ignored. Still much remains to be learned from continued investigation along these lines – be it "tightening the loose ends" or exploring the new avenues opened. Is the flattened dark halo of NGC 720 (and NGC 1332) typical for ellipticals? Is the position-angle offset of the X-rays and optical light observed in other galaxies, and is it a signal of triaxiality? Does the "geometric test" for dark matter applied to other galaxies give results inconsistent with alternative gravity theories like MOND?

As shown in Figure 12 of Chapter 3 the primary determinant of the precision of the X-ray constraints on the intrinsic shapes is the accuracy to which the ellipticity of the X-ray isophotes can be measured. There are only a handful of galaxies observed with the PSPC that have the appropriate flux, angular size, and degree of isolation from other galaxies to allow for a good estimate of the shape of a dark halo similar in quality to NGC 720 and NGC 1332. Although the ROSAT HRI has spatial resolution

superior to the PSPC, its much lower sensitivity makes these observations difficult. Claude and I, however, have obtained a relatively deep (60ks) observation of NGC 720 to complement our previous analysis with the PSPC. With the HRI observation we can probe the region within a few kpc from the center of the galaxy that may yield important clues to the origin of the position angle offset of the X-ray and optical distributions.

X-ray analysis of the intrinsic shapes will enter a new era with the launch of the X-ray Astrophysics Facility (AXAF) because of its expected enormous improvement in spatial resolution (PSF = 0.19″ FWHM at 1.5 keV) coupled with a very respectable quantum efficiency. At that time precise constraints on the shapes of the dark halos of a large sample of early-type galaxies will be feasible. Moreover, the high-quality spatial and spectral data should allow for a non-parametric treatment that simply involves solving the hydrostatic equation for the potential in terms of the gas density and temperature which may be obtained from general spheroidal deprojection following Palmer (1994).

To investigate these questions it is also imperative to verify the assumptions underlying the X-ray analysis using improved spectral data. The contribution to the X-ray emission in early-type galaxies from discrete sources must be accurately determined; much can be understood at present using data from the ASCA satellite. Although it is not a major source of uncertainty (since shape constraints are insensitive to the small temperature gradients that have been observed for ellipticals, including our analysis of NGC 720) the temperature profiles must be known as precisely as possible for the detailed hydrostatic modeling procedures; AXAF will have the necessary combined spectral and spatial resolution to map the temperature profiles of many bright galaxies. At present, the importance of rotation of the gas in ellipticals is unknown and although we argue that plausible rotation does not seriously affect the shapes, others have predicted that the effect could be significant in a rotating cooling flow (Kley & Mathews 1995). It is indeed unfortunate that there is no instrument on the astrophysics horizon that will have the capability to measure rotation of the X-ray–emitting gas in ellipticals, although AXAF should be able to constrain signatures of

a cooling flow.

The PSPC and ASCA data already allow precise constraints on the intrinsic shapes of bright, nearby clusters ($z \lesssim 0.1$) and non-parametric analysis is probably feasible for some of the clusters we studied in Chapter 5. AXAF will be particularly useful for analyzing more distant clusters, although the XMM might be more appropriate for some clusters because of its larger field of view. The key issue for analyzing cluster shapes is verifying the assumption of hydrostatic equilibrium. As mentioned above, spectral analysis of the quality to measure motions of the gas will not be feasible in the foreseeable future. However, the power ratios may provide a means to estimate whether a cluster is sufficiently relaxed for application of hydrostatic analysis of its shape.

The power ratios need to be explored on several fronts. It is of particular importance to examine the power ratios predicted by N-body / hydrodynamic simulations for different cosmological models in order to determine whether the structure of clusters can place important constraints on Ω, the primordial power spectrum, and perhaps the magnitude of a cosmological constant. The simulations also provide the means to construct a "template" for correcting X-ray measurements of the masses of clusters.

Since power ratios describe the dynamical states of clusters they can be used to examine the effects of evolution in other astrophysical quantities. Do the magnitudes of BCGs correlate with the power ratios? Do the power ratios correlate with the fraction of galaxy morphological types in clusters (i.e. the Dressler (1980) Morphology-Density relation)? Do the galaxy luminosity functions in clusters and power ratios correlate? Although these questions can be usefully investigated at present, definitive conclusions will have to wait for improved constraints on the power ratios obtained in Chapter 7 and other nearby clusters; it will be also necessary to obtain precise measurements of the power ratios for more distant clusters. Because of the larger angular sizes of nearby clusters, the XMM (rather than AXAF) is particularly suited to obtaining precise constraints on the power ratios. For distant clusters, though, AXAF will be the instrument of choice.

Because the power ratios do not require any assumptions about the dynamical state of a cluster (i.e. that is what they are measuring!), I think they will prove more useful than traditional X-ray methods for probing the dynamics of clusters. As an example, Kaiser (1991) makes the exciting prediction that morphological differences between the X-rays and mass in high-redshift clusters ($z \sim 0.5$) may provide important restrictions on the nature of the dark matter. The logical means to investigate this issue is to compare the dynamical state of the cluster as indicated by the X-ray gas with that indicated by the mass distribution obtained from weak lensing (Kaiser & Squiers 1993). The power ratios may be applied to both the X-rays and the weak-lensing maps to allow a consistent test of the evolutionary states given by the different distributions.

I can only hope that I am so fortunate to be granted the opportunity to investigate these issues in the years to come.

REFERENCES

Ashman, K. M. 1992, PASP, 104, 1119

Buote, D. A. 1992, S.M. Thesis, Massachusetts Institute of Technology

Buote, D. A., & Canizares, C. R. 1992, ApJ, 400, 385

Dressler, A. 1980, ApJ, 236, 351

Dubinski, J. 1994, ApJ, 431, 617

Efstathiou, G., Frenk, C. S., White, S. D. M., & Davis, M. 1988, MNRAS, 235, 715

Evrard, A. E., Mohr, J. J., Fabricant, D. G., & Geller, M. J. 1993, ApJ, 419, 9

Frenk, C. S., White, S. D. M., Efstathiou, G., & Davis, M. 1988, ApJ, 327, 507

Kaiser, N. 1991, ApJ, 383, 104

Kaiser, N., & Squiers, G. 1993, ApJ, 404, 441

Katz, N., & White, S. D. M. 1993, ApJ, 412, 455

Kley, W., & Mathews, W. G. 1995, 438, 100

Mohr, J. J., Evrard, A. E., Fabricant, D. G., & Geller, M. J. 1995, ApJ, in press

Palmer, P. L. 1994, MNRAS, 266, 697

Richstone, D. O., Loeb, A., & Turner, E. L. 1992, ApJ, 393, 477

Sackett, P., Rix, H-W, Jarvis, B. J., & Freeman, K. C. 1994 ApJ, 436, 629

White, S. D. M., Navarro, J. F., Evrard, A. E., & Frenk, C. S. 1993, Nature , 366, 429

5815-34